

# Dynamics and Applications of Dissipative Kerr Solitons

Présentée le 7 février 2020

à la Faculté des sciences de base  
Laboratoire de photonique et mesures quantiques (SB/STI)  
Programme doctoral en physique

pour l'obtention du grade de Docteur ès Sciences

par

**Maxim KARPOV**

Acceptée sur proposition du jury

Prof. F. Mila, président du jury  
Prof. T. Kippenberg, directeur de thèse  
Prof. A. M. Weiner, rapporteur  
Prof. M. Loncar, rapporteur  
Prof. N. Grandjean, rapporteur



To my parents Aleksandr and Alevtina,  
to my wife Tatiana.



# Acknowledgements

First, I would like to thank my advisor, Prof. Tobias Kippenberg for the opportunity to join LPQM as a PhD student and become a part of a very enthusiastic, friendly, knowledgeable and productive team. I thank Prof. Kippenberg for the tremendous research opportunities I have had during the past 5 years, and for his trust and support in all of the projects we accomplished. It would be also far less without his continuous drive, enthusiasm and his ability to spark motivation and new ideas.

I would like to express my sincere gratitude to Prof. M.L. Gorodetsky, who has become a good friend of mine during his summer visits to Lausanne, and who has regretfully passed away in January 2019. I enjoyed a lot working together on a number of joint projects between LPQM and his team at the Russian Quantum Center (RQC). I remember our late-evening discussions about science and life in our offices, and I always admired his modesty, visionary spirit and the deepest understanding of physics.

I thank all LPQM members, who warmly welcomed me, when I joined the group and helped a lot during my first steps in the area of Kerr combs. I am deeply thankful to Martin Pfeiffer for his guidance and support. We spent a lot of time establishing Kerr comb activity in the PHA lab, sharing the same optical table and using the “pumping setup” for numerous joint and our own experiments. I thank Arne Kordts, who fabricated the famous “golden batch”, which lies at the foundation of this Thesis, and which has enabled many studies on soliton dynamics and applications. I thank Victor Brasch, who was the first to obtain soliton states in silicon nitride, and openly shared all his knowledge and expertise. I highly appreciate his many pieces of advice and help in soliton experiments, which would not have gone that far without his support.

I thank a lot Hairun Guo and Erwan Lucas for our collaborative and enjoyable work together on soliton dynamics. Many simulations and simulation tools were initiated and developed by Hairun, who was always very educative and patient in working with me and my experimental results. I thank Erwan for our joint and mutually supportive adventure through the jungle of the soliton dynamics in microresonators. I learnt from his striving for excellence and attention to detail in both experiments and manuscript writing. I warmly remember our many hours of discussion of experimental results, simulations and manuscript corrections with both Hairun and Erwan. I believe that all fascinating phenomena, which were discovered, understood, and finally published were only due to the full dedication, enthusiasm and wish to get to the heart of the matter of all three of us.

## Acknowledgements

---

I thank Alexey Feofanov, who has made a crucial contribution to my decision on joining LPQM. He was always ready to share his wisdom and life experience, which I appreciate a lot. On many occasions, his advice or magical problem-solving skills were extremely useful not only within but also outside of the lab.

I also would like to thank other team members, with whom I had a chance to work with: John Jost, Nicolas Piro, Caroline Lecaplain, Clément Javerzac-Galy, Michael Geiselmann, Michael Zervas and Dalziel Wilson.

I would like to thank all my office mates, with whom I spent a good part of my PhD years, and who established and maintained a hard-working, but lovely and cozy atmosphere in our PH D3 305 office: Philippe Rölli, Hairun Guo, Ayman Kamel, Junqiu Liu, Anton Lukashchuk, Johann Riemensberger and Mikhail Churaev. I particularly thank Philippe, for all the conversations on the literature and music we had apart from our scientific discussions and attempts to build a joint experiment. I am proud that you had the courage to start learning Russian and were already able to understand some basics.

I also would like to thank a new generation of students and postdocs, who joined LPQM over the past years, and who already immensely contributed to our success: Clemens Herkommer, Tiago Morais, Junqui Liu, Arslan Raja, Wenle Weng, Alexey Tikan, Aleksandr Tusnin, Tianyi Liu, Xin Fu, Jijun He, Rui Ning Wang, Jordan Wachs, Connor Skehan and Anat Siddharth. I thank Miles Anderson for our enlightening discussions on soliton physics and his mastery to explain it not only with words, but also with incredible gesturing. I surely will not forget your ad-hoc English grammar lessons and the time you spent fixing my texts. I thank Anton Lukashchuk, who took over my experimental legacy in the PHA lab. We have become good friends sharing the same office during the past 2.5 years and I always appreciate our multiple discussion, mutual motivation and your ability to argue and challenge my point of view.

I thank our optomechanics team for being a good counterpart of the comb team: Itay Shomroni, Nils Engelsen, Liu Qiu, Sergey Fedorov, Alberto Beccari, Mohammad Bereyhi, Amir Youssefi, Guanhao Huang, Yash Joshi, Tatiana Vovk and Amirali Arabmoheghi. I appreciate the lunches we had together, our friendly mutual jokes as well as the help and advice they are always ready to provide.

A part of this Thesis has only become possible due to the great and fruitful collaborations I was involved in with teams from Germany, Russia, UK and USA. I would like to thank Prof. Christian Koos (KIT), Prof. Alan Willner (USC), Prof. Sunil Bhave (Purdue University), Prof. Wolfram Pernice (University of Münster) and Dr. Hitesh Ballani (Microsoft Research, Cambridge) for the great opportunities to learn new fascinating things outside of Kerr combs and often becoming the driving part of our collaborations. Of course, the actual work in the lab would have never been accomplished without all the efforts from students and postdocs from these teams. I thank all the people I have met during my visits, and had a chance to work with and learn from: Pablo Marin-Palomo (KIT), Juned Kemal (KIT), Philipp Trocha (KIT), Changjing Bao (USC), Peicheng Liao (USC), Sophie Lange (Microsoft), Kai Shi (Microsoft), and Johannes Feldmann (University of Münster).





# Abstract

Optical frequency combs are optical sources, whose spectra consist of a series of equally spaced narrowband frequencies. They have made an outstanding leap forward in the accuracy of optical frequency metrology and became an attractive tool for numerous applications including optical atomic clocks, fast telecommunications, astronomy, molecular spectroscopy, and microwave and optical waveform synthesis.

Discovered in 2007, microresonator-based frequency combs (also Kerr combs) have made a breakthrough in the field by enabling optical comb generation from a continuous-wave laser via nonlinear parametric frequency conversion effects, enhanced within a high-quality microresonator. Kerr combs have attracted significant attention due to their ability to operate in a soliton regime when self-sustaining optical pulses – dissipative Kerr solitons – are formed in the microresonator relying on a double balance between the dispersion and nonlinearity of the system, as well as cavity losses and the gain from the driving laser. Dissipative Kerr solitons allow access to broadband, coherent optical combs with large repetition rates from microwave to terahertz domains, which can be generated from chip-scale microresonators. Due to their compactness and unprecedented performance, such soliton-based Kerr combs represent a promising solution for a variety of real-world optical comb applications, which has been demonstrated over the last four years.

In this thesis, several aspects of dissipative Kerr soliton dynamics are investigated in integrated silicon nitride microresonators. The results include the first experimental study of the Raman-induced self-frequency shift in dissipative Kerr solitons, the discovery and explanation of the soliton switching phenomenon, which enables controllable successive elimination of soliton pulses from a microresonator, the experimental observation of breathing soliton states as well as the demonstration of collectively-ordered soliton ensembles – perfect soliton crystals. The results are universal across other soliton generating platforms. Apart from elucidating basic dynamical properties of dissipative Kerr solitons, they contribute to the understanding of soliton behavior in the presence of high-order nonlinear, dispersion and thermal effects in real systems. Besides the study of the soliton dynamics, probing and manipulation techniques for dissipative Kerr solitons are developed. They enable deterministic soliton switching and controllable access to application-relevant single soliton states. The techniques also allow for non-destructive monitoring of key soliton parameters, and controllable soliton state translations in the parameter space of the driven microresonator system. The developed understanding and control of soliton states are used to demonstrate dissipative Kerr solitons operating

## Acknowledgements

---

at 1- $\mu\text{m}$  wavelength and covering the biological imaging window. Furthermore, in collaboration with the Karlsruhe Institute of Technology, soliton-based combs generated in silicon nitride microresonators are employed for massively parallel optical coherent communications and ultrafast optical ranging, where the record performance of DKS states in both applications has been demonstrated. Lastly, a rack-mountable standalone system for the generation of dissipative Kerr solitons, which can be readily used outside of the laboratory environment, is developed, tested and is employed in the first experiments on optical circuit switching for data centers and all-optical convolution neural networks.

**Keywords:** nonlinear photonics, optical frequency combs, optical microresonators, Kerr combs, dissipative Kerr solitons, soliton crystals, soliton switching, Raman self-frequency shift, breathing dissipative solitons, optical coherent communication, LiDAR.

# Résumé

Les peignes de fréquence optiques sont des sources optiques, dont le spectre se compose d'une série de fréquences optique également equi-espacées et de grande finesse spectrale. Ils ont permis de réaliser une avancée remarquable dans la métrologie optique de haute précision et sont devenus un outil attrayant pour de nombreuses applications, telles que les horloges atomiques optiques, les télécommunications rapides, l'astronomie, la spectroscopie moléculaire, la synthèse de micro-ondes ou de formes d'ondes optiques. Découverts en 2007, les peignes de fréquence à base de microrésonateurs (également appelés peignes de Kerr) ont constitué une percée dans ce domaine, en permettant la génération de peignes optiques à partir d'un laser à onde continue via des effets de conversion de fréquence paramétrique, qui se trouvent renforcés dans un microrésonateur à haut facteur de qualité. Les peignes Kerr ont reçu une grande attention, en raison de leur capacité à fonctionner en régime de solitons, lorsque des impulsions optiques autonomes – des solitons dissipatifs de Kerr – se forment dans le microrésonateur, du fait d'un double équilibre entre la dispersion et la non-linéarité du système ainsi qu'entre les pertes de la cavité et le gain du laser de pompe. Les solitons dissipatifs de Kerr permettent d'obtenir des peignes optiques cohérents couvrant une large bande spectrale avec des taux de répétition très élevés, dans les domaines micro-ondes jusqu'aux térahertz, qui peuvent être générés par des micro-résonateurs intégrés sur puce. Grâce à leur compacité et à leurs performances sans précédent, ces peignes Kerr à base de solitons représentent une solution prometteuse pour certaines applications pratiques des peignes optiques, ce qui a été démontré au cours des quatre dernières années.

Dans cette thèse, plusieurs aspects de la dynamique des solitons dissipatifs de Kerr sont étudiés dans des microrésonateurs intégrés en nitrure de silicium. Les résultats comprennent la première étude expérimentale de l'auto-décalage spectral induit par effet Raman dans les solitons dissipatifs de Kerr, la découverte et l'explication du phénomène de transition entre états de solitons, qui permet l'élimination successive et contrôlable des impulsions de solitons d'un microrésonateur, l'observation expérimentale des oscillations soliton (respiration) ainsi que la démonstration d'ensembles solitoniques ordonnés – nommés cristaux parfaits de solitons. Ces résultats universels sont observés sur toutes les autres plates-formes permettant la génération de solitons dissipatifs, et permettent d'élucider les propriétés dynamiques fondamentales des solitons dissipatifs en cavité. De plus, ils contribuent à la compréhension du comportement de ces solitons en présence d'effets non linéaires additionnels tels que la dispersion d'ordre supérieur et les effets

## Acknowledgements

---

thermiques présents dans les systèmes réels. Outre l'étude de la dynamique des solitons, des techniques de sondage et de manipulation des solitons dissipatifs de Kerr sont développées. Ils permettent la transition déterministe entre états de solitons et la génération contrôlée d'un soliton unique dans la cavité, ce qui est importants pour les applications. Ces techniques permettent également un contrôle non destructif des principaux paramètres de solitons et des translations contrôlées de l'état des solitons dans l'espace des paramètres du système de microrésonateurs pompé. Cette meilleure compréhension et ce contrôle des états de solitons sont utilisés pour démontrer les solitons dissipatifs de Kerr fonctionnant à une longueur d'onde de 1  $\mu\text{m}$  et couvrant la fenêtre d'imagerie biologique. De plus, en collaboration avec l'Institut de technologie de Karlsruhe (KIT), des peignes à base de solitons dissipatifs de Kerr générés dans des micro-résonateurs en nitrure de silicium sont utilisés pour des expériences de communications optiques cohérentes massivement parallèles et des mesures optiques ultra-rapides, où les performances record des états DKS ont été démontrées dans les deux applications. Enfin, un système autonome assemblé en rack permettant la génération de solitons dissipatifs de Kerr, est développé, testé et utilisé dans les premières expériences de commutation de circuits optiques pour centres de données et réseaux neuronaux à convolution tout optique, démontrant les premières utilisations de cette technologie en dehors de l'environnement de laboratoire.

**Mots clés :** photonique non linéaire, peignes de fréquence optique, microrésonateurs optiques, peignes de Kerr, solitons dissipatifs de Kerr, cristaux de solitons, transition de solitons, d'auto-décalage spectral par effet Raman, solitons dissipatifs oscillant, communication optique cohérente, LiDAR.

# Publication List

## Main publications

- **M. Karpov**, M.H.P. Pfeiffer, H. Guo, W. Weng, J. Liu and T.J. Kippenberg, "Dynamics of soliton crystals in optical microresonators", *Nature Physics*, 15, pp.1071–1077, (2019).
- **M. Karpov**, M.H.P. Pfeiffer, J. Liu, A. Lukashchuk, T.J. Kippenberg, "Photonic chip-based soliton frequency combs covering the biological imaging window", *Nature communications*, 9(1), p.1146, (2018).
- P. Trocha\*, **M. Karpov\***, D. Ganin\*, M.H.P. Pfeiffer, A. Kordts, S. Wolf, J. Krockenberger, P. Marin-Palomo, C. Weimann, S. Randel, W. Freude, T.J. Kippenberg, C. Koos, "Ultrafast optical ranging using microresonator soliton frequency combs", *Science*, 359(6378), pp.887-891, (2018).
- E. Lucas\*, **M. Karpov\***, H. Guo, M.L. Gorodetsky and T.J. Kippenberg, "Breathing dissipative solitons in optical microresonators", *Nature Communications*, 8(1), p.736, (2017).
- P. Marin-Palomo\*, J.N. Kemal\*, **M. Karpov\***, A. Kordts, J. Pfeifle, M.H.P. Pfeiffer, P. Trocha, S. Wolf, V. Brasch, M.H. Anderson, R. Rosenberger, K. Vijayan, W. Freude, T.J. Kippenberg, C. Koos, "Microresonator-based solitons for massively parallel coherent optical communications", *Nature*, 546(7657), p.274, (2017).
- H. Guo\*, **M. Karpov\***, E. Lucas\*, A. Kordts, M.H.P. Pfeiffer, V. Brasch, G. Lihachev, V.E. Lobanov, M.L. Gorodetsky, T.J. Kippenberg, "Universal dynamics and deterministic switching of dissipative Kerr solitons in optical microresonators", *Nature Physics*, 13(1), p.94, (2017).
- **M. Karpov\***, H. Guo\*, A. Kordts, V. Brasch, M.H.P. Pfeiffer, M. Zervas, M. Geiselmann, T.J. Kippenberg, "Raman self-frequency shift of dissipative Kerr solitons in an optical microresonator", *Physical review letters*, 116(10), p.103902, (2016).

---

\*These authors contributed equally to the work

## Additional contributions

- J. Riemensberger, A. Lukashchuk, **M. Karpov**, W. Weng, E. Lucas, J. Liu, T.J. Kippenberg, "Massively parallel coherent laser ranging using soliton microcombs", arXiv:1912.11374, (2019).
- F. Samara, A. Martin, C. Autebert, **M. Karpov**, T.J. Kippenberg, H. Zbinden, R. Thew, "High-rate photon pairs and sequential Time-Bin entanglement with Si<sub>3</sub>N<sub>4</sub> microring resonators", *Optics Express*, 27(14), pp.19309-19318, (2019).
- A.S. Raja, A.S. Voloshin, H. Guo, S.E. Agafonova, J. Liu, A.S. Gorodnitskiy, **M. Karpov**, N.G. Pavlov, E. Lucas, R.R. Galiev, A. E. Shitikov, J.D. Jost, M.L. Gorodetsky and T.J. Kippenberg, "Electrically pumped photonic integrated soliton microcomb", *Nature Communications*, 10 (1), p.680, (2019).
- F. Alishahi, A. Fallahpour, A. Mohajerin-Ariaei, Y. Cao, A. Kordts, M.H.P. Pfeiffer, **M. Karpov**, A. Almainan, P. Liao, K. Zou, C. Liu, A.N. Willner, M. Tur, T.J Kippenberg, A.E Willner, "Reconfigurable optical generation of nine Nyquist WDM channels with sinc-shaped temporal pulse trains using a single microresonator-based Kerr frequency comb", *Optics Letters*, 44(7), pp.1852-1855, (2019).
- C. Bao, P. Liao, A. Kordts, L. Zhang, A. Matsko, **M. Karpov**, M.H.P. Pfeiffer, G. Xie, Y. Cao, A. Almainan, M. Tur, T.J. Kippenberg, A.E. Willner, "Orthogonally polarized frequency comb generation from a Kerr comb via cross-phase modulation", *Optics Letters*, 44(6), pp.1472-1475, (2019).
- J. Liu, E. Lucas, J. He, A.S. Raja, R.N. Wang, **M. Karpov**, H. Guo, R. Bouchand, T.J. Kippenberg, "Photonic microwave oscillators based on integrated soliton microcombs", arXiv:1901.10372, (2019).
- P. Liao, C. Bao, A. Almainan, A. Kordts, **M. Karpov**, M.H.P. Pfeiffer, L. Zhang, F. Alishahi, Y. Cao, K. Zou, A. Fallahpour, A.N. Willner, M. Tur, T.J. Kippenberg, A.E. Willner, "Demonstration of Multiple Kerr-Frequency-Comb Generation Using Different Lines From Another Kerr Comb Located Up To 50 km Away", *Journal of Lightwave Technology*, 37(2), pp.579-584, (2019).
- A.N. Willner, P.Liao, K.Zou, Y.Cao, A.Kordts, **M. Karpov**, M.H.P. Pfeiffer, A. Almainan, A. Fallahpour, F. Alishahi, K. Manukyan, M. Tur, T.J Kippenberg, A.E. Willner, "Scalable and reconfigurable optical tapped-delay-line for multichannel equalization and correlation using nonlinear wave mixing and a Kerr frequency comb", *Optics letters*, 43(22), pp.5563-5566, (2018).
- E. Lucas, G. Lihachev, R. Bouchand, N.G. Pavlov, A.S. Raja, **M. Karpov**, M.L. Gorodetsky, T.J. Kippenberg, "Spatial multiplexing of soliton microcombs", *Nature Photonics*, 12(11), p.699, (2018).

- J. Liu, A.S. Raja, **M. Karpov**, B. Ghadiani, M.H.P. Pfeiffer, B. Du, N.J. Engelsens, H. Guo, M. Zervas, T.J. Kippenberg, "Ultralow-power chip-based soliton microcombs for photonic integration", *Optica*, 5(10), pp.1347-1353, (2018).
- P. Liao, C. Bao, A. Kordts, **M. Karpov**, M.H.P. Pfeiffer, L. Zhang, Y. Cao, A. Almainan, A. Mohajerin-Ariaei, F. Alishahi, A. Fallahpour, K. Zou, M. Tur, T.J. Kippenberg, A.E. Willner, "Effects of erbium-doped fiber amplifier induced pump noise on soliton Kerr frequency combs for 64-quadrature amplitude modulation transmission", *Optics Letters*, 43(11), pp.2495-2498, (2018).
- H. Guo, E. Lucas, M.H.P. Pfeiffer, **M. Karpov**, M. Anderson, J. Liu, M. Geiselmann, J.D. Jost, T.J. Kippenberg, "Intermode breather solitons in optical microresonators", *Physical Review X*, 7(4), pp.041-055, (2017).
- C. Bao, P. Liao, A. Kordts, **M. Karpov**, M.H.P. Pfeiffer, L. Zhang, Y. Cao, G. Xie, C. Liu, Y. Yan, A. Almainan, A. Mohajerin-Ariaei, A. Fallahpour, M. Tur, T.J. Kippenberg, A.E. Willner, "Tunable insertion of multiple lines into a Kerr frequency comb using electro-optical modulators", *Optics letters*, 42(19), pp.3765-3768, (2017).
- P. Liao, C. Bao, A. Kordts, **M. Karpov**, M.H.P. Pfeiffer, L. Zhang, Y. Cao, A. Almainan, A. Mohajerin-Ariaei, M. Tur, M.M. Fejer, T.J. Kippenberg, A.E. Willner, "Pump-linewidth-tolerant wavelength multicasting using soliton Kerr frequency combs", *Optics letters*, 42(16), pp.3177-3180, (2017).
- M.H.P. Pfeiffer, C.Herkommer, J.Liu, H.Guo, **M. Karpov**, E.Lucas, M. Zervas, T.J. Kippenberg, "Octave-spanning dissipative Kerr soliton frequency combs in Si<sub>3</sub>N<sub>4</sub> microresonators", *Optica*, 4(7), pp.684-691, (2017).
- E. Lucas, H. Guo, J.D. Jost, **M. Karpov**, T.J. Kippenberg, "Detuning-dependent properties and dispersion-induced instabilities of temporal dissipative Kerr solitons in optical microresonators", *Physical Review A*, 95(4), p.043822, (2017).
- P. Liao, C. Bao, A. Kordts, **M. Karpov**, M.H.P. Pfeiffer, L. Zhang, A. Mohajerin-Ariaei, Y. Cao, A. Almainan, M. Ziyadi, S.R. Wilkinson, M. Tur, T.J. Kippenberg, A.E. Willner, "Dependence of a microresonator Kerr frequency comb on the pump linewidth", *Optics letters*, 42(4), pp.779-782, (2017).
- N.G. Pavlov, G. Lihachev, S. Koptyaev, E. Lucas, **M. Karpov**, N.M. Kondratiev, I.A. Bilenko, T.J. Kippenberg, M.L. Gorodetsky, "Soliton dual frequency combs in crystalline microresonators", *Optics letters*, 42(3), pp.514-517, (2017).
- C. Bao, P. Liao, A. Kordts, L. Zhang, **M. Karpov**, M.H.P. Pfeiffer, Y. Cao, Y. Yan, A. Almainan, G. Xie, A. Mohajerin-Ariaei, L. Li, M. Ziyadi, S.R. Wilkinson, M. Tur, T.J. Kippenberg, A.E. Willner, "Dual-pump generation of high-coherence primary Kerr combs with multiple sub-lines", *Optics letters*, 42(3), pp.595-598, (2017).

## Acknowledgements

---

- C. Bao, P. Liao, A. Kordts, **M. Karpov**, M.H.P. Pfeiffer, L. Zhang, Y. Yan, G. Xie, Y. Cao, A. Almaiman, M. Ziyadi, L. Li, Z. Zhao, A. Mohajerin-Ariaei, S.R. Wilkinson, M. Tur, M.M. Fejer, T.J. Kippenberg, A.E. Willner, "Demonstration of optical multicasting using Kerr frequency comb lines", *Optics letters*, 41(16), pp.3876-3879, (2016).

# Contents

<b>Acknowledgements</b>	<b>v</b>
<b>Abstract (English/Français)</b>	<b>ix</b>
<b>Publication List</b>	<b>xiii</b>
<b>Acronyms</b>	<b>xxi</b>
<b>1 Microresonator-based frequency combs</b>	<b>1</b>
1.1 Optical microresonator platforms . . . . .	1
1.2 Resonator fundamentals . . . . .	8
1.2.1 Free spectral range, intracavity build-up, quality factor . . . . .	8
1.2.2 Waveguide-resonator coupling . . . . .	11
1.2.3 Resonator dispersion . . . . .	14
1.2.4 Nonlinearity, resonator bistability . . . . .	19
1.2.5 Thermal effects . . . . .	24
1.3 Kerr frequency combs . . . . .	27
1.3.1 Primary sidebands . . . . .	28
1.3.2 Modulation instability . . . . .	31
1.3.3 Coupled-mode equations for Kerr combs . . . . .	34
1.3.4 Lugiato-Lefever equation . . . . .	35
1.4 Dissipative Kerr solitons . . . . .	38
1.4.1 Theoretical description of DKS . . . . .	40
1.4.2 Excitation of DKS . . . . .	42
1.5 DKS applications . . . . .	50
<b>2 Raman induced soliton self-frequency shift of dissipative Kerr solitons</b>	<b>55</b>
2.1 Introduction . . . . .	55
2.2 Experimental observation of the soliton self-frequency shift . . . . .	56
2.2.1 Compensation of the Raman self-frequency shift by the dispersive wave recoil . . . . .	59
2.3 Theory of the DKS self-frequency shift . . . . .	61
2.3.1 Moment analysis for solitons in microresonators . . . . .	62
2.4 Simulations of the DKS self-frequency shift . . . . .	64

2.5	Conclusion	66
<b>3</b>	<b>Universal dynamics and deterministic switching of DKS states in optical microresonators</b>	<b>69</b>
3.1	Introduction	69
3.2	Backward tuning and switching	71
3.3	Nondestructive soliton probing	73
3.4	Deterministic switching	79
3.5	Mapping of the soliton multistability in optical microresonators	83
3.6	Conclusion	86
<b>4</b>	<b>Soliton breathers in optical microresonators</b>	<b>87</b>
4.1	Introduction	87
4.2	Experimental observation of breathers	89
4.2.1	Access and identification of soliton breathing states	89
4.2.2	Breathing dynamics	93
4.2.3	Approximate breather ansatz	97
4.3	Breathing region	98
4.4	Real-time observation of breathers	99
4.5	Conclusion	102
<b>5</b>	<b>Soliton crystals in optical microresonators</b>	<b>103</b>
5.1	Introduction	104
5.2	Perfect soliton crystals	106
5.3	Generation of perfect soliton crystals	109
5.3.1	Experimental generation of PSC	109
5.3.2	Simulations of the PSC generation	111
5.3.3	PSC stability chart	112
5.3.4	Chaotic regions and the PSC generation process	115
5.4	PSC switching	118
5.4.1	Translation of PSC states	118
5.4.2	PSC switching in experiments	119
5.4.3	Link to DKS switching	122
5.5	Dynamics of soliton crystal states	125
5.6	Conclusion	129
<b>6</b>	<b>Photonic-based dissipative Kerr solitons covering the biological imaging window</b>	<b>131</b>
6.1	Introduction	131
6.2	Microresonator design and characterization	133
6.3	DKS states at 1 $\mu\text{m}$	135
6.4	Octave-spanning soliton states driven at 1 $\mu\text{m}$	137
6.4.1	Dispersion engineering of silicon nitride microresonators at 1 $\mu\text{m}$	137

6.4.2	Experimental generation of octave-spanning DKS states . . . . .	139
6.5	DKS states in hybridized modes . . . . .	140
6.6	Conclusion . . . . .	145
<b>7</b>	<b>Applications of dissipative Kerr solitons</b>	<b>147</b>
7.1	Dissipative Kerr solitons for massively parallel coherent communication .	147
7.2	Microresonator device and experimental setup . . . . .	149
7.3	Optical coherent communication experiments with DKS . . . . .	149
7.3.1	Optical transmission using single DKS . . . . .	151
7.3.2	Optical coherent communication using two DKS . . . . .	154
7.4	Dissipative Kerr solitons for ultrafast optical ranging . . . . .	156
7.5	Synthetic-wavelength interferometry . . . . .	158
7.6	Experiment - reproducibility and benchmarking . . . . .	160
7.7	Experiment - profiling of a flying bullet . . . . .	164
7.8	Vision of the chip-scale DKS-based LiDAR system . . . . .	165
7.9	Conclusion . . . . .	166
<b>8</b>	<b>Standalone microcomb source</b>	<b>169</b>
8.1	Introduction . . . . .	169
8.2	Breadboard-based prototype . . . . .	171
8.2.1	Hardware . . . . .	172
8.2.2	Control software . . . . .	174
8.2.3	Microresonator chip packaging . . . . .	176
8.2.4	Prototype system testing . . . . .	177
8.3	Prototype application in optical circuit switching experiment . . . . .	179
8.3.1	First experimental results . . . . .	180
8.4	Rack-mountable microcomb source . . . . .	182
8.4.1	Hardware . . . . .	183
8.4.2	Software . . . . .	185
8.4.3	Testing . . . . .	185
8.5	Conclusion . . . . .	186
<b>9</b>	<b>Conclusion and Outlook</b>	<b>187</b>
	<b>Bibliography</b>	<b>207</b>
	<b>Curriculum Vitae</b>	<b>209</b>



# Acronyms

**AFG** - arbitrary function generator  
**AMX** - avoided modal crossing  
**AOM** - acousto-optic modulator  
**ASE** - amplified spontaneous emission

**BPF** - bandpass filter

**CME** - coupled mode equations  
**CMI** - chaotic modulation instability  
**CMP** - chemical-mechanical polishing  
**CVD** - chemical vapor deposition  
**CW** - continuous wave  
**CWDM** - coarse wavelength division multiplexing

**DKS** - dissipative Kerr soliton  
**DUV** - deep ultraviolet  
**DW** - dispersive wave  
**DWDM** - dense wavelength-division multiplexing

**ECDL** - external-cavity diode laser  
**EDFA** - erbium-doped fiber amplifier  
**EO** - electro-optical  
**EOM** - electro-optical modulator  
**ESA** - electrical spectrum analyzer

**FBG** - fiber Bragg grating  
**FEM** - finite element method  
**FPC** - fiber polarization controller

**FPU** - Fermi-Pasta-Ulam (recurrence)  
**FLR** - frequency-locked Raman (soliton)  
**FSR** - free spectral range  
**FWM** - four-wave mixing  
**FWHD** - full width at half depth  
**FWHM** - full width at half maximum

**GVD** - group velocity dispersion

**IRS** - intrapulse Raman scattering

**LiDAR** - light detection and ranging  
**LLE** - Lugiato-Lefever equation  
**LPCVD** - low-pressure chemical vapor deposition  
**LTO** - low-temperature oxide

**MI** - modulation instability  
**MMS** - multi-mode spaced (Kerr combs)  
**MZI** - Mach-Zehnder interferometer

**NLSE** - nonlinear Schrödinger equation  
**NMS** - natively-mode spaced (Kerr combs)

**OCT** - optical coherence tomography  
**OSA** - optical spectrum analyzer  
**OSC** - oscilloscope  
**OSNR** - optical signal-to-noise ratio

**PD** - photodiode  
**PIC** - photonic integrated circuit  
**PM** - powermeter

## Contents

---

**PSC** - perfect soliton crystal

**QAM** - quadrature amplitude modulation

**RBW** - resolution bandwidth

**RF** - radio frequency

**SEM** - scanning electron microscope

**SMI** - stable modulation instability

**SMF** - single-mode optical fiber

**SPM** - self-phase modulation

**SRS** - stimulated Raman scattering

**SSB** - single-sideband modulator

**STC** - spatiotemporal chaos

**SWaP** - size , weight and power

**TC** - transient chaos

**TE** - transverse electric

**TEOS** - tetraethylorthosilicate

**THG** - third-harmonic generation

**TM** - transverse magnetic

**TOF** - time of flight

**TPA** - two-photon absorption

**VCO** - voltage controlled oscillator

**VNA** - vector network analyzer

**WDM** - wavelength division multiplexing

**WGM** - whispering gallery mode

**WM** - wavelength meter

**XPM** - cross-phase modulation

# 1 Microresonator-based frequency combs

This chapter covers the fundamentals of microresonator-based optical frequency combs and dissipative Kerr solitons.

## 1.1 Optical microresonator platforms

Optical resonators are one of the most ubiquitous basic elements of modern optics. They are at the core of fundamental studies across different fields in science as well as numerous industrial and research applications. A conventional optical resonator, or often optical "cavity" (the term "cavity" came from microwave technologies, where the conventional resonator is represented by a closed metallic cavity), is formed when the light propagation is restricted to a closed path. In the simplest case the resonator can be built out of two mirrors or light guiding material (for example optical fiber) arranged in a loop geometry (waveguide resonator). The closed path allows storage and accumulation of the light, which effectively enhances light-matter interaction with the resonator material or other systems placed inside the cavity. Bulk resonators have a number of limitations in terms of their size, weight, alignment complexity (for the mirror-based systems) or limited stability (for fiber-based systems). Most of these limitations can be efficiently addressed by optical *microresonators*, which are able to confine light to a very small volume of micro- or millimeter size.

In the context of microresonator-based optical frequency combs, which will be discussed in the present work, the term optical microresonator is often referred to a device made of transparent dielectric material, where the process of the light guiding is based on the total internal reflection and is guaranteed by the refractive index contrast between the dielectric material of the resonator medium (higher refractive index) and the surroundings (lower refractive index). The majority of such dielectric optical microresonators of interest are organized in a loop geometry, allowing the light to circulate inside and, through the coherent build-up of the intracavity intensity, facilitate access to optical nonlinear effects

arising from the resonator medium. Dielectric resonators can be formally distinguished into two main categories: *whispering gallery mode* (WGM) resonators and *travelling waveguide* integrated resonators.

The first category includes dielectric resonators with circular symmetry having spherical, disk or toroidal shapes. The term "whispering gallery modes" originates from the work of Lord Rayleigh, who investigated efficient sound propagation due to the refocussing effect of curved wall surfaces in the Whispering Gallery - circular gallery in the dome of St. Paul's Cathedral in London. He also suggested that electromagnetic waves can experience a similar effect. The WGM resonators can be fabricated from a variety of crystalline and amorphous materials, including, among others, silicon-based materials like fused silica [1, 2, 3, 4], silicon oxynitride (also "hydex", or high-index doped silica glass) [5] or fluoride materials such as  $\text{MgF}_2$ ,  $\text{CaF}_2$ ,  $\text{BaF}_2$  and  $\text{SrF}_2$  [6]. Due to their high quality factors ( $Q$ -factors), which can be achieved with relatively simple and reproducible fabrication procedures, the WGM resonators were historically first, where the generation of microresonator-based optical combs was observed [3, 7].

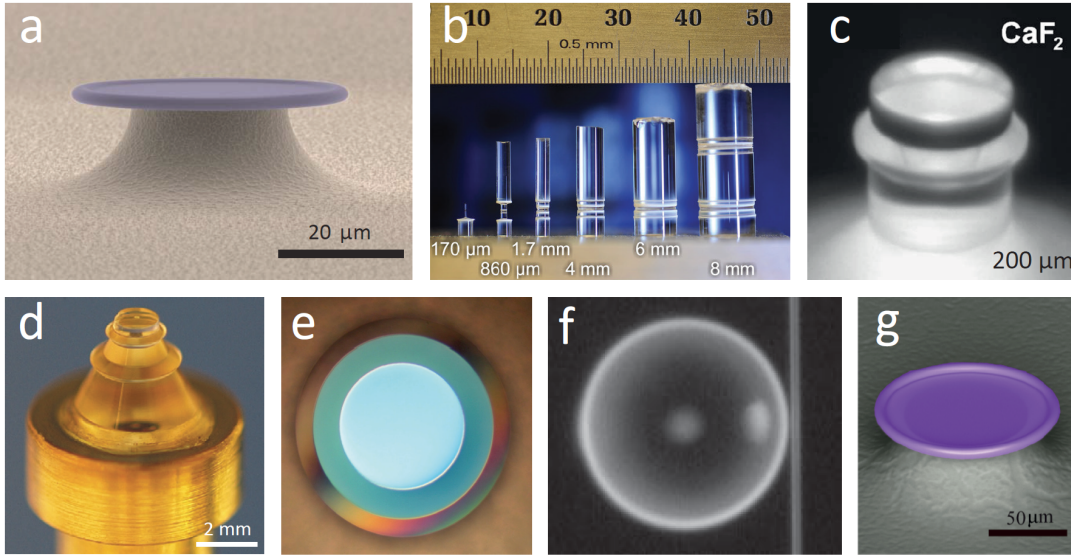


Figure 1.1 – Variety of WGM resonators used in the area of microresonator-based optical frequency combs (all images are adapted from corresponding cited sources); (a) microfabricated fused silica ( $\text{SiO}_2$ ) microtoroid [7]; (b) laser-machined fused silica microtoroids [8]; (c) calcium fluoride ( $\text{CaF}_2$ ) crystalline resonator [6]; (d) magnesium fluoride ( $\text{MgF}_2$ ) crystalline resonator [9]; (e) silica wedge-shaped microresonator [4]; (f) silica microspheres [1]; (g) silicon oxynitride ( $\text{SiO}_x\text{N}_y$ ) microtoroid resonator [5].

The second category contains resonators based on integrated waveguides. In these devices the light is confined in the transverse direction due to the propagation in the dielectric waveguide, which is arranged in the closed loop geometry. In contrast to WGM resonators, circular symmetry is not required for such resonators, and they can take a number of different planar forms ranging from simple rings to racetracks or even complex meander-

## 1.1. Optical microresonator platforms

like shapes. Such integrated resonators are usually implemented on silicon wafers or chips using microfabrication techniques. The majority of integrated resonators are also silicon-based materials. They are widely accessible and have established fabrication techniques due to the active development of silicon semiconductor technologies over the past 80 years: silicon oxynitride [10], silicon nitride ( $\text{Si}_3\text{N}_4$ ) [11] and silicon resonators [12]. Few groups have also developed methods to fabricate crystalline integrated resonators of diamond [13], aluminum nitride (AlN) [14], aluminum gallium arsenide (AlGaAs) [15] and recently - lithium niobate ( $\text{LiNbO}_3$ ) [16, 17] and gallium phosphide (GaP) [18].

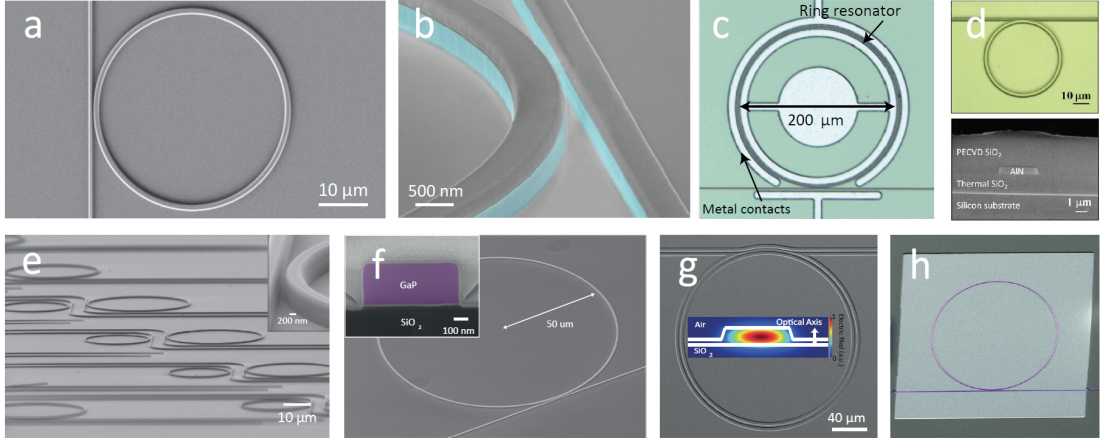


Figure 1.2 – Variety of integrated waveguide microresonators used in the area of microresonator-based optical frequency combs (all images adapted from corresponding cited sources); (a) silicon nitride ( $\text{Si}_3\text{N}_4$ ) microring resonator [11] (b) aluminum gallium arsenide ( $\text{Al}_x\text{Ga}_{1-x}\text{As}$ ) microring resonator [15]; (c) silicon microresonator [12]; (d) aluminum nitride (AlN) microresonator [14]; (e) diamond microresonators [13]; (f) gallium phosphide (GaP) microring resonator [18]; (g, h) lithium niobate ( $\text{LiNbO}_3$ ) microresonators [16, 17];

Figures 1.1 and 1.2 contain the majority of current microresonator platforms, which were employed for the generation of optical combs. We also note that while Fabry-Pérot microresonators were not widely used in the field, they were still used for the generation of optical frequency combs [19, 20].

### Resonator coupling

For the generation of optical frequency combs, one needs to supply the microresonator with continuous wave laser light. Due to the large contrast in refractive indexes between air and the dielectric materials of optical microresonators, free space coupling is inefficient due to poor phase-matching of the propagating modes in both media. Instead, an *evanescent coupling* approach is often used [21]. It is based on bringing another light guiding material with a similar refractive index into close proximity with the resonator. When the evanescent field of the mode propagating in such a bus waveguide overlaps with the optical mode in the microresonator, and the phase matching condition is satisfied for

a given optical frequency, photons of the incident light can be efficiently transferred to the microresonator.

Different implementations of such evanescent coupling are based on prisms, D-shaped polished or tapered optical fibers, all of which are often used for the WGM resonators. Since they are usually not required to be physically connected to the microresonator, such coupling can often be changed and optimized during system operation. For the integrated systems, evanescent coupling is usually implemented through an additional bus waveguide with transverse geometry similar to the one forming the microresonator. While such integrated waveguide coupling provides less flexibility than others, it is advantageous in terms of mechanical stability and robustness against environmental changes.

### Optical microresonators used in the present work

The present work is mainly focused on the integrated silicon nitride ( $\text{Si}_3\text{N}_4$ ) microresonators. Over the past years silicon nitride has become one of the main integrated platforms for nonlinear [22] and quantum photonics [23, 24]. It has a number of advantages over other platforms, such as (i) CMOS compatibility, which enables the fabrication of silicon nitride waveguides using instruments, techniques and processes developed and well established over the past 50 years in the semiconductor industry. Moreover, such microfabrication can be implemented on wafer-scale, providing mass production and the possibility of intergration with other on-chip electrical and optical components for building complex photonic integrated circuits (PIC). (ii) Silicon nitride has a wide transparency window ranging from visible to mid-infrared with low linear losses. In combination with negligible two-photon absorption (TPA) for telecom wavelengths due to the high bandgap energy of around 5 eV, silicon nitride is suitable for telecom application, and can be used to fabricate resonators with higher quality factors. (iii) Comparably high nonlinearity, which overcomes silica glass by an order of magnitude at 1.55  $\mu\text{m}$  and, due to the high confinement of the light in the waveguide and high quality factors, enables the nonlinear processes in microresonators. (iv) Silicon nitride is robust with respect to external effects, like extreme temperatures [25] or proton radiation [26], which makes it suitable for space applications.

The microresonators used in this work are silicon nitride ring or racetrack waveguide resonators with silica cladding. They are fabricated on silicon wafers and further separated in individual chips of 5x5 mm, shown in Fig. 1.3(a, b). In the simplest configuration each microresonator is fabricated with a single bus waveguide for the evanescent coupling. Figure 1.3(c) shows examples of silicon nitride microresonators with different free spectral ranges (20 – 1000 GHz) used in the present work. Since the bus waveguide is monolithically integrated on the same substrate as the resonator (see Fig. 1.3(d)), the coupling distance (gap) is fixed. It is usually designed to have a consistent change within a single chip from one microresonator to another, to find an optimum one. Typical waveguide height is about 800 nm, and waveguide width is about 1500 nm. The exact values are varied in

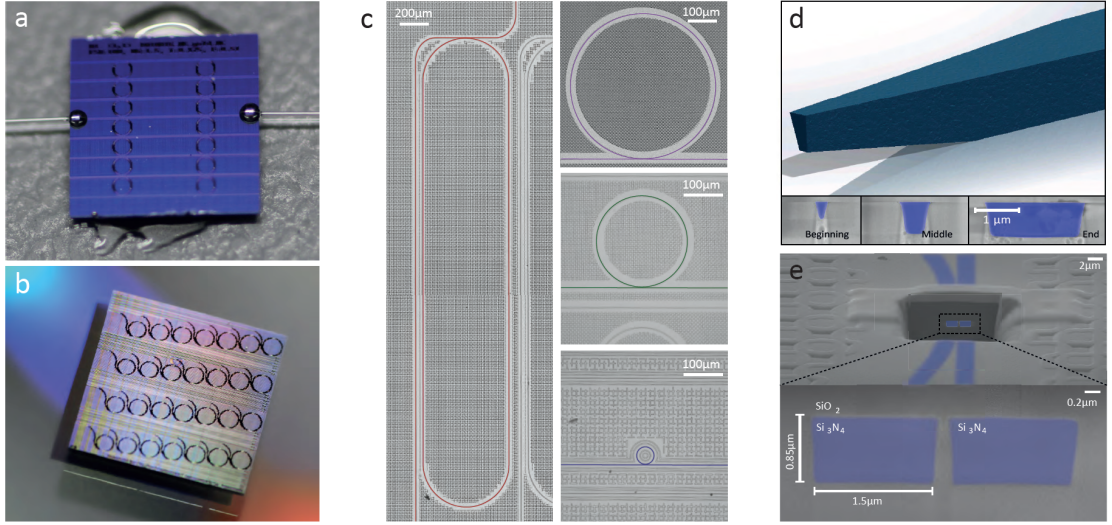


Figure 1.3 – (a, b) Examples of silicon chips used in the present work with fabricated  $\text{Si}_3\text{N}_4$  microresonators. (a) Fiber-packaged chip with old-generation design used at LPQM. (b) Chip with new-generation design allowing for dense microresonator organization. (c) Variety of integrated  $\text{Si}_3\text{N}_4$  microresonators used in the present work: left - 20 GHz; right (from top to bottom) - 100 GHz, 200 GHz, 1000 GHz. (d) Geometry of the inverse tapering structure used to couple light from off the chip into the integrated bus waveguide. The image is taken from [27]. (e) SEM crosssection of the coupling region between the resonator (left) and the bus waveguide (right) with their typical dimensions. The image is adapted from [28].

order to engineer the waveguide properties such as dispersion or quality factors, as well as adapt the microresonator operation to the new spectral window.

Apart from the bus-to-resonator coupling, coupling of the light into the chip is also challenging. Due to significant difference between the sizes of propagating modes in the integrated waveguide (with characteristic size of  $\sim 1 \mu\text{m}$ ) and optical fiber ( $\sim 9 \mu\text{m}$  core diameter), as well as the difference between the refractive indexes of silicon nitride and silica of the fiber core, direct coupling between the chip and the waveguide is very inefficient. In order to overcome the challenge, we use inverse taper mode converters [29], which expands the optical mode size due to adiabatic reduction of the waveguide dimensions close to the chip facet, such that the majority of the light is concentrated in the evanescent field propagating into the cladding. The benefits are twofold: first, the reduction of refractive index contrast for the mode exiting or entering the chip leading to lower reflection losses; second, the better mode-size matching between the fiber and waveguide modes. To further increase the efficiency of the light coupling, we use lensed fibers, which can help to reduce the spot size of the mode and focus the mode on the taper facet.

**Device fabrication** Two methods were used to fabricate integrated silicon nitride

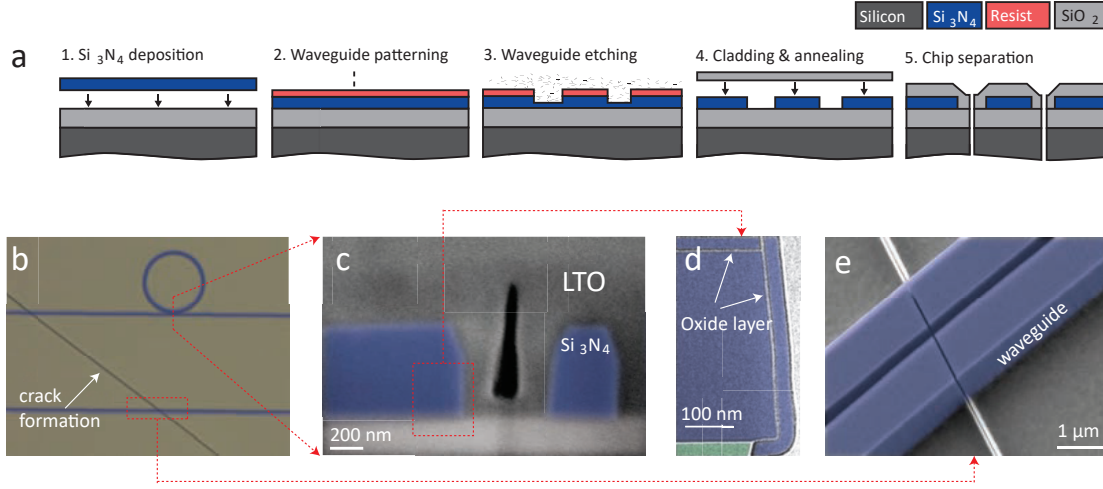


Figure 1.4 – (a) Schematic description of the subtractive process: 1 - deposition of thick ( $\sim 800$  nm) waveguide  $\text{Si}_3\text{N}_4$  layer using multi-step LPCVD process; 2 - patterning of the waveguide structures in the layer of negative resist using E-beam lithography or DUV photolithography; 3 - etching of the patterned waveguides; 4 - deposition of silica (TEOS and LTO) as cladding layer; 5 - chip separation. (b) Top view of the  $\text{Si}_3\text{N}_4$  microresonator and bus waveguides (highlighted in blue) and a crack formed across bus waveguides. (c) Scanning electron microscope (SEM) image (cross-section) of the void formation in the silica cladding layer between adjacent waveguides (highlighted in blue) in the subtractive process. (d) SEM cross-section image of the  $\text{Si}_3\text{N}_4$  waveguide (highlighted in blue), with oxide layer formed with multistep LPCVD deposition of the  $\text{Si}_3\text{N}_4$ . (e) Formation of the cracks across  $\text{Si}_3\text{N}_4$  waveguides (highlighted in blue) due to tensile stress of the  $\text{Si}_3\text{N}_4$  films. Images are adapted from [31].

microresonators: the subtractive process [30] and the Photonic Damascene process [28]. Both of them are well established in our group.

**Subtractive process** - the conventional process for the fabrication of silicon nitride integrated structures. It is schematically shown in Fig. 1.4(a) and starts with the growing of the stoichiometric  $\text{Si}_3\text{N}_4$  using a low-pressure chemical vapor deposition (LPCVD) process in two or more steps (multi-step deposition with intermediate cooling to room temperature [30] is used to reduce the number of cracks in thick silicon nitride films). The waveguide structures are then patterned using electron-beam (E-beam) lithography or deep ultraviolet (DUV) photolithography with negative resist, followed by the dry etching in  $\text{CHF}_3$ -based plasma. The resulting structures are then covered with a silica cladding layer using the Tetraethylorthosilicate ( $\text{Si}(\text{OC}_2\text{H}_5)_4$ , TEOS) and low-temperature oxide (LTO) CVD processes. Despite being well-developed and widely used, subtractive process have several issues limiting the performance of the fabricated waveguides and device yield. They include crack formation due to high tensile stress of the silicon nitride films after deposition as shown in Fig. 1.4(b, e), limited quality factors of the fabricated microresonators due to the surface roughness induced by the etching and lithography

steps, as well as the formation of voids during cladding deposition between closely-spaced waveguides forming high aspect ratio gaps, see Fig. 1.4(c). Nevertheless, devices fabricated with the subtractive process were successfully used for the optical comb generation in Chapters 2 and 5. Furthermore, recent advances demonstrate that careful optimization of all process steps can significantly reduce the losses of the integrated waveguides fabricated with the subtractive process [32].

**The Photonic Damascene process** was initially developed by Martin Pfeiffer during his PhD time at LPQM [28, 33], and then further advanced by Arne Kordts, Clemens Herkommer, Michael Zervas, Junqiu Liu and Rui Ning Wang. The process is based on the pre patterning of the silica substrate to form smooth trenches for waveguides and a dense stress-release pattern (Fig. 1.5(a – c)). After filling the trenches with waveguide material – silicon nitride – excessive material is removed using chemical-mechanical polishing (CMP). Finally, the waveguides are cladded with LTO and TEOS oxides. The Photonic Damascene process has been shown to significantly improve the performance and yield of the integrated microring resonators. It has provided access to previously unattainable waveguide dimensions and aspect-ratio gaps without void formation, as well as record-low losses with the introduction of an additional reflow step for smoothing the waveguide walls [33]. Moreover, the Photonic Damascene also enables custom control of not only the width of the resulting structures, but their height as well, which can be useful for the fabrication of tapers [27]. Detailed description of the Photonic Damascene process can be found in [31, 28, 33].

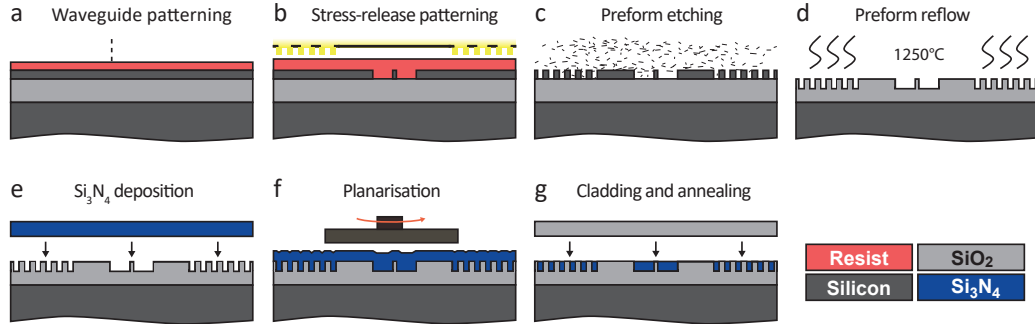


Figure 1.5 – Schematic description of the Photonic Damascene process. (a) Waveguide patterning in the layer of positive resist using electron-beam lithography or deep-UV photolithography. (b) Formation of the stress-release pattern using photolithography. (c) Transferring of waveguide and stress-release patterns in the silica of the substrate; (d) preform reflow to smooth the surface roughness. (e) LPCVD deposition of thin  $\text{Si}_3\text{N}_4$  film. (f) Removal of the excess  $\text{Si}_3\text{N}_4$  and planarization of the top surface. (g) Deposition of the LTO as a cladding layer and further annealing. Images are adapted from [33].

## 1.2 Resonator fundamentals

### 1.2.1 Free spectral range, intracavity build-up, quality factor

We start by introducing the basic concepts of optical resonators. For this purpose we use a model of a typical microring resonator with a single straight bus waveguide. Such a configuration is also often referred to as an all-pass resonator [34, 35] and schematically shown in Fig. 1.6. It should be noted, however, that the results of the present section are not restricted to only microring resonators, but in general are valid for other types of optical resonators including integrated microresonators of different shapes (racetracks, spirals, meander structures) as well as WGM resonators.

We assume that the bus waveguide (which can also be replaced with tapered optical fiber) is placed sufficiently close to the resonator to provide evanescent coupling at optical frequencies. Let  $L$  be a resonator length (circumference) and  $n$  - is a refractive index of the dielectric resonator material, which is considered to be frequency-independent for all optical frequencies of interest ( $\sim 200$  THz). Resonator losses (due to the scattering or absorption) are introduced through the real part of the propagation constant and denoted as  $\alpha$ . We treat the coupling region between the resonator and the waveguide as the four-port device, mark the ports with  $i = 1...4$  as shown in Fig. 1.6, and assume that it is driven by monochromatic light with angular frequency  $\omega$  from port 1. For simplicity we also omit the transverse distribution of the field within the waveguides. In the steady state of such a system the field at each port is  $E_i(t) = E_i e^{-i\omega t} + c.c.$ , with complex field amplitudes  $E_i, i = 1...4$ . Considering positive frequency components and assuming that we have no reflections from the coupler (no light is propagating in reverse directions in all ports), we can write a scattering matrix for this coupling region:

$$\begin{bmatrix} E_4 \\ E_2 \end{bmatrix} = \begin{bmatrix} r & it \\ it & r \end{bmatrix} \begin{bmatrix} E_3 \\ E_1 \end{bmatrix}, \quad (1.1)$$

where  $r$  and  $t$  are field reflection and transmission coefficients, such that  $r^2 + t^2 = 1$  (coupling is lossless). In the case when light can travel multiple roundtrips before fully leaving the cavity, all complex field amplitudes except  $E_1(t)$  are represented by an infinite sum of the field amplitudes corresponding to different roundtrip numbers. Furthermore, due to the feedback provided by the resonator, we can connect field amplitudes  $E_3$  and  $E_4$  using the phase constant  $k$  and earlier-introduced losses  $\alpha$ :

$$E_3 = E_4 e^{ikL} e^{-\alpha L/2} \equiv E_4 a e^{i\phi}, \quad (1.2)$$

where the first exponent  $e^{ikL}$  describes the phase  $\phi$  accumulated by the field over a single roundtrip and the second term  $e^{-\alpha L/2} \equiv a$  describes the fraction of the field amplitude, which is left in the cavity after one roundtrip. In our simple example of plane waves which do not experience the constraining effect of the waveguides, the phase constant can

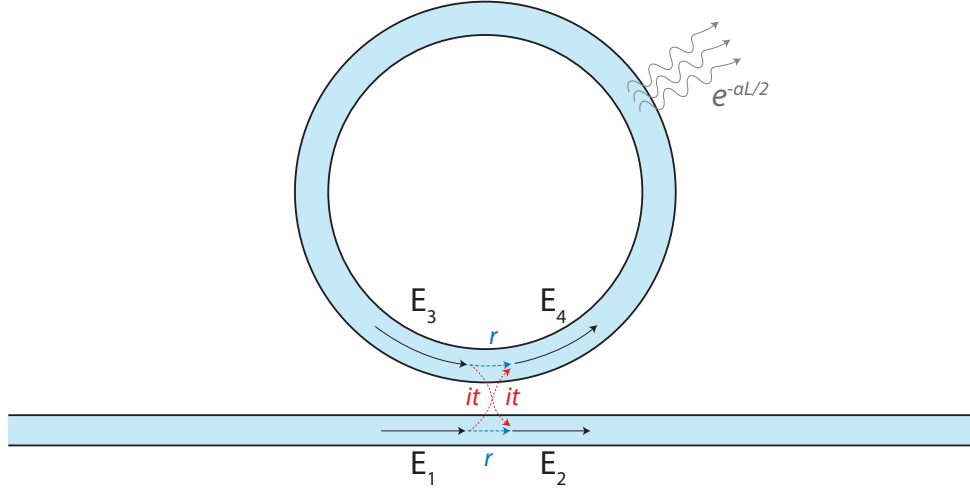


Figure 1.6 – Schematic model of an all-pass ring resonator with a section of straight bus waveguide. The field reflection and transmission coefficients are denoted as  $r$  and  $t$  correspondingly.  $E_1 \dots E_4$  mark the fields at different ports of the coupling region.

be written as:  $k = 2\pi n/\lambda$ , where  $\lambda$  - is the vacuum wavelength of our monochromatic light:  $\lambda = c/\omega$ . Combining both equations (1.1) and (1.2), we can derive the ratios between intracavity  $E_3$  and output field amplitudes  $E_2$  to the input field amplitude  $E_1$  for the steady state:

$$\frac{E_3}{E_1} = \frac{itae^{i\phi}}{1 - rae^{i\phi}}, \quad \frac{E_2}{E_1} = \frac{r - ae^{i\phi}}{1 - rae^{i\phi}}. \quad (1.3)$$

This allows to derive the intracavity intensity build-up  $\mathcal{B} = |E_3/E_1|^2$  and the resonator transmission measured through the bus waveguide  $\mathcal{T} = |E_2/E_1|^2$ :

$$\mathcal{B} = \left| \frac{E_3}{E_1} \right|^2 = \frac{(1 - r^2)a^2}{1 + r^2a^2 - 2ra \cos(\phi)}, \quad \mathcal{T} = \left| \frac{E_2}{E_1} \right|^2 = \frac{a^2 - 2ra \cos(\phi) + r^2}{1 + r^2a^2 - 2ra \cos(\phi)}. \quad (1.4)$$

The build-up curve as a function of accumulated phase  $\phi$  is shown in Fig. 1.7 and describes the resonance structure, which exists in such an all-pass ring resonator. One can see that intracavity intensity  $\mathcal{B}$  is maximized each time when  $\cos(\phi) = 1$ , or when  $\phi = \phi_m = 2\pi m, m \in \mathbb{N}$  (we note that we use  $\mathbb{N}$  to highlight positive phase accumulation). This gives us another understanding of the resonance conditions - the resonance of the cavity happens each time, when accumulated phase is a multiple of  $2\pi$  (equivalently, when the resonator length is a multiple of the light wavelength in the dielectric medium of the resonator). Using the cavity roundtrip time, which is introduced for our ring resonator as  $\tau_{\text{rt}} = Ln/c$ , we can also rewrite the resonance conditions in terms of angular frequencies:  $\omega_m = \phi_m/\tau_{\text{rt}}$ , and introduce the frequency spacing between adjacent resonances in terms

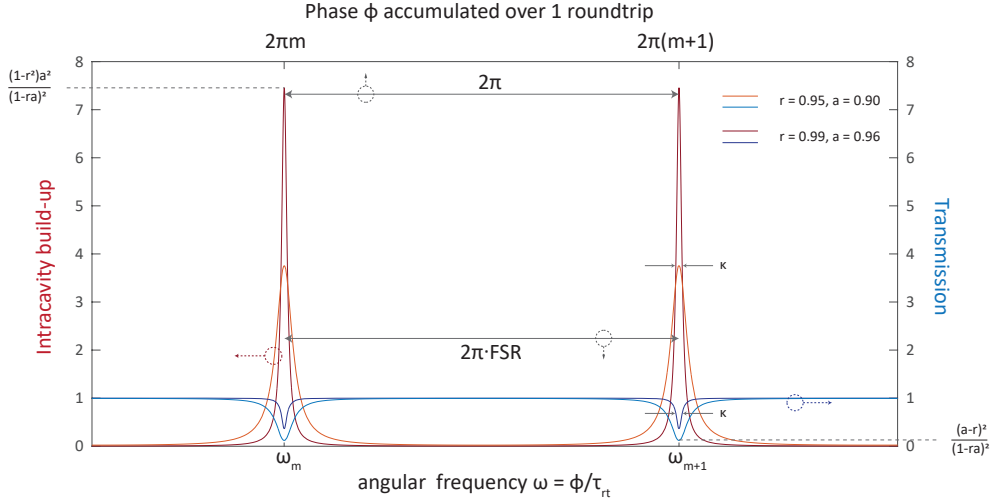


Figure 1.7 – Intracavity intensity build-up (red, dark red) and transmission (blue, dark blue) through the bus waveguide as a function of accumulated phase  $\phi$  (top axis) or angular frequency (bottom axis) for two pairs  $(r, a)$ . Maximum intracavity build-up ( $\mathcal{B}_{\max}$ ) is shown on the left axis (minimum is 0), minimum transmission ( $\mathcal{T}_{\min}$ ) is shown on the right axis (maximum is 1)

of regular frequencies [Hz] - the free spectral range (FSR):

$$\text{FSR} = \frac{\omega_{m+1} - \omega_m}{2\pi} = \frac{c}{nL} . \quad (1.5)$$

We should emphasize here that this formula for the FSR derived for our model assumes frequency-independent refractive index (does not include chromatic dispersion). While such simplification does not affect other results in the present subsection and, in principle, can be used to make estimations in certain cases, a strict expression for the FSR will be given later in eq. (1.23). In case of  $\phi \neq \phi_m$  it is convenient to use the value  $\Delta\phi = \phi_m - \phi$ , which we will refer to as phase detuning, or  $\Delta = (\phi_m - \phi)/\tau_{\text{rt}}$ , which is the conventional detuning. There are two more resonator parameters which are often used to describe its ability to store and enhance light intensity. The first one - *Finesse* ( $\mathcal{F}$ ) - is formally introduced as the FSR divided by the full width at half maximum (FWHM) of the intensity build-up, or equivalently in terms of the accumulated phase  $\phi$ :

$$\mathcal{F} = \frac{2\pi}{\Delta\phi_{\text{FWHM}}} = \frac{\pi\sqrt{ra}}{1 - ra} , \quad (1.6)$$

where we used approximation  $r, a \rightarrow 1$ , meaning low resonator losses (weak damping) through internal channels  $a$  or external coupling  $r$ , and also assumed that  $\cos(\phi) \sim 1$ . Since both parameters are not easy to measure directly for ring resonators, we introduce two new related parameters - photon (energy) decay rates:  $\kappa_{\text{ex}}$  [rad/s] and  $\kappa_0$  [rad/s], where the first one describes the photon escape rate through the coupling region and is connected with  $r$  through the photon (energy) loss per roundtrip:  $\kappa_{\text{ex}}\tau_{\text{rt}} \approx 1 - r^2$ , and

the second one  $\kappa_0$  describes the photon escape rate from the cavity through internal channels (scattering or absorption):  $\kappa_0\tau_{\text{rt}} \approx 1 - a^2$ .<sup>1</sup> Using these decay rates and the same approximation of weak damping ( $\kappa_{\text{ex}}\tau, \kappa_0\tau \rightarrow 0$ ) the finesse is:

$$\mathcal{F} = \frac{\text{FSR}}{\kappa/2\pi} . \quad (1.7)$$

We introduce here  $\kappa = \kappa_{\text{ex}} + \kappa_0$ , which will be further referred to as the total cavity decay rate, or resonator linewidth, since in experiment this value can be easily identified from the transmission trace, taking full width at half depth (FWHD) of the measured resonances (Fig. 1.7). Using equation (1.4) we can show that for the resonance condition, finesse describes the magnitude of the intracavity intensity build-up  $\mathcal{B}_{\text{max}}$ :

$$\mathcal{B}_{\text{max}} = \frac{4\kappa_{\text{ex}}}{(\kappa_{\text{ex}} + \kappa_0)^2\tau_{\text{rt}}} = \{\text{in case } \kappa_{\text{ex}} = \kappa_0\} = \frac{\mathcal{F}}{\pi} . \quad (1.8)$$

The second important resonator parameter is a quality factor ( $Q$ -factor or just  $Q$ ), which according to the formal definition is  $2\pi$  of the energy stored in the resonator divided by the energy loss per cycle:

$$Q = 2\pi \frac{\text{energy stored in the cavity}}{\text{energy loss per cycle}} = 2\pi \frac{1}{1 - e^{-\kappa T}} = \frac{\omega}{\kappa} . \quad (1.9)$$

Quality factor shows effective interaction time with the resonator. Comparing equations (1.7) and (1.9), we can see their physical meaning. Quality factor reflects the losses of the resonator per light cycle, while finesse shows losses per cavity roundtrip time.

### 1.2.2 Waveguide-resonator coupling

Resonator-waveguide coupling used in the previous subsection to derive the resonance conditions is often also described using input-output cavity formalism, similar to the one developed by Haus [37]. For this purpose we first switch from real electric fields  $E(t)$  to energy-normalized fields  $\tilde{a}(t) = \tilde{a}e^{-i\omega t} + c.c.$  with the real part of the complex amplitude  $\text{Re}[\tilde{a}] = \sqrt{n^2|E(t)|^2\epsilon_0 V_{\text{eff}}/2\hbar\omega}$ , where  $V_{\text{eff}} = LA_{\text{eff}}$  is the effective mode volume of the resonator mode, and  $A_{\text{eff}}$  - is the effective mode area, which is a measure of the mode size propagating inside the waveguide. For the  $A_{\text{eff}}$  calculation we have to assume a certain field distribution inside the transverse plain of the resonator waveguide:  $E(x, y)$ , then effective mode area is formally defined as:

$$A_{\text{eff}} = \frac{(\int |E(x, y)|^2 dS)^2}{\int |E(x, y)|^4 dS} , \quad (1.10)$$

---

<sup>1</sup>Despite dimensional nonhomogeneity of these approximations, they are still correct. This can be shown explicitly using, for example, an approach shown in [36].

where both integrals are taken over the full transverse plane and are not restricted to the waveguide areas. Using such normalized field values, intracavity number of photons is just  $|\tilde{a}(t)|^2$ .

Taking again the positive frequencies, cavity input-output formalism around a certain resonance  $\omega_m$  can be reduced to [37]:

$$\frac{d\tilde{a}(t)}{dt} = -\left(\frac{\kappa_0}{2} + \frac{\kappa_{\text{ex}}}{2}\right)\tilde{a}(t) - i\omega_m\tilde{a}(t) + \sqrt{\kappa_{\text{ex}}}s_{\text{in}}e^{-i\omega_p t}, \quad (1.11)$$

where we use the same photon decay rates  $\kappa_{\text{ex}}, \kappa_0$  as introduced above,  $\omega_p$  is the angular frequency of the driving laser field,  $s_{\text{in}}$  is defined such that  $|s_{\text{in}}|^2 = \text{input normalized laser power}$  (number of input photons per unit time). By moving into the rotating frame oscillating with the angular frequency of the driving laser (making a change  $\tilde{a}(t) = a(t)e^{-i\omega_p t}$ ), and introducing the detuning  $\Delta = \omega_m - \omega_p$ , we can avoid time dependence of the pumping term:

$$\frac{da(t)}{dt} = -\left(\frac{\kappa_0}{2} + \frac{\kappa_{\text{ex}}}{2}\right)a(t) - i\Delta a(t) + \sqrt{\kappa_{\text{ex}}}s_{\text{in}}. \quad (1.12)$$

We note that the detuning of the driving laser from the resonance is defined to be positive for a red-detuned laser position ( $\omega_p < \omega_m$ ). Considering the steady state ( $da(t)/dt = 0$ ) of eq. (1.12) we can calculate the corresponding complex field amplitude  $a$ :

$$a(t) = \frac{\sqrt{\kappa_{\text{ex}}}s_{\text{in}}}{\frac{\kappa_0 + \kappa_{\text{ex}}}{2} + i\Delta}, \quad (1.13)$$

and for the total intracavity energy  $|a(t)|^2$  (or photon number) in a steady state:

$$|a(t)|^2 = |s_{\text{in}}|^2 \frac{4\kappa_{\text{ex}}}{(\kappa_0 + \kappa_{\text{ex}})^2 + (2\Delta)^2}. \quad (1.14)$$

We note that the last equation shows the number of the photons inside the cavity as a function of the laser-cavity detuning  $\Delta$  and has a well-known Lorentzian shape. Such a resonance shape can be also obtained from the transmission eq. (1.4) in the weak damping regime for  $(\phi - \phi_m) \ll 2\pi$  ( $\Delta \ll \text{FSR}/2\pi$ ), and in case of zero detuning:  $\Delta = 0$  (pump is on resonance) it is as expected reproduces an earlier derived eq. (1.8). For the transmitted field:

$$s_{\text{out}} = s_{\text{in}} - \sqrt{\kappa_{\text{ex}}}a(t). \quad (1.15)$$

Thus, the transmitted light intensity is:

$$|s_{\text{out}}|^2 = |s_{\text{in}}|^2 \frac{(\kappa_0 - \kappa_{\text{ex}})^2 + (2\Delta)^2}{(\kappa_0 + \kappa_{\text{ex}})^2 + (2\Delta)^2}, \quad (1.16)$$

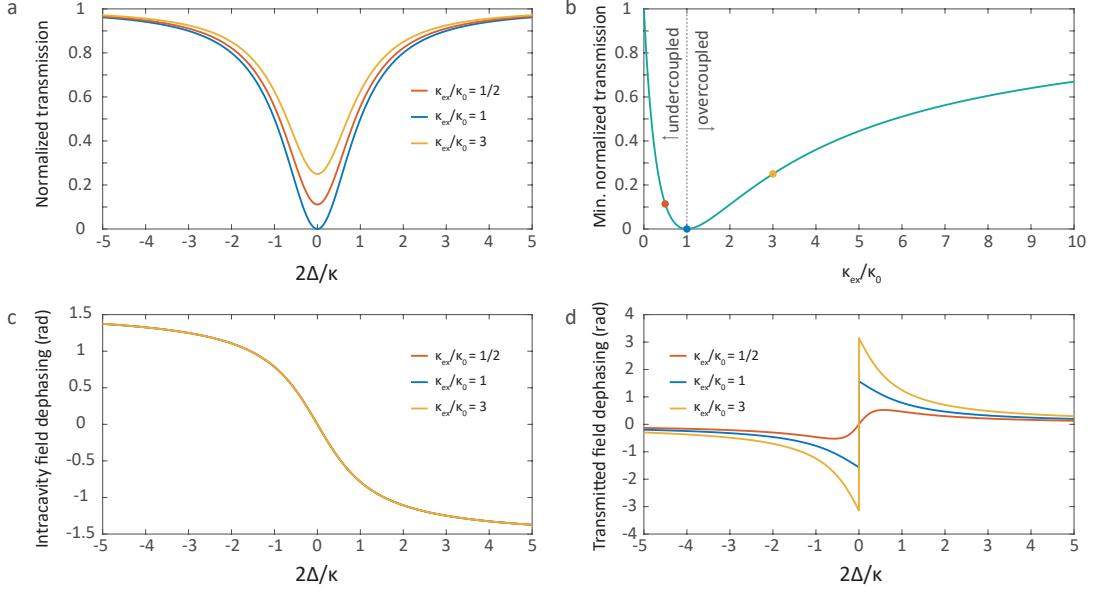


Figure 1.8 – (a) Normalized transmission as a function of normalized detuning ( $2\Delta/\kappa$ ) for three different ratios  $\kappa_{\text{ex}}/\kappa_0$ : 0.5, 1 and 3. (b) Minimum of the normalized transmission as a function of  $\kappa_{\text{ex}}/\kappa_0$ . Three colored dots represent corresponding curves from (a). (c) Dephasing of the intracavity field  $a$  with respect to the pump field  $s_{\text{in}}$  for three different  $\kappa_{\text{ex}}/\kappa_0$  as in (a). Traces coincide. (d) Dephasing of the transmitted field  $s_{\text{out}}$  with respect to the pump field  $s_{\text{in}}$ .

which, as expected from energy conservation, is always smaller than  $|s_{\text{in}}|^2$ . Equation (1.16) describes well the actual transmission traces observed for microring resonator in the simplest linear case (absence of splitting, small input powers, absence of other resonances). Figure 1.8(a) shows the normalized transmission value ( $s_{\text{out}}/s_{\text{in}}$ ) as a function of normalized detuning  $2\Delta/\kappa$ . Equations (1.13) and (1.15) can be also used to describe dephasing between the intracavity field, transmission field and input field as a function of the detuning, which are also shown in Fig. 1.8(b, c).

There are three different cases, which are typically distinguished depending on the ratio between internal resonator losses and bus coupling losses:

**Undercoupled case**, when  $\kappa_{\text{ex}} < \kappa_0$  - internal loss rate is stronger than external. The dissipation of the energy from the cavity happens faster through the internal channels including absorption or scattering, than through the evanescent coupling to the bus waveguide.

**Critical coupling**, when  $\kappa_{\text{ex}} = \kappa_0$  - loss rates are equal. This is the case which is most preferable for nonlinear optics in microresonators, since in the case of the fixed  $\kappa_0$ , which is the usual case for monolithic microresonators, the system reaches maximum intracavity power, when  $\kappa_{\text{ex}}$  is adjusted to be equal with  $\kappa_0$ .

**Overcoupled case**, when  $\kappa_{\text{ex}} > \kappa_0$  - external loss rate is stronger. While the intracavity power is small, this case can be useful for certain applications of the microresonator-based combs, since it may allow more power to be extracted from the resonator. This however comes at the expense of higher driving fields required to generate comb states.

In experiment, the different cases are controlled by changing the coupling gap - the distance between the resonator and the bus waveguide. For integrated microresonators this value is usually fixed, and the ratio between  $\kappa_{\text{ex}}$  and  $\kappa_0$  is not easily changeable (one would need access to  $\kappa_0$  by modifying the internal elastic or non-elastic scattering processes, or introduce way to tune the gap distance between the microresonator and the bus waveguide). In contrast, for crystalline microresonators, where the input field is supplied through the tapered fiber or prism,  $\kappa_{\text{ex}}$  can be accessed directly.

We finally note that the present subsection reviews the ideal case of the bus-to-resonator coupling assuming that the coupling is lossless in a sense that there is no photon leakage during the coupling process (each photon coming from the input port is either reflected from the resonator and contributes to  $|s_{\text{out}}|^2$ , or couples to the cavity mode and appears inside the resonator). A real system usually has parasitic losses, which can occur due to the photon scattering to other resonator modes or even to the free-space [38, 39].

### 1.2.3 Resonator dispersion

In a general case, the dispersion (or chromatic dispersion) of the medium describes the frequency-dependent phase velocity of light in this medium, which is introduced through the frequency-dependent refractive index  $n = n(\omega)$  as  $v_\phi = c/n(\omega)$ . The fundamental reason for the presence of dispersion is the resonance absorption by the bound electrons, which by modifying the absorption coefficient of the medium introduce the phase delay to the propagating light [40].

Far from these electronic resonances the refractive index  $n(\omega)$  can be well approximated by Sellmeier equation:

$$n^2(\omega) = 1 + \sum_{j=1}^m \frac{B_j \omega_j^2}{\omega_j^2 - \omega^2}, \quad (1.17)$$

where the parameters  $B_j$  and  $\omega_j$  correspond to different electronic resonances obtained experimentally and fitted for bulk materials.

In the field of fiber and waveguide optics the light propagation is often constrained by the channel (fiber or waveguide) geometry. Thus the light propagates not in the bulk material, but close to the interface with other media (e.g. core-cladding interface in fibers and integrated waveguides). In this case the concept of *effective refractive index*,  $n_{\text{eff}}$  is used. It takes into account not only the material dispersion (the contribution

from refractive indexes of different bulk materials participating in the light guiding), but also the geometry of the fiber or waveguide - also called geometrical dispersion. Due to the complexity of the analytical solution to the Helmholtz equation of light propagation in waveguides or fibers with complex structure, usually finite-element method (FEM) simulations are used to compute  $n_{\text{eff}}$ .

In order to describe light propagation in material, the propagation phase constant  $\beta$  is used. It takes into account the intensity-dependent refractive index, and in the general case should be distinguished from the wavenumber  $k = 2\pi n/\lambda$ . Due to the frequency dependence of the refractive index:  $\beta = \beta(\omega)$ . It can also be expanded around frequency  $\omega_m$  in a Taylor series:

$$\beta = \frac{n(\omega)\omega}{c} = \beta_0 + \beta_1(\omega - \omega_m) + \beta_2 \frac{(\omega - \omega_m)^2}{2} + \dots, \quad (1.18)$$

where  $\beta_j = \partial^j \beta / \partial \omega^j|_{\omega_m}$ . Here and further we use  $n(\omega)$  to denote the *effective* refractive index of the waveguide we consider. The first term,  $\beta_0$  is linked to the phase velocity of the light:  $v_\phi = c/n(\omega_m) = 1/\beta_0$ . The second one,  $\beta_1$ , is related to the group velocity  $v_g$  and the group refractive index  $n_g$ , which describes the speed of the pulse propagation:

$$\beta_1 = \frac{1}{v_g} = \frac{n_g}{c} = \frac{1}{c} \left( n + \omega \frac{dn}{d\omega} \right). \quad (1.19)$$

The second term,  $\beta_2$ , describes the group velocity dispersion (GVD):

$$\beta_2 = \frac{1}{c} \left( 2n \frac{dn}{d\omega} + \omega \frac{d^2 n}{d\omega^2} \right). \quad (1.20)$$

It is generally responsible for pulse broadening, which can be estimated for pulses of the width  $\Delta\omega$  propagating along the distance  $z$  to be:  $\Delta T \simeq z\beta_2\Delta\omega$ .

Other terms are usually referred to as higher-order dispersion terms. Depending on the sign of the  $\beta_2$  two cases are distinguished: *normal* dispersion ( $\beta_2 > 0$ ), when higher frequencies travel slower than the lower frequencies, and *anomalous* dispersion ( $\beta_2 < 0$ ), when the higher frequencies travel faster. We note that so far we did not make any statements about whether light propagates in a straight waveguide, fiber or resonator. This means that a similar approach can be used for any light guiding system, including resonators. In particular, the dispersion properties of fiber resonators are often described using such an approach [41, 42].

In the microresonator-based optical combs community it is common, however, to describe the resonator's dispersion in a different way. The frequency of the resonances  $\omega_m$  is introduced as a Taylor expansion around certain resonance  $\omega_{m_0}$  with respect to equidistant frequency grid. This becomes particularly convenient for the simulations of frequency combs, as they naturally establish equidistant frequency grid of the oscillating modes

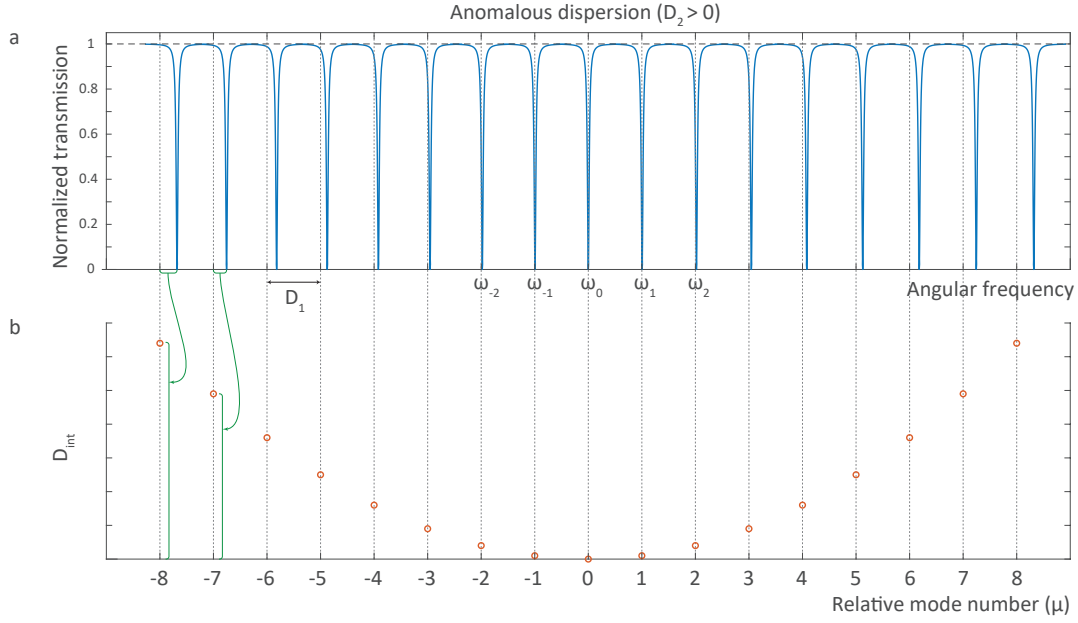


Figure 1.9 – (a) Resonance structure of the microresonator with dispersion limited to the second order with anomalous GVD ( $D_2 > 0$ ). Resonances are located at frequencies  $\omega_\mu$ . Dashed grey lines spaced by the  $D_1(\omega_0)$ . (b) Integrated dispersion of the resonance structure shown in (a) plotted as a function of relative mode number  $\mu$ .

separated by the comb line spacing. We first introduce the relative mode index  $\mu = m - m_0$  and consider a set of indexed resonator modes  $\omega_\mu, \mu \in \mathbb{Z}$  around resonance mode with  $\mu = 0$  ( $m = m_0$ ). The choice of the mode with  $\mu = 0$  will be in the following discussion associated with the pumped mode. Since we use another indexing  $\mu$ , which in contrast to  $m$  no longer represents the number of intracavity field oscillations over the roundtrip, it can be any integer number. The Taylor expansion for the resonator modes around  $\omega_0$ :

$$\omega_\mu = \omega_0 + \mu D_1 + \frac{D_2}{2} \mu^2 + \frac{D_3}{6} \mu^3 + \dots = \omega_0 + \sum_{n=1}^{\infty} D_n \frac{\mu^n}{n!} \quad (1.21)$$

where each of the expansion terms is defined as:  $D_n = d^n \omega_\mu / d\mu^n$  at  $\omega = \omega_0$ . In this expansion, the first dispersion term merely represents the FSR of the cavity around the frequency  $\omega_0$ :  $D_1(\omega_0) = \text{FSR}(\omega_0)/2\pi$ , and the second-order dispersion term is related to GVD:

$$D_2 = -\frac{\beta_2 D_1^2}{\beta_1} = -\frac{\beta_2 D_1^2 c}{n_g} \quad (1.22)$$

For this notation, anomalous dispersion corresponds to the case when  $D_2 > 0$ , and normal - when  $D_2 < 0$ . For the resonators, chromatic dispersion with a frequency-dependent refractive index  $n = n(\omega)$  results in the frequency dependency of the cavity FSR. In particular, one can show that introducing the dispersion modifies the FSR formula (1.5)

to be:

$$\text{FSR} = \frac{c}{Ln_g} . \quad (1.23)$$

In the resonator case, when describing the comb formation, it is convenient to use so-called *integrated dispersion*, which is introduced as:

$$D_{\text{int}}(\omega_0) = \omega_\mu - (\omega_0 + \mu D_1) = \sum_{n=2}^{\infty} D_n \frac{\mu^n}{n!} . \quad (1.24)$$

Integrated dispersion and its connection to the resonance structure are shown in Fig. 1.9. Figure 1.9(a) shows a conventional case for microresonator resonance structure (blue) having anomalous GVD (FSR grows with frequency,  $D_2 > 0$ ). The resonance positions at  $\omega_\mu$  coincide with an equidistant frequency grid  $\omega_0 + \mu D_1$  (grey dashed lines) at  $\omega = \omega_0$ , but start to acquire walk-off with increasing  $|\mu|$  due to the frequency-dependent FSR. As shown in Fig. 1.9(b) the integrated dispersion describes this walk-off of cavity resonance positions from the equidistant frequency grid established by the  $D_1(\omega_0)$  in the case when the integrated dispersion is limited by the GVD term only ( $D_n = 0, n \geq 3$ ). The concept of integrated dispersion for frequency combs is convenient for several reasons. First, as will be shown in the following sections, the integrated dispersion naturally appears in the simulation models of microresonator-based frequency combs and describes the detunings of the comb lines with respect to the resonances they oscillate in. Second, it allows an easy way to visualize higher-order dispersion terms (deviation from parabolic curve) as well as linear phase-matching condition (zero crossings).

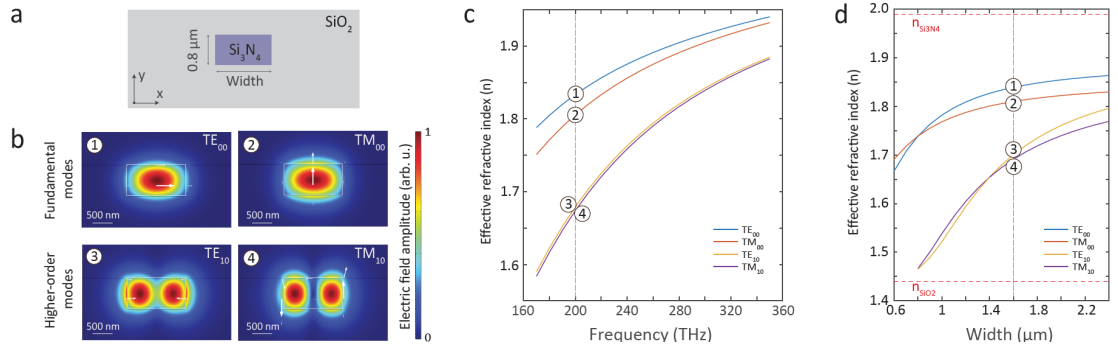


Figure 1.10 – (a) Model of the resonator waveguide cross-section with  $\text{Si}_3\text{N}_4$  core and  $\text{SiO}_2$  cladding used for the dispersion simulations. (b) Transverse mode profiles ( $|E(x, y)|$ ) obtained from COMSOL simulations for the waveguide model shown in (a); white arrows indicate direction and magnitude of electric field; (c) Simulated effective refractive indexes as a function of optical frequency for 4 transverse modes shown in (b) and fixed waveguide dimensions of  $1.5 \times 0.8 \mu\text{m}$ ; (d) Simulated effective refractive indexes as a function of waveguide width for waveguide height of  $0.8 \mu\text{m}$  and frequency  $200 \text{ THz}$ . Crossing of the fundamental modes appearing at around  $0.8 \mu\text{m}$  corresponds to the change of the aspect ratio from  $> 1$  to  $< 1$ .

So far we have assumed that the resonator we consider supports only a single transverse mode (spatial field distribution in the transverse plane of the waveguide -  $E(x, y)$ ). In real microresonators, depending on the size and shape of the integrated waveguide (or the protrusion of the WGM resonator) it can support a variety of transverse modes distinguished by their polarization and the number of "nodes" in the intensity profile along  $x$ - and  $y$ -axes. An example of the modes for the rectangular  $\text{Si}_3\text{N}_4$  waveguide with silica cladding is shown in Fig. 1.10. Depending on the direction of the electric field, they are distinguished between transverse electric (TE) modes and transverse magnetic (TM) modes. The modes with simplest profile (no nodes) in both transverse direction are called fundamental modes, and they also denoted as  $\text{TE}_{00}$  or  $\text{TM}_{00}$ . Their profiles are shown in Fig. 1.10(b, top). Other modes with the nodes in their spatial intensity distribution are often referred to as higher-order modes, and in general for rectangular waveguides they are indexed in accordance to the number of nodes along the transverse directions ( $x$  and  $y$ ). Figure 1.10(b, bottom) shows the spatial field distribution of the first high-order modes, that have a single node in  $x$ -direction:  $\text{TE}_{10}$  and  $\text{TM}_{10}$ . As can be understood from the difference in the spatial profiles of transverse modes, they have different effective refractive indexes (see Fig. 1.10(c)), and consequently different FSR, GVD and higher-order dispersion terms. We also note that the number of possible transverse mode families also scales with the waveguide dimensions, and smaller waveguides can support only limited amount of higher order modes, or even do not support them at all. This happens when the mode profile becomes too large to fit in the waveguide, making the mode leaky and not guided. This in particular can be observed for the simulations of effective refractive index for different waveguide dimensions as shown in Fig. 1.10(d). For the waveguide width  $< 0.8 \mu\text{m}$  higher-order modes disappear because a small waveguide cannot support the guiding effect for their large transverse field distribution.

In a real microresonator, the resonance structure is often complex, consisting of several transverse mode families. Apart from having distinct dispersion profiles, the modes can additionally alter it due to the mutual interaction. This happens when two transverse modes appear at close frequencies, and the waveguide has any mechanism that provides scattering of the photons from one mode to another (coupling). In the case when such coupling is described with a rate  $\gamma$  for two mode families  $\omega_\mu^1$  and  $\omega_\mu^2$

$$\omega_\mu^{(\pm)} = \frac{\omega_\mu^1 + \omega_\mu^2}{2} \pm \sqrt{\gamma^2 + \left(\frac{\omega_\mu^1 - \omega_\mu^2}{2}\right)^2}. \quad (1.25)$$

This results in frequency-localized modifications of the integrated dispersion. Such hyperbolic-shaped disruptions of the dispersion curve, which can be experimentally traced in the dispersion measurements [43, 44] are called *avoided modal crossings* (AMXs). AMX locally modifies dispersion profiles of both interacting modes adding strong localized

normal or anomalous contribution, which in turn can significantly impact the dynamics of microresonator-based optical frequency combs [45, 46].

### 1.2.4 Nonlinearity, resonator bistability

Optical nonlinearity describes the situation when the response of the medium - its polarization (density of the electric dipole moments) - depends nonlinearly on the optical field of incident light. Physically this can be attributed to anharmonism in the oscillations of bound medium electrons, which appears when incident light achieve strong field amplitudes. In general, the time-dependent polarization should be treated as a vector for a certain point  $\mathbf{r}$  of the material at time instant  $t$ , which takes into account the amplitudes and direction of different optical fields in the given point and their "history". We restrict ourselves to the simple case and for the purposes of this section assume that all fields are aligned along the same direction transverse to the propagation direction  $z$ . As before the fields can be represented as  $E(t) = Ee^{-i\omega t} + c.c.$  with complex amplitude  $E$ , and the material polarization  $P(t)$  depends only on their instantaneous magnitude:

$$P(t) = \varepsilon_0(\chi^{(1)}E(t) + \chi^{(2)}E(t) \cdot E(t) + \chi^{(3)}E(t) \cdot E(t) \cdot E(t) + \dots), \quad (1.26)$$

here  $\varepsilon_0$  indicates vacuum permittivity, and  $\chi^k$  denotes the  $k$ -th order of optical susceptibility, which in the general case is  $k + 1$ -th order tensor, but here is assumed to be just a constant.  $\chi^{(1)}$  is usually called the linear susceptibility and is related to the effective refractive index as  $n = \sqrt{1 + \chi^{(1)}}$ . The two first nonlinear terms of the polarization are represented by the second-order susceptibility  $\chi^{(2)}$ , and third-order susceptibility  $\chi^{(3)}$ . Since  $\text{Si}_3\text{N}_4$  used in our work is inversion symmetric, the second-order nonlinear susceptibility is zero. Consequently, the effect of second-order nonlinearity is negligible (due to symmetry breaking at the waveguide boundaries it can still be present, but we neglect it in the calculations). Thus the smallest nonlinearity that plays a role in the processes in which we are interested is represented by a third-order or *Kerr* nonlinearity. The tensor describing the Kerr nonlinearity  $\chi^{(3)}$  in general is a complex value,  $\chi^{(3)} = \chi_{\text{Re}}^{(3)} + i\chi_{\text{Im}}^{(3)}$ , where the real part describes the *parametric* conversion processes, which undergo conserving the energy of interacting photons and introduces no change to the quantum state of the medium. In contrast, the imaginary part describes inelastic processes, such as Raman scattering (on optical phonons), Brillouin [Brillouin - Mandelstam] scattering (on acoustic phonons) and multi-photon absorption.

We next consider nonlinear polarization responsible for the parametric processes:  $P_{\text{NL}}(t) = \varepsilon_0\chi_{\text{Re}}^{(3)}E(t) \cdot E(t) \cdot E(t)$ , and assume that the field is represented by the sum of three components, propagating in the same  $z$  direction with phase constants  $\beta_1, \beta_2, \beta_3$  and oscillating at different frequencies  $\omega_1, \omega_2, \omega_3$ :  $E(z, t) = E_1e^{-i(\omega_1 t - \beta_1 z)} + E_2e^{-i(\omega_2 t - \beta_2 z)} + E_3e^{-i(\omega_3 t - \beta_3 z)} + c.c.$  The nonlinear polarization in this case will have several terms, which can be attributed to different physical processes, listed below and also schematically

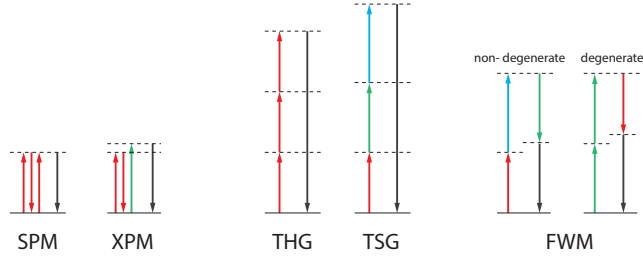


Figure 1.11 – Energy-level diagrams for the third-order nonlinear parametric processes.

shown in Fig. 1.11:

**Self-phase modulation (SPM)** - describes the terms of nonlinear polarizations in the form of  $3\varepsilon_0\chi_{\text{Re}}^{(3)}|E_j|^2E_j e^{-i(\omega_j t - \beta_j z)}$  for  $j = 1, 2, 3$ . The process can be thought of as the modification of the refractive index due to the light intensity. The resulting nonlinear polarization term will oscillate at the same frequency as the incident field  $E_j(t)$  similar to the case of linear polarization, but its amplitude will be proportional to the  $3\varepsilon_0\chi_{\text{Re}}^{(3)}|E_j|^2$ , which can be described through the introduction of the intensity-dependent nonlinear refractive index. Since the field in a such process is acting on itself (on its phase propagation constant) through the medium nonlinearity the process is called self-phase modulation.

**Cross-phase modulation (XPM)** - describes the terms of nonlinear polarization in the form of  $6\varepsilon_0\chi_{\text{Re}}^{(3)}|E_k|^2E_j e^{-i(\omega_j t - \beta_j z)}$  for  $j, k = 1, 2, 3; j \neq k$ . The process is similar to SPM, but describes the modification of the refractive index induced on one field  $E_j(t)$  by the intensity of other co-propagating fields  $E_k(t), j \neq k$ .

Both SPM and XPM are phase-insensitive processes, meaning that they do not require phase matching to develop, and their strength depends linearly on the intensity of the corresponding fields. Thus they can both be described in a form of intensity-dependent nonlinear refractive index, which will appear as a contribution to a regular effective refractive index  $n$ :  $n = n_0 + n_2 I$ , where intensity is introduced as  $I_j = \varepsilon_0 n_0 c |E_j|^2 / 2$ , and nonlinear refractive index:

$$n_2 = \frac{3}{4n^2\varepsilon_0 c} \chi_{\text{Re}}^{(3)}, \quad (1.27)$$

when both processes are involved, the resulting change in the refractive index due to nonlinear effects experienced by a light field  $E_j$  is

$$\delta n_{\text{NL}} = n_2 I_j + 2n_2 (I_k + I_l). \quad (1.28)$$

**Third-harmonic generation (THG)** - describes the terms of nonlinear polarization in the form of  $\varepsilon_0\chi_{\text{Re}}^{(3)}E_j^3 e^{-i(3\omega_j t - 3\beta_j z)}$ ,  $j = 1, 2, 3$ , which is responsible for the generation of new photons having triple the frequency of the incident field.

**Triple-sum generation (TSG)** - describes the terms of nonlinear polarization in the form of  $\varepsilon_0 \chi_{\text{Re}}^{(3)} E_j E_i E_k e^{-i((\omega_j + \omega_k)t - (\beta_j + \beta_k + \beta_l)z)}$ , which is similar to THG, but appears when mixing fields have different frequencies.

**Four-wave mixing (FWM)** - describes the terms of nonlinear polarization in the form of  $6\varepsilon_0 \chi_{\text{Re}}^{(3)} E_j E_k^* E_l e^{-i((\omega_j - \omega_k + \omega_l)t - (\beta_j - \beta_k + \beta_l)z)}$  or  $3\varepsilon_0 \chi_{\text{Re}}^{(3)} E_j E_k^* E_j e^{-i((2\omega_j - \omega_k)t - (2\beta_j - \beta_k)z)}$ . In both processes the photons at new frequencies are being generated according to the energy conservation law. In the first case, which is referred to as *non-degenerate* FWM, the newly generated photons will have frequencies  $\omega' = \omega_j - \omega_k + \omega_l$  in the degenerate case or  $\omega' = 2\omega_j - \omega_k$  in the non-degenerate case. Since FWM is a phase-sensitive process, the mixing waves need to satisfy the momentum conservation law for the  $\beta$ -vectors – phase-matching. For the FWM processes we consider, phase matching happens when  $\beta$ -vector of the resulting field satisfies:  $\beta' \approx \beta_j - \beta_k + \beta_l$  ( $\approx 2\beta_j - \beta_k$ ) for non-degenerate (degenerate) case. In terms of the photon creation-annihilation picture the four-wave mixing can be interpreted as the interaction between four photons (here the term FWM comes), where two photons are annihilated and two photons are created according to the energy conservation condition:  $\omega_j + \omega_l = \omega_k + \omega'$ .

We next consider how the nonlinearity can be included in the resonator description. Since the nonlinearity is associated with the presence of the field and its strength, we now have to make assumptions about the optical fields in the resonator. We consider linearly polarized monochromatic light in the fundamental transverse mode propagating along the resonator. We start to consider only one field. The only third-order nonlinear process which impacts the field propagation in such case is SPM. Through the intensity-dependent change in the refractive index SPM introduces additional contribution to the phase of the propagating light depending on its power  $P$ :

$$\phi_{\text{NL}} = \frac{2\pi}{\lambda} n_2 \frac{P}{A_{\text{eff}}} = \gamma PL, \quad (1.29)$$

where we used the nonlinear coefficient  $\gamma = \omega n_2 / c A_{\text{eff}}$  [rad/m·W]. The nonlinear phase shift can be introduced in the derivations of the resonance conditions and intracavity intensity build-up  $\mathcal{B}$ , shown earlier in section 1.2.1 for dispersion-free cavity, which leads to the modification of the formula (1.4):

$$\mathcal{B} = \left| \frac{E_3}{E_1} \right|^2 = \frac{(1 - r^2)a^2}{1 + r^2 a^2 - 2ra \cos(\phi_0 + \phi_{\text{NL}})}. \quad (1.30)$$

Thus, for small input powers, when the nonlinear phase shift acquired over one roundtrip is small the system behaves as in the linear case. When the nonlinear phase shift becomes comparable with the linear phase shift  $\phi_0$ , the resonance picture becomes "tilted" as shown in Fig. 1.12. It can be understood that higher intracavity powers accumulate stronger phase shift due to the nonlinear contribution, which leads to the modification of the resonance conditions for the nonlinear resonator, and in particular is translated

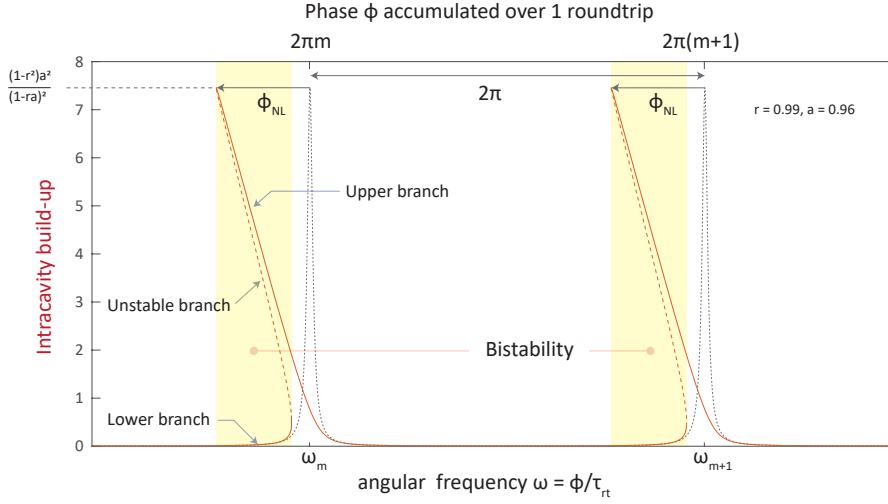


Figure 1.12 – Intracavity intensity build-up of the nonlinear dispersion-free resonator. The nonlinearity, and in particular SPM considered here induce an additional phase shift on the light field propagating in the cavity proportional to the intracavity power. This leads to the resonance "tilting" (red) in comparison with initial resonance structure without nonlinearity (grey). Such resonance tilting also leads to the formation of bistability regions (highlighted in yellow), where three intracavity field solutions can exist and form upper and lower stable branches and one unstable solution branch.

in "dragging" the resonance in experiment. One of the important consequences, which can be straightforwardly noted from the figure is that for a certain range of the phase, the system has three solutions (areas shaded yellow). This phenomenon is called optical *bistability*, because only two of these solutions are stable, which will be noted later. Optical bistability is common for optical systems with a feedback, and in particular was observed in driven optical cavities [47]. As will be seen further, the bistability plays a crucial role in the formation of microresonator-based combs and solitons. The equation (1.30) describing nonlinear cavity resonances, however, is transcendent and can not be used to study the bistability analytically. In order to simplify it, we again, as in the section 1.2.1 assume that the resonator we consider operates in the high finesse limit ( $r \rightarrow 1$ ). This means that our field is non-zero only in the vicinity of the resonances, and the range of the phase detunings of the optical field propagating in the cavity we consider should be small in comparison with  $2\pi$ . Another approximation we introduce is that the nonlinear phase shift is also significantly smaller than  $2\pi$ . Using intracavity energy-normalized fields and input field  $s_{\text{in}}$ , as was introduced for the input-output coupling formalism of the cavity 1.11, we can write for the field evolution from the roundtrip  $p$  to the roundtrip  $p + 1$ :

$$a^{(p+1)}(0) = r a^{(p)}(0) e^{i\phi_0} e^{i\gamma L P} + \sqrt{(1-r^2)\tau_{\text{rt}}} s_{\text{in}}. \quad (1.31)$$

The last term on r.h.s. represents a continuous coherent pumping of the microresonator,

which spans over the full roundtrip, so the total number of the photons entering the cavity over one roundtrip is  $(1 - r^2)\tau_{\text{rt}}|s_{\text{in}}|^2$ . Considering approximations above and noting that  $da/dt = (a^{(p+1)}(0) - a^{(p)}(0))/\tau_{\text{rt}}$ , the equation (1.31) can be reduced to:

$$\frac{da}{dt} = - \left( \frac{\kappa}{2} + i\Delta - ig|a|^2 \right) a + f, \quad (1.32)$$

where we have introduced the Kerr-nonlinear frequency shift per photon -  $g$ :

$$g = \frac{\hbar\omega_p^2 cn_2}{n_g^2 V_{\text{eff}}}. \quad (1.33)$$

We also draw the reader's attention to the similarity of the introduced earlier input-output cavity formalism and equation (1.32), which augments the former one with an additional nonlinear term proportional to the number of intracavity photons  $|a|^2$ .

**Bistability.** To further explore the bistability, we simplify eq. (1.32) using a normalized detuning  $\zeta_0 = 2\Delta/\kappa$ ,  $a_0 = a \cdot \sqrt{2g/\kappa}$  and consider a steady state of the resulting equation:

$$f = [1 + i\zeta_0]a_0(t) - i|a_0(t)|^2 a_0(t). \quad (1.34)$$

After squaring both sides and denoting  $\rho = |a_0|^2$ , we obtain a cubic equation for  $\rho$ :

$$\rho^3 - 2\zeta_0\rho^2 + (\zeta_0^2 + 1)\rho - |f|^2 = 0, \quad (1.35)$$

which can have either one or three real roots depending on the parameters  $\zeta_0$  and  $|f|^2$ . Using the Thcrinhaus approach for the reduction to a depressed cubic equation (without quadratic term) and the Vieta substitution, one can show that for the equation  $ax^3 + bx^2 + cx + d = 0$ , three real roots are available when  $p = \frac{3ac-b^2}{3a^2} < 0$ , otherwise ( $p > 0$ ) - only one real root is presented. In our case three real roots are available when  $\zeta_0 > \sqrt{3}$ . Thus there is a critical detuning value  $\sqrt{3}$ , above which the system equation has three solutions. Note, however, that the availability of three real roots doesn't mean that one can always find them, they only become available within a certain range of pump terms  $|f|^2$ , and even if  $p < 0$  the cubic equation can still have either three or one real root, while for  $p > 0$  three real roots are not possible at all. Denoting the boundaries for the pump amplitude, where with  $\zeta_0 > \sqrt{3}$  equation (1.35) has three real roots as  $f_{\pm}$ , one can derive them as a function of  $\zeta_0$ . We find the extrema  $\rho_{\mp}$  of the  $G(\rho) = \rho^3 - 2\zeta_0\rho^2 + (\zeta_0^2 + 1)\rho$ , by taking the derivative  $\frac{\partial G(\rho, \zeta_0)}{\partial \rho}$ :

$$\frac{\partial G(\rho, \zeta_0)}{\partial \rho} = 3\rho^2 - 4\zeta_0\rho + (1 + \zeta_0^2), \quad (1.36)$$

$$\rho_{\pm} = \frac{2\zeta_0}{3} \mp \frac{1}{3}\sqrt{\zeta_0^2 - 3}. \quad (1.37)$$

Using eq. (1.37) in  $G(\rho)$ , one can derive  $f_{\pm}$ :

$$f_{\pm} = \frac{2\zeta_0 \mp \sqrt{\zeta_0^2 - 3}}{3} \left[ 1 + \left( \frac{\sqrt{\zeta_0^2 - 3} \pm \zeta_0}{3} \right)^2 \right]. \quad (1.38)$$

Three available roots  $\rho_1, \rho_2, \rho_3$ , which can be found at a fixed input power  $f$  in the bistability region, are well visualized in Fig. 1.12 as a function of  $\zeta_0$  despite the number of approximations we introduced. They form three solution branches of the tilted resonance for detuning values  $\zeta_0$  within the bistability region. One can show that for three real roots  $\rho_1 < \rho_2 < \rho_3$ , which appear on these branches,  $\rho_1, \rho_3$  - are always stable and  $\rho_2$  is always unstable [48]. Two stable solutions branches, shown with solid lines in Fig. 1.12 are often referred to as "upper" and "lower" branches.

### 1.2.5 Thermal effects

Thermal effects play a significant role in the behavior of microresonators. In contrast to large free-space resonators, microcavities have a small mode volume, which together with the resonant enhancement of the intracavity field facilitates access to the nonlinear effects [49]. On the other hand, small mode volume, high intracavity intensities and small surface area limiting the heat dissipation lead to a high temperature sensitivity to light dissipation [50]. Furthermore, such temperature sensitivity of the microresonator is also important in the context of microresonator-based optical frequency combs, where the microresonators are often driven at relatively high powers and can experience significant changes in their dynamics due to light absorption in a small volume, followed by the temperature changes.

There are two main processes, which contribute to the temperature-induced changes in microresonator properties: material thermal expansion and temperature dependence of the effective refractive index [51]. The first process impacts the size of the cavity and is described through the coefficient of linear thermal expansion of the material  $\alpha_L = 1/L \cdot dL/dT$ . The second process induces a change in effective refractive index and is introduced in a similar way through the coefficient of thermally-induced effective refractive index  $\alpha_n = 1/n \cdot dn/dT$ . Similar to the effect of SPM, the change in the cavity length or cavity refractive index leads to the additional thermally-induced phase shift, acquired by the light travelling inside the microresonator  $\phi_T$ , which can be introduced in the equation (1.30). For the resonance structure such thermally-induced phase shift leads to the resonant shift appearing in addition to the shift caused by optical nonlinearity

and can be described as follows:

$$\omega(T) = \omega(T_0) \cdot \left( 1 - \frac{1}{n} \frac{dn}{dT} (T - T_0) - \frac{1}{L} \frac{dL}{dT} (T - T_0) - \frac{1}{n} \frac{n_2 P}{A_{\text{eff}}} \right), \quad (1.39)$$

where  $\omega(T)$  - is the resonance frequency of the microresonator driven with a continuous monochromatic pump field, and  $\omega(T_0)$  - is the resonance frequency of the resonator at ambient temperature  $T_0$  (e.g. room temperature) without driving. We assumed that the system in both states is at thermal equilibrium, and  $P$  - is the intracavity circulating power, when the system is driven. First two terms on the r.h.s. responsible for thermally-induced cavity shift, while the last term describes the contribution of nonlinearity. The initial position of the cavity resonance  $\omega_0$  is called the *cold* cavity resonance, referring to the fact that the microresonator is not driven. The position of the thermally and Kerr shifted resonance  $\omega(T(P), P)$  is referred to as the *hot* cavity resonance. For the  $\text{Si}_3\text{N}_4$  microresonators explored in this work, both thermal coefficients are positive. This leads to the cumulative shifting of the resonance to smaller frequencies (both thermal effects and nonlinearity act together). Despite mentioning above that the thermal effect acts similarly to the nonlinear effects, we should however highlight several important differences between both processes. First, the effect of SPM acts only on the pumped resonance, and other cavity resonances experience the effect of optical nonlinearity through XPM. In contrast, temperature effects act similarly on all cavity resonances leading to their shifting. Second, the nonlinear and thermal effect have a significant difference in their characteristic timescales. The nonlinearity shift is considered to be instant (or on the order of  $10^{-15}\text{s}$ ), while the thermal effect acts at the millisecond scales.

Since the resulting nonlinear shift changes the position of the resonance with intracavity intensity build-up, when the driving laser scans over such a resonance, the laser detuning can not be counted anymore from the position of the cold cavity resonance  $\omega(T_0)$  due to the resonance shift. Thus it is convenient to introduce the concept of *effective* detuning:

$$\Delta_{\text{eff}} = \omega(T) - \omega_p. \quad (1.40)$$

The importance of effective detuning becomes particularly clear for microresonator-based frequency combs and the generation of solitons covered in the following sections. As will be shown further the soliton dynamics relies significantly on the effective detuning.

### Thermal locking, thermal triangle

An important consequence of the thermal- and Kerr-induced resonance shift is the spontaneous *locking* of the resonator to the pump. It can be understood in the following way: assume that the pump is blue detuned with respect to the resonance, and the cavity experiences an external fluctuation which moves the cavity resonance closer to the pump. In such case intracavity power will grow due to intensity build-up at smaller detunings,

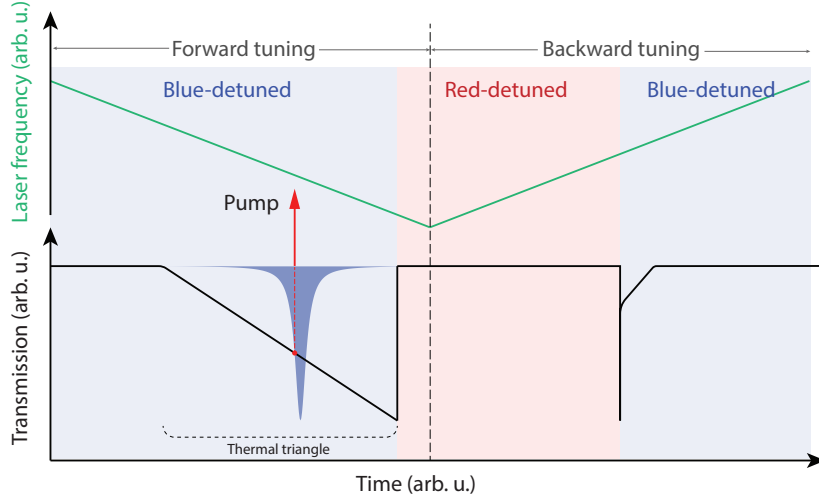


Figure 1.13 – Schematics of thermal and Kerr locking, when frequency of the pump laser is scanned over the resonance in forward direction (increasing wavelength) and backward direction (decreasing wavelength). In forward direction the pump is initially blue-detuned. The resonance locks to the pump, when the pump approaches, and is dragged towards lower frequencies. When the pump overcomes the resonance and appears red-detuned, the resonance unlocks and returns to its initial cold cavity position completing characteristic triangle in transmission shown in the bottom of the figure. In contrast, due to the thermal and Kerr instability in the red-detuned regime, the triangle is significantly compressed, when the pump is scanned in backward direction. When the pump approaches from the red-detuned side, the resonance quickly relaxes to the blue-detuned state drawing characteristic spike in the transmission.

which will cause an additional increase in temperature and Kerr shift of the resonance in the opposite direction. A similar mechanism will tend to restore the initial effective detuning when the external fluctuation increases it. This process is called thermal and Kerr locking of the microresonator to the driving laser. In general it depends on the signs of the thermal coefficients  $\alpha_L$ ,  $\alpha_n$  and  $n_2$  and will appear when all contributions of the resonance shifts act in the same direction. In the case where one of the contributions is having a different sign, the system might reveal an oscillatory behavior instead of locking [52]. Furthermore, even if all the contributions are acting in the same direction, such behavior is only valid on one side of the resonance. In our  $\text{Si}_3\text{N}_4$  platform it appears only for the blue-detuned position of the resonance. On the red-detuned side the external fluctuations will not be damped, but supported and lead to instability. This effect leads to a peculiar behavior of the cavity resonance when probing it with a laser: when the pump laser is scanned from the blue-detuned side, the resonance cavity experiences a thermal and nonlinear shift and moves away from the driving laser. However, when the position of zero effective detuning is reached, the system quickly relaxes to the cold cavity position due to being unstable. One of the consequences of such behavior is the so-called *thermal (and Kerr) triangle*, which is often observed in microresonators when the laser

scans over a cavity resonance [50]. In the opposite direction, due to this instability, an approaching laser will induce a quick resonance jump to the blue-detuned position as shown in Fig. 1.13.

### 1.3 Kerr frequency combs

As we described earlier, the nonlinear processes, and in particular FWM can lead to the generation of new frequencies when pump photons accumulated in the resonator start the parametric conversion process. This process however, requires the phase-matching condition to be satisfied, which enables the constructive build up of the newly generated fields.

In the case of resonators and particularly microresonators, which are mostly interesting for us, the generated fields with frequencies  $\tilde{\omega}_\mu$  (which we will further also refer to as "comb lines", or just "lines") can only build up close to the resonance frequencies  $\omega_\mu$  (or in the following also - "resonator modes"). As in the previous section we use relative mode number  $\mu$  for indexing, and note that indexing of both sets of frequencies is mutual - meaning in our context that a comb line oscillating at  $\tilde{\omega}_{\mu'}$  appears close to the resonator modes with the same index  $\mu'$ . The purpose of using two different notations for the resonances and fields generated in the microcavity is to highlight the fact that despite low resonance linewidths, the comb lines are not necessary generated *exactly* on the resonances ( $\tilde{\omega}_\mu = \omega_\mu$ ) but may have non-zero detuning with respect to the resonances they appear in. According to energy conservation, the mixing lines with frequencies  $\mu = j, k, l, m$  satisfy  $\tilde{\omega}_j + \tilde{\omega}_k = \tilde{\omega}_l + \tilde{\omega}_m$ , or  $j + k = l + m$ . On the other hand, the propagation constants of the corresponding fields are described by:

$$\tilde{\beta}_m = \frac{\tilde{\omega}_m n(\tilde{\omega}_m)}{c}, \quad (1.41)$$

which, in the case when the frequencies of the mixing fields are close to each other and far from the electronic resonance of the material such that  $n(\tilde{\omega}_j) \approx n(\tilde{\omega}_k) \approx n(\tilde{\omega}_l) \approx n(\tilde{\omega}_m)$ , leads to phase matching for the mixing lines:  $\tilde{\beta}_j + \tilde{\beta}_k \approx \tilde{\beta}_l + \tilde{\beta}_m$ . Due to this result, it is often said that the FWM processes are intrinsically phase-matched in the microresonator geometry. While being correct with given above approximations, the discrepancy between the frequencies of the generated comb lines, which are strictly equispaced due to energy conservation, and the resonator modes, whose spacing varies due to the dispersion, can result in a large walk-off of  $\tilde{\omega}_m$  from  $\omega_m$  leading to the suppression of the FWM process efficiency.

The first parametric oscillations in optical microcavity were demonstrated in silica microtoroids [3], where the generation of a few signal and idler lines produced by a strong CW laser coupled to a high- $Q$  microresonator was observed. Being already in some sense the first frequency comb generated in a microresonator, these observations have

became a driver for the establishing of the area of microresonator-based optical frequency combs later [7]. Due to the central role which third-order nonlinearity plays together with high-quality microresonator in the formation of these combs, several names are used interchangeably - microresonator-based frequency combs, Kerr frequency combs or just Kerr combs.

The formation of Kerr frequency combs has complex dynamics and involves different stages with various time-domain behavior and noise properties, which we briefly review in the present section. We consider a general nonlinear microresonator, one of whose modes, denoted by  $\omega_0$  is driven by monochromatic CW light at the frequency  $\omega_p$  through the evanescently coupled waveguide, which is a general scheme for the Kerr-comb generation. A typical approach to the Kerr comb generation consists of fixing the power of the pump and tuning the pump frequency over the cavity resonance in order to achieve a strong build-up of the intracavity intensity, enabling the initiation of the nonlinear mixing processes. We also assume that the tuning of the pump laser is mode-hop-free, which allows a smooth approach and scan over the resonance, and is slow enough to let the system behave quasi-statically. In order to satisfy this condition, the system should be stable when the pump is tuned over the resonance. As we discuss earlier in section 1.2.5 in  $\text{Si}_3\text{N}_4$  microresonators (and in the majority of others, which were used for the generation of Kerr combs) this can only be achieved when approaching from the blue-detuned side of the resonance.

When the pump is approaching the resonance, intracavity intensity of the driving field grows in accordance with a steady-state solution of (1.32) for each given detuning  $\Delta$  (we omit the thermal effects for simplicity). Since at low intracavity powers there are photons of only one frequency (pump frequency) in the resonator, the generation of new frequencies starts with the degenerate FWM process involving the annihilation of two pump photons and the creation of two new signal and idler photons of different frequencies, appearing symmetrically with respect to the pump. Following the numeration of the modes with relative mode indexes  $\mu$ , the driving mode corresponds to  $\mu = 0$ , and parametrically generated new fields, also called *primary sidebands*, will appear at  $\pm\mu_{sb}$ . The development of the primary sidebands [53] and their energy exchange with the pump can be described using three coupled equations for each of the oscillating lines - three mode model.

### 1.3.1 Primary sidebands

The three mode model can give several insights into the development of the primary sidebands, and in general, initiation dynamics of Kerr frequency combs [53, 54]. With a good level of precision it allows one to predict the threshold intracavity power, at which the primary sidebands appear (the threshold for the FWM process), as well as their amplitude and positions  $\pm\mu_{sb}$ . We consider three modes, oscillating in the resonator:

$a_0(t)$  - field oscillating at pump frequency, and  $a_{\mu_{sb}}(t)$  - fields of the primary sidebands, which we for convenience denote as  $b_{\pm}$ . As before  $|a_0(t)|^2$  and  $|b_{\pm}|^2$  correspond to the number of photons in each of the modes multiplied by a factor  $2g/\kappa$ . We start with the equation on the pump mode  $a_0(t)$  (1.34), which should be augmented with the XPM terms and FWM terms taking into account the presence of the sidebands  $b_{\pm}$ :

$$\frac{da_0}{dt} = -[1 + i\zeta_0]a_0 + i(|a_0|^2 a_0 + 2|b_+|^2 a_0 + 2|b_-|^2 a_0 + 2b_+ b_- a_0^*) . \quad (1.42)$$

Terms  $2|b_{\pm}|^2 a_0$  describe XPM induced by the sidebands, which are included with a factor of 2 in comparison to SPM, as described earlier in section 1.2.4. The last term describes FWM. Similar equations can be also derived for the sidebands:

$$\frac{db_{\pm}}{dt} = -[1 + i\zeta_{\pm\mu}]b_{\pm} + i(|b_{\pm}|^2 b_{\pm} + 2|a_0|^2 b_{\pm} + 2|b_{\mp}|^2 b_{\pm} + a_0^2 b_{\mp}^*) . \quad (1.43)$$

One key difference of these two equations from the equation on the pump mode - is the presence of  $\zeta_{\pm\mu}$  - detunings of the sidebands from their resonances. As was noted earlier in section 1.3, the comb lines generated in the FWM process can have a significant walk-off (detuning) from the resonance positions due to the cavity dispersion.  $\zeta_{\pm\mu}$  is taking into account such contributions together with the detuning of the pump  $\zeta_0$ . The nonlinear terms are represented by  $|b_{\pm}|^2 b_{\pm}$  - SPM,  $2|a_0|^2 b_{\pm}$  - XPM from the pump and  $2|b_{\mp}|^2 b_{\pm}$  XPM - from the other sideband,  $a_0^2 b_{\mp}^*$  - FWM. Taking the complex conjugate of the equation for  $b_-$ , and omitting the terms proportional to  $|b_{\pm}|^2$  as being small, we can arrive to two linearized coupled equations for the sidebands, which can be written in a matrix form  $d\mathbf{b}/dt = \mathbf{M} \cdot \mathbf{b}$ :

$$\frac{d}{dt} \begin{bmatrix} b_+ \\ b_-^* \end{bmatrix} = \begin{bmatrix} -[1 + i\zeta_{\mu} - 2i|a_0|^2] & ia_0^2 \\ -ia_0^2 & -[1 - i\zeta_{\mu} + 2i|a_0|^2] \end{bmatrix} \begin{bmatrix} b_+ \\ b_-^* \end{bmatrix} .$$

Since the system is linearized, we can consider linear variations of  $\mathbf{b}$  in order to check its stability. If matrix  $\mathbf{M}$  has positive eigenvalues, the amplitude of the sidebands will grow with time exponentially. The equation for the eigenvalues gives:  $\lambda^2 - 2\lambda + (1 + (\zeta_{\mu} - 2|a_0|^2)^2) - a_0^4 = 0$ . Two real solutions are available when discriminant  $\Delta_{\lambda} = 2\sqrt{a_0^4 - (\zeta_{\mu} - 2|a_0|^2)^2} > 0$ . We assume that the dispersion of our cavity can be well approximated around the pump using only the GVD term, then the detunings of the corresponding sidebands are:  $\zeta_{\pm\mu} = \zeta_0 + d_2\mu^2$ , where  $\zeta_0 = 2(\omega_0 - \omega_p)/\kappa$  is the normalized detuning as introduced earlier, and  $d_2 = 2D_2/\kappa$  - normalized GVD term. Although we consider the system without thermal effects, the nonlinearity terms, as shown in section 1.2.5, through the Kerr locking, will lock our pump term ( $a_0$ ) on the resonance only on the blue-detuned side, i.e. when detuning is negative:  $\omega_p > \omega_0$ , and thus  $\zeta_0 < 0$ . This leads to the first important consequence for the stable primary comb formation -  $d_2 > 0$  or *anomalous* group velocity dispersion. This is a central and basic requirement for the initiation of the primary sidebands and, as a consequence, Kerr

frequency combs. Empirically it can be understood such that the nonlinear resonance shift induced by the pump through the XPM compensates the detuning of the sidebands induced by the dispersion. We should note, however, that the possibility of the primary comb formation as well as Kerr frequency combs in the normal dispersion regime has also been investigated and shown experimentally [48, 55, 56, 57].

We can further calculate and interpret the eigenvalues  $\lambda_{1,2}$  of  $\mathbf{M}$ :

$$\lambda_{1,2} = -1 \pm \sqrt{a_0^4 - (\zeta_\mu - 2|a_0|^2)^2} . \quad (1.44)$$

These eigenvalues mean that amplitude of the random field fluctuations, which appear in the corresponding sideband modes will develop as  $e^{(-1+\sqrt{a^4-(\zeta_\mu-2|a|^2)^2})t} = e^{g_\lambda t}$ , where we consider the "+" case as it can correspond to a growing amplitude, and in fact describes the gain of the FWM nonlinear process. We note that due to the normalization introduced for our linearized coupled modes (all angular frequency terms, such as total cavity loss rate  $\kappa$ , nonlinear Kerr shift per photon  $g$  or detuning  $\Delta$  were normalized using  $\kappa/2$ ), the losses are represented by "-1", and the sidebands will grow when they overcome losses in the microresonator:  $\text{Re}(g_\lambda) > 0$

Now, using the equation (1.44) we can derive the number of intracavity pump photons  $|a_{0,th}|^2 \kappa / 2g$  needed to initiate the generation of the primary sidebands:

$$-1 + \sqrt{(a_{0,th}^4 - (\zeta_\mu - 2|a_{0,th}|^2)^2)} = 0 , \quad (1.45)$$

where again considering anomalous GVD with moderate  $D_2$ , which can reduce the second term in the radicand to zero for certain  $\mu > 1$ , we can show that the threshold conditions for the intracavity pump photon number:  $|a_{th}|^2 = 1$ . Taking into account the earlier-introduced normalizations, we can write the intracavity threshold power:

$$P_{th}^{cav} = \frac{\kappa}{2g\tau_{rt}} \hbar\omega_p , \quad (1.46)$$

which can be further used to calculate the minimum normalized driving power  $|f|^2$  in the bus waveguide, required to reach the FWM threshold for the intracavity power and initiate the generation of the sidebands. For this we recall eq. (1.35), obtained from the normalized field evolution equation in the nonlinear resonator, and estimate the minimum  $|f|^2$  at which the threshold intracavity power can be achieved:  $\rho = |a_{th}|^2 = 1$ . One can show that the minimum  $|f|^2$  will appear when the normalized effective detuning (in our present consideration it includes only the Kerr nonlinear component from SPM and excludes thermal contribution) is 0:  $\zeta_0 - |a_{0,th}|^2 = 0$ , or in other words, when the Kerr frequency shift equals half the cavity linewidth  $\kappa$  [53, 58]. The resulting condition for the external driving is  $|f|^2 \geq 1$ , and thus writing the threshold value in the real,

non-normalized units:

$$P_{\text{th}}^{\text{in}} = \frac{\kappa^3 n_g^2 V_{\text{eff}}}{\kappa_{\text{ex}} \omega_p c n_2}. \quad (1.47)$$

**Position of the primary sidebands.** Finally, the position of primary sidebands  $\pm\mu_{sb}$ , with respect to the pump mode, indicating the number of FSRs between the pump frequency and the frequencies of the sidebands can also be estimated based on eq. (1.35) with  $\rho = |a_0(t)|^2$ . It can be shown [59], that the positions of the sidebands at the threshold (when the FWM is just initiated) depends on the driving power and normalized cavity dispersion  $d_2$ :

$$\mu_{\text{th}} = \sqrt{\frac{1}{d_2} \left( \sqrt{f^2 - 1} + 1 \right)}. \quad (1.48)$$

Thus the minimum position of the first sidebands at the threshold power can be written in non-normalized units as

$$\mu_{\text{min}} = \sqrt{\frac{\kappa}{D_2}}. \quad (1.49)$$

Besides showing the minimum position of the primary sidebands, this dimensionless parameter represents one of the key figure-of-merits for the Kerr frequency combs and appears in several roles characterizing their dynamics and some properties of dissipative Kerr solitons. In particular, later we will show that this parameter is also related to the soliton duration and can estimate the maximum number of solitons which can coexist in the cavity without annihilation.

### 1.3.2 Modulation instability

The development of the spectral sidebands from the initial CW field due to the third-order nonlinearity is common for optics, fluid dynamics and other fields. The process is also called *modulation instability* (MI), referring to the behavior of the system, where it does not inhibit random spectral fluctuations (modulations) at certain frequencies as it would be the case for a stable state, but enhances them, forming the strongly oscillating sidebands. In Kerr combs the term modulation instability is used for several operation regimes, when the pump is located on the blue-detuned side of the driven resonance, and the microresonator operates above the FWM threshold (1.47). Fig. 1.14 shows these regimes schematically (Fig. 1.14(b)) and in actual experiment with a 100-GHz Si<sub>3</sub>N<sub>4</sub> microresonator (Fig. 1.14(c)), when the pump frequency is tuned into the cavity resonance from the blue-detuned side. The first regime is the process of degenerate FWM described in the previous subsection, which leads to the generation of two primary sidebands located at  $\pm\mu_{sb}$ . Once the primary sidebands have been initiated however, their mixing with the pump immediately enables the non-degenerated FWM (e.g. for

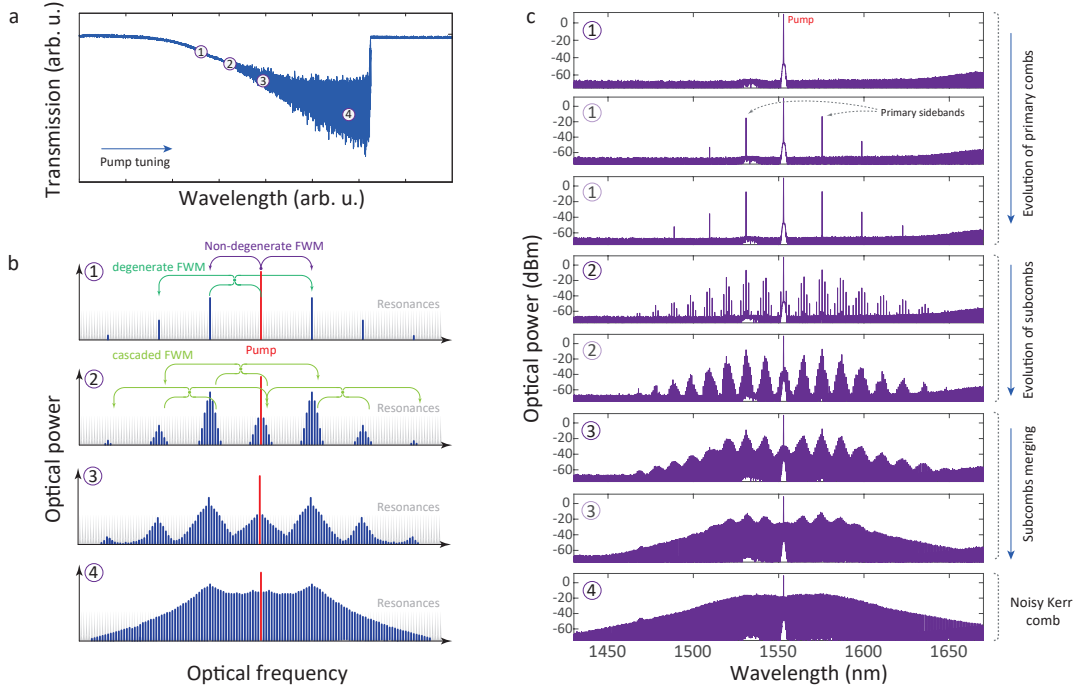


Figure 1.14 – Modulation instability (MI) in CW-driven nonlinear microresonator. (a) Schematic transmission trace of the pump frequency tuning in the cavity resonance. Numbered circles indicate different stages of the MI: 1- primary combs, 2 - subcomb formation, 3 - subcomb merging, 4 - fully filled noisy Kerr comb. (b) Schematic representation of the MI stages shown indicated in (a). Green and violet schemes show non-degenerate and degenerate FWM processes. (c) Experimental spectra of different MI stages of the 100-GHz  $\text{Si}_3\text{N}_4$  microresonator.

the modes with relative mode numbers  $-\mu_{sb}, 0 \rightarrow \mu_{sb}, -2\mu_{sb}$ , which in turn leads to more sidebands following the same spacing (if the primary sidebands are located close to the resonances with indexes  $\pm\mu_{sb}$ , the new sidebands will appear at the resonances  $\pm\mu_{sb} \cdot j$ ,  $j \in \mathbb{N}$ ). When the pump frequency is tuned further into resonance, which increases intracavity intensity of the pump mode, the sidebands will also obtain higher intensities leading to the broader spectrum of the generated lines. Thus the pump photons following complex cascaded nondegenerate FWM processes can mix to produce photons in spectral positions far from the pump line (see stage 1 in Fig. 1.14(b, c)). The resulting optical frequency comb spaced by  $\mu_{sb} \cdot \text{FSR}$  is called a *primary comb*, and is often observed in a variety of nonlinear microresonator platforms with anomalous GVD.

The width of the primary comb is linked to the cavity dispersion. While the parametric generation of optical lines strictly maintains initial line spacing established by the primary sidebands, the dispersion induces a larger walk-off of the cavity resonances from the position of the corresponding sidebands for large  $j$  thus reducing their intracavity build-up. It should also be noted that, by introducing high-order dispersion terms such walk off-can

be reduced, and even lead to the significant enhancement of the lines far away from the pump [60, 61, 26].

In the time domain, the formation of primary sidebands corresponds to the breaking of the continuous-wave intracavity solution, which is "flat" in the cavity (the intensity is spatially-uniform over the cavity circumference) into the integer number of pulses, whose number -  $\mu_{sb}$  - corresponds to the relative mode index of the resonances, where the primary sidebands appear. While just above the threshold, the intracavity waveform simply looks like a weakly modulated continuous wave field, the fully developed primary comb will have higher contrast between the field maxima and minima. Such intracavity formations are called "Turing rolls" (or also Turing patterns) [62], and represent a stable steady state solution of the system. Due to this reason, the first stage of modulation instability observed in the CW-driven microresonators is often referred to as *stable* MI (SMI).

The comb evolution process, however, does not end in the SMI regime. By further increasing intracavity power (tuning the pump frequency further into the resonance) the second stage of the comb formation can be initiated. It starts when primary sidebands become strong enough to initiate non-degenerate FWM around their positions, leading to the formation of *secondary* comb lines, whose spacing in the general case deviates from the spacing of the primary sidebands [59], but is constant over the comb bandwidth. Appearing around primary comb lines they form "subcombs", adding more oscillating lines inside the cavity and more potential channels for the FWM processes (see stage 2 in Fig. 1.14(b, c)). The subcombs can further merge with each other filling all cavity resonances with oscillating modes (stage 3 in Fig. 1.14(b, c)) and thus forming an optical comb with the characteristic shape shown in stage 4 of Fig. 1.14(b, c). The first observation of such an optical frequency comb was made by Del'Haye *al* [7] in a monolithic toroidal silica microresonator and can be considered as the first step in the development of microresonator-based Kerr frequency combs. Later, Kerr combs were also observed in multiple microresonator platforms, including crystalline microresonators [63], chip-integrated microrings [11, 10] and silica wedge resonators [64].

One of the main issues of these microresonator-based Kerr frequency combs, is their noise performance. Despite strict maintenance of the line spacing between generated comb lines, which follows from the energy conservation, the mismatch between the spacings of the primary and secondary sets of comb lines often leads to the situation when multiple lines oscillate in the same resonance. This leads to the mutual incoherence of the resulting comb lines oscillating at different resonances and their significant broadening in the frequency domain, which can be directly measured with low-bandwidth photodiodes [64, 59, 65]. Such fully or partially filled combs are often referred to as "noisy" Kerr combs, highlighting their noisy and incoherent nature.

In the time domain, the formation and merging of the subcombs leads to the breaking of

the stable Turing rolls in the spatially and temporally chaotic intracavity waveform. Due to the absence of coherence and chaotic dynamics, the system behavior in a noisy Kerr comb state is called *chaotic* modulation instability (CMI).

So far we assumed the case of moderately low anomalous dispersion, which enables the formation of the primary sidebands at  $|\mu_{sb}| > 1$ , which are called **multi-mode spaced combs (MMS)** (or alternatively - Type-II combs) [66, 59]. It was shown, however, that the cascaded FWM processes can also develop and form an optical comb, when the dispersion is strong enough to induce  $|\mu_{sb}| = 1$ . Resulting combs, called **natively mode-spaced combs (NMS)** (also Type-I combs) [66], usually have a rather small spectral bandwidth, because the dispersion induces a large walk-off of the resonances from the oscillating lines even at small  $\mu$ . The advantage of such combs is in their noiseless nature since no formation of secondary combs is being initiated, and the system essentially represents a primary comb having single-FSR spacing.

Despite providing access to ultra-high repetition rates, the development of the Kerr combs and their applications was largely hindered by their noise properties (MMS combs) or their bandwidth (NMS combs). Most of the applications were based on either the primary combs and NMS combs [67, 68] or accidentally generated low-noise states of the MMS combs in a certain sample [69, 70], which can appear as the result of integer matching between the spacings of primary and secondary comb lines (" $\delta - \Delta$  matching" [59]).

### 1.3.3 Coupled-mode equations for Kerr combs

The analytical description of Kerr frequency combs due to historical reasons was initially implemented in the frequency domain. Following the first experiments, where the parametric oscillations were observed [3], few generated comb lines could be easily described with coupled equations corresponding to the oscillating modes and coupled through the nonlinear FWM terms [53]. A similar frequency-domain description of the FWM processes was initially also adopted to describe fully developed Kerr combs, consisting of a multitude (reaching several hundreds) of coupled modes. The model can be derived from the nonlinear wave equation in the resonator medium together with the quantum Langevin equations [71]. In the slowly varying envelope approximation for the fields  $A_\mu$  in the resonator modes  $\omega_\mu$  one can obtain the following set of coupled mode equations (CME):

$$\begin{aligned} \frac{\partial A_\mu}{\partial t} = & -\frac{\kappa}{2}A_\mu + ig \sum_{\mu', \mu'', \mu'''} A_{\mu'} A_{\mu''} A_{\mu'''}^* e^{-i(\omega_{\mu'} + \omega_{\mu''} - \omega_{\mu'''} - \omega_\mu)t} \\ & + \delta_{\mu 0} \sqrt{\kappa_{\text{ex}}} s_{\text{in}} e^{-i(\omega_p - \omega_0)t}, \quad (1.50) \end{aligned}$$

where the summation is only implemented for the frequencies whose indexes  $\mu', \mu'', \mu'''$ :  $\omega_{\mu'} + \omega_{\mu''} = \omega_{\mu'''} + \omega_{\mu}$ . The fields  $A_{\mu}$  indicate time-varying complex field amplitude normalized such that  $|A_{\mu}|^2$  represents the number of photons in the corresponding mode with index  $\mu$ . The pumped mode, as before, is denoted with index 0, and  $\delta_{\mu 0}$  is the Kronecker delta, restricting the pumping term (last on r.h.s.) only to the pumped mode. The pump, as before, includes  $s_{\text{in}} = \sqrt{P_{\text{in}}/\hbar\omega_p}$ , and we also use the earlier-introduced total cavity decay rate:  $\kappa = \kappa_{\text{ex}} + \kappa_0$ , and  $g$  - Kerr shift per photon defined in eq. (1.33).

One can further remove the time-dependency of the nonlinear terms using the Taylor expansion for the cavity resonances around  $\omega_0$  (see eq. (1.21)) limited to the GVD term:  $\omega_{\mu} = \omega_0 + \mu D_1 + \frac{D_2}{2}\mu^2$  - and make a transition from terms oscillating at cavity resonances to the terms oscillating on the equidistant frequency grid  $a_{\mu}$ :  $a_{\mu}(t) = A_{\mu}(t) \cdot e^{-i(\omega_{\mu}-\omega_p-\mu D_1)t} = A_{\mu}(t) \cdot e^{-i(\omega_0-\omega_p+\mu^2 D_2/2)t}$ .

$$\frac{\partial a_{\mu}}{\partial t} = -i \left( \omega_0 - \omega_p + \frac{D_2}{2}\mu^2 \right) a_{\mu} - \frac{\kappa}{2} a_{\mu} + ig \sum_{\mu', \mu'', \mu'''} a_{\mu'} a_{\mu''} a_{\mu'''}^* + \delta_{\mu 0} \sqrt{\kappa_{\text{ex}}} s_{\text{in}} . \quad (1.51)$$

The choice of the equidistant grid as the basis for the model is defined by the strict equidistance of the generated comb lines, and is chosen such that  $D_1/2\pi$  matches the spacing of the adjacent (generated in adjacent resonances) comb lines.

The model can be further reduced to dimensionless form. If we use:  $a_{\mu} = a_{\mu} \sqrt{2g/\kappa}$ ,  $\zeta_{\mu} = 2(\omega_0 - \omega_p + \frac{D_2}{2}\mu^2)/\kappa$ ,  $\tau = \kappa t/2$ ,  $f = \sqrt{8g\kappa_{\text{ex}}/\kappa^3} s_{\text{in}}$ :

$$\frac{\partial a_{\mu}}{\partial t} = -(1 + i\zeta_{\mu}) a_{\mu} + i \sum_{\mu' \leq \mu''} (2 - \delta_{\mu', \mu''}) a_{\mu'} a_{\mu''} a_{\mu' + \mu'' - \mu}^* + \delta_{\mu 0} f . \quad (1.52)$$

It can be also seen that this infinite set of equations can be reduced to the earlier-introduced equation for single mode (eq. (1.32)) or three-mode model (eqs. (1.42) and (1.43)) used for the calculations of optical bistability (see eq. 1.2.4) and the parametric threshold (eq. 1.3.1).

#### 1.3.4 Lugiato-Lefever equation

While the coupled mode equations allow the description of Kerr comb dynamics and straightforward implementation in the simulations, the analytical description of the system is rather complicated in particular due to the complex summation of the nonlinear terms. Another issue with the frequency-domain description is the computational difficulty of the resulting set of nonlinear coupled equations.

An alternative approach to build the convenient analytical model for the Kerr combs lies in the temporal domain. Historically, the model was first derived for spatial dissipative

structures of light generated in a CW-driven, simple four-mirror cavity by L. Lugiato and R. Lefever [72]. In this work the spatially-localized dissipative structures were formed in the plane transverse to the light propagation direction as the result of the interaction between the focusing Kerr nonlinearity and diffraction of the radiation. Later, the model was also formulated in the temporal domain for the driven nonlinear dispersive cavity [73], where the dispersion has taken the place of the diffraction, and the possibility of the temporally-localized structures was shown.

The derivation of the model is based on the *Ikeda map* [74] - an approach which was introduced for the description of the instabilities of the light transmitted by the ring cavity. In this approach, the light field  $E = E(z, \tau)$  is described from roundtrip ( $n$ ) to roundtrip ( $n + 1$ ) using cavity boundary conditions, and assuming that during the roundtrip the field propagation is described by the nonlinear Schrödinger equation (NLSE) [40]:

$$\begin{aligned} E_{n+1}(0, \tau) &= tE_{\text{in}} + re^{-i\delta_0} E_n(L, \tau) , \\ \frac{\partial E_n(z, \tau)}{\partial z} &= - \left( \frac{\alpha_L}{2} - i \frac{\beta_2}{2} \frac{\partial^2}{\partial \tau^2} + i\gamma |E_n(z, \tau)|^2 \right) E_n(z, \tau) , \end{aligned} \quad (1.53)$$

where we used earlier introduced notations of field-transmission and reflection coefficients  $t, r$ , cavity length  $L$  nonlinearity coefficient  $\gamma$ , linear cavity losses  $\alpha$  and GVD dispersion  $\beta_2$ . The propagation spatial coordinate is denoted as  $z$  and time is denoted as  $\tau$ .  $\delta_0$  represents the phase cavity detuning for the center frequency of the  $E$  spectrum in the linear case (zero intensity inside the cavity). The field  $E$  is normalized to represent intracavity power  $[\sqrt{W}]$ , and similarly the input field  $E_{\text{in}}$  is normalized to represent power coupled to the cavity  $P_{\text{in}} = |E_{\text{in}}|^2$ .

The Ikeda map can be further reduced to a partial derivative equation, which allows for analytical study of the light evolution in the cavity. If we assume the limiting case of high-finesse cavities, where the temporal evolution of the intracavity field is much slower than the roundtrip time  $\tau_r$ , and if the dispersion and nonlinear length of the cavity are much longer than the cavity length, one can replace the nonlinear field propagation in (1.53) with simple integration. Furthermore, introducing the new independent variable - "slow" or "retarded" time:  $t = \tau - z/v_g$ , where  $v_g$  - is the group velocity of light, we can define  $E(t, \tau)$  as the cavity field envelope at  $z = 0$ :  $E(t = n\tau_r, \tau) = E_n(z = L, \tau), n = 0, 1, 2, \dots$  [73]. The slow time also allows us to introduce the slow time derivative, which is the change of the intracavity field envelope over one roundtrip:  $\partial E(t, \tau)/\partial t = (E_{n+1}(z = 0, \tau) - E_n(z = 0, \tau))/\tau_r$ :

$$\tau_r \frac{\partial E(t, \tau)}{\partial t} = \left[ -\alpha - i\delta_0 + i \frac{\beta_2}{2} \frac{\partial^2}{\partial \tau^2} + i\gamma L |E(t, \tau)|^2 \right] E(t, \tau) + rE_{\text{in}} . \quad (1.54)$$

This partial derivative equation is called *Lugiato-Lefever equation* (LLE). From the

mathematical point of view it represents an externally driven damped and detuned NLSE and successfully describes the dynamics of Kerr combs in various regimes. The LLE has two time variables -  $\tau$  - usual time, also called "fast" time in the frame of this equation, which describes the behavior of the intracavity field within one roundtrip, and  $t$  - slow time, described above. We stop a bit on the physical interpretation of slow and fast times. While fast time is just regular continuous time, the slow in the form it is introduced is discrete, and essentially just "counts" the roundtrips. Given that the evolution of the system over one roundtrip is almost negligible, we can treat this slow time as being continuous, but having meaning only when it is equal to the integer multiples of the roundtrip time. Since the intracavity field evolution, which we consider in the LLE evolves slowly, LLE is often referred to as time-domain mean-field theory of the Kerr comb evolution [75]. It should be noted that the dispersion in (1.54) is truncated to the second order, giving us the present temporal form of the LLE to be similar to the earlier introduced spatial form [72]. Nevertheless, higher-order dispersion terms can be also included in the model [76], enabling the description of broadband combs with complex dispersion profiles.

The form of the LLE shown here is based on the work of Haelterman *et al.* [73] and was originally used for the modulation instability and pattern formation in fiber cavities [41]. The idea to employ a mean-field equation for the description of Kerr combs appeared around the same time [77], but already after the CME approach has already been established [78]. It was also shown that the modal expansion approach used in the CME and Ikeda map are strongly connected, and both converge to the LLE in the mean-field approximation limit. While being used in the form shown in eq. (1.54) [76], many researchers including our group are using the LLE with the CME-like notations, where the slowly varying intracavity field  $A(\phi, t) = \sum_{\mu} e^{i\mu\phi - i(\omega_{\mu} - \omega_p - \mu D_1)t}$  is defined using the co-rotating frame:  $\phi = \varphi - D_1 t$ , where  $\varphi$  - regular polar angle inside the cavity.

$$\frac{\partial A(\phi, t)}{\partial t} = \left[ -\frac{\kappa}{2} - i\Delta + i\frac{D_2}{2} \frac{\partial^2}{\partial \phi^2} + ig|A(\phi, t)|^2 \right] A(\phi, t) + \sqrt{\frac{\kappa_{\text{ex}} P_{\text{in}}}{\hbar \omega_0}}. \quad (1.55)$$

This form of the LLE uses earlier introduced notation for the total cavity decay rate  $\kappa$ , angular frequency detuning  $\Delta = \omega_0 - \omega_p$ , second-order dispersion expansion term  $D_2$ , Kerr-shift per photon  $g$  and external driving power  $P_{\text{in}}$ . The intracavity solution is thus defined on the interval  $\phi \in [-\pi, \pi]$ , and should satisfy periodic boundary conditions imposed by the cavity:  $A(\phi + \pi, t) = A(\phi - \pi, t)$ . We should also note some counter-intuitive difference in the coordinate notation used in both versions of the LLE: (1.54), (1.55). In the first form,  $\tau$  is used for the regular (fast) time coordinate, while  $t$  is used for the slow time. In the second form, in contrast, the phase angle  $\phi$  in the co-rotating frame is used as the formal equivalent of the fast time, and  $t$  again represents the slow time.

For analytical derivation and for simulations, the LLE is often being reduced to its

dimensionless version [9]:

$$\frac{\partial \Psi(\theta, t)}{\partial \tau} = \left( -1 - i\zeta_0 + i\frac{\partial^2}{\partial \theta^2} + i|\Psi(\theta, t)|^2 \right) \Psi(\theta, t) + f, \quad (1.56)$$

From this dimensionless equation of the LLE, we can observe one important feature - LLE dynamics essentially depends only on the two parameters: dimensionless pump power  $f$ , and dimensionless detuning  $\zeta_0$ .

We finally note, that despite computational complexity, the Ikeda map introduced in (1.53) can also be directly used for the simulations of Kerr frequency combs and temporal structures appearing in the intracavity field, which was demonstrated in microresonators [79] and fiber cavities [80, 81]. In particular, it can be useful for the calculations beyond the LLE approximations, for example when calculating multi-stability behavior of the system, when nonlinearity-induced resonance shift can overcome the FSR.

### 1.4 Dissipative Kerr solitons

So far we discussed the formation of noisy Kerr combs, which appear when the pump is located on the blue-detuned side of the driven cavity resonance and the detuning is small enough to achieve intracavity powers above the FWM threshold. While being very interesting from the perspective of the microresonator size, and relatively small initiation power of nonlinear effects, the low coherence of the resulting optical combs and the chaotic intracavity waveform in these states significantly limit the number of applications where Kerr combs could be employed.

The idea of phase synchronization of the comb lines (also known as mode-locking), which could be achieved in microresonator Kerr combs, and associated with the formation of intracavity pulses was first introduced by Matsko *et al.* [77, 78] and later refined by Gorodetsky in an arXiv preprint of the work [9]. On the other hand, earlier theoretical works on the LLE, its spatial and temporal forms have also reported the possibilities of the formation of stable spatially localized structures - optical solitons. The term "soliton" is used here to refer to the spatially inhomogeneous waveform (usually - a pulse with a characteristic  $\text{sech}^2$  profile), which maintains its shape and energy during the propagation in a nonlinear medium with losses and dispersion or diffraction. Solitons were first introduced for integrable systems [82], and later in the beginning of 1990 they were also discovered for dissipative systems including optical ones, where they relied on the double-balance between nonlinearity and dispersion (temporal case) or diffraction (spatial case), and gain and losses of the system [83]. Optical solitons have attracted particular attention in the context of fiber optics, where they were suggested in order to increase the capacity of telecommunication links. While optical cavity solitons did not have such clear applications, they were also broadly studied from theoretical and

numerical points of view, which led to the early development of the LLE framework. Soliton formation was experimentally demonstrated first in the fiber cavities [41], where additional short seeding pulses were used for soliton initiation.

In microresonators the first indication of the low-noise Kerr comb states were reported in the  $\text{Si}_3\text{N}_4$  platform [59], however no underlying pulse formation was shown. Later, an unambiguous demonstration of soliton formation in  $\text{MgF}_2$  crystalline resonators and the associated low-noise state of the Kerr frequency comb was established by Herr *et al.* [9]. Similar to other dissipative solitons [83] the formation of stable solitons in microresonators is enabled by the double-balance between nonlinearity and dispersion, as well as between cavity losses and the gain from the parametric FWM processes. The first two effects maintain the pulse duration unchanged by compensating each other, and the second two processes maintain the pulse energy (see Fig. 1.15(a)). Since these solitons could only exist while the system is driven, and the governing nonlinearity is the Kerr nonlinearity, they were also named *Dissipative Kerr solitons* (DKS), which we will broadly use in the present work alongside with "DKS state". Alternatively, terms such as "dissipative cavity solitons", or "temporal solitons" as well as just "solitons" are also often used in the area of Kerr combs.

The formation of DKS states in microresonators have revolutionized the area of Kerr combs. They have enabled the generation of short optical pulses from monolithic CW-driven microresonators without the need for complex external means for the pulse formation, maintenance and synchronization of phases as in mode-locking lasers. Furthermore, with the demonstration of DKS states in chip-integrated platforms [84], they have gained access to the advances of on-chip photonics, including mass-producibility, chip-scale footprint as well as the possibility for heterogeneous integration with laser sources and locking or control electronics and electro-optics. On-chip platforms also allow for convenient dispersion engineering of the resonators, which have enabled the generation of broadband optical combs spanning a full octave and have shifted the operating window of soliton combs towards visible [85, 86, 87] or mid-IR wavelengths [88, 89].

In recent years, DKS states have been demonstrated in a number of microresonator platforms, including crystalline  $\text{MgF}_2$  resonators [9, 90],  $\text{SiO}_2$  wedge disks [91],  $\text{Si}_3\text{N}_4$  [84], Si [88], high-index doped  $\text{SiO}_2$  [92], AlN [93] and  $\text{LiNbO}_3$  integrated microrings [17, 94], and silica microspheres [2].

In the following subsections we focus on the theoretical description of solitons in optical microcavities, experimental ways to access these states as well as briefly cover their applications.

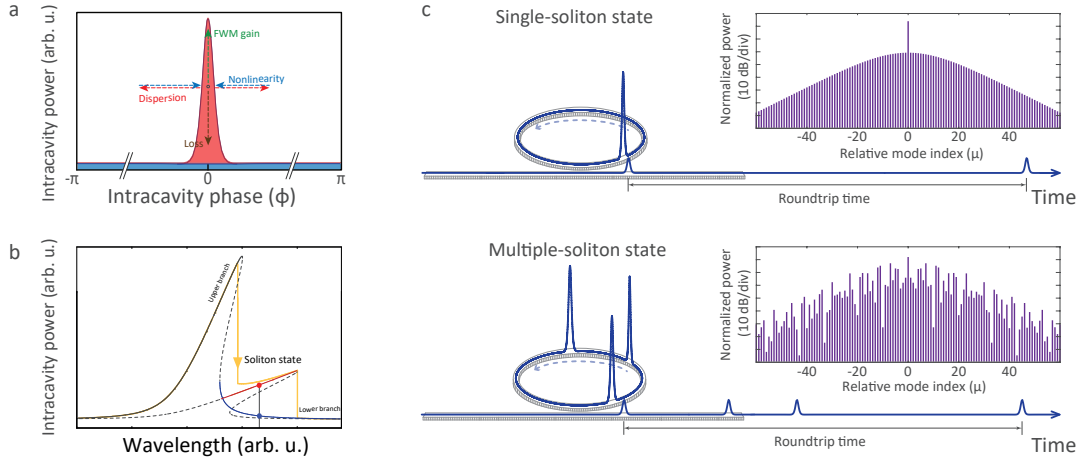


Figure 1.15 – (a) Soliton (red) and CW (blue) solutions defined inside the cavity on the interval  $\phi \in [-\pi, \pi]$ . Arrows schematically show various effects acting on the DKS and maintaining its stable pulse shape during the propagation. (b) Nonlinearity-induced bistability of the microresonator resonance. (c) Single soliton (top) and multiple-soliton (bottom) states in the cavity, when they are coupled out of the cavity and their spectra in the  $\mu$ -domain. Note that the strong CW contribution from the cavity-reflected pump was removed in the outcoupled light for illustrative purposes.

#### 1.4.1 Theoretical description of DKS

The first correct expression for the parameters of a dissipative Kerr soliton solution of the LLE was derived by Gorodetsky in the work [9]. The derivation relied on the dimensionless form of the LLE (1.56), and followed the derivations of solitons made by Wabnitz [95] in the limit of low losses ( $\zeta_0 \gg 1$ ), which in turn was also based on earlier work of Nozaki and Bekki [96]. The full soliton solution of the LLE can be represented as the sum of two parts - CW background ( $\Psi_c$ ) and the soliton itself ( $\Psi_s$ ):

$$\Psi(\theta, t) = \Psi_c(\theta, t) + \Psi_s(\theta, t) \simeq \Psi_c + \sqrt{2\zeta_0} e^{i\varphi_0} \text{sech}(\sqrt{2\zeta_0} \cdot \theta), \quad (1.57)$$

where the parameter  $\varphi_0$  is responsible for the phase detuning of the soliton with respect to the pump, and is shown to satisfy  $\cos \varphi_0 \simeq \sqrt{8\zeta_0/\pi f}$ . The CW solution part  $\Psi_c$  can be obtained from the stationary LLE ( $\partial\Psi(\theta, t)/\partial\tau = 0$ ) and approximately derived as [9]:

$$\Psi_c(\theta, t) \simeq \frac{f}{\zeta_0^2} - i \frac{f}{\zeta_0}. \quad (1.58)$$

The coexistence of two solutions of the LLE is a direct consequence of the optical bistability, which we derived earlier in section 1.2.4, and which can be similarly derived for the LLE (see Fig. 1.15(b)). Two solutions correspond to different branches of the intracavity field solutions, one of which exists on the upper branch of the strongly Kerr-shifted resonance associated with the propagation of the high-intensity stable intracavity

pattern, while another one exists on the lower branch of the weakly Kerr-shifted resonance associated with the propagation of the background.

In the following we focus on the solitonic part of the solution and establish several characteristic parameters of the DKS pulses. First, we express the soliton solution in the physical parameters for the energy-normalized intracavity field:

$$A_s(\phi, t) = \sqrt{\frac{2\Delta}{g}} \operatorname{sech}\left(\frac{\phi}{\phi_s}\right), \quad (1.59)$$

where  $\phi_s = \sqrt{D_2/2\Delta}$  indicates the soliton duration in the spatial angle domain. It should also be reminded that the soliton duration and FWHM of the soliton pulse are different by the factor of  $2\ln(\sqrt{2}+1) \approx 1.76$ :  $\phi_{\text{FWHM}} = 1.76\phi_s$ . The solution is defined in the spatial angle domain  $\phi$  on the interval  $[-\pi, \pi]$  and is shown in Fig. 1.15(a). Since it was defined on the reference frame rotating with angular velocity  $D_1$ , the soliton circulates inside the cavity with the same angular velocity in the laboratory frame (see Fig. 1.15(c)). Each time when the soliton passes the coupling region it is partially coupled out thus forming a pulse train with repetition rate of  $D_1/2\pi$ . The optical spectrum of the thus generated pulse train can be expressed in the  $\mu$ -domain (frequency domain with  $\omega = \omega_p + \mu D_1$ ) using Fourier transformation and the output cavity relation:

$$P(\mu) = \frac{\kappa_{\text{ex}} D_2 \hbar \omega_p}{4g} \operatorname{sech}^2\left(\frac{\pi\mu}{2} \sqrt{\frac{D_2}{2\Delta}}\right). \quad (1.60)$$

Comparing eq. (1.59) and eq. (1.60) we can note that the DKS peak power  $\sim |A_s(\phi, t)|^2$  grows linearly inside the cavity with detuning, however in the frequency domain the maximum power-per-comb-line is fixed. The maximum available detuning for the given pump power can be derived from the condition  $|\cos\phi_0| < 1$ , which gives a maximum available detuning for the soliton state as a function of the normalized pump amplitude:

$$\zeta_{\text{max}} = \frac{\pi^2 f^2}{8}. \quad (1.61)$$

Another limiting condition for the soliton state was shown for the stationary damped driven NLSE to which the LLE can be reduced [9, 97]. The existence of DKS states is tightly linked with the system's bistability, which appears at  $\zeta_0 > \sqrt{3}$  and similarly eq. (1.38) limited by two curves:

$$f_{\pm} = \frac{2\zeta_0 \mp \sqrt{\zeta_0^2 - 3}}{3} \left[ 1 + \left( \frac{\sqrt{\zeta_0^2 - 3} \pm \zeta_0}{3} \right)^2 \right], \quad (1.62)$$

which can be also recalculated into maximum and minimum detuning values  $\zeta_+$  and  $\zeta_-$  for a given power:  $f_+ = f_-$ . The bistability region guarantees the existence of upper

and lower solution branches, and the coexistence of the CW and solitonic parts in the LLE solution can be interpreted as evidence of the system bistable behavior. On the other hand, the region of stable solitons is smaller than the bistability range even in ideal system due to the presence of various chaotic regions, which will be further discussed in the Chapters 4 and 5.

The intracavity waveform in the DKS state does not necessary consist of just a single soliton pulse. It can contain multiple pulses comprising a *multiple-soliton state* shown in Fig. 1.15(c). An important consequence of the dissipative nature of DKS pulses is the uniqueness of the soliton parameters which can satisfy the double balance of the system with given parameters. This leads to the similarity of all soliton pulses forming the multiple-soliton state. The intracavity solution for the multiple soliton state can be described as a sum of independent soliton solutions located at different positions  $\phi_j \in [-\pi, \pi]$ ,  $j = 1, 2, 3, \dots$  within the cavity, which can be approximated as [9]:

$$A_{ms}(\phi, t) = \sqrt{\frac{2\Delta}{g}} e^{i\phi_0} \sum_j \text{sech}\left(\frac{\phi - \phi_j}{\phi_s}\right). \quad (1.63)$$

Due to the mutual coherence of the soliton pulses constructing the multiple-soliton state, the resulting spectrum can have a complex but regular structure arising from the interference of their frequency components (see Fig. 1.15(c)). Since adjacent solitons can interact with each other when their tails start to overlap, the maximum number of soliton pulses, which can stably coexist in the cavity, is limited by [9]:

$$N_{\max} \approx \sqrt{\frac{\kappa}{D_2}}. \quad (1.64)$$

### 1.4.2 Excitation of DKS

The derivations for the DKS presented above were implemented for the stationary case, when the solution is independent of slow time  $t$  in variables  $(\phi, t)$ . We implicitly assumed that the soliton pulse initially exists in the cavity, without specifying how it was seeded. Since the formation of the DKS is related to the subcritical bifurcation [48], the pulse in the soliton existence range (the range of detunings, where the formation of stable DKS is possible at a given pump power) can not develop from noise fluctuations. Instead, such fluctuations would quickly relax to the CW solution. The system requires a seed pulse with energy high enough to be able to self-stabilize into a soliton pulse. Thus, in order to access the soliton state using a CW pump one needs to develop a tuning procedure which would first enable the generation of intracavity pulses in order to further use them as seeds for the soliton formation. Such a tuning procedure was one of the key advances of the work [9], which particularly enabled consistent and reproducible excitation of DKS.

We recall that the system can spontaneously generate intracavity Turing rolls in the

regime of stable MI (SMI), which we discussed earlier in section 1.3.2. Turing rolls can further develop into a chaotic intracavity waveform (CMI) when approaching from the blue-detuned side to the cavity resonance due to the self-stabilization of the system when the pump is located on the blue-detuned resonance side. The dynamics of this behavior is shown in Fig. 1.16(a, b), where the simulations of intracavity waveform and total intracavity power are shown as a function of detuning. The intracavity waveform is simulated (thermal effects are not included) during the pump sweep from the blue-detuned position to the red-detuned one. Figure 1.16(c) shows instant intracavity waveforms at different stages of its evolution. First, the intracavity waveform is represented by a flat (CW) solution and grows steadily, as the pump approaches the resonance reducing the effective detuning and thus increasing the intracavity power due to the intensity build-up. Once the FWM gain overcomes the cavity losses, the CW solution breaks into MI, and produces primary sidebands forming the primary comb. In the time domain this regime corresponds to the formation of stable intracavity pulses - Turing rolls, which were mentioned earlier. Proceeding further, the system enters CMI, and the intracavity waveform becomes chaotic. As we can see from figure 1.16(b), the intracavity waveform in this state represents a set of transient pulses, which actively move inside the cavity and interact with each other leading to the random collisions and stochastic continuous generation (and decay) of other unstable intracavity pulses of different amplitude and duration. This process is associated with strong intensity noise inside the cavity, which can also be detected in the outcoupled light. When the pump overcomes the resonance, the system enters the bistability regime, where the solitons can be stabilized. Their formation is associated with a characteristic "step" (or steps) in the total intracavity power (see Fig. 1.16(a)). At the time instant when the pump crosses the effective zero-detuning region, the cavity contains a stochastically obtained set of intracavity pulses, which depending on their power and mutual positions (whether they are too close to interact or not) can become soliton seeds. The system, however, does not land in the regime of stationary solitons immediately, it first passes through instability regions - chaotic ones followed by the region of soliton breathing (will be further reviewed in Chapters 4 and 5). Those transient pulses that survive all instabilities form stationary DKS pulses (in the rotating frame) of a resulting multiple-soliton state. The soliton formation is often associated with a significant drop in the intracavity power, which is caused by two main reasons. First, among multiple transient cavity pulses only a few of them are able to form a DKS - the majority of the others do not have enough energy to become a seed and simply decays. Second, and more important, due to the presence of chaotic regions, whose impact can be simplified to a stochastic reduction of the intracavity number of pulses, the number of soliton seeds is additionally reduced. We note that the number of pulses generated in the cavity depends on multiple parameters, and is often even different for exactly the same parameters due to the chaotic nature of the process, which generates soliton seeds, and removes them in the chaotic regions. Furthermore, depending on system parameters (e.g. such as the dispersion profile), it can spontaneously switch between soliton states (to the lower number of solitons), or rest in the stabilized soliton

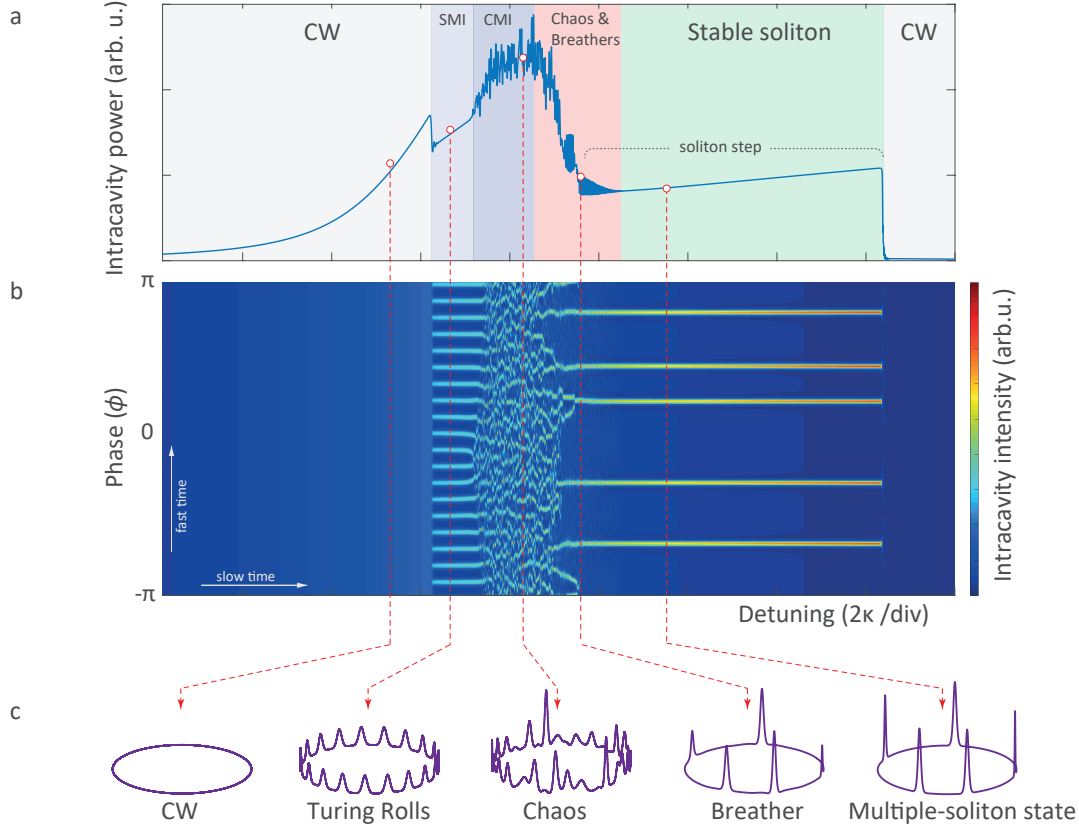


Figure 1.16 – Simulations of the DKS excitation process using a CW pump linearly scanned over the cavity resonance from the blue-detuned side to the red-detuned. (a) Evolution of the total intracavity power. Different regimes of intracavity waveform dynamics are color-coded. (b) Intracavity waveform evolution. (c) Intracavity waveform snapshots at various stages of the DKS excitation process.

state while detuning is below the  $\zeta_{\max}$  [98]. Once the system leaves the bistability region - the intracavity waveform decays back to the CW solution.

**Stability chart.** As was noted earlier in subsection 1.3.4, the simplest form of the LLE, where the dispersion is limited to the second order, can be reduced to the partial derivative equation of only two dimensionless parameters - normalized detuning  $\zeta_0$  and normalized pump amplitude  $f$  [42, 9]. It is thus possible to map different stable solutions, which the system can converge to, as a function of these two parameters [42, 48]. Figure 1.17 shows such a stability chart (attractor chart) adapted from [48]. Depending on the form of the stable solution, which can be obtained at different values of  $f$  and  $\zeta_0$ , the stability chart can be subdivided into several regions. The first is the region of CW (homogeneous) intracavity solutions, where the cavity contains only photons of the pump frequency. It is limited by the parabolic boundary, which can be derived from eq. (1.35) for the boundary condition  $\rho = |\Psi(\phi, t)|^2 = 1$ . The region is colored white in Fig. 1.17 and exists at large detunings from the cavity, or at small input powers, where the total

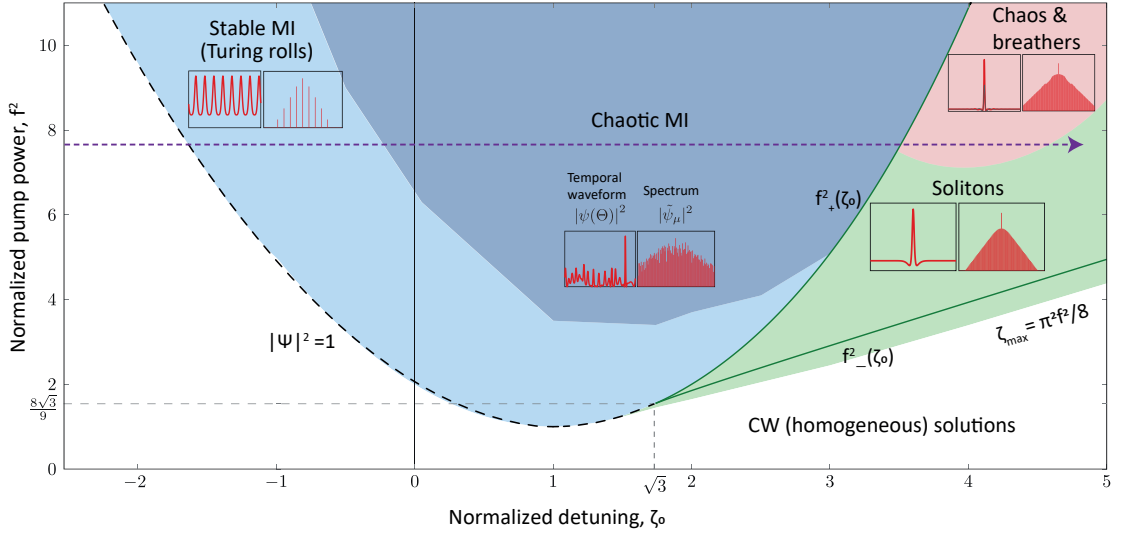


Figure 1.17 – Stability chart of the dimensionless LLE with dispersion limited to the second order. Different stability regimes are color-coded: SMI (light blue), CMI (dark blue), bistability (red - chaotic regimes and breathers, green - stationary soliton states). Violet dashed line schematically indicates the conventional procedure of tuning in the DKS state. The stability chart was adapted from [99, 48]

intracavity power does not reach the threshold enabling FWM processes. Above this curve the system reveals regions of stable (light blue) and chaotic (dark blue) MI, which are schematically distinguished on our figure from each other. SMI exist with larger detunings and smaller pump powers, in comparison to the CMI, which corresponds to larger values of the intracavity power. Next, and one of the most interesting regions here - is the bistability region, limited with  $f_+$  and  $f_-$  curves (see (1.38)), where solitons can be generated. The bistability region, as expected, overlays with the region of CW solutions, meaning that with a proper excitation pathway, the system can have a stable CW solution within these boundaries. It should be also noted that with using the conventional term "bistability", we should be aware that the ability to generate several solitons in the cavity means that the bistability region is in fact *multifold*. It covers a large set of intracavity solutions with a different number of solitons (and thus intracavity powers) and their mutual separations. Since here we consider a simple system without thermal effects, all of these solutions are degenerate in terms of the area they cover in the given map. However, as will be shown in detail in Chapter 3, this condition is only held in real systems that are close to ideal, and for the stability chart plotted in terms of the effective detuning. The internal structure of the bistability region is complex. It includes different chaotic regimes, soliton breathers with various breathing periods and stationary solitons. We review these regions in more detail in the following Chapters.

After describing the stability chart, we can now link it to the soliton excitation process, described earlier in this section and shown in Fig. 1.16. Since the soliton excitation is



piezoelectric-based wide tuning range ( $> 5$  GHz) and low linewidth  $< 100$  KHz<sup>2</sup>. The laser is tuned with an arbitrary function generator (AFG), which is connected to the laser piezo controller and enables relatively fast scanning of the laser frequency over the cavity resonance. The laser light is amplified using an Erbium-doped fiber amplifier (EDFA) to bring it to the power levels able to overcome the FWM threshold in the cavity and cover the in-coupling losses in the on-chip bus waveguide. Due to the recent advances in the  $Q$ -factors and chip input-output coupling techniques, the EDFA now can be eliminated even for the integrated devices [102, 103]. After polarization adjustment using a fiber polarization controller (FPC) to match one of the microresonator transverse mode families, amplified laser light is coupled to the chip. For the chip coupling we usually used ferrule-embodied conical shaped lensed fiber (working distance 12 - 20  $\mu\text{m}$ , spot diameter 2.5 - 5  $\mu\text{m}$ ). Ferrules help to rigidly fix the fibers on the mounts and prevent their mechanical movements, which are detrimental for a DKS generation at higher powers. The output light from the chip is collected using a similar lensed fiber. Two powermeters (PM) with 99-1 fiber splitters are used to control the chip transmission during the operation of the setup. Due to a high optical power  $\sim 1\text{W}$ , which is partially dissipated in the chip and induces its heating, the thermal expansion of the chip material (and even the material of the chip holder) can shift the optimal positions of the lensed fibers towards higher ones. Constantly monitoring power transmission can help to adjust the lensed fiber position to adapt them to the new thermal states of the setup at high pump powers. The light after the chip is split between several measurement instruments, including an optical spectrum analyzer (OSA) and oscilloscope (OSC) to monitor the transmitted light and generated light (which is obtained by suppressing the strong CW component using a fiber Bragg grating (FBG)), and the optical spectrum of the DKS state.

To generate the soliton state, we use a V-shape ramp programmed on the AFG (shown in red in Fig. 1.18(c)), which allows one to implement the required tuning from the blue-detuned resonance side to the red-detuned one. It is usually more convenient to use generated light of the system for the detection of the soliton steps and soliton excitation. The initial position of the pump, which is located on the red-detuned side, is chosen to appear on the soliton step when the tuning is stopped, as shown in Fig. 1.18(c). If the tuning speed and final position of the scan are properly adjusted, a DKS state can be obtained. Example spectra of single-soliton states generated in devices with different FSR ( $\sim 20 - 200$  GHz) are shown in Fig. 1.18(b). While seeming to be quite straightforward, in general, the generation of the soliton states is a very non-trivial process. This in particular can be noted from the almost 5-year gap between the discovery of the Kerr combs [7] and the first generation of soliton states [9]. The excitation of DKS states often relies on the observation of soliton steps and the attempt to stabilize the pump frequency

<sup>2</sup>The seed laser performance, however, is not required to be even on the order of what we use. Recently the DKS formation has been shown with frequency-fixed lasers [100], or even broad, multimode Fabry-Perot laser diodes [101], which can still successfully generate soliton states.

on them. The appearance of the soliton steps, however, largely depends on the tuning speed and parameters of the system including  $Q$ -factors, dispersion profile, thermal effects and others. We especially note a role of thermal effects in the DKS generation process. After landing in the soliton regime, due to their delayed nature (since the thermal time scales are the largest among the cavity decay rate and roundtrip times) the thermal effects are able to induce additional shift on the cavity resonance and change the effective soliton detuning moving the system out of the soliton existence range. This can be noted directly from the experimental trace of the generated light (blue) shown in Fig. 1.18(c). When the pump tuning is stopped (dashed vertical grey line) the system thermal state is not at equilibrium yet and the system keeps relaxing to it over several hundreds of milliseconds (in the figure the system is heating up). One of the main breakthroughs of the work by Herr *et al.* [9], was to suggest high-speed tuning procedures (shown in the figure and further referred to as "forward tuning"), which allowed access to a soliton state such that the thermal state of the cavity achieved during the tuning procedure would appropriately match the thermal state of the cavity with several solitons inside. In such a case the cavity would not suffer from the large temperature variations after the pump tuning is stopped in the soliton existence range maintaining the DKS state. Another issue, which is often observed in  $\text{Si}_3\text{N}_4$  microresonators is that large thermal effects cause significant resonance tilting before the pump reaches the bistability region. Such resonance tilting hides the soliton steps with lower intracavity power and prohibits access to those DKS states. This can also happen for the high-number and low-number soliton states such that only the soliton step with the highest soliton number is accessible and the rest are hidden (more details are shown in Chapter 3). We note that such behavior is not unique for silicon nitride, and can be also observed in other platforms.

In every case additional techniques are required to consistently generate DKS states. Over the past years several approaches have been suggested for the soliton formation, which can overcome the limitations of the standard forward tuning process, which uses the laser piezo controller to sweep the wavelength and is limited by its speed (usually  $\sim 100$  Hz and range of  $\sim 60$  GHz for current laser systems). We first note that all of the new procedures still include the tuning over the cavity resonance from the blue-detuned to the red-detuned sides. This is associated with the system stability, and the requirement to seed the soliton pulses in the cavity. Ideal candidates for such seeding are SMI and CMI, which appear at the blue-detuned side of the resonance. Different tuning techniques are mostly focused on overcoming the thermal effects associated with the change in the intracavity power resulting from the transition between different regimes of Kerr combs, as well as provide robust and repeatable access to the soliton states with the required number of solitons and, in particular, a single soliton state. They typically involve high-speed tuning of the pump frequency or combine tuning of the pump power and pump frequency. These approaches are used to bring the system enriched with soliton seeds to the operating region, where DKS can be maintained, while guaranteeing that the thermal relaxation of the cavity (happens at longer timescale) after establishing

of the stable optical intracavity waveform (happens on the shorter timescale) would have minimal impact on the DKS state.

The first alternative to the standard forward tuning was developed by Victor Brasch [104, 84], and included a complex tuning profile of the pump power, together with a linear change in the pump frequency using a "fast" electro-optical modulator (EOM) and a "slow" acousto-optic modulator (AOM). Due to the strong pump power boost initiated closer to the end of the tuning profile it is called "power-kick" method. It was developed to reliably tune into soliton states in  $\text{Si}_3\text{N}_4$  microresonators, when the soliton steps are extremely short and can hardly be landed directly due to the system fluctuations. An exact scheme and procedure are carefully presented in [104]. Despite being highly efficient, this approach requires the adjustment of several parameters of the tuning profile, which may be necessary for each new device. Nevertheless it was adopted and used for other systems, including  $\text{SiO}_2$  microdisks [91].

Another significant improvement in the approach to tune into the soliton states was usage of the single-sideband modulator (SSB) [105, 106]. It allowed the tuning speed of the laser to be decoupled from its internal piezoelectric transducer, and instead uses the voltage-controlled oscillator (VCO) for this purpose. We also establish the SSB technique in our group. It relies on the dual Mach-Zehnder interferometer (MZI) system with an additional bias control of both arms. Both internal MZIs are driven with an RF signal produced by the VCO shifted by  $90^\circ$ , and can adjust the power of the pump and generated modulation sidebands. The biases can be adjusted in a way to suppress all the lines besides a single sideband. The tuning can be implemented by changing the VCO frequency, and can reach 5000 THz/s. Such high-speed tuning essentially ignores the thermal effects, because the thermal effects do not have enough time to develop during the tuning process. Thus the soliton excitation essentially becomes athermal and provides access to multiple soliton steps.

One of the recently developed interesting approaches for the initiation of the DKS state is the replacing of the CW pump with a pulsed source - *pulsed pumping*. The original work has relied on an electro-optical (EO) comb consisting of phase and intensity modulators to form optical pulses, and standard single-mode fiber (SMF) to compress them. One of the largest benefits of such an approach is a significantly reduced threshold for soliton generation, because the power inside the cavity is not distributed uniformly, but instead provides a spatially-localized intracavity seed pulse directly supplying the soliton with energy. While being very reliable, the procedure however requires careful adjustment of the driving EO comb repetition rate to match the repetition rate of the soliton comb to be created. Also, it is limited by the performance and bandwidth of the EO modulators and RF amplifiers used to create optical pulses from the initial CW light.

Finally, we note other works, where tuning into the soliton state was also implemented using thermal tuning of the cavity [107, 100]. This approach allows the usage of lasers

with much better stability, whose tuning is often limited. However, it can also suffer from a reduced tuning speed as it relies on thermal effects.

### 1.5 DKS applications

The generation of the DKS states in optical microresonators has paved the way for the employment of Kerr combs in a large variety of applications including spectroscopy, optical ranging, optical clocks, telecommunications and others. Apart from chip-scale footprint and the possibility of mass fabrication on silicon wafers, soliton microcomb sources offer a series of advantages such as broad spectral coverage, low linewidth and mutual coherence of the generated comb lines, as well as straightforward access to large comb spacings from GHz to THz levels. In the time domain the DKS states act as sources of ultrashort optical pulses with femtosecond duration and high repetition rates corresponding to the comb line spacing or microresonator FSRs at the wavelength of interest. Furthermore, DKS states can serve as a convenient testbench to study the general aspects of temporal soliton dynamics and nonlinear systems in general. Figure 1.19 combines a majority of the applications demonstrated with DKS-based combs, which are described below in more detail.

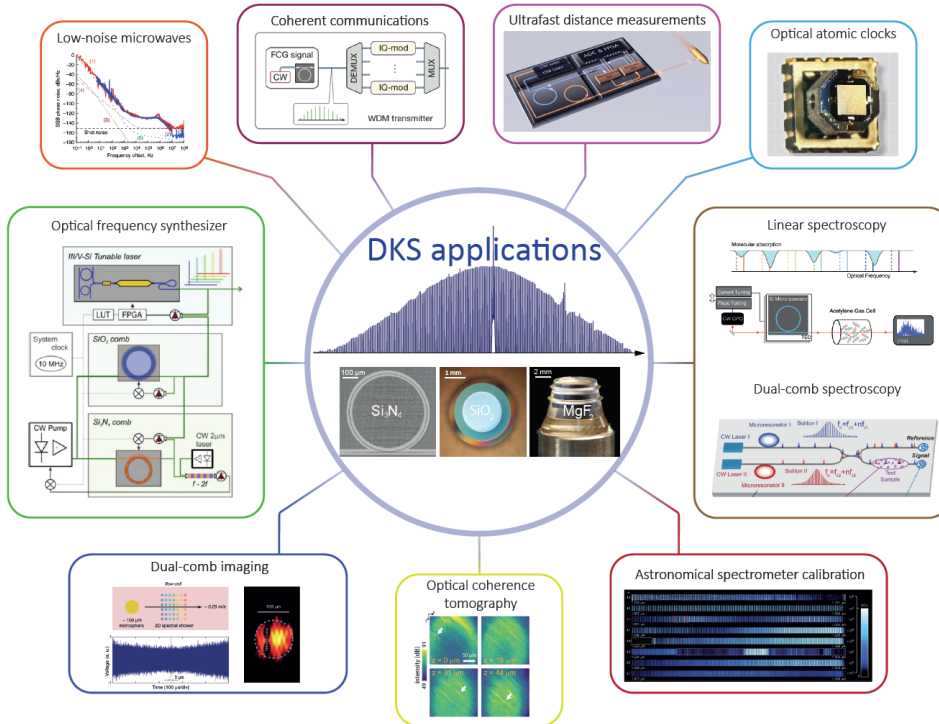


Figure 1.19 – Application areas of microresonator-based DKS combs. The scheme was initially prepared by the author for [108], and adapted for the present work using images from [109, 110, 90, 111, 112].

### Telecom applications

Optical communications is one of the key application areas of Kerr combs, which have drawn a lot of attention even before DKS formation was discovered [113, 68]. Due to the strict spacing of comb lines matching the standard frequency grids of coarse (20 nm, CWDM) and dense wavelength division multiplexing (25/50/100 GHz, DWDM), chip integration, high OSNR and the ability to operate in low-noise states with additional locking, Kerr combs have become an attractive solution for WDM optical coherent communications [113]. Once stable access to the DKS states has been established, it has enabled an on-demand generation of broadband combs with hundreds of optical channels covering several communication bands [9, 84, 114] for massively parallel optical coherent communication [115]. Furthermore, due to the large existence range of the DKS states and noise-free coherence transfer between the pump and comb lines, they can serve as unique sources of multiple low-linewidth optical communication channels able to work with high-order data modulation formats utilizing a single low-noise CW laser and having no need for additional locking. Present work will review one of the first experiments with DKS combs in integrated  $\text{Si}_3\text{N}_4$  microresonators that demonstrated the record-high data rates (see Chapter 7). Other telecom applications of the DKS states include wavelength multicasting [116], using DKS for optical communications with high-modulation formats reaching 256-QAM and superchannel engineering [117, 118, 119, 120].

### Spectroscopy applications

As a broadband optical source, optical combs can be used to detect molecular absorption features of materials. The spectroscopic information is encoded in the variation of the comb spectrum during the propagation through the studied material and can be measured using an optical spectrum analyzer or spectrometer. DKS states are able to provide very high frequency resolution of the measured spectra due to the low linewidth of the soliton comb lines, but the spectral sampling is rather sparse due to large repetition rates defined by the microresonator sizes. This issue is usually addressed with soliton spectral tuning using temperature [111, 121, 122]. Two important advantages of DKS-based combs for spectroscopy applications are the possibility to employ dual-comb techniques for the fast data acquisition without the need for spectrometers (see below under separate point), and the possibility to engineer the spectral coverage of the combs from visible to Mid-IR [85, 86, 87, 88]. We also note that so far all demonstrations of DKS-based spectroscopy applications were limited to linear absorption spectroscopy, which is result of small soliton pulse energies [123].

### Microwave-to-optical link

Similarly to conventional optical frequency combs based on mode-locked lasers, soliton Kerr combs are able to establish a phase-coherent link between optical and RF frequencies. Due to their chip-scale footprints, monolithic nature and reduced power consumption,

they can provide a compact and power-efficient solution for numerous applications, for which such a phase-coherent link is critical, including optical clocks [124, 125], optical frequency synthesis [126] and the generation of low-noise microwave signals [103, 127, 90]. Soliton Kerr combs have been already employed for establishing such a microwave-to-optical link (counting of the light cycles), using an externally broadened soliton comb [128, 129] or  $2f - 3f$  [130] of  $f - 2f$  [129] self-referenced microcomb sources.

### **Microwave (RF) photonics**

Microwave photonics applications relies on the producing or processing of microwave signals ( $<100$  GHz) using Kerr frequency combs. Besides their size, power advantages and silicon-chip integration, Kerr combs also provide direct access to microwave frequencies through their repetition rates [131]. One of the most interesting microwave applications enabled by soliton combs is the generation of ultra-low-noise RF signals. Due to optical phase noise division for the RF beatnotes of the comb sources, microresonator-based systems working in the soliton regime are able to efficiently transfer the optical stability of the ultralow-noise lasers to the microwave domain, or directly synthesize RF oscillations with a high spectral purity. [127, 90, 103]. Other applications of DKS combs for microwave photonics also include true time delay lines for the RF signals [132], photonic-based RF filters [133, 134], and RF differentiators [135].

### **Optical coherence tomography**

DKS states generated in microresonators can serve as sources for spectral-domain optical coherence tomography (OCT) replacing conventional sources such as superluminescence diodes [110, 136].

### **Astronomical applications**

DKS-based combs can be used for the calibration of astronomical spectrometers in order to facilitate the detection of tiny Doppler shifts caused by the wobbling of distant stars caused by the orbiting of their planets. The measurements of such fine spectral changes has a broad application in searching for exoplanets [137, 109].

### **Dual-comb applications: spectroscopy, optical ranging, imaging**

A large number of frequency comb applications rely not only on a single comb, but on the operation of two combs with slightly different repetition rates – *dual comb*. In this case the spectroscopic, distance or other information encoded on the lines of one comb can be coherently resolved using the second comb by beating them with each other. Due to the repetition rate difference, the information encoded on optical carriers is transferred to the individual RF tones in the baseband and can be directly detected with a single photodiode enabling fast data acquisition. The dual-comb schemes for spectroscopy, distance ranging and other applications were actively developed and tested with fiber

frequency combs [138, 139, 140], but their acquisition speed was limited by small free spectral ranges  $< 1$  GHz. Besides advantages in size, power and wafer-scale manufacturing, which DKS states in microresonators can offer, access to the large comb spacings they provide can significantly boost the data acquisition speed in dual-comb based applications. The performance of the DKS states has been demonstrated for dual-comb spectroscopy [141, 100, 142, 143, 144], dual-comb distance measurements (LiDAR - Light detection and ranging) using time-of-flight and massively-parallel synthetic wavelength interferometry [145, 146], dual-comb imaging [112].



## 2 Raman induced soliton self-frequency shift of dissipative Kerr solitons

This chapter reports on the experimental observation and theoretical description of the Raman-induced self-frequency shift, observed in dissipative Kerr solitons generated in  $\text{Si}_3\text{N}_4$  microresonators. The results are adapted from M. Karpov *et al.*, "Raman self-frequency shift of dissipative Kerr solitons in an optical microresonator", *Physical review letters*, 116(10), p.103902, (2016).

### 2.1 Introduction

Stimulated Raman scattering (SRS) is a nonlinear optical process, which can be observed in nonlinear media. It is responsible for the energy transfer between the pump wavelength and lower (Stokes) or higher (anti-Stokes) frequencies via the photon interaction with the optical phonons (quanta of lattice vibrations).

The effect of SRS on the optical pulses was broadly investigated in optical fibers, where it is responsible for various energy transfer processes, leading to the SRS-mediated interaction of the pulses centered at the same or different wavelengths [147, 148, 149, 150]. In addition, for sufficiently short pulses (with the duration  $< 1$  ps), whose spectral width becomes comparable with the Raman gain profile, the energy transfer can occur within the same pulse. These energy transfer processes were particularly well-studied for optical solitons in silica fibers, where they can stably propagate over long distances and lead to a number of experimentally observed and theoretically described phenomena such as generation of Raman pulses and Raman solitons [151], Raman-induced pulse compression in dispersive media [152] as well as soliton self-frequency shift [153, 154, 155, 156, 157]. The last phenomenon - soliton self-frequency shift - is a particularly interesting one, it appears as a continuous shift of the pulse spectrum towards longer wavelengths upon propagation, and originates from the effect of intrapulse Raman scattering (IRS).

In microresonators, the formation of the DKS state also corresponds to the continuous propagation of the soliton pulses, which in contrast to optical fibers are continuously

## Chapter 2. Raman induced soliton self-frequency shift of dissipative Kerr solitons

---

circulating inside the cavity. These pulses are able to carry intense peak power and have ultrashort duration below 100 fs, which together with the high material nonlinearity and waveguide-induced mode confinement is expected to lead to an even stronger impact of nonlinear effects for pulse propagation than for silica fibers. However, early experiments with DKS in crystalline materials did not show any evidence of the Raman-induced spectrum changes and presence of IRS [9, 45].

Several simulations studied the impact of Raman effects on DKS states for amorphous silica- and  $\text{Si}_3\text{N}_4$ -based microresonators [158, 159, 160]. It was found that in the presence of Raman effects the system is also able to support stable DKS states, however its optical spectrum acquires significant spectral shift towards longer wavelengths.

The first experimental observations of intrapulse Raman scattering and its impact on the dynamics of the DKS states were made in silica-cladded amorphous-material  $\text{Si}_3\text{N}_4$  microresonators and are summarized in the following sections of the present Chapter. In contrast to crystalline materials, where the Raman gain consists of a set of narrow well-defined peaks, corresponding to different vibrational modes of optical photons, the Raman gain in amorphous materials is usually broadband. We show how such broadband Raman gain provided by amorphous materials of the core [161] and the cladding [162] of the microresonator waveguides changes the optical spectrum of the DKS state and interplays with high-order dispersion effects.

### 2.2 Experimental observation of the soliton self-frequency shift

As already mentioned in the previous section, we study the impact of stimulated Raman scattering on the DKS states in photonic-chip integrated  $\text{Si}_3\text{N}_4$  microring resonators. The devices were fabricated with the Photonic Damascene process [28] and had a nominal  $\text{Si}_3\text{N}_4$  core height of 0.9  $\mu\text{m}$  and width 1.65  $\mu\text{m}$  in order to guarantee anomalous group velocity dispersion at 1550 nm for the fundamental modes. The DKS states were excited in the  $\text{TE}_{00}$  fundamental microresonator mode, whose FSR was about 100 GHz, and resonance linewidth  $\kappa/2\pi$  ( $\sim 200$  MHz) that corresponds to a loaded  $Q$ -factor of  $\sim 10^6$ . The measured dispersion at the pump wavelength has GVD term  $D_2/2\pi = 1 - 2$  MHz and negligible third-order dispersion term  $D_3/2\pi = \mathcal{O}(1)$  kHz, which has resulted in the absence of dispersive wave formation and overall symmetric envelopes of the generated DKS states.

In experiments we employ a standard setup for DKS generation in the chip-scale microresonators (see Fig. 2.1(a)), where the microresonator is pumped by a tunable external cavity diode laser (operating at 1550 nm in our experiment) followed by an erbium-doped fiber amplifier (EDFA). The wavelength of the seed laser can be tuned by an embedded piezoelectric transducer, driven by an arbitrary function generator (AFG). Single mode

## 2.2. Experimental observation of the soliton self-frequency shift

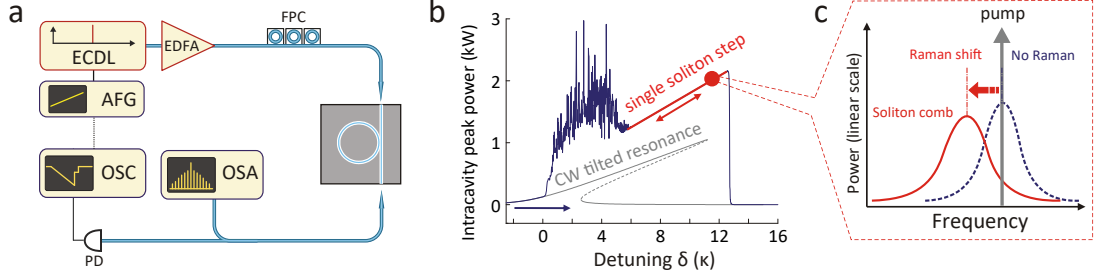


Figure 2.1 – (a) Scheme of the experimental setup: AFG, arbitrary function generator; ECDL, external cavity diode laser; EDFA, erbium doped fiber amplifier; FPC, fiber polarization controller; OSA, optical spectrum analyzer; OSC, oscilloscope; PD, photodiode; (b) Illustration of the pump laser tuning in the DKS excitation process (forward tuning, where approaches the cavity resonance from the blue-detuned side [9]). The gray line shows the Kerr-nonlinearity-tilted cavity resonance profile with bistability referring to the CW, the blue line shows the trace of intracavity peak power with an increase of the cavity resonance–pump detuning  $\delta$  ( $\delta = (\omega_0 - \omega_p)/2\pi$ , where  $\omega_0$  and  $\omega_p$  are the resonance and pump angular frequencies), the red line shows the single soliton existence range. (c) Illustration of the Raman-induced spectral red-shift of the soliton comb envelope (solid red line) compared to the one without Raman contribution (blue dashed line).

lensed fibers are used both at the input and output coupling, which provide an overall coupling efficiency of  $\sim 30\%$ . The input light polarization is adjusted by a fiber polarization controller (FPC) so we can choose to pump either the fundamental  $\text{TM}_{00}$  mode or the  $\text{TE}_{00}$  mode of the resonator waveguide. The output light is connected both to an optical spectrum analyzer (OSA) for spectrum measurement and a photodetector (PD) to monitor the power transmission.

We generated single-soliton DKS states using forward tuning technique [9] with additional switching procedure implemented via the *backward tuning*, which will be in details reviewed in the following Chapter 3. The experiment was carried out at several pump powers from 1 to 3 W, at which the stable access to DKS states was achieved. In contrast to early experiments in crystalline microresonators we observed that the typical  $\text{sech}^2$ -shaped envelopes of the obtained DKS states acquire significant *spectral shift towards longer wavelengths* with respect to the pump frequency. The observation is schematically sketched in Fig. 2.1(c), where the two cases of the DKS state are shown: DKS state without spectral shift as was observed in crystalline  $\text{MgF}_2$  devices (blue), and with spectral shift as in  $\text{Si}_3\text{N}_4$ . We also note, that no evidence of the Raman-mediated pump conversion was observed.

Once the single soliton state is stabilized, we can explore its laser detuning dependence by tuning the pump either to longer or shorter wavelengths. The DKS state persists during such variations within a limited range of the pump-cavity detunings – soliton existence range, which here corresponds to  $\sim 2$  GHz ( $10 \times \kappa/2\pi$ ). By choosing the blue end (low

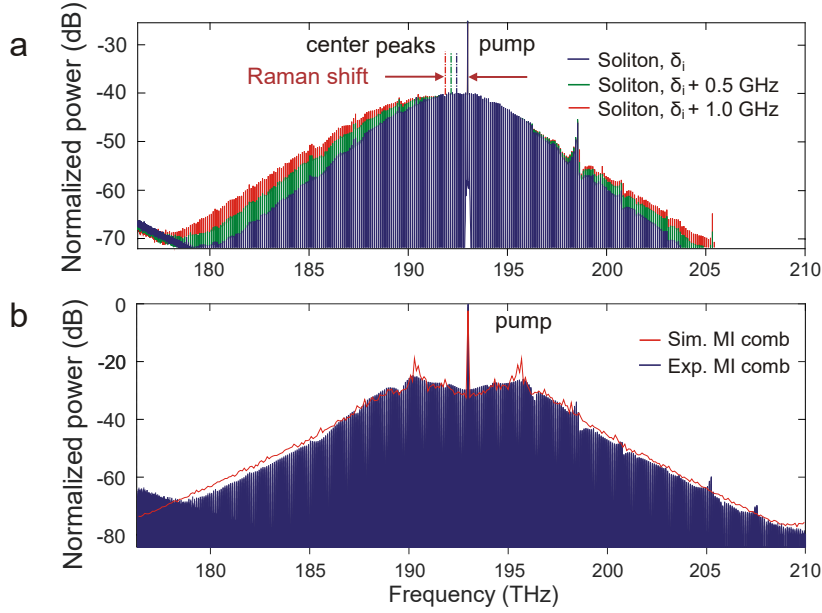


Figure 2.2 – (a) Spectra of single-soliton state obtained in a 100-GHz  $\text{Si}_3\text{N}_4$  microresonator at different detunings: red comb has  $\delta = \delta_i + 1.0$  GHz, the green one corresponds to  $\delta = \delta_i + 0.5$  GHz, and the blue one corresponds  $\delta = \delta_i$ . Vertical dashed lines indicate central frequency of the fitted comb envelopes. (b) Experimental measurements and simulation (the envelope) of a noisy Kerr comb generated in the same device as in (a), with the detuning value outside of the soliton existence range.

detuning) of the single soliton existence range as the initial detuning ( $\delta_i$ ), we explored the tuning behavior of the pump wavelength over entire soliton existence range. As shown in Fig. 2.2(a) the slowly evolving comb spectrum shows two apparent trends when the detuning is increased: (1) the spectral red-shift of the soliton is increased, and (2) the spectrum is broadened, which implies soliton compression to shorter pulse duration and higher peak power [9]. Both processes are reversible as the detuning decreased and show no visible hysteresis. For comparison, we also recorded the spectrum of the noisy Kerr comb, obtained outside of the soliton existence range, when the pump is blue-detuned and the system is in chaotic MI state. In contrast to the soliton state, the system does not show any shift of the spectrum, and the envelope is symmetric with respect to the pump (Fig. 2.2(b)).

In order to quantify the changes of the DKS states, the measured spectra were fit with hyperbolic secant envelope. The difference between pump and maximum of the fitting envelope corresponds to the frequency shift of the soliton spectrum with respect to the pump. The amount of such soliton spectral shift as a function of the detuning is shown in Fig. 2.3(a) for different pump powers. First, it can be observed that the single soliton step length is enlarged with an increase in pump power, which is in accordance with the theoretical prediction [9]. Second, the spectral shift (ranging within 0.5 –

---

## 2.2. Experimental observation of the soliton self-frequency shift

1.75 THz) is significant compared to the resonator FSR (100 GHz), and exhibits linear dependence on the laser detuning. Meanwhile, the soliton pulse duration is also tuned by the laser detuning, see Fig. 2.3(b). With an increase of the detuning  $\delta$  the soliton is compressed from 75 to 47 fs (sub-10 cycle). We note that at every detuning within the soliton existence range the system is stable. Both the spectral red-shift and the pulse compression of the DKS pulses are reversible and controllable.

The observed dynamics are in agreement with theoretical predictions by Milián *et al.* [158], who studied the impact of Raman effects on the DKS states in optical microresonators, and their interplay with high-order dispersion effects. It was shown that Raman effects, and in particular IRS can result in the formation of a new type of stable DKS states - *frequency-locked Raman solitons*, which in contrast to regular DKS acquire significant time-independent spectral shift of their envelope towards longer wavelengths.

The DKS states in our devices also reveal similar red spectral shift of their envelopes, which can be attributed to the presence of Raman effects associated with the cumulative nonlinearity of the silica cladding and silicon-nitride core of our waveguides. We can also exclude the impacts other high-order nonlinear effects, such as the third order dispersion and self-steepening, which are able to induce spectral shifts on the soliton comb envelope [163, 159]. The first effect can be excluded because of negligible third-order dispersion term  $D_3$  that is also confirmed by absence of dispersive wave in the measured range of OSA (800 – 1700 nm). In turn, the self-steepening naturally produces blue-sided spectral shift and can only counterbalance red-sided shift from intrapulse Raman scattering [159].

We furthermore note, that the observed Raman-induced soliton spectral shift was only observed in the soliton state, when a stable, self-sustained pulse is formed inside the cavity. In contrast to the soliton state, the spectrum of the noisy Kerr comb state, when the system operates in the regime of the modulation instability (MI) and has chaotic intracavity waveform, was symmetric with respect to the pump. This indicates that the observed effect is only associated with the pulse formation and thus can be attributed to the intrapulse Raman scattering, which is a well-known reason for the Raman-induced soliton self-frequency shift for solitons in optical fibers.

### 2.2.1 Compensation of the Raman self-frequency shift by the dispersive wave recoil

We also investigate how the Raman effect influences the DKS state with the presence of higher-order dispersion effects. For this we use two other  $\text{Si}_3\text{N}_4$  microresonators with different structural geometries that allow shorter soliton pulses and enable coherent dispersive wave (DW) generation as demonstrated by Brasch *et al.* [84]. In these samples, the  $\text{Si}_3\text{N}_4$  core has a nominal thickness of 0.8  $\mu\text{m}$  and the width is designed as large as 1.7 – 2.0  $\mu\text{m}$  (here we utilize width 1.8  $\mu\text{m}$  (Fig. 2.4(a)) and 2  $\mu\text{m}$  (Fig. 2.4(b))). The

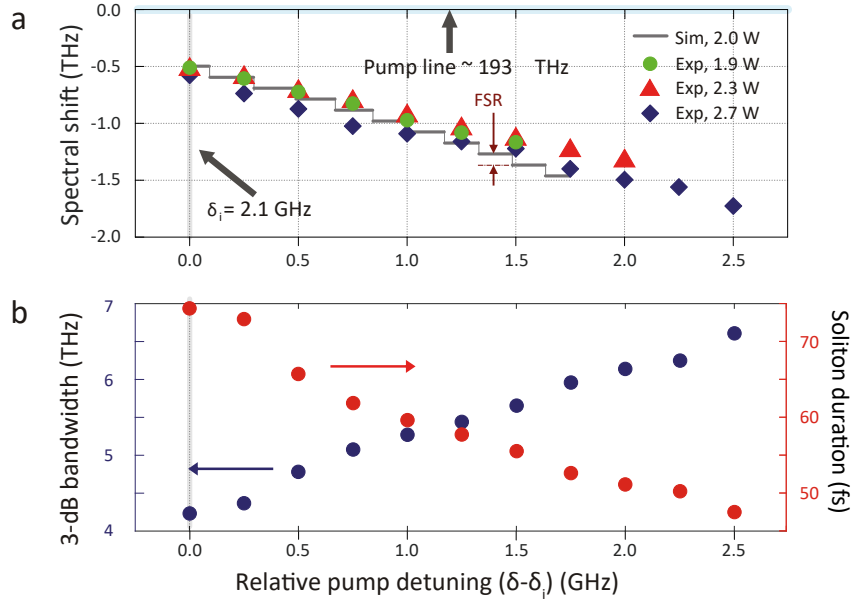


Figure 2.3 – (a) Measured variation of the comb spectral red-shift as a function of the detuning ( $x$ -axis:  $\delta - \delta_i$ ), at three pump powers: 1.9 W (green), 2.3 W (red) and 2.7 W (blue). Grey line indicates the same trend of the spectral shift, obtained from the simulations with 2.0 W of input power (see section 2.4). Note that the trend from the simulations is discrete (gray line) as we mark the specific comb line of highest power (despite the strong pump line). (b) variation of the spectral 3-dB bandwidth and the (Fourier-limited) pulse duration of single temporal dissipative Kerr soliton with the pump power of 2.7 W.

DKS states were excited in the fundamental  $TM_{00}$  mode, which has FSR of about 190 GHz, and comparably high third order dispersion term:  $D_3/2\pi = \mathcal{O}(10)$  kHz, leading to an estimated zero-dispersion wavelength at  $\sim 1700$  nm. Single-soliton states were obtained using power-kicking method [104] and a DW is identified at around 155 THz (1920 nm) in both devices, providing significant increase of the resulting comb span to  $\sim 75$  THz and its extension into normal-dispersion region. The comparison of the two spectra in Fig. 2.4 shows the influence of the third-order dispersion on the position of the DW frequency. The soliton comb in the first sample (width  $1.8 \mu\text{m}$ , Fig. 2.4(a)) has a 3-dB bandwidth of 10.8 THz, while in the second sample (width  $2.0 \mu\text{m}$ , Fig. 2.4(b)) the soliton comb 3-dB bandwidth is 8 THz.

It is generally known that the emission of a DW leads to the soliton spectral recoil [164, 163], such that the comb profile around the CW pump frequency will be shifted away from the DW, as illustrated schematically in the insets of Fig. 2.4(a, b). However, in above-mentioned  $\text{Si}_3\text{N}_4$  microresonators the blue-recoil (resulting from the DW being on the red side) was not clearly observed [84], see Fig. 2.4(a), and even a red-shift (Fig. 2.4(b)) of the comb profile is identified. This can be explained by the mutual compensation of two

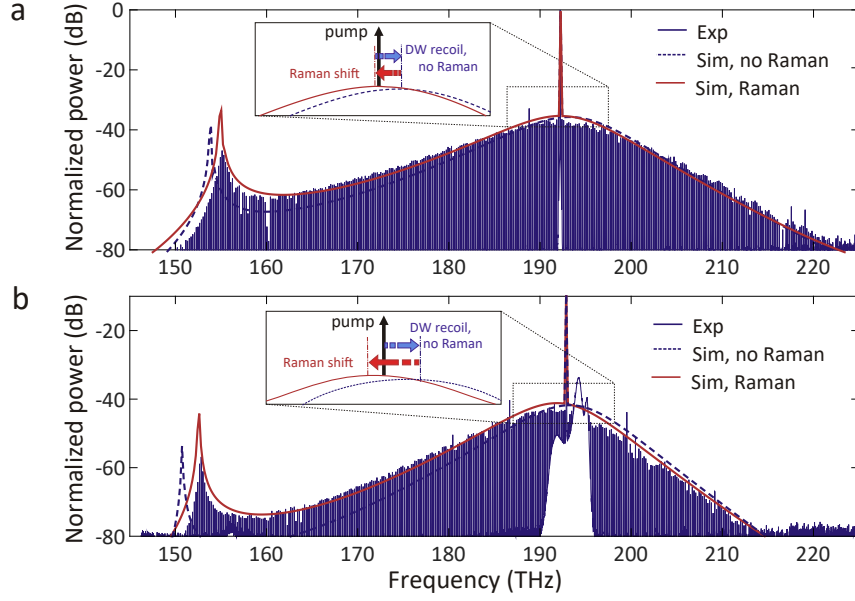


Figure 2.4 – Experimental generation and simulation of single soliton combs with dispersive wave in two different Si<sub>3</sub>N<sub>4</sub> microresonator geometries (both having a Si<sub>3</sub>N<sub>4</sub> thickness of 0.8 μm and FSR of ∼ 190 GHz). (a) The sample with the Si<sub>3</sub>N<sub>4</sub> core width of 1.8 μm (sample taken from [12]), and measured dispersion terms  $D_2/2\pi = 2.2$  MHz,  $D_3/2\pi = 18$  kHz,  $D_4/2\pi = -350$  Hz. The pumped resonance is at 1560 nm employing 1 W of power. (b) The sample with Si<sub>3</sub>N<sub>4</sub> core width of 2.0 μm, and measured dispersion terms of  $D_2/2\pi = 3.2$  MHz,  $D_3/2\pi = 26$  kHz, and  $D_4/2\pi = -340$  Hz. The pumped resonance is at 1554 nm, the power is 1 W. Dispersion and effective mode area are calculated by finite element modelling using COMSOL, while  $D_2/2\pi$  is also measured [43], showing close agreement to simulations. Blue dashed (red solid) lines indicate comb envelopes without (with) the Raman contribution.

different spectral shifts: the Raman induced soliton self-frequency shift and DW-induced soliton spectral recoil towards higher wavelengths. A similar effect has been observed in the case of soliton propagation in optical fibers [165].

## 2.3 Theory of the DKS self-frequency shift

In order to theoretically describe the impact of Raman effects on the DKS states, we use standard LLE equation in the  $(t, \phi)$  domain (see eq. (1.55)), and add the delayed nonlinear response function  $R(t, \phi)$  in the general form by the analogy with optical solitons in fibers [40]:

$$\frac{\partial A(\phi, t)}{\partial t} = \sqrt{\frac{\kappa_{\text{ex}} P_{\text{in}}}{\hbar \omega_0}} - \left( \frac{\kappa}{2} + i2\pi\delta \right) A - i \frac{D_2}{2} \frac{\partial^2 A}{\partial \phi^2} + igA \left( R(t, \phi) \otimes |A(t, \phi)|^2 \right), \quad (2.1)$$

## Chapter 2. Raman induced soliton self-frequency shift of dissipative Kerr solitons

---

where, we consider  $R(t, \phi)$  to have two contributions, which account for instantaneous electronic response of the material, and delayed Raman response from the optical phonons:

$$R(t, \phi) = (1 - f_R)\delta(t, \phi) + f_R h_R(t, \phi), \quad (2.2)$$

here  $f_R$  denotes the fractional contribution of the vibrational Raman part in the response,  $h_R(t, \phi)$  - is an actual Raman response function, rescaled in the  $(t, \phi)$  domain, and  $R(t, \phi)$  satisfies normalization condition  $\int R(t, \phi) d\phi = 1$ . Following the slowly-varying envelope approximation introduced for the LLE, and using linear approximation for the Raman gain, we can simplify the nonlinear part of eq. (2.1):

$$\frac{\partial A(\phi, t)}{\partial t} = \sqrt{\frac{\kappa_{\text{ex}} P_{\text{in}}}{\hbar \omega_0}} - \left( \frac{\kappa}{2} + i2\pi\delta \right) A - i \frac{D_2}{2} \frac{\partial^2 A}{\partial \phi^2} + ig \left( |A|^2 A - f_R \phi_R A \frac{\partial |A|^2}{\partial \phi} \right), \quad (2.3)$$

where we denoted  $\phi_R = \int_{-\pi}^{\pi} h_R(t, \phi') \phi' d\phi'$ .

### 2.3.1 Moment analysis for solitons in microresonators

In order to quantitatively estimate the Raman-induced soliton self frequency shift, we employed the moment analysis method that has been widely used for tracing soliton pulse dynamics in fiber optics, perturbed by the Raman shock-term [166, 155]. Since we experimentally observed pure effects of the Raman-induced soliton self-frequency shift and with the purpose to simplify the analysis, we ignore high order dispersion and the self-steepening effects and keep the simplified Raman response as derived in eq. (2.3). The idea of the moment method is to consider the pulse as a particle with the energy  $E$  (in terms of number of photons), position  $\phi_c$  and a frequency shift  $\mu_c$  (in terms of mode number). For the temporal DKS such parameters are defined as:

$$E = \int_{-\pi}^{\pi} |A(\phi, t)|^2 d\phi, \quad (2.4)$$

$$\phi_c = \frac{1}{E} \int_{-\pi}^{\pi} \phi |A(\phi, t)|^2 d\phi, \quad (2.5)$$

$$\mu_c = \frac{i}{2E} \int_{-\pi}^{\pi} \left( A(\phi, t)^* \frac{\partial A(\phi, t)}{\partial \phi} - A(\phi, t) \frac{\partial A(\phi, t)^*}{\partial \phi} \right) d\phi, \quad (2.6)$$

### 2.3. Theory of the DKS self-frequency shift

Applying derivatives with respect to the slow time ( $t$ ) on these moment parameters and using equation (2.3), we obtain the following set of differential equations:

$$\frac{\partial E}{\partial t} = -\kappa E + 2\sqrt{\kappa_{\text{ex}}} s_{\text{in}} \int_{-\pi}^{\pi} \text{Re}[A(\phi, t)] d\phi, \quad (2.7)$$

$$\frac{\partial \phi_c}{\partial t} = D_2 \mu_c, \quad (2.8)$$

$$\frac{\partial \mu_c}{\partial t} = -\frac{g f_R \phi_R}{E} \int_{-\pi}^{\pi} \left( \frac{\partial |A(\phi, t)|^2}{\partial \phi} \right)^2 d\phi, \quad (2.9)$$

where  $\text{Re}[\cdot]$  denotes the real part.

These dynamics are valid when there is an integrable light pattern in the cavity that is convergent on the boundary  $[-\pi, \pi]$ . We note that the first equation (2.7) doesn't include the Raman term, because it deals with the number of photons  $|A|^2$  that is a conservable quantity. As expected, the total intracavity energy which builds up over cavity roundtrips, depends on the loss factor  $\kappa$  and the gain from the external laser source  $s_{\text{in}} = \sqrt{P_{\text{in}}/\hbar\omega_0}$ . The second equation (2.8) indicates an additional change in the group velocity of the intracavity light patterns, which is linked to their spectral shift  $\mu_c$  and cavity dispersion  $D_2$ . The third equation (2.9), describes the evolution of the frequency shift and is only determined by the Raman term.

In the stable soliton state, the intracavity waveform consists of two parts: weak CW background and a  $\text{sech}^2$ -shaped soliton component [9]:

$$|A_c|^2 \approx \frac{\kappa_{\text{ex}} s_{\text{in}}^2}{(2\pi\delta)^2}, \quad (2.10)$$

$$|A_s(\phi)|^2 \approx \frac{4\pi\delta}{g} \text{sech}^2 \left( \sqrt{\frac{2\pi\delta}{D_2}} \phi \right) = N \cdot \text{sech}^2 \left( \frac{\phi}{\phi_0} \right), \quad (2.11)$$

where  $N$  indicates the number of photons in the soliton pulse and  $\phi_0$  is the pulse duration. Therefore the energy  $E_s$  (expressed in the number of photons) of the soliton component:

$$E_s = \int_{-\pi}^{\pi} N \cdot \text{sech}^2 \left( \frac{\phi}{\phi_0} \right) d\phi \approx 2N\phi_0 = 4 \frac{\sqrt{2\pi\delta D_2}}{g}, \quad (2.12)$$

and the dynamics of the soliton frequency shift is calculated with equation (2.9)

$$\frac{\partial \mu_c}{\partial t} \approx -\frac{8}{15} \left( \frac{4\pi\delta D_2}{g} \right) \left( \frac{2\pi\delta}{D_2} \right) g f_R \phi_R = -\frac{64\pi^2 \delta^2 f_R \phi_R}{15 D_2}. \quad (2.13)$$

For the final step, we adapt the notion of soliton period  $z_0$ , which for the fundamental optical solitons in fibers corresponds to the interaction length over which the system

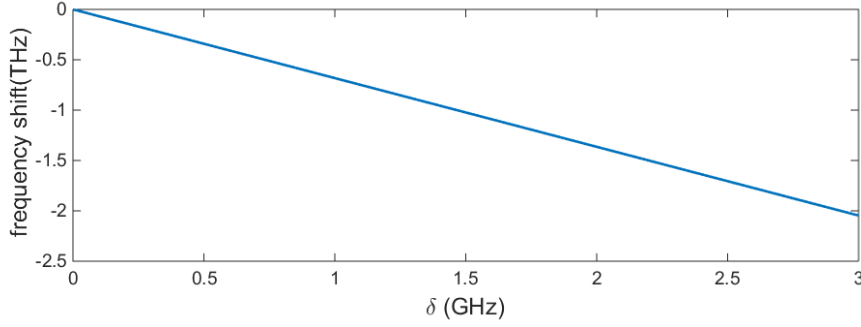


Figure 2.5 – Analytically estimated soliton frequency shift in optical microresonators as a function of pump-cavity detuning.

experience significant impact of the nonlinear effects [40]. We note that single DKS states also corresponds to the fundamental soliton solution of the LLE system, and its soliton period ( $T_0$ ) can be estimated as:

$$T_0 = 2\pi \left| \frac{\phi_0^2}{D_2} \right| = 2\pi \left( \frac{1}{2}g \frac{4\pi\delta}{g} \right)^{-1} = \frac{1}{\delta} . \quad (2.14)$$

Eventually, with such an effective interaction time, we may calculate the frequency shift of the intracavity soliton:

$$\mu_c = -\frac{32\pi}{15} \left( \frac{2\pi\delta}{D_2} \right) f_R \phi_R , \quad (2.15)$$

and in the scale of actual angular frequency, it reads:

$$\omega_c = -\frac{32\pi}{15} \left( \frac{2\pi\delta}{D_2} \right) f_R \left( \frac{2\pi\tau_R}{t_R} \right) D_1 . \quad (2.16)$$

We can see that in the first approximation the soliton self-frequency shift is linearly proportional to the laser frequency detuning  $\delta$ . The negative sign implies the carrier frequency is *red*-shifted. The rate of the frequency shift is determined by the Raman shock time (in terms of  $f_R\tau_R$ , where  $\tau_R = \phi_R/D_1$ ), but is independent on the pump power. For the parameters of the experimentally studied samples:  $D_1 = 2\pi \times 100$  GHz,  $D_2 = 2\pi \times 2$  MHz,  $f_R = 20\%$ ,  $2\pi\tau_R = 20$  fs, the frequency shift is estimated in Fig. 2.5, which matches the order of magnitude of experimental results.

## 2.4 Simulations of the DKS self-frequency shift

We numerically simulated the formation of the single DKS states with the presence of the Raman effects in the LLE. As in previous simulation works and our experiments, we observed the formation of stable DKS states with red-shifted optical spectrum. In the simulations we assume the same Raman fraction ( $f_R$ ) as for optical fibers - 20%, and

## 2.4. Simulations of the DKS self-frequency shift

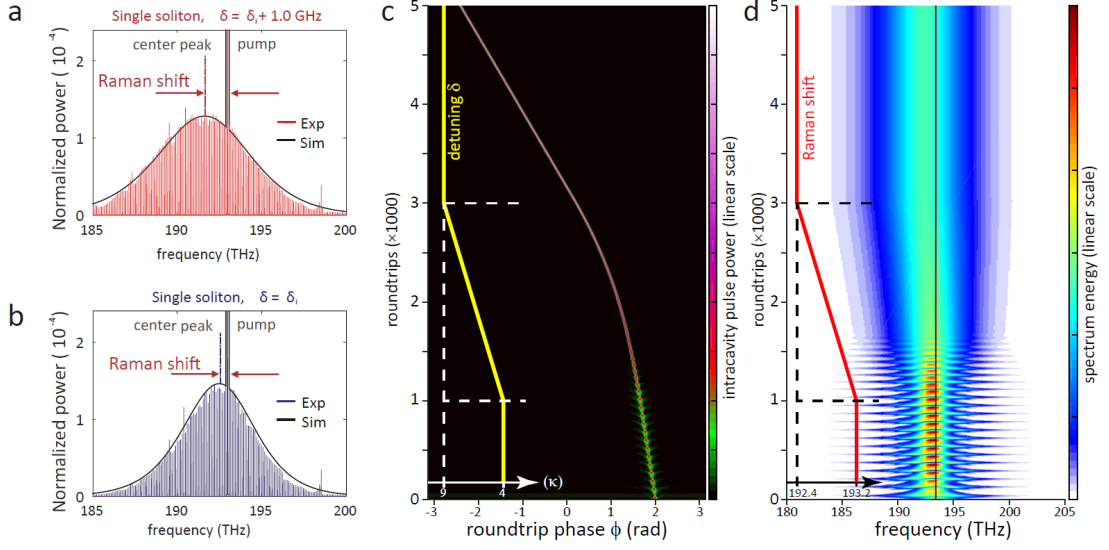


Figure 2.6 – (a, b) Comparison between experimentally obtained and simulated soliton spectra in 100-GHz  $\text{Si}_3\text{N}_4$  microresonator, shown in linear scale. The envelopes are from numerical simulations. The comb power ( $y$ -axis) is normalized to the CW pump power. For soliton comb simulations, we use  $D_2/2\pi = 2$  MHz,  $D_3/2\pi = 4$  kHz,  $\kappa/2\pi = 350$  MHz,  $\delta_i = 2.1$  GHz. (c) Single soliton propagation evolution from the soliton breather state to the stable soliton state; the inset shows change of the detuning (yellow). (d) Evolution frequency comb spectral envelope; the inset reveals the Raman red-shift.

used unknown value of the Raman shock time to fit our experiments. Fig. 2.6(a, b) show the comparison between the experimentally obtained optical spectra and the resulting simulated envelopes of soliton spectra. The extracted Raman shock time ( $\tau_R$ ) is 20 fs.

Furthermore, to demonstrate the evolution of the soliton pulse and its independence on roundtrips (propagation distance), we also simulate the intracavity pulse dynamics from the breather state to the stable soliton state, accompanied with the Raman effect. Fig. 2.6(c) shows the evolution of both the pulse and spectral profiles. The detuning ( $2\pi\delta$ ) is fixed at the initial stage of the simulation and there is no spectral shift being acquired over the round-trip propagation. Then when the detuning is linearly increased from  $4\kappa$  to  $9\kappa$ , the spectral red shift is also linearly increased and the soliton continuously evolves to the stable state. Finally, if the detuning is fixed again (in the stable soliton state), previously acquired spectral shift remains unchanged.

We also simulate the formation of the single DKS states under the combined effect of the IRS and third order dispersion, as observed in the second part of our work (section 2.2.1), which was implemented by including both the Raman shock term and the full dispersion landscape  $D_{\text{int}}$ , while keeping the same value of the Raman shock time of 20 fs and Raman fraction of 20%. As shown in Fig. 2.4, the simulations are in good agreement and in particular, reproduce the experimentally observed cancellation and overcompensation of the soliton spectral recoil by the Raman induced red-shift.

We note that the Raman shock-time we extracted  $\text{Si}_3\text{N}_4$  and verified in simulations of different devices ( $\tau_R = 20$  fs) is actually much smaller than that in silica, the latter being  $\tau_R \approx 89$  fs [167]. A long shock-time enables the observation of soliton self-frequency shift in silica-based fibers with short lengths ( $\mathcal{O}(10)$  cm) and intense pump powers ( $\mathcal{O}(1)$  kW) [168], while in  $\text{Si}_3\text{N}_4$ -waveguide-based supercontinuum generation experiments, the Raman redshift has not been observed [169, 170, 171]. Observation of the Raman effect in  $\text{Si}_3\text{N}_4$  microresonators can be attributed to two factors. First, it is the cavity buildup (finesse  $\mathcal{F} = D_1/\kappa \approx \mathcal{O}(100 - 1000)$  in the present work), which effectively increases light-material interaction length (to  $\mathcal{O}(1)$  m) and promotes the pulse peak power (e.g., in Fig. 2.1 (b), the intracavity soliton peak power reaches 2 kW under a CW pump of 2 W), which can excite weak Raman effects of  $\text{Si}_3\text{N}_4$ . Second, the silica cladding can also provide a contribution to the Raman response in our microresonators. However, we should note that due to the significantly reduced overlap with the transverse mode of the propagating soliton, the actual Raman fraction can be much smaller than estimated in our simulations 20%.

## 2.5 Conclusion

We experimentally demonstrate the impact of the Raman effects and their interplay with third-order dispersion for the DKS states in optical microresonators. In a standard CW-driven microresonator (without Raman, e.g. a crystalline resonator), the temporal dissipative Kerr soliton relies on the energy balance between the drive and the cavity loss, and the phase balance between dispersive and nonlinear effects. In the presence of material Raman effects, solitons still exist and reveal distinct behavior, compared to the solitons in fiber optics where IRS continuously transfers the pulse energy from the short to long wavelength side. In microresonators this leads to a new type of the dissipative Kerr solitons - FLR solitons [158], where the energy balance is among drive, loss, the IRS-induced intrapulse energy transfer and the possible Cherenkov radiation [84] (energy shedding off from the soliton). The soliton pulse profile is consequently distorted and reveals a fixed amount of spectral red-shift from the pump wavelength, while in optical fibers, the IRS will induce a *continuous* red-shift on a local pulse that grows with propagation distance.

Finally, we add few words on the comparison of the observed soliton self-frequency shift in microresonator platforms to the well-known Raman-induced soliton redshift in optical fibers. Despite the similarity in the physics of the effect that originates from IRS, the microresonator platform (and associated temporal dissipative soliton class) causes considerable differences in soliton dynamics compared to the case of soliton propagation in a fiber.

First, the soliton state in microresonators is fundamentally different to that in optical fibers. Intracavity solitons in microresonators are generated from a CW laser pump

via parametric four wave mixing processes of the Kerr nonlinearity, upon tuning the pump frequency into a bistability region of the cavity resonance [9]. Solitons generated in this way belong to the class of temporal dissipative Kerr solitons, which are physically eigenstates of the microresonator system and mathematically the eigensolution of LLE. The pump frequency detuning  $\delta$  is a key parameter to such solitons as it determines the soliton formation (via a soliton existence range) and defines the pulse peak intensity as well as the duration [9]. Moreover, such an eigenstate of solitons could also withstand impacts from system higher-order effects (the self-steepening effect, higher-order dispersion effects and the Raman effects), leading to a consistent pulse train forming the fully coherent optical frequency comb. In contrast to microresonators, solitons in fibers are excited by launching *external* pulses (i.e., pulsed laser sources), while higher-order effects in the fiber would distort the soliton pulse profile. Therefore, solitons would evolve during the propagation along the fiber, resulting from the competition of higher-order effects, rather than showing a stable eigenstate.

Second, the role of the Raman effect in the soliton state in microresonators reflects distinct physics. Since the soliton state represents an eigenstate that could also withstand the presence of the Raman effect, it implies that the Raman effect directly plays a role in the double balance of dissipative Kerr solitons. In details, the Raman shock-term would continuously redshift the soliton spectrum representing an intrapulse energy transfer. This effect, together with the double balance on both the soliton energy and the pulse chirping, reveals a novel type of eigenstate of the microresonator system. In optical fibers, however, it is commonly known that the Raman shock-term would *continuously* redshift the soliton spectrum during the propagation. The Raman effect in this way is understood as an external perturbation to the soliton state rather than an intrinsic feature.

Finally, it should be highlighted, that as in fibers, the impact of Raman effects on the DKS dynamics in microresonators is not just limited to the soliton self-frequency shift, which was studied in the present and other works [172, 158]. Raman effects can induce the formation of Stokes solitons [173], and are found to impose fundamental limitations on the soliton duration and bandwidth [174]. Furthermore, the Raman processes can also interplay or compete with the FWM processes of the Kerr comb formation in crystalline or polycrystalline microresonators [175, 94, 176, 177]



# 3 Universal dynamics and deterministic switching of DKS states in optical microresonators

This chapter reports on the observation and theoretical description of *soliton switching* - a universal phenomenon of DKS states dynamics, which enables deterministic reduction in their number of pulses. The chapter also introduces a novel non-destructive soliton probing scheme, enabling controllable switching and monitoring of the DKS parameters using weak phase modulation of the pump at RF frequencies. The results and partially adapted from H. Guo\*, **M. Karpov\***, *et al.*, "Universal dynamics and deterministic switching of dissipative Kerr solitons in optical microresonators", *Nature Physics*, 13(1), p.94, (2017).

The swithing process to access multiple and single soliton states as well as soliton probing scheme are also patented: **M. Karpov**, V. Brasch, T.J. Kippenberg, "Single and multiple soliton generation device and method", US Patent №: US 10,270,529 B2

## 3.1 Introduction

One of the key challenges associated with DKS states in optical microresonators - is the absence of deterministic and reliable approach to their generation, which would work for different devices and even platforms with minimum adjustments. Another challenge, which is related to the previous one - is the access to the single-soliton state, when only one intracavity pulse is present in the cavity. The access to a single soliton states is important, because they provide optical combs with single-FSR spacing, have smooth and predictable spectral envelope with low line-to-line power variation. So far all DKS applications have been mostly focused on single soliton states due to the simplicity and reproducibility of their envelope as well as other advantages they offer in comparison to other states.

---

\*These authors contributed equally to the work.

### Chapter 3. Universal dynamics and deterministic switching of DKS states in optical microresonators

---

The first and most widely used technique for the DKS generation is the *forward tuning* [9]. In this approach the pump laser is scanned over the cavity resonance from the blue-detuned position to the red-detuned one, where is then stopped in the soliton existence range (see more details in section 1.4.2 of Chapter 1). Forward tuning works well for the resonators with moderate thermal effects (for example,  $\text{MgF}_2$  crystalline WGM microresonators). It can provide reliable access to the single-soliton step and stabilize the system in the corresponding DKS state. In contrast, in the majority of on-chip devices such as  $\text{Si}_3\text{N}_4$ , Si or AlN integrated microresonators, where an impact of the thermal effects is stronger, the same approach enables the access to the steps which correspond to only high soliton numbers ( $N$ ). Low-number soliton steps appears to be hidden and inaccessible. Such issue of forward tuning can be partially solved using fast-tuning schemes, which can help to overcome thermal effects. They include single-sideband modulation for fast frequency sweeps or direct current tuning of the diode lasers [178, 106], but require additional equipment and have limited tuning bandwidth not suitable for the DKS generation in all platforms. Another approach, which was developed by Brasch *et al.* [104], - *power kicking* - is able to provide reliable access to single soliton states in  $\text{Si}_3\text{N}_4$  [84] and silica microresonators [91], but is rather complex and requires tedious adaptation of tuning parameters for each new device.

Furthermore, even though the states with various soliton numbers could be generated in optical microresonators, the transitions between them take place stochastically (via e.g. pairwise interactions of solitons), when the pump is tuned, and could not be predicted. Due to these effects deterministic generation of the single-soliton state is often represents an outstanding challenge. A further challenge, which is also associated with the DKS dynamics is the state monitoring and stabilization. The soliton regime in microresonators is fragile (though self-sustainable) and is not persistent against significant thermal drifts and other external perturbations, which define DKS rather limited passive lifetime of several hours in a stable laboratory environment [84, 9].

In the following sections we report the discovery of a soliton switching phenomenon that allows the number of DKS in microresonators to be deterministically reduced one-by-one to reliably reach the single-soliton state. Apart from this, we present a non-destructive soliton probing scheme, which allows monitoring of the DKS parameters and enable feedback-stabilized control of the soliton state. The results were obtained and inspected in two microresonator platforms:  $\text{Si}_3\text{N}_4$  on-chip microring resonators [22, 179, 84] and  $\text{MgF}_2$  crystalline WGM resonators [180, 181, 182, 9]. We however mainly focus on the results obtained in the integrated  $\text{Si}_3\text{N}_4$  microresonators as the primary platform, where the effect was first found and studied.

### 3.2 Backward tuning and switching

The  $\text{Si}_3\text{N}_4$  devices with 100 GHz FSR used in experiments have similar design and parameters as described in section 2.2 of previous Chapter 2. Following the standard pump tuning procedure we try to excite DKS states by tuning the pump frequency over the cavity resonance from the blue-detuned side to the red-detuned. When the pump enters effectively red-detuned regime we observe the formation of multiple soliton states, which represent themselves with a step-like fall of power of the generated comb light at the end of thermal triangle (see schematics in Fig. 3.1(a)). In the studied  $\text{Si}_3\text{N}_4$  microresonators the fall typically consist of only one step that corresponds to multiple soliton states with stochastically generated number of intracavity pulses. Such singleness of the step implies that the transition to multiple soliton states with lower number of solitons, which is often observed in the  $\text{MgF}_2$  resonators [9], can be hardly achieved using forward tuning approach.

We next investigate the statistics of the observed soliton steps and record multiple experimental attempts using forward tuning. Figure 3.1(b) shows 200 overlaid traces of the generated comb light obtained in one of the devices. As can be seen from the figure, only multiple-soliton states are stochastically accessed having  $N = 6$  (predominantly), 7, 8 or 9 solitons. The step distribution is discrete with respect to the generated light power and has equal spacing between adjacent steps (in terms of the power), indicating the formation of different number of solitons  $N$ . The intensity of the plot shows the probability to land on the corresponding soliton step. We repeat the same experiments at different pump powers ranging from 2 to 4 W in order to track the evolution of the steps distribution and occurrences of different multiple soliton states (see Fig. 3.1(d)). It was observed that several common features can be indentified irrespective of the employed pump power and the laser tuning speed: (1) the distributions mostly consist of the traces with one step corresponding to high- $N$  multiple-soliton state; (2) the accessible step length decreases with decreasing  $N$ ; furthermore, Fig. 3.1(c) shows the occurrences of different number of steps for various pump powers within the measured range of 2 – 4 W, where we observed (3) a significant reduction of the probability to generate a soliton state as the pump power increases, because the total number of traces showing soliton formation (dark blue, green, and yellow histogram bars) decreases as the pump power approaches 4 W.

All of these observations imply that the single soliton state is *not* readily accessible with the forward tuning technique in our  $\text{Si}_3\text{N}_4$  microresonators. Such behavior can be mainly attributed to the presence of strong thermal effects in the system. For DKS states with higher intracavity power (higher  $N$ ) the thermal effects induce stronger thermal shift of the soliton existence range towards longer wavelengths (see section 1.2.5). When, during the pump frequency tuning, the system falls on the soliton steps from the MI, this results in the masking effect imposed by the DKS states with high  $N$  on the states with smaller soliton number. Such behavior particularly explains the singleness of the DKS

### Chapter 3. Universal dynamics and deterministic switching of DKS states in optical microresonators

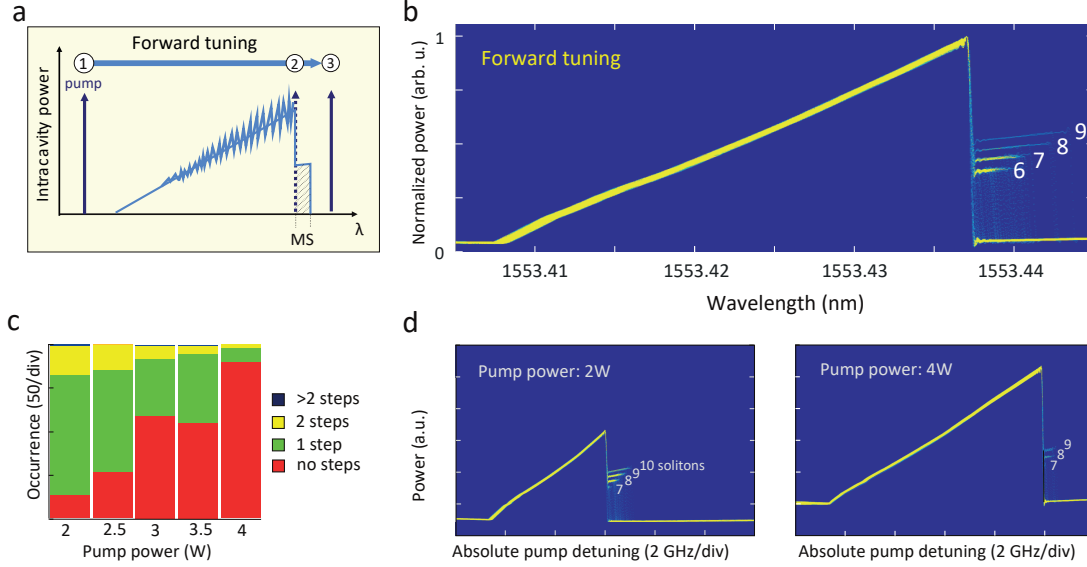


Figure 3.1 – (a) Scheme of the laser tuning method for the soliton generation in optical microresonators. The pump laser is tuned over the resonance from short to long wavelengths (forward tuning). Hatched region indicates the pump detuning range of multiple solitons (MS); (b) Histogram plot of 200 overlaid experimental traces of the output comb light in the pump forward tuning over the resonance with the same pump power and tuning speed, which reveals the formation of a predominant multiple soliton state with  $N = 6$ ; The noise pattern in the forward detuning was not captured by the measurements due to the averaging by slow photodetector. (c) Histogram of soliton steps occurrences in the forward pump tuning at different pump powers. The red color corresponds to the absence of soliton states, the green color corresponds to the appearance of 1 soliton step, yellow - 2 steps, dark blue - more than 2 steps. For each pump power 200 traces were recorded. (d) Histogram plots of 200 overlaid experimental traces (each) of the output comb light in the pump forward tuning over the resonance of 100 GHz  $\text{Si}_3\text{N}_4$  microresonator at two pump powers of 2 and 4 W with the same tuning speed.

step observed in most of the experiments, as well as decrease of available step length for smaller  $N$ . Furthermore, it should be also noted that the blue-detuned MI state of the cavity has even higher intracavity power than all other DKS states. The thermal shift it experiences can be even stronger, despite of the unstable intracavity waveform. Thus MI state can in turn impose similar masking effect on all DKS states. It is observed for increased pump power of the system in our experiments and can be also noted in other microresonator platforms, when the pump tuning speed is comparably low.

Remarkably, we discovered that an additional laser tuning towards shorter wavelengths (*backward tuning*) applied to any multiple-soliton state generated in the experiments described above provides a way to reliably access the single soliton state. The result of this backward tuning sequence, shown schematically in Fig. 3.2(a), allows for successive extinction of intracavity solitons (soliton switching) down to the single soliton state

( $N \rightarrow N-1 \rightarrow \dots \rightarrow 1$ ). Figure 3.2(b) shows one experimental trace of the generated light from a  $\text{Si}_3\text{N}_4$  microresonator, where switching from seven solitons to the single soliton is observed. Strikingly, the power trace of the generated comb light reveals a *regular staircase* pattern with equal the stairs having equal lengths and heights. The exact soliton number in each step can be precisely inferred from the step height. The pattern is almost identical over multiple experimental runs (using the same tuning speed and pump power) *regardless* of the initial soliton number  $N$ . Each transition between multiple-soliton states occurs with the extinction of *one* soliton at a time, which is confirmed by the relative positions of the intracavity solitons that are retrieved from the optical spectra (see insets in Fig. 3.2(c-e)).

In the experiments, the backward tuning process must be adiabatic to induce the successive reduction of the soliton number: the thermal equilibrium is required at each multiple-soliton state. This prerequisite is satisfied by choosing a tuning speed much slower than the thermal relaxation rate that depends on the effective mode volume and the thermal diffusivity of a microresonator [183]. For  $\text{Si}_3\text{N}_4$  microresonator used in these experiments the backward tuning speed is chosen to be  $\sim 40$  MHz/s, while the forward tuning speed is  $\sim 100$  GHz/s. In this way all soliton states ( $\leq N$ ) are deterministically accessible. In contrast to the robust backward tuning that enables successive extinction of intracavity solitons, the forward tuning in  $\text{Si}_3\text{N}_4$  microresonators typically leads to collective extinction of solitons.

We also studied the backward tuning in  $\text{MgF}_2$  crystalline microresonators, where the deterministic soliton switching to the single soliton state is equally observed. In contrast to the  $\text{Si}_3\text{N}_4$  platform, the single soliton state can directly be accessed via the forward tuning in  $\text{MgF}_2$  microresonators [9]. Yet, this requires suitable adjustments on the coupling, the pump power and the tuning speed. By contrast, it was observed that the backward tuning, is significantly more robust and facilitates the generation of single soliton states in crystalline resonators.

The soliton switching observed in both  $\text{Si}_3\text{N}_4$  and crystalline  $\text{MgF}_2$  resonator, reveals that the backward tuning represents a universal approach to the generation of a single soliton state in microresonators, provided that the thermal locking can be achieved<sup>1</sup>.

### 3.3 Nondestructive soliton probing

One of the key parameters of DKS states is the effective frequency detuning between the driving laser and cavity resonance that determines both the amplitude and the duration of soliton pulses [97, 9]. We recall that the effective frequency detuning is introduced with respect to the actual position of the cavity resonance (see section 1.2.5, Chapter 1).

<sup>1</sup>As for all modern platforms, where the generation of DKS states has been demonstrated, it is assumed that we are working with focusing nonlinearity, and positive thermal effects.

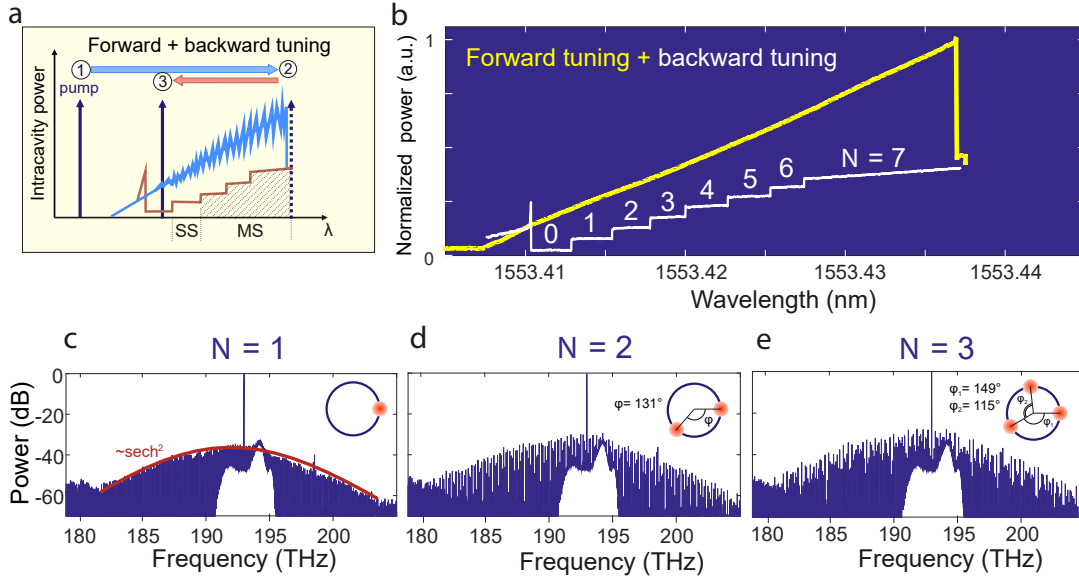


Figure 3.2 – (a) Scheme of the laser backward tuning. To initiate the sequence, the forward tuning is first applied, and the pump is stopped in a multiple soliton state (which can be stable by suitable choice of the laser tuning speed). In the second stage, the pump is tuned back to short wavelengths, which leads to successive soliton switching,  $N \rightarrow N - 1 \rightarrow \dots \rightarrow 1$ . The MS area indicates the detuning range of multiple soliton states, which is much larger compared to the forward tuning method. There also exists the range of the single soliton state (SS); (b) Experimental trace in the forward tuning (yellow curve) followed by one trace in the backward tuning (white curve) with successive transitions of multiple-soliton states from  $N = 7$  to  $N = 0$  (no solitons); (c-e) frequency comb spectra in soliton states with  $N = 1, 2, 3$ , measured during the backward tuning in a 100 GHz  $\text{Si}_3\text{N}_4$  microresonator. The relative positions of the solitons result from the forward excitation path and are mostly random. They are retrieved via inverse Fourier transform of the optical spectrum.

When microresonator operates in the DKS state, the resonance position can be thermally shifted with respect to the position of the cold-cavity resonance, which is induced by the field presence inside the cavity.

For the further exploration of switching phenomenon we developed a non-destructive soliton probing scheme that allows the tracking of the effective detuning and the determination of the soliton number  $N$ . It is based on measuring the conversion (i.e. transfer function) of a phase-modulated pump to amplitude modulation on the comb power, using a network analyzer (see Fig. 3.3(a)). Starting from the standard setup for soliton generation in the integrated microresonators, we introduce an additional phase modulation on the pump laser using an electro-optical modulator (EOM, bandwidth 10 GHz). We employed a vector network analyzer (VNA) to drive the EOM with a swept frequency from 5 kHz to 4.5 GHz. A portion of the transmitted light is used to measure the system transfer function by recording the cavity-induced quadrature

### 3.3. Nondestructive soliton probing

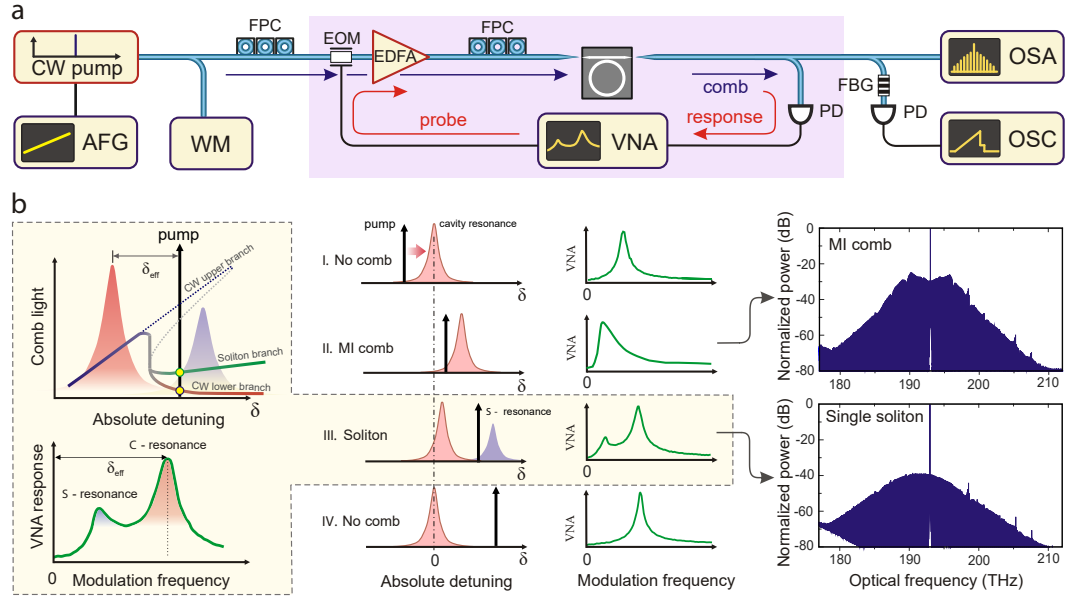


Figure 3.3 – (a) Setup scheme used for soliton generation, non-destructive soliton probing and deterministic soliton switching. An external cavity diode laser (CW pump) is used as a pump source. AFG, arbitrary function generator; EDFA, erbium doped amplifier; FPC, fiber polarization controller; WM, wavelength meter; VNA, vector network analyzer; OSA, optical spectrum analyzer; OSC, oscilloscope; PD, photodiode; EOM, electro-optical phase modulator; PM, phase modulator; FBG, fiber Bragg grating. (b) (Left, top) Diagram of the double-resonance cavity transfer function in the soliton state. The green line indicates the power trace of the soliton component which is evolved from the high-intensity branch of the bistability (blue line). The pump is tuned in the bistability range (in the effectively-red-detuned regime). Therefore, both the soliton branch and the low-intensity continuous (CW) branch (red line) are supported in the system, each corresponds to a resonance, i.e. the  $\mathcal{S}$ -resonance and the  $\mathcal{C}$ -resonance. (Left, down) Double-resonance cavity transfer function measured with VNA. The high-frequency peak indicates the  $\mathcal{C}$ -resonance and the low-frequency is the  $\mathcal{S}$ -resonance. (Middle) Four stages of the microresonator frequency comb formation and corresponding cavity transfer function measured with VNA when the pump laser is forward tuned over the resonance: (I) No comb, the pump is blue-detuned; (II) Chaotic MI comb state; (III) Soliton state; (IV) No comb, the pump is red-detuned. (right) Frequency comb spectra corresponding to the chaotic MI operation regime and the single soliton state.

rotation from the phase to the amplitude quadrature with a photodiode, and subsequent demodulation via a RF-homodyne detection inside the VNA. The phase modulation imprints two out-of-phase sidebands symmetrically around the pump (we use a small modulation index of 0.01, so that only first-order sidebands are considered). Passing through the cavity, the sidebands pick up a different relative phase, which leads to an amplitude modulation of the measured signal.

This probing method enables the identification of the different stages of Kerr comb

### Chapter 3. Universal dynamics and deterministic switching of DKS states in optical microresonators

---

formation including the presence of DKS state as schematically shown in Fig. 3.3(b). First, when the pump is in the blue-detuned regime and is reasonably far from the resonance, such that almost no power is coupled in the cavity, the system transfer function exhibits a Lorentzian-like resonance profile that originates from the cavity resonance. The frequency position of the resonance response in the VNA trace can be directly interpreted as effective detuning of the system. Second, when the pump frequency is tuned (forward) into the resonance to launch chaotic MI regime, the transfer function shows an asymmetric profile with fixed peak position, indicating the thermal and Kerr locking of the cavity resonance to the pump frequency. Third, when the pump laser is tuned into the soliton existence range (i.e. in the effective red-detuned regime), the transfer function (VNA response) shows unexpectedly a *double-resonance* feature. Finally, when the pump frequency is tuned out of the soliton existence range, where no comb is observed, the transfer function shows again a single, Lorentzian-like resonance similar to the first stage.

The most intriguing part of the response function is the presence of the *second* resonance, which appears in the DKS states. We applied the modulation probing scheme to both  $\text{Si}_3\text{N}_4$  and  $\text{MgF}_2$  microresonators and observed that such behavior is qualitatively similar among different platforms when a soliton state is obtained. It turned out to be strongly dependent on two characteristic parameters of the DKS state - effective detuning and the number of soliton pulses inside the cavity. Fig. 3.4 shows such dependencies in our 100-GHz  $\text{Si}_3\text{N}_4$  microresonator. For the clarity, we denote the resonances of the VNA response as follows: the low-frequency one -  $\mathcal{S}$ -resonance, the high-frequency one -  $\mathcal{C}$ -resonance, where the choice of the letters will be explained later in the present chapter. First, we observed that with the fixed detuning the amplitude of the  $\mathcal{S}$ -resonance scales with the number of pulses in the DKS state, while  $\mathcal{C}$ -resonance stays intact (Fig. 3.4 (a)). When the system is loosing DKS state, the second resonance ( $\mathcal{S}$ ) could not be identified. Even more significant difference between DKS and CW states can be identified by measuring the phase of the transfer function. For the case of the DKS state it reveals two  $\pi$  jumps, while in the absence of soliton, the response has only single  $\pi$  jump, highlighting that both features in the transfer function are actual resonance frequencies of the system in the DKS state.

The double-resonance feature is attributed the fundamental cavity bistability, which appears in the presence of the Kerr nonlinearity. In the DKS state, the intracavity field consists of a weak CW background and intense soliton pulses. The CW component represents the “lower branch” of the intracavity field solution, which is effectively red-detuned with respect to the cavity resonance. It contributes to the formation of the  $\mathcal{C}$ -resonance, which as in the case with a transfer function of a non-DKS states represent a single Lorentian-like response located at the frequency corresponding to the effective detuning. This can be particularly observed in Fig. 3.4(a, b), where black curves represent a CW-state, when the pump is red-detuned, and have single resonance in the transfer function confirmed by a single  $\pi$  jump of the phase response. When the

### 3.3. Nondestructive soliton probing

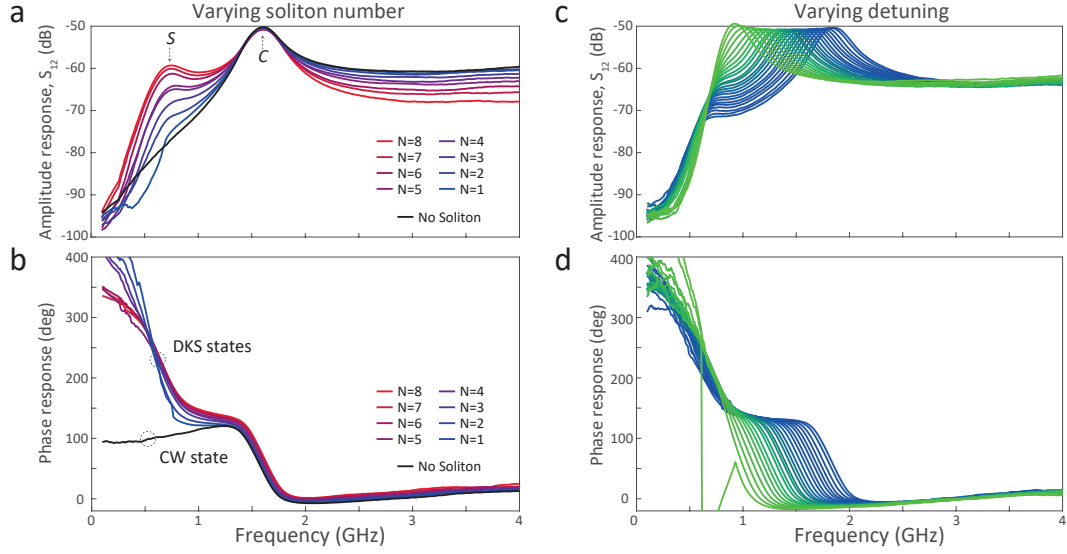


Figure 3.4 – (a, b) Experimentally obtained transfer functions ((a) - amplitude response, (b) - phase response of the system)) of the DKS states with different number of solitons inside the cavity. The soliton number is maximum for red-colored trace, and equals 1 for the blue-colored trace. Black trace shows the response function of the system in the absence of DKS. 2-resonance profile, as well as phase jump of  $\sim 2\pi$  can be observed for all DKS states, while in the absence of DKS system shows only single  $\sim \pi$  phase jump. Low-frequency data are noisy due to the weak signal. (c, d) Experimentally obtained transfer functions ((c) - amplitude response, (d) - phase response of the system)) of the 3-soliton DKS state with different pump-cavity detunings. The effective detuning is maximum for the blue-colored trace, and is minimum for the green-colored trace. The few points for the minimum-detuning data in (d) obtained  $2\pi$  jump due to the errors in data processing.

soliton pulses with their high peak intensity are present in the cavity, they are able to induce an additional shift of the cavity resonance, due to the intensity-dependent Kerr phase shift. This process in return allows the pump laser to be coupled into the resonance, such that the soliton experiences gain. Therefore, the soliton presence in the DKS state contributes to the appearance of the second resonance, which is blue-detuned with respect to the cavity, as shown in Fig. 3.3(b). Thus there exist two resonance states, each having a different detuning to the pump frequency, and thereby each inducing a different quadrature rotations on the incoming probing sidebands. The net result appears as a double-resonance feature – the soliton-induced “ $\mathcal{S}$ -resonance” and “ $\mathcal{C}$ -resonance” related to the CW.

As can be seen, the measured transfer function can provide rich information about the soliton states. First, it provides unique signature, which can help to identify the presence of a DKS states with any repetition rates (including (10s, 100s and 1000s of GHz) using low-frequency RF equipment. Second, the  $\mathcal{C}$ -resonance peak (frequency) indicates the

### Chapter 3. Universal dynamics and deterministic switching of DKS states in optical microresonators

---

effective detuning between the pump and the cavity resonance. Third, the amplitude of the  $\mathcal{S}$ -resonance is related to the number ( $N$ ) of solitons, as the response signal is enhanced by higher comb power generated with a larger number of solitons.

The direct probing of the effective detuning, which can be implemented with the developed technique, allows to monitor and control the DKS state. Since, the thermal drifts of the cavity resonance originating from various external sources may cause variations of the effective detuning, the transfer function measurements can help to restore it (e.g. by tuning the pump frequency) in order to maintain the state within the soliton existence range. In practice, feedback-locking of the effective is also possible and allows for long-term operation of soliton state in a microresonator [184, 185].

Transfer function measurements of this type were also applied in mode locked laser systems but the soliton feature was not captured [186, 187, 188]. We also note, that the cavity transfer function between a weak pump modulation and the modulation on the comb power in the soliton state was earlier numerically investigated in [189]. While two peaks of the transfer function were also numerically observed in this work, they were attributed conceptually to Feshbach and relaxation oscillations in the presence of third order dispersion. The present work reveals clearly the different underlying physical origin of the two resonance, which do not result from higher order dispersion.

#### Analytical description of the VNA measurements

We briefly stop at the theoretical description of both resonances in the VNA response. As highlighted above, the  $\mathcal{C}$ -resonance represents the response of the CW intracavity field to the input pump phase modulation. When this intracavity field is small enough, which is the case for large detunings ( $> \kappa$ ) on the blue- or red-detuned sides of the cavity, including the DKS state, one can use linear cavity formalism (1.12) to describe its position. We consider the pump phase modulation in the form:

$$s_{\text{in}}(\Omega, t) = s_{\text{in}}(1 - i \cdot m e^{-i\Omega t} - i \cdot m e^{i\Omega t}) , \quad (3.1)$$

where  $\Omega$  - is the modulation frequency, and  $2m$  is the modulation amplitude. Denoting  $D = -(i\Delta + \kappa/2)$  and using (3.1) in (1.12) together with (1.15), we can obtain transmitted signal:

$$s_{\text{out}}(\Omega, t) = s_{\text{in}}(A + B e^{-i\Omega t} + C e^{i\Omega t}) , \quad (3.2)$$

$$A = 1 + \frac{\kappa_{\text{ex}}}{D} , \quad (3.3)$$

$$B = -i \cdot m \left( \frac{\kappa_{\text{ex}}}{D + i\Omega} + 1 \right) , \quad (3.4)$$

$$C = -i \cdot m \left( \frac{\kappa_{\text{ex}}}{D - i\Omega} + 1 \right) . \quad (3.5)$$

Here coefficients  $A$ ,  $B$  and  $C$  can be interpreted as field-transmission coefficients at the

pump frequency and at the frequencies of two sidebands appearing from the phase modulation. The resulting photocurrent  $I(\Omega, t) \propto |s_{\text{out}}(\Omega, t)|^2$  recorded with the photodiode and detected with the VNA can be estimated as:

$$I(\Omega, t) \propto s_{\text{in}}^2 |A^* B + AC^*| \cdot \cos(\arg(A^* B + AC^*)) , \quad (3.6)$$

which demonstrates the single-resonance response located at  $\Delta$  and  $\pi$  jump in the phase at the same frequency.

The position of soliton-attributed  $\mathcal{S}$ -resonance as well as more accurate description of the  $\mathcal{C}$ -resonance in the DKS state, however, should be implemented with the LLE equation, which it is convenient to use its dimensionless form (1.56). The approximate expressions for the positions of both peaks were derived analytically by M.L. Gorodetsky in the Supplementary information of [114].

Using the flat solution  $\Psi_c$  in the dimensionless LLE with pump phase modulation it was shown that the background modulation oscillates at dimensionless frequency  $\Omega_{\mathcal{C}}$  (normalized to  $\kappa/2$ ):

$$\Omega_{\mathcal{C}} = (\zeta_0 - |\Psi_c|^2)(\zeta_0 - 3|\Psi_c|^2) + 1 . \quad (3.7)$$

Since the background is small, and  $\zeta_0 \gg 1$ ,  $\Omega_{\mathcal{C}} \simeq \zeta_0$ , and thus the position of the  $\mathcal{C}$ -resonance coincides with the detuning  $\delta$  of the system.

In order to derive another response feature -  $\mathcal{S}$ -resonance, one can consider the pump phase modulation as an additional perturbation to LLE, and using Lagrangian density approach derive the modulation of the soliton parameters (in two- or three-parameter ansatz) as the function of  $\Omega$ . Thus, the soliton response is derived to be located close to (case of two-parameter ansatz):

$$\Omega_{\mathcal{S}}^2 = \pi f \sin(\phi_0) \sqrt{2\zeta_0} , \quad (3.8)$$

where  $\phi_0 = \sqrt{8\zeta_0/\pi f}$ .  $\Omega_{\mathcal{S}}$  is much weakly depends on detuning than  $\Omega_{\mathcal{C}}$  and is closer to zero, which is observed in experiment. It is interesting to note that for both resonances the width of the response corresponds to the cold-cavity resonance linewidth -  $\kappa$ .

## 3.4 Deterministic switching

We next investigate the transitions of soliton states obtained using the backward tuning scheme by applying the non-destructive soliton probing technique described in the previous section in  $\text{Si}_3\text{N}_4$  microresonators. We first employ forward tuning of the driving laser in order to generate a multiple-soliton state with  $N = 6$ , and subsequently perform a slow backward tuning. As before, the power trace of the generated light in the

### Chapter 3. Universal dynamics and deterministic switching of DKS states in optical microresonators

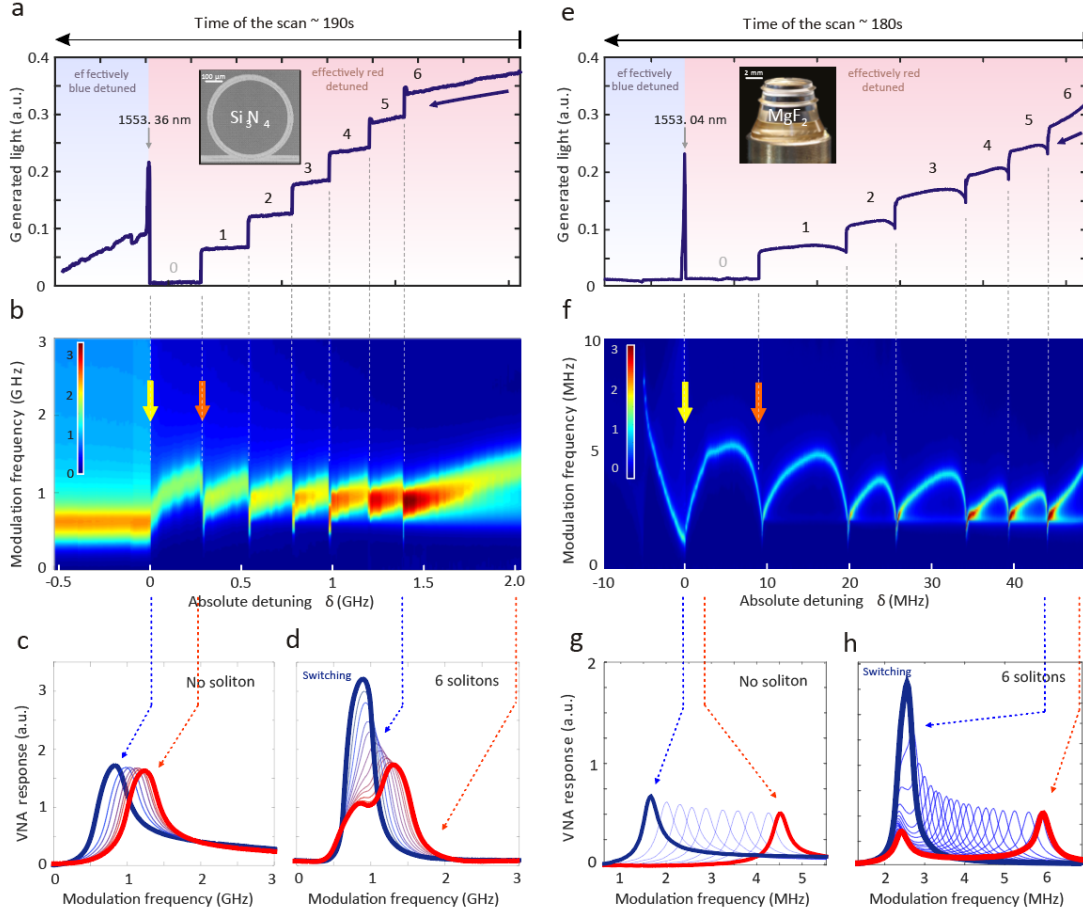


Figure 3.5 – (a) The power trace of the generated light obtained from 100-GHz  $\text{Si}_3\text{N}_4$  microresonator with the backward pump tuning from multiple-soliton with  $N = 6$  (effectively red detuned) to the effectively blue detuned regime; (b) Set of 500 concatenated VNA traces that were taken during the backward tuning shown in (a). The orange arrow indicates the transition from a single soliton state to no-soliton state, while the pump is still red detuned with respect to the cavity resonance. The yellow arrow indicates the transition from the red detuned operating regime to the blue detuned regime; (c) Evolution of the transfer function during the backward tuning process in the effectively-red-detuned regime, with no soliton presented ( $N = 0$ ); (d) Evolution of the transfer function in the multiple-soliton state with  $N = 6$ ; (e) The power trace of the generated light obtained from 14 GHz  $\text{MgF}_2$  crystalline resonator with the backward pump tuning from multiple-soliton state with  $N = 6$  (effectively-red-detuned) to the effectively blue detuned regime; (f) Set of  $\sim 1700$  concatenated VNA traces that were taken during the backward tuning shown in (e); (g) Evolution of the transfer function during backward tuning in the state with no soliton presented; (h) Evolution of modulation response in the multiple-soliton state with  $N = 6$ .

microresonator shows the staircase pattern in the backward tuning, which corresponds to successive soliton switching from  $N = 6$  to the single soliton state (Fig. 3.5(a)). The

traces of system transfer function measured with the VNA are simultaneously recorded and continuously stacked in order to monitor its evolution during the backward tuning process (see Fig. 3.5(b)).

The experiments reveal a strong correlation between the evolution of the transfer function and the soliton switching. Within each soliton step, the  $\mathcal{C}$ -resonance shifts towards the  $\mathcal{S}$ -resonance, which is interpreted as the decrease of the effective detuning when the laser is tuned backward. When the two resonances overlap, the amplitude of  $\mathcal{S}$ -resonance is significantly enhanced, leading to a high-intensity single-peak profile (Fig. 3.5(d)). After the peak merging, the soliton switching occurs, which results in a drop in the comb power as one soliton is lost ( $N \rightarrow N-1$ ). After the switching, the  $\mathcal{C}$ -resonance abruptly separates from the  $\mathcal{S}$ -resonance moving to higher frequencies. Simultaneously, while still being Kerr locked, the  $\mathcal{S}$ -resonance intensity is reduced to a lower level than in the previous state, since the number of solitons is reduced by one. In the absence of solitons ( $N = 0$ ), the  $\mathcal{S}$ -resonance is absent in the transfer function, but the  $\mathcal{C}$ -resonance is still present (Fig. 3.5(c)).

The same measurement was carried out in  $\text{MgF}_2$  resonators, see Fig. 3.5(e-h). While similar switching dynamics are observed, there are several details which differ between  $\text{Si}_3\text{N}_4$  and  $\text{MgF}_2$  platforms. First, the optical  $Q$ -factor of  $\text{MgF}_2$  crystalline resonators ( $\sim 10^9$ ) is three order of magnitude higher than for  $\text{Si}_3\text{N}_4$  microrings ( $\sim 10^6$ ). The  $\mathcal{C}$ - and  $\mathcal{S}$ -resonances in the transfer function of crystalline resonator are therefore better resolved as a result of the narrower resonance linewidth. The soliton existence range in  $\text{Si}_3\text{N}_4$  microresonators is typically  $\mathcal{O}(1 \text{ GHz})$ , while in  $\text{MgF}_2$  resonators it is  $\mathcal{O}(1 \text{ MHz})$ . Second, after each soliton switching the  $\text{MgF}_2$  resonator shows slower recoil of the  $\mathcal{C}$ -resonance than the  $\text{Si}_3\text{N}_4$  microresonator. This is attributed to the distinct thermal relaxation of the two platforms. The  $\text{MgF}_2$  resonator has larger effective mode volume and physical size than the chip-scale  $\text{Si}_3\text{N}_4$  microring resonators such that the thermal relaxation time is longer. This explains why in the evolution of the transfer function of the  $\text{MgF}_2$  resonator (Fig. 3.5(f)), the recoil of the  $\mathcal{C}$ -resonance leaves curved trajectory while it is very abrupt in the  $\text{Si}_3\text{N}_4$  microresonator (Fig. 3.5(b)).

The soliton probing scheme using the phase modulation, combined with the backward tuning, allows an understanding of the soliton switching dynamics in microresonators. The successive soliton switching in backward tuning is attributed to the thermal nonlinearity of optical microresonators and can be interpreted as follows. Due to material absorption, the intracavity energy thermally shifts the cavity resonance via thermal expansion and thermal change of the refractive index. The thermally-shifted pumped cavity resonance is therefore  $\tilde{\omega}_0 = \omega_0 - \Delta_T$ , where  $\omega_0$  is the angular frequency of the cold-cavity resonance and  $\Delta_T$  is the thermally-induced resonance shift which, in the soliton state with thermal equilibrium, is approximately proportional to the energy of the intracavity field:

$$\Delta_T(N) \propto E_{\mathcal{C}} + N \cdot E_{\mathcal{S}} , \quad (3.9)$$

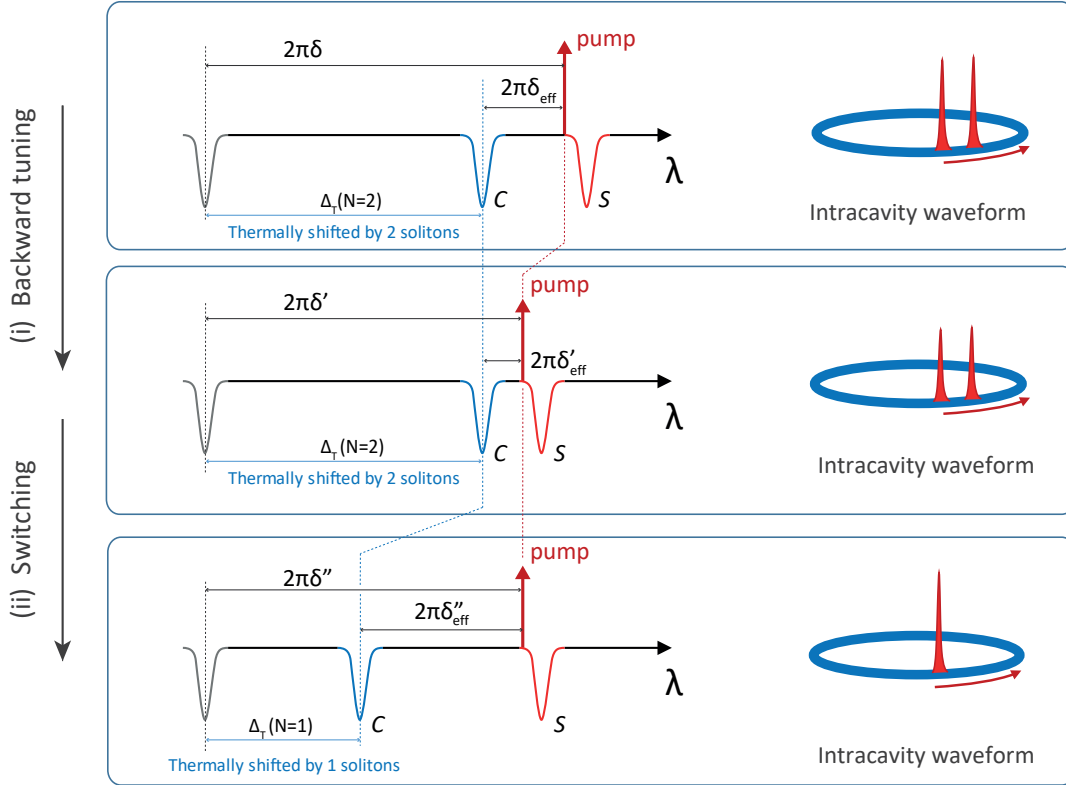


Figure 3.6 – Simplified schematics of the pump and resonance shifts in the backward tuning procedure involving single switching event. From top - to middle: (i) backward tuning - pump wavelength is reduced, which causes the reduction of the effective detuning from  $2\pi\delta_{\text{eff}}$  to  $2\pi\delta'_{\text{eff}}$ . Absolute detuning  $2\pi\delta$  from the cold cavity resonance is also decreasing to  $2\pi\delta'$ . Blue resonance indicates the position of the cavity resonance, thermally shifted by the presence of two solitons in the cavity. Red-colored Kerr-shifted soliton resonance follows the pump. Middle - bottom: (ii) switching - the pump frequency is fixed, the system loses one soliton and relaxes to a new thermally stable state, where the cavity resonance is now shifted by the presence of only a single pulse inside the cavity. This also increases effective detuning from  $2\pi\delta'_{\text{eff}}$  to  $2\pi\delta''_{\text{eff}}$ , but conserves the absolute detuning of the pump:  $2\pi\delta' = 2\pi\delta''$ .

where  $E_{\mathcal{C}}$  is the energy of the cw component,  $E_{\mathcal{S}}$  is the energy of one soliton pulse and  $N$  is the number of solitons. Thus, the effective detuning can be expressed as  $2\pi\delta_{\text{eff}} = 2\pi\delta - \Delta_T$ , where  $\delta$  indicates the absolute detuning  $2\pi\delta = \omega_0 - \omega_p$ . While in a simple LLE system without thermal effects, the soliton existence range is the same for different soliton numbers (i.e. degenerate with respect to  $N$ ), in the presence of thermal nonlinearity the DKS states with larger soliton numbers acquire additional shift proportional to  $N$ . When in the backward tuning process the system approaches lower boundary of the soliton existence range, which is approximately defined by the position of the  $\mathcal{S}$ -resonance, it maintains the same number of solitons, and therefore the thermal contribution from the soliton number is constant (here we consider that the thermal

### 3.5. Mapping of the soliton multistability in optical microresonators

effects caused by the change in the soliton power within the soliton existence range are negligible). After the  $\mathcal{C}$ -resonance overcomes the  $\mathcal{S}$ -resonance, the soliton switching occurs: one DKS pulse is lost and the thermally-induced resonance shift  $\Delta_T$  is reduced, which in turn increases the effective detuning of the pump, and the  $\mathcal{C}$ - and  $\mathcal{S}$ -resonances are separated again (see Fig. 3.5(b)). It is important to note, that each time a soliton is lost, the thermal shift  $\Delta_T$  is reduced and thus the effective detuning is increased leaving the system in the soliton existence range, which enables the stabilization of the new state. Therefore, this reopens the possibility of tuning the laser further backward (reducing  $\delta$ ), and deterministically reaching the single soliton state.

The process is schematically shown in Fig. 3.6, where two stages of the described process are shown schematically: (i) backward tuning stage in the 2-soliton DKS state, where the pump wavelengths is reduced until the detuning from cold-cavity resonance reaches  $2\pi\delta'$ , at which the switching occurs; (ii) the switching process, where the pump is fixed, the system losses one pulse and relaxes to the new thermal state, where  $\Delta_T$  is reduced by half.

### 3.5 Mapping of the soliton multistability in optical microresonators

The pump backward tuning enables deterministic and successive soliton switching, opening access to soliton states  $N, N - 1, \dots, 1$ . It is therefore possible to experimentally explore the soliton existence range in terms of the absolute and the effective detuning in each state (thus forming multi-stability diagram of the microresonator system [190, 97, 9]). In order to express the boundaries of the soliton existence range in terms of the effective detuning, we use  $\delta_s$  as low-detuning boundary and  $\delta_{\max}$  as high-detuning boundary:  $\delta_s < \delta_{\text{eff}} < \delta_{\max}$ . The lower boundary  $\delta_s$  is identified in the backward tuning through the soliton switching: it corresponds to the RF frequency in the VNA response trace, where the  $\mathcal{C}$ -resonance and the fixed  $\mathcal{S}$ -resonance overlap. In the studied  $\text{Si}_3\text{N}_4$  microresonator with the chosen fixed pumping conditions this quantity is measured to be  $\delta_s \sim 0.78$  GHz. The upper detuning boundary  $\delta_{\max}$  of the soliton existence range can be explored for each soliton state when the pump laser is tuned forward until the soliton state decays. Based on the theory (see eq. (1.61)) and LLE simulations this detuning is expected to be identical for all states with different soliton numbers at the same pump power [9], as the boundary of the energy balance of individual DKS. In experiment, the maximum effective detuning  $\delta_{\max}$  for all soliton states obtained at the same power is found to be  $\sim 2.0$  GHz. We note that unfortunately there is no clear feature in the measured transfer function, which would enable the prediction of the maximum boundary. Figure 3.7 displays a *one-trace* mapping of six steps of soliton states in  $\text{Si}_3\text{N}_4$  microresonator as a function of the absolute pump frequency (wavelength) (i.e. the absolute detuning  $\delta$ ). For each soliton step, we first tune the pump forward approaching the maximum

### Chapter 3. Universal dynamics and deterministic switching of DKS states in optical microresonators

---

detuning ( $\delta \rightarrow \delta_{\max}$ ), and subsequently tune backward towards the soliton switching point ( $\delta \rightarrow \delta_s$ ) where the soliton state is switched from  $N$  to  $N - 1$ . Since the thermally induced cavity resonance shift is included in the absolute frequency detuning, we observe that the soliton existence range in units of absolute laser detuning is increasingly offset for a larger number of soliton. This creates a staircase pattern of the generated light and enables successive soliton switching. However, if the generated light trace is plotted with respect to the *effective* laser detuning ( $\delta_{\text{eff}}$ ) as done in Fig. 3.7(b), all the soliton steps are stacked vertically within the range  $\delta_s < \delta_{\text{eff}} < \delta_{\max}$ , which corresponds to the expected theoretical degeneracy when the thermal effect is neglected [9].

In order to verify that deterministic soliton switching is enabled by the thermal nonlinearity of the microresonator, we performed numerical simulations based on coupled-mode equations with the additional thermal relaxation equation (see Fig. 3.7(c, d)). We use dimensionless coupled nonlinear mode equations (1.51), which were modified to take into account the thermal effects. For this purpose an additional equation for the normalized variation of temperature  $\Theta = \frac{1}{n} \frac{dn}{dT} \frac{2\omega_0}{\kappa} \delta T$  was solved simultaneously with conventional system. Throughout the simulations we neglected the frequency dependence of nonlinearity, losses and mode-overlap, interactions with other mode families, and any particularities of the resonator geometry. Thus, the modified set of coupled mode equations reads:

$$\begin{aligned} \frac{\partial a_\mu}{\partial \tau} &= -(1 + i\zeta_\mu(\tau) - i\Theta)a_\mu + i \sum_{\mu' \leq \mu''} (2 - \delta_{\mu'\mu''})a_{\mu'}a_{\mu''}a_{\mu'+\mu''-\mu}^* + \delta_{0\mu}f, \\ \frac{\partial \Theta}{\partial \tau} &= \frac{2}{\kappa\tau_T} \left( \frac{n_{2T}}{n_2} \sum |a_\mu|^2 - \Theta \right). \end{aligned} \quad (3.10)$$

Here  $\tau_T$  is the thermal relaxation time,  $n_T$  is the coefficient of thermal nonlinearity. For numerical analysis we consider the following parameters corresponding to  $\text{Si}_3\text{N}_4$  microresonator:  $\lambda = 1.553 \times 10^{-6}$  m,  $n_0 = 2.4$ ,  $n_2 = 2.4 \times 10^{-19}$  m<sup>2</sup>/W,  $V_0 = 10^{-15}$  m<sup>3</sup>,  $\kappa/2\pi = 3 \times 10^8$  Hz,  $D_2/2\pi = 2.5 \times 10^6$  Hz,  $D_3 = 0$ ,  $\eta = 0.36$ ,  $P = 2$  W. These parameters correspond to dimensionless force term  $f = 5.8$ . The ratio  $n_T/n_2 = 10$  was chosen to resemble experimental data,  $\tau_T$  was chosen reasonably short to perform the simulation during a reasonable time.

By including the thermal effects into numerical simulations, we are able to reproduce the staircase feature, corresponding to the successive reduction of the soliton number in the backward pump tuning (see red curve in Fig. 3.7(c, d)). Analytical power traces of soliton steps (black dashed lines) indicate soliton existence ranges for multiple-soliton states with different  $N$ . They reveal a displacement of the soliton existence range between different soliton states (qualitatively similar to the measurement in Fig. 3.7(a)) as a consequence of the thermal nonlinearity. When thermal effects in the simulations are ‘switched off’, soliton steps are well aligned and the soliton existence range is again

### 3.5. Mapping of the soliton multistability in optical microresonators

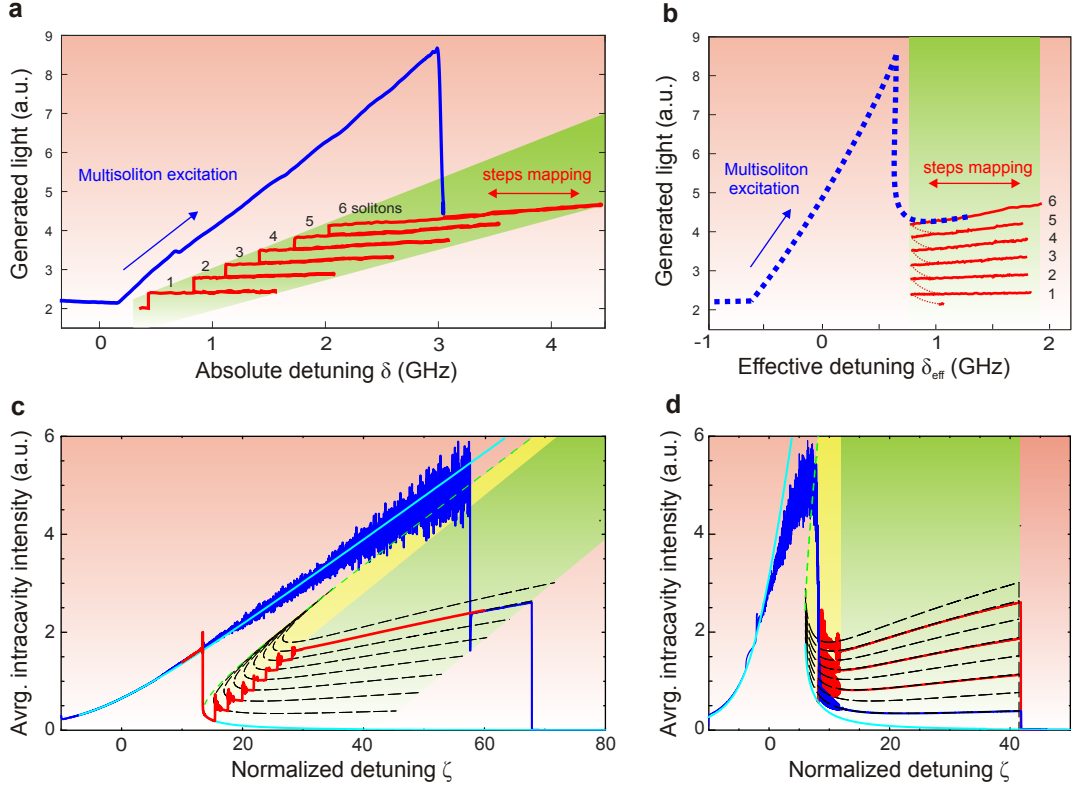


Figure 3.7 – (a) Experimental measurements of the generated comb light with respect to the absolute detuning. The blue curve shows the trace in the forward tuning. The red curve indicates the entire soliton existence range. Zero absolute detuning corresponds to  $\sim 1553.4\text{nm}$ . (b) Experimental trace from (a) plotted in terms of the effective detuning measured from the modulation response with the VNA. Hypothetical trace of forward tuning is shown in blue dashed line, because the effective detuning in this process can not be reliably measured with the VNA. (c, d) Numerical simulations and analytical solutions of the backward tuning in  $\text{Si}_3\text{N}_4$  with (c) and without (d) thermal effects. Normalized detuning used in the simulation:  $\zeta_0 = 2(\omega_0 - \omega_p)/\kappa$ , where  $\omega_0$  is the resonance frequency,  $\omega_p$  is the pump frequency and  $\kappa$  is the resonance linewidth. Blue lines indicate initial excitation of a multiple-soliton state in the forward tuning. Red lines indicate the backward tuning. Light blue lines indicate the stable branch of the nonlinear induced tilted resonance (in the CW mode). Dashed green lines indicate the unstable branch. The yellow area allows for the formation of breathing soliton states. The green area indicates the formation of stable solitons. Solitons cannot exist in red area. The dashed lines show analytical description of soliton steps, with analytical solution of soliton states in the system.

degenerate with respect to the soliton number ( $N$ ), see Fig. 3.7(d). No soliton switching is therefore observed in the backward tuning. These measurements and simulations clearly demonstrate the enabling role of the thermal effect in the deterministic switching process of the DKS states.

Numerical simulation also revealed the soliton breather states that are considered as an intermediate state between the chaotic MI regime and the stable soliton state. In the breather state, the soliton pulse peak power and the pulse duration, as well as the average intracavity energy, will experience periodical oscillations. This induces thermal perturbations to the cavity resonance and initiates the soliton switching. The breather states were indeed experimentally observed and identified, and will be presented in the next Chapter.

## 3.6 Conclusion

We demonstrate a novel platform-independent phenomenon of the DKS dynamics - switching, which enables a successive reduction of the soliton number in microresonators. We show that the process is enabled by thermal nonlinearity of the microresonator, which lifts the detuning degeneracy of the soliton states with different  $N$  and allows for deterministic and controllable access to any soliton state including application-relevant single soliton states via simple backward tuning approach. We also introduced non-destructive soliton probing scheme, which uses VNA to measure cavity transfer function of the microresonator system, between phase modulation on the pump and amplitude modulation on the system's transmitted power. We observed a unique double-resonance feature in the transfer function when the microresonator is in the state of DKS, which is induced by the nonlinear cavity bistability. This feature reveals the effective laser-resonance detuning, can be used to estimate the number of solitons and provides insights into the dynamics of the soliton switching.

The backward tuning procedure, which enabled deterministic access to single soliton states in a variety of  $\text{Si}_3\text{N}_4$  microresonators used in our group, has played a pivotal role for the first demonstrated applications of DKS states in optical coherent communications and ultrafast distance ranging (see Chapter 7), optical coherence tomography [110] and works of other groups [116, 191, 192, 81]. It also enabled the demonstration of octave-spanning soliton states [87], the generation of DKS at 1  $\mu\text{m}$  wavelength (Chapter 6) as well as played a major role in the exploration of soliton breathing states, which were performed in  $\text{Si}_3\text{N}_4$  microresonators (see Chapter 4 and work by Guo *et al.* [193]).

## 4 Soliton breathers in optical microresonators

This chapter reports on the experimental observation of dissipative Kerr soliton breathers in optical microresonators. The results are partially adapted from E. Lucas\*, M. Karpov\* *et al.*, "Breathing dissipative solitons in optical microresonators", *Nature Communications*, 8(1), p. 736, (2017).

### 4.1 Introduction

The CW-driven Kerr-nonlinear resonator system is able to support a rich variety of stable non-homogeneous intracavity field patterns, as reported both in numerical simulations [97, 194, 48, 98] and in experiments [57, 9, 91, 84], including bright dissipative Kerr solitons [9, 91, 84], dark pulses [57], platicons [195], Turing patterns [196] or soliton crystals [197].

While all of these states were initially reported to be stationary with respect to the rotating frame of reference (i.e. time-independent on the slow time axis, apart from the linear drift which may be caused by spectral recoil due to Raman, dispersive waves or AMX), some of them can exhibit a rich panel of nonstationary dynamics. In this Chapter we focus on one of the intrinsic dynamical phenomena of dissipative Kerr solitons, which leads to their non stationary behavior, – the formation of *breathing* soliton states (breathers). For the driven nonlinear resonator system the breathers represent stable soliton states, which intracavity pulses undergo periodic oscillations in their amplitude and duration as schematically shown in Fig. 4.1 [198, 42, 191, 199]. The period of such oscillations – breathing period (or breathing frequency in the frequency domain) – represents the time of a single cycle, after which the system returns to its initial state.

The formation of soliton breathers was widely studied in the context of the NLSE for conservative nonlinear systems, where space- and time-periodic soliton solutions –

---

\*These authors contributed equally to the work

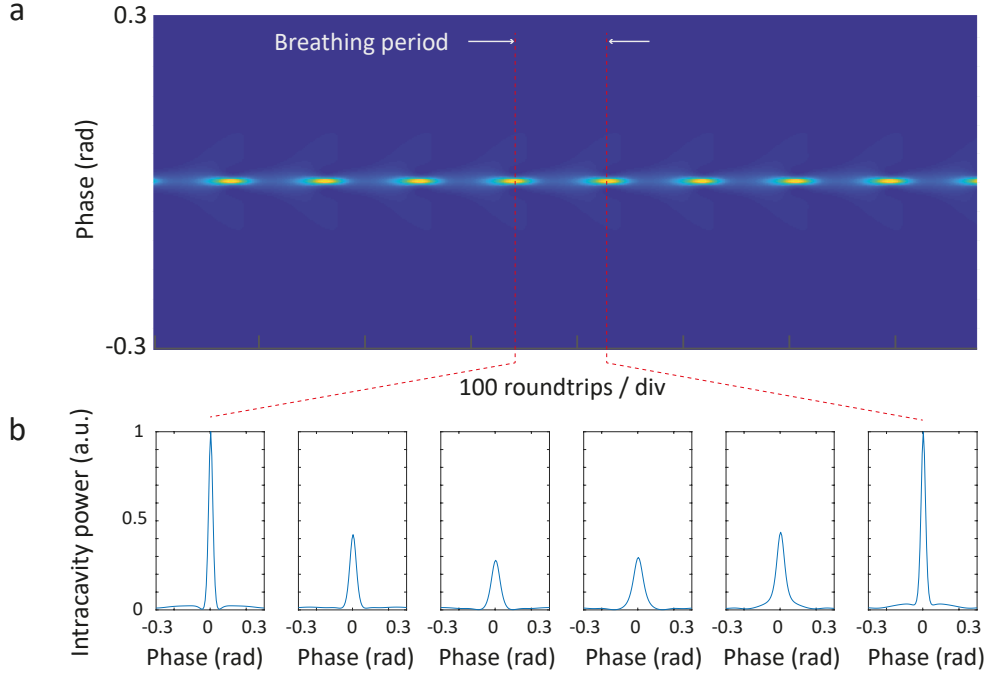


Figure 4.1 – (a) Simulated intracavity waveform evolution in the DKS breathing state; All parameters of the system are fixed, but the soliton experiences regular oscillations in its amplitude and duration during with a period of  $\sim 100$  roundtrips. (b) Snapshots of the intracavity waveform showing the periodic out-of-phase evolution of the amplitude and duration within one period of the breathing DKS state in (a).

Kuznetsov-Ma [200, 201] and Akhmediev breathers [202] were discovered. Their dynamics was shown to be linked to two fundamental phenomena of nonlinear systems - modulation instability[203] and the Fermi-Pasta-Ulam (FPU) recurrence [204] – a paradoxical evolution of nonlinearly coupled oscillators that periodically return to the initial state [205]. Soliton breathers with periodic oscillations in their duration and amplitude were observed in a number of real-world system including optical fibers [206] and water waves [207, 208]. The studies of these phenomena are strongly motivated in the context of the physics of extreme waves (rogue waves) [209, 210] as well as the general understanding of driven nonlinear systems and their nonstationary dynamics.

The formation of cavity breathers in the temporal LLE model used for dissipative Kerr solitons was first predicted in the work by Matsko *et al.* [198], where the basic stability properties and oscillatory behavior were shown in simulations. Later Leo *et al.* experimentally demonstrated the first breathers in optical fiber resonators [42] and studied breathing regions in the stability chart of the LLE. In contrast, the experimental observation of breathers in optical microresonators has posed a significant challenge. First, due to the non-trivial soliton generation process [9, 84] associated with the thermal

---

We note that the formation of breathers in damped driven NLSE equation without cavity-induced boundary conditions was also investigated earlier by Baraschenkov and Smirnov [97]

---

## 4.2. Experimental observation of breathers

nonlinearity that may impact the effective laser detuning [50, 114], and second, due to high repetition rates ( $> 10$  GHz) of the resulting soliton states which make direct time-resolved observations difficult.

Two groups before our work have reported the observation of soliton breathers in microresonators [191, 211]. They demonstrate an appearance of stable oscillations in the outcoupled soliton pulse trains as well as a periodic energy exchange between the central modes and the spectral wings of the DKS states. An attempt to characterize breather dynamics was also made, in which the oscillation frequency (breathing frequency) was shown to depend on the pump detuning, however the direct relation was not unambiguously determined [211]. Apart from this ambiguity a number of other open questions still remains unexplored. They include reliable access to the DKS breathers, detailed characterization of breathing dynamics and its regimes, as well as direct observation of the pulse evolution. Understanding the breathing regime in microresonators is not only of fundamental interest, but a necessity for applications. The accurate knowledge of the conditions for the existence of breathers allows the prevention of extreme events [212], ensuring the stable operation of DKS-based microresonator devices and avoiding excess noise induced by breathing [184].

In the following sections we demonstrate a deterministic route to access, indentify and characterize DKS breathers in two microresonator platforms - crystalline WGM  $\text{MgF}_2$  resonator and  $\text{Si}_3\text{N}_4$  integrated microrings. We also map the breathing regime in the stability chart of the LLE, and demonstrate a detailed study of the DKS breathing dynamics including the link between the breathing frequency and effective detuning. Finally we also demonstrate the direct time-resolved observation of the DKS breathers and their complex dynamics.

## 4.2 Experimental observation of breathers

### 4.2.1 Access and identification of soliton breathing states

We start with the discussion on how to access the DKS breathers in the CW-driven resonator. The theoretical investigation of the breathing states in fiber cavities and the stability chart of the CW-driven Kerr cavity system, explored in [42], infer that the formation of breathers can be observed at the low-detuning side of the stable soliton region. It turns out that the earlier discovered *backward tuning* approach shown in Chapter 3 can provide reliable access to this parameter space of the system. We also note that a similar approach was explored for the study of various spatiotemporal instabilities in fiber cavities [213].

Following the backward tuning procedure, a stationary multiple soliton state is first excited by sweeping the CW driving laser “forward“ (toward longer wavelengths) over the

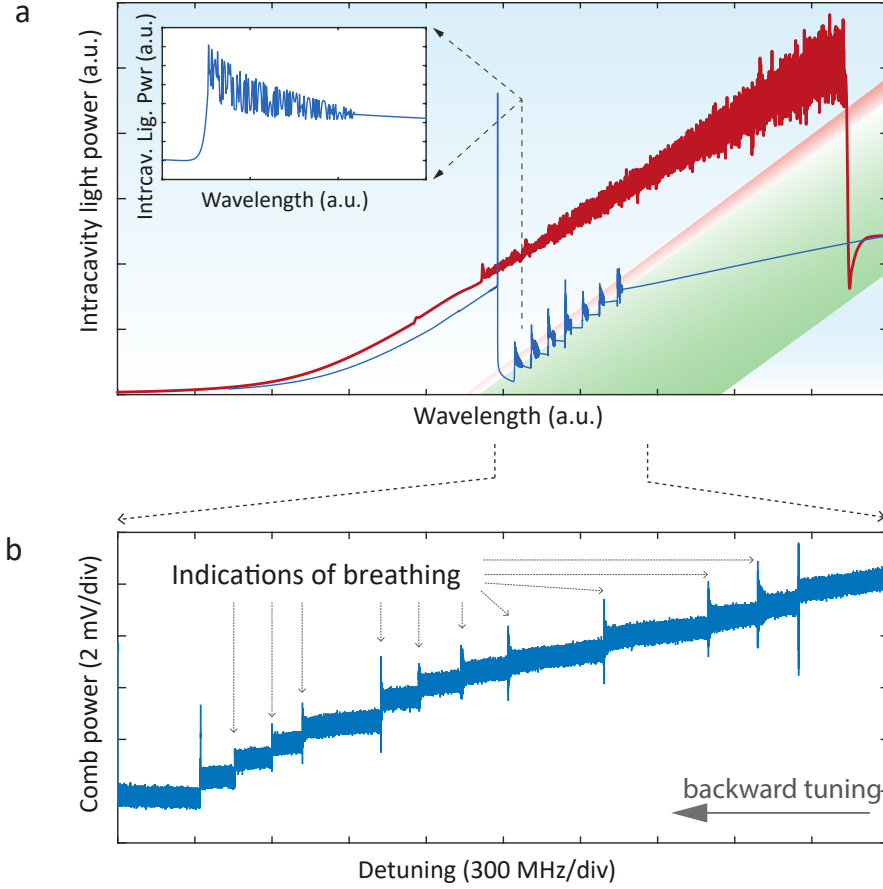


Figure 4.2 – (a) Simulation of the intracavity power, illustrating the backward tuning method used to trigger breathing. The generation of a stable multiple soliton state is achieved by forward tuning the pump laser (red curve). The backward tuning is applied next (blue curve) in order to reach the low-detuning boundary of the soliton existence range where the breathing regime (increased noise) and switching effect (step features) occur, allowing transition to the single-soliton state. The blue shading corresponds to the region where modulation instability occurs, the green marks stationary solitons existence and the red area indicates breathing. The inset details the single soliton breathing and switching during the backward tuning. (b) Experimental trace of the generated light power during the backward tuning process in the 100-GHz  $\text{Si}_3\text{N}_4$  microring resonator. The tuning is implemented from the right to the left, noise-like spikes before every switching event (step down) are attributed to the breathing behavior of the corresponding multiple-soliton state.

pumped resonance and stopping on the effectively red-detuned side, where solitons are sustained [9]. Second, the driving laser is tuned “backward” (toward shorter wavelength), thus reducing the effective detuning. Due to the microresonator thermal nonlinearity that lifts the fundamental degeneracy of multiple soliton states and enables switching to the DKS states with lower numbers of intracavity pulses, we can deterministically access the low-detuning boundary of the soliton existence ranges of soliton states with various

## 4.2. Experimental observation of breathers

numbers of intracavity pulses [114], and particularly focus on the single-soliton states.

Figure 4.2(a) shows a simulation (thermal effects are included) of this excitation scheme in the  $\text{Si}_3\text{N}_4$  microresonator. Forward and backward tuning stages are indicated with red and blue colors correspondingly. The system experiences a series of consecutive switchings, as reflected by the stair-like trace of the intracavity power. It was observed that the breathing regime is characterized by periodic oscillations in the intracavity power and occurs in the vicinity of the switching points in each step (see inset in the Fig. 4.2(a)).

We implement the same tuning procedure in experiment and apply backward tuning to a 100-GHz  $\text{Si}_3\text{N}_4$  microresonator from an initially excited multiple-soliton state. The backward tuning trace of the generated light was recorded with a fast photodiode, and we indeed detected the characteristic breathing features, which reveal themselves as noise-like spikes right before the switching events at the low-detuning boundary of the DKS states with various soliton number  $N$  (see Fig. 4.2(b)).

We focus on single DKS states ( $N = 1$ ) and closely investigate these breathing features in two microresonator platforms -  $\text{Si}_3\text{N}_4$  and  $\text{MgF}_2$  using the above-described procedure and generic setup for the DKS excitation shown in Fig. 4.3(a) (see Chapter 1). In both platforms, a single DKS state was first obtained using backward tuning and stabilized in the soliton existence range far from its boundaries. Then the pump frequency was slowly tuned backward with constant speed to reduce the pump-cavity effective detuning and move the system through the breathing regime until it experiences switching to a homogeneous state. Figures 4.3(c, d) show the results for this process in both platforms. One can observe that the onset of breathing regime coincides with an increase in the intensity noise of the generated light, which progressively increases as the system is tuned further in the breathing region. A detailed measurement with an increased sampling rate in the  $\text{MgF}_2$  microresonator shown in the inset of Fig. 4.3(d) reveals that in this region the generated light power experiences regular oscillations as predicted for soliton breathers. Despite these intrinsic power oscillations, the DKS breathing state is stable. As for the stationary DKS, the stability of the breathers is defined by the stability of the driving laser, chip input-output coupling and environment. Given that the effective detuning of the system does not experience dramatic fluctuations due to these external reasons, the pump tuning process can be stopped anywhere in the breathing region and the system will maintain its breathing state with no additional stabilization. The breathing is thus highly controllable and even reversible - one can repeatedly initiate and suppress the soliton breathing by changing the effective detuning of the DKS state. Such state stability is important, as it simplifies the study of the breathing dynamics which will be implemented in the following sections.

The oscillatory nature of the system in the breathing state can also be characterized by measuring the radio frequency (RF) spectrum of the out-coupled pulse train. Since

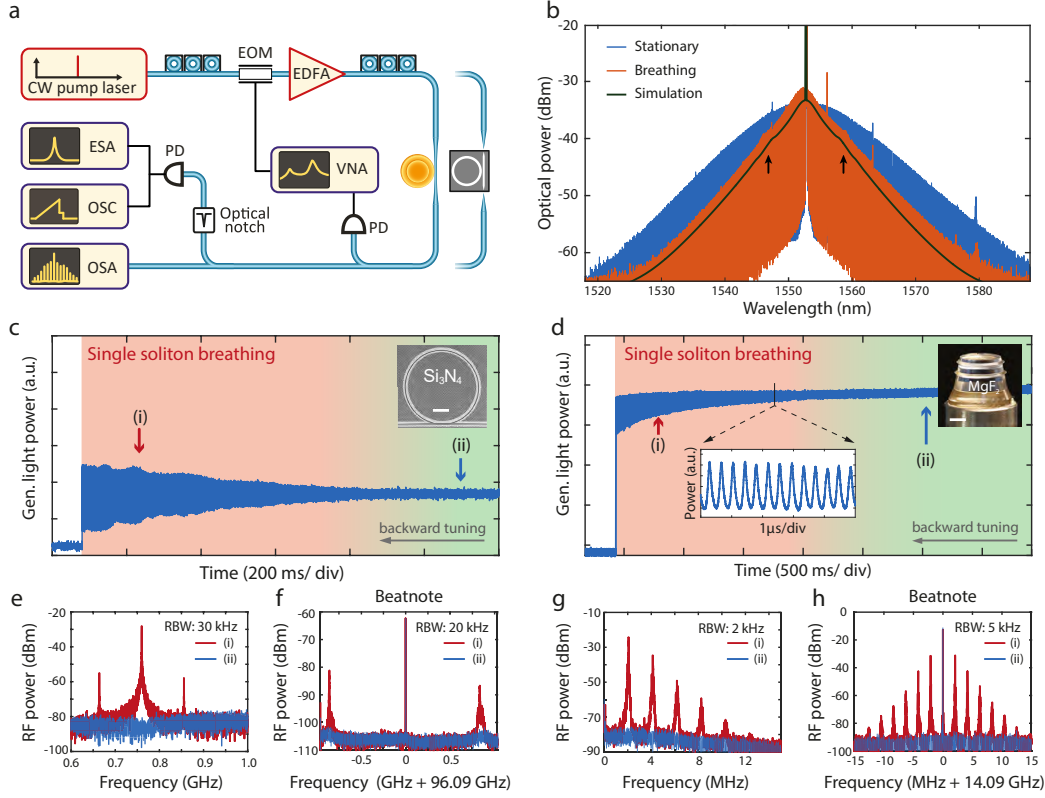


Figure 4.3 – (a) A similar experimental setup is used for both platforms: A tunable continuous wave laser is used as a pump source. EDFA, erbium-doped fiber amplifier; EOM, electro-optical phase modulator; OSA, optical spectrum analyzer; PD, photodiode; OSC, oscilloscope; ESA, electronic spectrum analyzer; VNA, vector network analyzer. (b) Experimental optical spectra of a stationary (blue) and breathing soliton states (red), in the 14 GHz FSR  $\text{MgF}_2$  crystalline resonator. The effective detuning  $\delta$  is varied by 0.5 MHz between the two states. The simulated optical spectrum averaged over one breathing period (black line) was offset by 3 dB for better visibility. The arrows mark the positions of weak sidebands visible in both the simulated and measured spectra. (c) Generated-light power evolution for a single soliton state in the 100 GHz  $\text{Si}_3\text{N}_4$  microresonator as the pump is tuned backward, showing the transition from stationary state (green shading) to breathing (red shading) and final decay. The inset shows an SEM image of the microresonator used (the scale bar corresponds to 100  $\mu\text{m}$ ). (d) In the  $\text{MgF}_2$  crystalline resonator (see inset, the scale bar corresponds to 2 mm), the comb light evolution features a similar behavior as in (c), when tuning backward. The inset shows the oscillations of the generated comb power, resolved with a fast photodiode and high sampling rate. (e, f) RF spectra of the generated light for a breathing (point (i) in (c, d), red trace) and stationary (point (ii) in (c, d), blue trace) soliton state respectively in the  $\text{Si}_3\text{N}_4$  and  $\text{MgF}_2$  resonators. In (f), the 0.4 GHz span is centred at 0.8 GHz, close to the fundamental breathing frequency. The resolution bandwidth (RBW) is indicated. (g, h) Repetition rate beatnote for a breathing (i, red) and stationary (ii, blue) soliton state in the  $\text{Si}_3\text{N}_4$  and  $\text{MgF}_2$  resonators.

the total power oscillations are stable and close to sinusoidal for moderate breathing amplitudes, the corresponding RF tones can be detected. In order to demonstrate this we recorded RF spectra of the DKS breathing state for stationary and breathing DKS in both platforms. Figures 4.3(e, g) show the low frequency RF spectra at points marked in Fig. 4.3(c, d). The stationary soliton state (blue traces) corresponds to a low-noise state of the system in both plots, while the breathing state (red traces) reveals sharp peaks indicating the fundamental breathing frequency. For our systems, the breathing frequencies were in the range of 0.5–1 GHz for  $\text{Si}_3\text{N}_4$  microresonators (FSR  $\sim 100$  GHz) and 1–4 MHz for  $\text{MgF}_2$  platform (FSR  $\sim 14$  GHz). The breather regime can also be evidenced when measuring the repetition rate beatnote. The oscillating pulse dynamics gives rise to additional sidebands around the repetition rate, spaced by the breathing frequency (see Fig. 4.3(f, h) which also compare stationary and breathing states).

Another characteristic signature of the breathing state is observed in the optical spectrum. Figure 4.3(b) shows the measured spectra of both stationary and breathing single soliton based frequency combs, in a  $\text{MgF}_2$  resonator. In the stationary state, the spectrum has a squared hyperbolic secant envelope corresponding to the stationary soliton solution, while in the breathing state, the spectrum features a triangular envelope (on a logarithmic scale), resulting from the averaging of the oscillating comb bandwidth, by the optical spectrum analyzer. The simulated spectrum (averaged over one breathing period) reproduces well the triangular feature. The weak sidebands on the optical spectrum are also captured on both measured spectrum and averaged simulated spectrum (marked by arrows in Fig. 4.3(b)).

We experimentally verified the presence of all above-described features for the breathing states in  $\text{Si}_3\text{N}_4$  and  $\text{MgF}_2$  resonators, where breathing single solitons were generated using the backward tuning method. Despite significant differences in the resonators properties ( $Q$  factor, FSR, dispersion profile and nonlinearity), both systems behave qualitatively similarly when approaching and entering the breathing regime.

### 4.2.2 Breathing dynamics

Having established a deterministic access to breathing DKS and their characteristic features, we next characterize the breathing dynamics. For this purpose we use a VNA response measurements described in Chapter 3, which is able to determine the effective laser detuning of the driven nonlinear system [114, 189]. We remind the reader that in the stationary soliton state, the VNA response of the system to the weak phase modulation exhibits two characteristic resonances which reflect the bistable nature of the intracavity field. The first one ( $\mathcal{C}$ -resonance) corresponds to the background Kerr-shifted cavity resonance and indicates the effective pump laser detuning  $\delta$  with good approximation. The second one ( $\mathcal{S}$ -resonance) corresponds to a resonant response of the soliton to the pump modulation. It emerges at lower frequency, and is weakly dependent on the pump

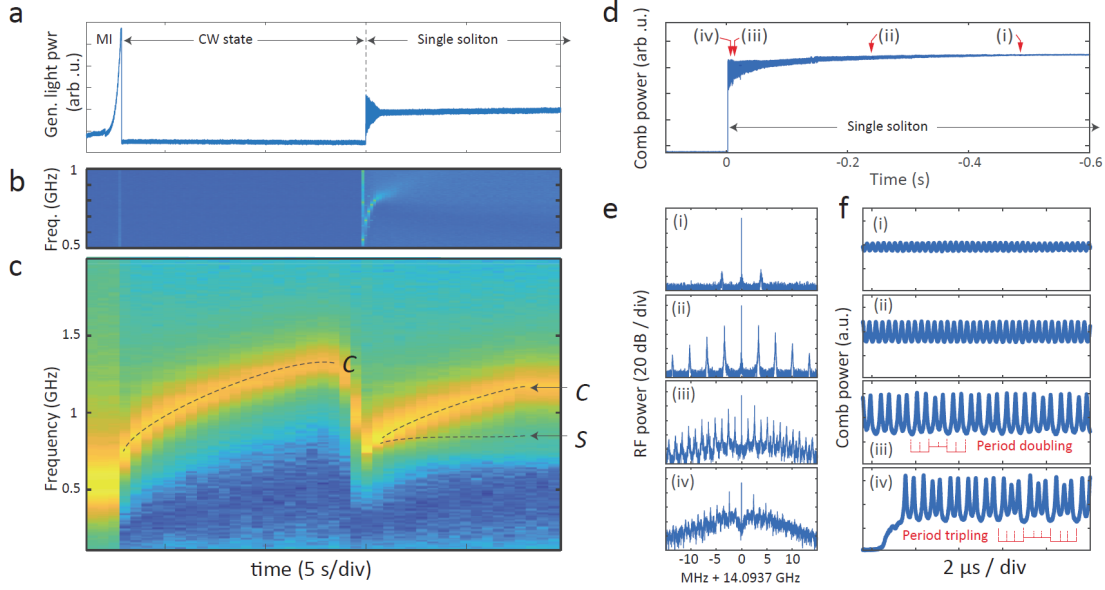


Figure 4.4 – (a) Generated light power evolution of a single-soliton state in a 100-GHz  $\text{Si}_3\text{N}_4$  microresonator as the pump is tuned backward from the stable DKS state to MI through the breathing DKS and homogeneous state. (b) Map of concatenated RF spectrum traces of the soliton pulse train power during the tuning process shown in (a). (c) Map of concatenated VNA traces showing the evolution of the system response (log scale) from stationary soliton on the right of the time axis to the MI state on the left. As the laser is tuned towards shorter wavelength, the effective detuning ( $\mathcal{C}$ -resonance) is reduced. The breathing starts typically when the separation of the  $\mathcal{C}$ - and  $\mathcal{S}$ -resonances is on the order of the resonator linewidth. (d) Generated light power evolution of a single-soliton state in the  $\text{MgF}_2$  microresonator as the pump is tuned backward from a stable DKS state to the homogeneous state through the breathing and switching event. (i)-(iv) mark different points of the trace, where the system dynamics was closely investigated using a fast photodiode in terms of the repetition rate beatnote and time-domain envelope of the total power. (e) RF spectra of the repetition rate beatnote in the various breathing stages (i)-(iv) highlighted in (d) (resolution bandwidth 2 kHz). (f) Recording of generated light power oscillations at the points (i)-(iv) highlighted in (d).

laser detuning.

In order to study the breathing dynamics we again used the same backward tuning of the pump frequency in order to sweep through the breathing region and simultaneously record the evolution of the DKS parameters. Figures 4.4(a - c) show the described DKS tuning from a stationary single soliton state to an MI state via the breathing region and homogeneous state in a 100 GHz  $\text{Si}_3\text{N}_4$  microresonator with the pump power of about 1.6 W (operating power of EDFA). During the scan, the system's transfer function is monitored simultaneously with the low-frequency part (0.5 - 1 GHz) of the total output power RF spectrum. As the laser detuning is reduced, the  $\mathcal{C}$ -resonance progressively shifts to lower frequencies (see Fig. 4.4(c)). The transition from a stationary to breathing

## 4.2. Experimental observation of breathers

soliton occurs when the  $\mathcal{C}$ - and  $\mathcal{S}$ -resonance separation is on the order of the linewidth ( $\kappa/2\pi$ ), for a detuning  $\delta \sim 900$  MHz. In the breathing region the DKS state starts to develop periodic oscillations at the breathing frequency, which are detected in the RF spectrum of the total power. Due to limited oscilloscope resolution and weak generated light power, these oscillations can be clearly recognized in the generated light signal only when the breathing acquires a significant amplitude. By comparing Fig. 4.4(a) and (c) we can see that a strong and narrow tone appears in the RF spectrum, indicating the breathing frequency, and shifts progressively closer to smaller frequencies when the detuning is reduced. At the same time, the amplitude of the breathing grows significantly when approaching the switching point, but maintains the average generated light power.

In the breathing state, the VNA response measurement features a strong peak at the breathing frequency, but the precise dynamics of different resonances can hardly be understood from given  $\text{Si}_3\text{N}_4$  samples due to their relatively low  $Q$ -factors leading to broad response resonances, which interleave and mask each other. Instead, we investigated the breathing dynamics in the  $\text{MgF}_2$  platform, where the high  $Q$ -factors allow the precise dynamics of the transfer function to be tracked up to the switching together with the breathing frequency tone [185]. The second advantage of this platform is the low breathing frequencies, which lie within MHz range, allowing for an easy detection and time-domain characterization of the oscillating soliton pulse trains.

First, we studied the time-domain breathing dynamics of the outcoupled DKS pulse train in different parts of the breathing region and the breathing imprinted on the repetition rate beatnote 4.4(d-f). The comb power was measured in two ways. First, the global evolution is monitored continuously on a DC coupled photodiode with a slow sampling of  $\sim 100$  kSa/s (Fig. 4.4(d)). Since the breathing oscillations are faster than this sampling rate, they appear as increased amplitude noise in this measurement. Second, the fast dynamics resolving the intracavity soliton is also recorded on a real-time oscilloscope with 120 GSa/s, but in short sequences spread over the scan. The breathing pattern in each sequence is then recovered by detecting the envelope of the resolved “pulse train”, down sampled and shown in Fig. 4.4(f). The breathing starts with a weak oscillation of the soliton pulse train power (stage i,  $\delta \sim 4$  MHz). This corresponds to a single pair of weak sidebands on the comb beatnote. For smaller detuning, the breathing becomes stronger, so that the first sidebands (fundamental breathing frequency) increase, and breathing harmonics emerge (stage ii) as the breathing pattern is not sinusoidal. At  $\delta \sim 3.3$  MHz (stage iii) the system exhibits a *period doubling*, which corresponds to the appearance of sub-sidebands located at half the initial breathing frequency. At last, the breathing turns into strong and irregular oscillations (stage iv,  $\delta \sim 2.9$  MHz), exhibiting sporadic transitions to period tripling. This coincides with a large increase in the noise pedestal around the beatnote, although the fundamental breathing frequency remains distinguishable. Finally, the soliton decays quickly thereafter. Such transitions to higher periodicity, the appearance of temporal chaos and the collapse match the predicted evolution from numerical studies of the LLE [42, 194].

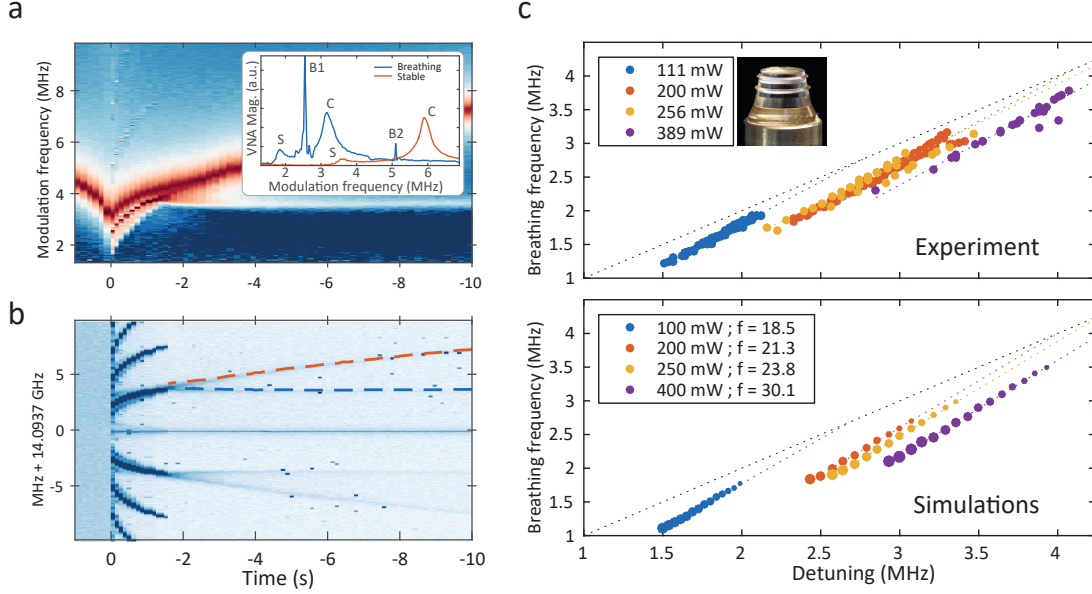


Figure 4.5 – (a) Map of concatenated VNA traces showing the evolution of the system response (log scale) in the  $\text{MgF}_2$  microresonator from stationary soliton on the right of the time axis to the homogeneous state on the left (the time origin  $t = 0$  s, is set at the soliton decay). As the laser is tuned towards shorter wavelength, the effective detuning ( $\mathcal{C}$ -resonance) is reduced. Inset demonstrates a comparison between the VNA response in the stable state (red) and in the breathing state (blue). The VNA response in the breathing state serves to clearly distinguish the effective detuning (corresponding resonance is marked with letter  $C$ ), breathing frequency - B1 and its harmonic - B2. (b) Map of concatenated RF beatnote spectra during the system evolution described in (a). The modulation response measured on the VNA is also visible in the noise of the RF beatnote spectrum (the dotted lines correspond to the  $\mathcal{C}$ - and  $\mathcal{S}$ - frequencies determined on the VNA). The breathing is indicated by the formation of sidebands around the repetition rate beatnote. As the detuning is reduced, the breathing frequency decreases until the soliton is lost. (c) Top: experimental determination of the breathing frequency evolution with the detuning for different pump powers, retrieved by the VNA response measurement. Bottom: simulated evolution of the breathing frequency using the LLE

Another feature which can be directly studied in the  $\text{MgF}_2$  platform is the link between the effective detuning of the DKS state and the breathing frequency. Comparing the position of the  $\mathcal{C}$ -resonance in the VNA response to the breathing tone shown in Fig. 4.4(b, c) one can indeed observe the relation in their frequency and behavior in  $\text{Si}_3\text{N}_4$  microresonators. Similar measurements implemented in the  $\text{MgF}_2$  platform are shown in Fig. 4.5(a, b). Using the set of VNA measurements implemented during the slow backward tuning through the breathing region we can identify the relation between the breathing frequency and effective detuning of the soliton breathing state measured as the position of the  $\mathcal{C}$ -resonance. The relation was found to be linear with the proportionality parameter close

to 1.2, and was similar for different pump powers of the system as shown in Fig. 4.5(c). We also performed LLE-based numerical simulations and obtained an almost identical result matching both qualitatively and quantitatively. We furthermore note that this surprising linear dependency between the breathing frequency and effective detuning of the system is also suggested by the approximate analytical breather expression derived in the next section.

### 4.2.3 Approximate breather ansatz

In order to analytically inspect the relation of the breathing regime parameters to the pump power and the effective detuning, an approximate breather solution for the dimensionless LLE (see eq. (1.56)) was developed within the present work by M.L. Gorodetsky. We recall that an approximate *stationary* solution of the LLE for positive dimensionless detuning  $\zeta_0$  may be found as a sum of the soliton and a background:  $\Psi(\theta) \approx \Psi_C + \Psi_S(\theta)e^{i\phi_0}$ , where  $\Psi(\theta)$  is the intracavity waveform,  $\theta = \phi\sqrt{\frac{1}{2d_2}}$  is the dimensionless longitudinal coordinate,  $\phi$  is the co-rotating angular coordinate of the resonator and  $d_2 = D_2/\kappa$  is the dimensionless dispersion.  $\Psi_C \approx -if/\zeta_0$  represents the constant background solution of (1.56), while  $\Psi_S = B \operatorname{sech}(B\theta)$  is the exact stationary conservative soliton solution of (1.56) without loss or drive, with  $B = \sqrt{2\zeta_0}$ . The phase  $\phi_0$  may be found by perturbation methods from  $\cos \phi_0 = 2B/\pi f$  [214].

The exact Kuznetsov-Ma breather solution [200, 201] of eq. (1.56) without loss and pump can be employed to derive an approximate ansatz for dissipative breathing solitons in the driven cavity:

$$\begin{aligned} \Psi_S(\theta, \tau) &= \left( \frac{K_1 \cos \Omega\tau + iK_2 \sin \Omega\tau}{\cosh B\theta - K_3 \cos \Omega\tau} - \epsilon \right) e^{iK_4\tau}, \\ \Omega &= \frac{B}{2} \sqrt{B^2 + 4\epsilon^2}, \\ K_1 &= \frac{B^2}{\sqrt{B^2 + 4\epsilon^2}}, \quad K_2 = B, \\ K_3 &= \frac{2\epsilon}{\sqrt{B^2 + 4\epsilon^2}}, \quad K_4 = \epsilon^2 - \zeta_0. \end{aligned} \tag{4.1}$$

If the time-dependent part of the background  $\epsilon$  is small, then leaving only terms up to the first order on  $\epsilon \rightarrow 0$  we arrive at:

$$\Psi_S(\theta, \tau) = B \operatorname{sech}(B\theta) + 2\epsilon \cos(\zeta_0 t) \operatorname{sech}^2(B\theta) - \epsilon e^{-i\zeta_0 t}. \tag{4.2}$$

We notice, that for  $\epsilon = 0$  this breather converges to a simple stationary soliton, and for small  $\epsilon$  the oscillation frequency of both the background and soliton itself simply coincides with the dimensionless laser detuning  $\zeta_0$ .

Thus, the analytical breather ansatz confirms the direct relation of the breathing frequency

to the detuning observed in experiment and further allows us to conclude the presence of true dissipative breathers in our system.

### 4.3 Breathing region

So far we have investigated the formation of breathing states at a fixed pump power, and observed their formation when approaching the lower-detuning boundary of the soliton existence range as suggested by the simulations [42]. However, it should be noted, that the breathing region of the DKS states also scales with power and, in general, should occupy the whole low-detuning boundary of the stable DKS region in the two-parameter space (pump power  $P_{\text{in}}$  and effective detuning  $\delta$ ) of the CW-pumped microresonator system [48, 41, 215].

It is thus interesting to experimentally map the breathing regime and compare it with the simulations of the stability chart of our systems. For this purpose we use the  $\text{Si}_3\text{N}_4$  microresonator platform and generate a single soliton state using the backward tuning method at different pump powers. After this, we gradually tune these states across the breathing region until their decay, while probing the system with the VNA technique.

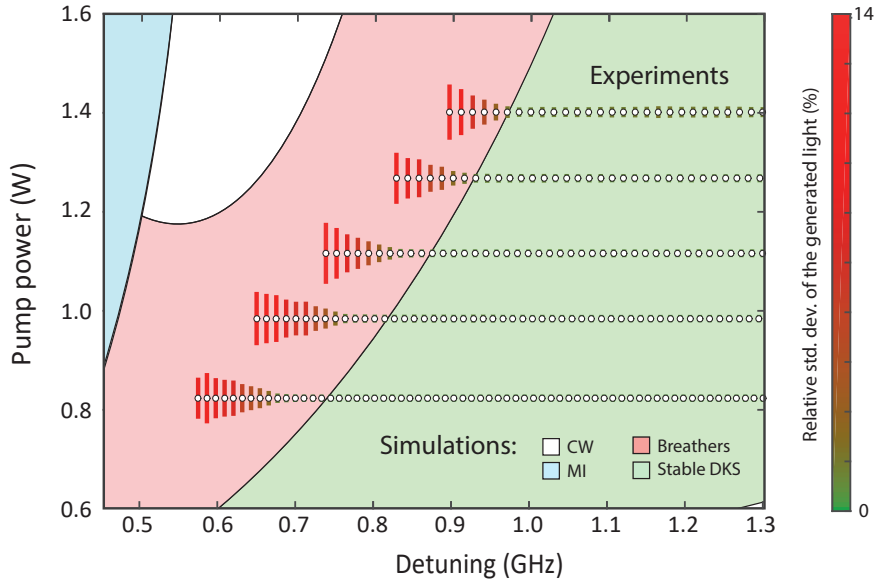


Figure 4.6 – Stability chart of the CW-pumped  $\text{Si}_3\text{N}_4$  microresonator in pump power over effective detuning coordinates. White filled circles indicate experimentally accessed DKS states. The colour-coded vertical lines indicate the measured relative standard deviation of the generated light power. The coloured background regions and boundaries are interpolated from simulation results and correspond to: CW-state (white) – the soliton decays to the homogeneous background, chaotic modulation instability (blue), stationary DKS state (green) and breathing DKS state (red).

This allows tracking the evolution of the effective detuning for the precise mapping of experimentally obtained DKS states on the stability chart. The white circles in Fig. 4.6 mark the operation points  $(P_{\text{in}}, \delta)$  accessed experimentally. The color-coded vertical line around each circle indicates the relative standard deviation of the output power measured at the corresponding point, which directly relates to the breathing amplitude. The results reveal a pump power dependency of the breathing region, whose location shifts towards higher effective detunings and range reduces with increasing pump power.

We compare experimental mapping of the breathing region to LLE-based simulations of the stability chart of our 100-GHz  $\text{Si}_3\text{N}_4$  microresonator. The simulations of the soliton comb dynamics was performed on 512 modes. Using the hard excitation scheme, stationary DKS were seeded at fixed input powers and large detunings. Then the laser detuning was reduced step by step to map over the stability chart. In each step, the intracavity field pattern is characterized after  $\sim 5000$  roundtrips to exclude early-stage transient formations. Depending on the dynamics of the intracavity field, different regions of the stability chart were classified in the following color-coded regimes on the Fig. 4.6: CW state (white color), where the soliton decays to the homogeneous background; chaotic modulation instability (blue); stationary soliton state (green) and breathing soliton state (red). The experimentally accessed stationary and breathing states are well within the corresponding regions predicted by the simulations. The mismatch between experimental results and simulations for the low-detuning boundary can be attributed to the discrepancy between the measured and real detuning values that may differ at the low-detuning boundary due to the higher background [114]. Also, highly unstable and short-living breathers just before the switching point make the detuning hard to resolve. Finally, high-order dispersion and nonlinear effects (e.g. Raman scattering, avoided mode crossings and third order dispersion) were not-included for simplicity in the simulations, but are present in the real microresonator system.

#### 4.4 Real-time observation of breathers

The results of the previous sections allow us deterministic access to the breathing states and suggest several ways to identify their presence. However, all of these ways of the breathing detection do not allow us to trace individual pulses and track their dynamics, which would unambiguously confirm the periodic soliton evolution during the propagation inside the cavity.

Due to high repetition rates of the outcoupled pulse trains in the DKS state, the direct measurement of the soliton pulses, which is widely used in experiments in fiber cavities [42, 41], is limited by the photodiode bandwidth and the resolution capabilities of oscilloscopes. Even a single DKS generated in a 100-GHz  $\text{Si}_3\text{N}_4$  microresonators can hardly be directly detected with the means available in the laboratory. On the other hand, the dynamics of the DKS states with 14 GHz soliton generated in the  $\text{MgF}_2$

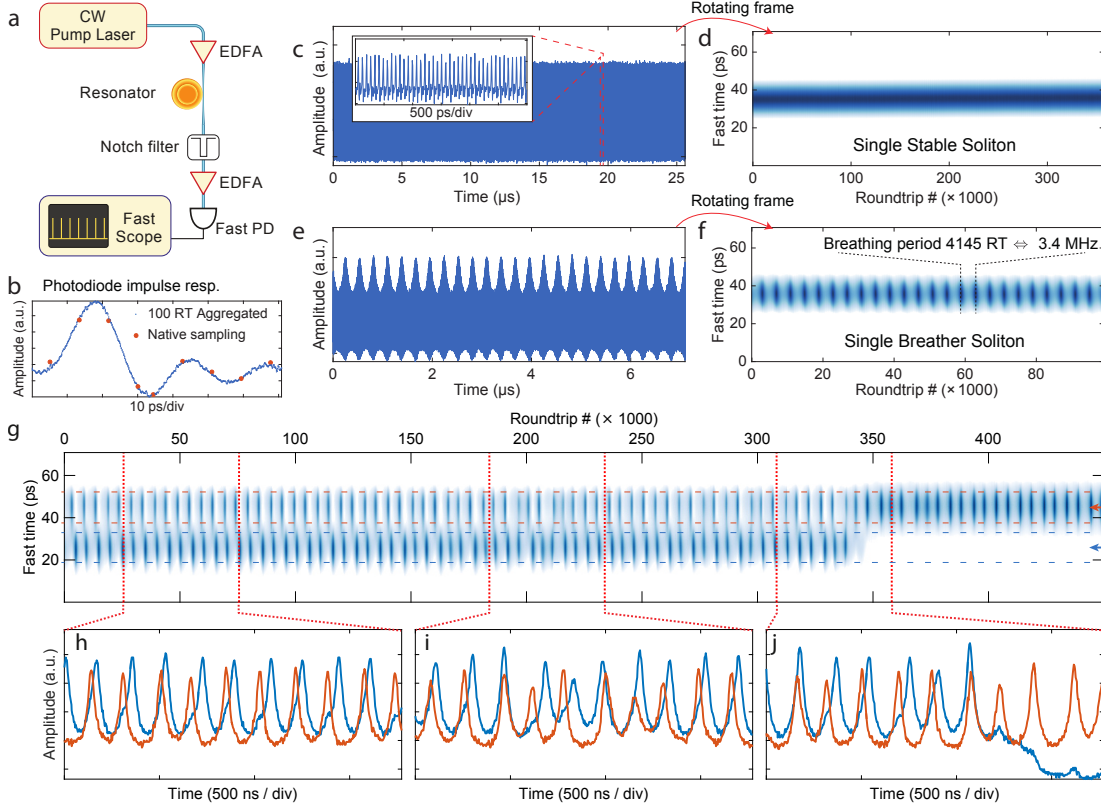


Figure 4.7 – (a) Experimental setup. Erbium doped fiber amplifier (EDFA) ; Photodiode (PD). (b) Photodiode response. The red dots mark the original sampling over a single roundtrip period (RT). With 9 points per period, the pulse amplitude cannot be accurately resolved. This problem is solved by aggregating 100 roundtrips to increase the effective sampling rate and retrieve the impulse response to a single soliton. (c) Single soliton pulse train, containing  $3.5 \times 10^5$  roundtrips. The inset shown a short section of the trace, where individual pulses can be coarsely located. (d) Dividing the trace into groups of 100 aggregated roundtrips, and stacking reveals the spatiotemporal evolution of the soliton. The soliton position and amplitude is fixed as the soliton is stable. In this map, the colourmap is set to remove the ripples of the photodiode response. (e) Single breathing soliton pulse train. (f) Applying the same procedure as in (d) reveals the oscillating pulse amplitude while its position remains stable. (g) Spatiotemporal evolution of a breathing two-soliton state undergoing a transition to a breathing single-soliton state (switching). The panels h-j show the evolution of the amplitude of each soliton. (h) Traces showing a  $\pi/2$  phase difference between the breathing oscillations of the solitons. (i) Unstable breathing, after which the quadrature relation is restored. (j) Collapse of one soliton, while the other survives and remains in the breathing region.

resonator can still be sparsely sampled with available equipment.

For the direct real-time detection of the soliton dynamics, the portion of the generated light of the outcoupled pulse train is amplified and detected on a fast photodiode (70 GHz bandwidth) connected to a real-time oscilloscope with a 45 GHz analogue bandwidth (sampling rate 120 GSa/s) as shown in Fig. 4.7(a). This configuration allows for the measurement of  $\sim 9$  samples per roundtrip and enables a coarse localization of the soliton pulse within one roundtrip (see Fig. 4.7 (b, c)). Since we observe that the soliton breathing dynamics evolve over a large number of roundtrips ( $> 1000$ ), we aggregate together the samples contained in segments of 100 roundtrips, to achieve an effectively larger sampling rate. Such averaging over the slow time axis produces smoother traces, revealing the impulse response of the acquisition system (matching with the photodiode response), where the instantaneous soliton peak amplitude can be reliably retrieved (Fig. 4.7(b)). Longer traces (Fig. 4.7(c, e)) that measure the evolution over a large number of roundtrips are divided in 100-roundtrips segments, which are aggregated and stacked. This facilitates the visualisation of a spatiotemporal evolution of the cavity content over a large number of roundtrips.

We first benchmarked our measurement procedure in the single soliton state. As expected, at a pump power of 230 mW and for the effective laser detuning  $\sim 10$  MHz the soliton is stationary with a constant amplitude (see Fig. 4.7(d)). For a smaller detuning  $\sim 3.5$  MHz, the soliton is breathing and the time trace reveals the oscillatory envelope of the soliton amplitude (Fig. 4.7(e)). In the spatiotemporal frame, this leaves a dotted pattern at the breathing period (see Fig. 4.7(f)), where the blue shading indicates the soliton amplitude. The breathing frequency is  $\sim 3.4$  MHz corresponding to 4145 roundtrips.

The fast recording on the real-time oscilloscope also enables us to delineate the breathing dynamics of individual pulses in a multiple soliton state. Figure 4.7(g) shows the evolution of a breathing two-soliton state during a backward tuning around  $\delta \sim 2.1$  MHz. The state experiences a switching [114] where one soliton decays and the other survives. Furthermore, in this small detuning condition, the breathing is typically irregular and might be locally identified as period doubling or tripling, as reflected on the traces (Fig. 4.7(g-j)). The measurement reveals that the two solitons breathe overall at the same frequency but are not in phase. In the present case, there seems to exist a preferred phase relation of  $\sim \pi/2$ . Even if the breathing is irregular and the phase relation can be locally altered as shown in Fig. 4.7(i), the relative phases seem to quickly recover this relation. Such behavior has been predicted by Turaev *et al.* [216], showing that the longer interaction length of breathing solitons can lead them to form bound states with a specific inter-distance and breathing phase relation. A quadrature breathing should correspond to a comparatively large soliton separation, which matches the case above as the pulses are separated by more than the photodiode response time. However, we could not derive a clear correlation between the soliton separation and the relative breathing phase.

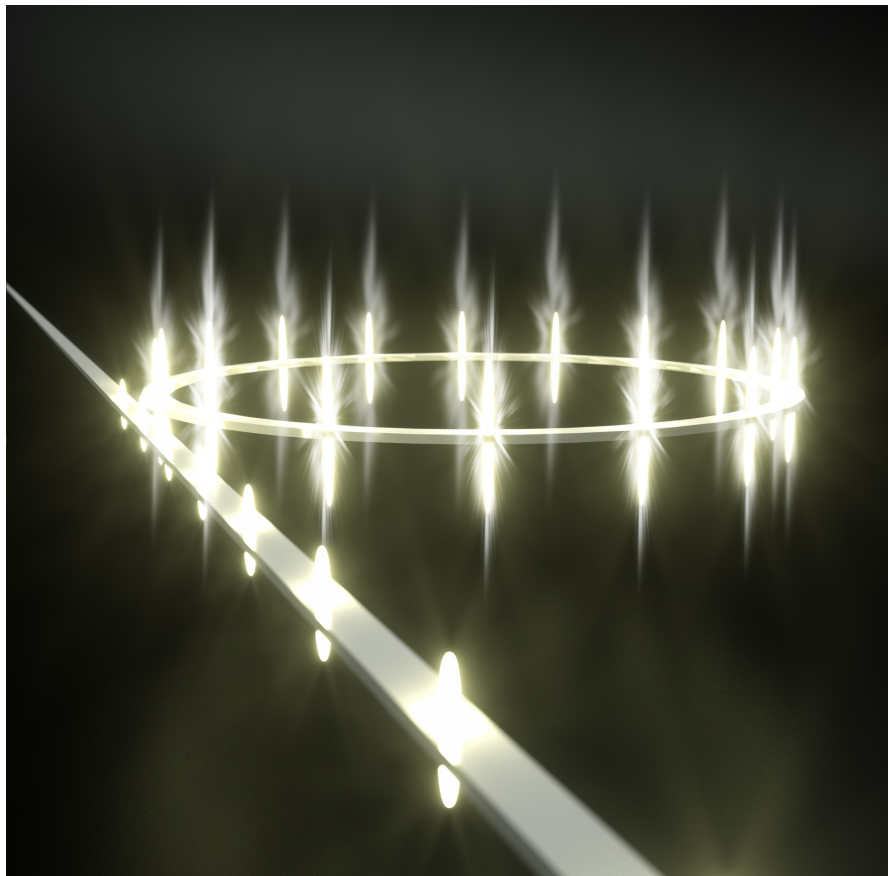
### 4.5 Conclusion

We have experimentally demonstrated the formation of breathing dissipative solitons in two distinct microresonator platforms. The large difference in the characteristics of the  $\text{MgF}_2$  crystalline resonator and photonic chip  $\text{Si}_3\text{N}_4$  microresonator validates the universal nature of our observations. We implemented a laser tuning method which enables reliable access to soliton breathing. Typical signatures of breathing solitons, including a periodically varying soliton peak intensity and a triangular spectral envelope are observed. Moreover, we presented the first direct time-resolved observation of dissipative Kerr solitons in microresonators, revealing the breathing dynamics of individual solitons in both single and multiple breathing soliton states. Such measurements unambiguously reveal the transition to higher breathing periodicity and a more chaotic type of behavior. By monitoring the laser detuning of the driven nonlinear system, we present direct measurements of the breathing frequency dependence on the laser detuning. These studies evidenced a linear relation, which agrees remarkably well with numerical simulations and provides further insights into this breathing property.

These findings not only carry importance from an application perspective, but also contribute more broadly to the fundamental understanding of dissipative soliton physics.

In the context of low-noise operation of soliton-based Kerr frequency combs, breathing degrades the soliton stability and should generally be avoided. We should note, however, that the soliton breathing inspected in the present Chapter is not the only source of the instabilities of the DKS states. As we showed recently, intracavity solitons can also form inter-mode breathing states, which can be induced by the presence of AMX and can appear within the stable DKS regime [193].

## 5 Soliton crystals in optical microresonators



This chapter reports on the experimental observation of perfect soliton crystal states in optical microresonators and study of their formation and switching dynamics. The results are partially adapted from M. Karpov *et al.*, "Dynamics of soliton crystals in optical microresonators", *Nature Physics*, 15, pp.1071–1077, (2019).

### 5.1 Introduction

So far we mostly focused on the investigation the single-soliton states, and impacts on their dynamics induced by microresonator material (e.g. Raman effect - see Chapter 2), or internal reasons (e.g. breathing - see Chapter 4 ). There is, however, another level of the system dynamics, which concerns not the self-organization of light and the dynamics of individual solitons, but *collective* self-organization phenomena of the DKS.

As was shown in Chapter 1, the microresonator system is able to support several coexisting intracavity pulses, which results in the formation of multiple-soliton states. These states can be obtained quite regularly from devices with significant thermal effects (e.g.  $\text{Si}_3\text{N}_4$  microresonators [84, 114, 107]), which is associated with thermally-induced lifting of the soliton existence range degeneracy for DKS states containing different number ( $N$ ) of soliton pulses. Optical spectra of these states represent complex, highly structured but regular patterns resulting from the interference of  $N$  single-soliton pulse envelopes with different phase positions  $\phi_1 \dots \phi_N \in [-\pi, \pi]$  (see eq. 1.63). The complexity of the patterns grows with the number of intracavity pulses, which also reduces or completely vanishes the pattern regularity for high-soliton-number states.

Another feature, which is usually observed in experiments, is that for a given generated multiple-soliton state, the separation distance between soliton pulses remains fixed. It is particularly interesting, because such behavior is not directly captured by the simple LLE model with the dispersion limited to the second order. The DKS pulses obtained in such "pure" system can coexist with arbitrary separation distances, and only start to mutually interact when their tails start to overlap, which happens at very short distances on the order of several soliton pulse durations [217]. Moreover, the translation invariance of such LLE system also implies that DKS pulses should move under any external, even noise-like perturbation, as there is no restoration force, holding them at certain separation distance. In contrast, in experiment, the soliton separation distance remains fixed even for the low-number soliton states, when the pulses are separated by multiple soliton separation distances or even located on the opposite sides of the cavity. These observations let us assume that there are mechanisms which establish the long-range interaction between DKS pulses inside the cavity, which can be also referred to as the formation of long-range bound states.

The formation of soliton bound states in the NLSE with dissipation was extensively studied in early 1990 by Boris Malomed for spatial solitons [218, 219, 220]. He found that perturbation on the soliton spectrum can lead to the formation of the soliton bound states with discrete set of separation distances. These ideas were recently extended to temporal cavity solitons in the work by Wang *et al.* [217], where the formation of bound states in fiber cavities was shown to be also linked to various phenomena responsible for perturbations of soliton spectra: dispersive wave emission [221, 84] presence of Kelly sidebands [222] and fiber birefringence.

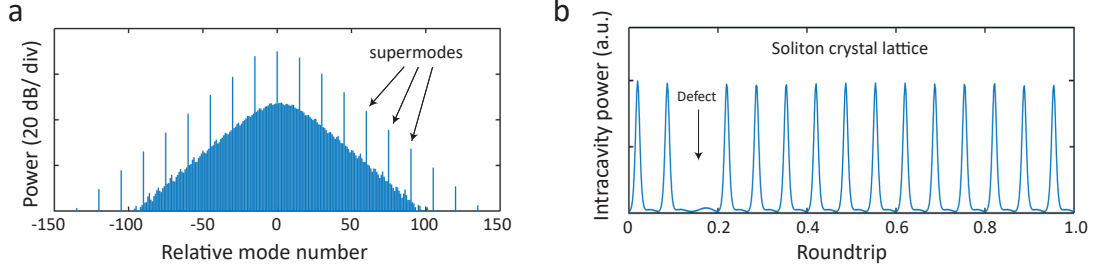


Figure 5.1 – (a) Frequency-domain picture of the soliton crystal state with a single defect (single vacancy) formed in the cavity. (b) Time-domain picture of the intracavity power showing the underlying optical pulse lattice consisting of multiple DKS pulses with one defect - missing pulse.

In microresonators, there are also processes resulting in the deviations of the stable DKS states from the typical  $\text{sech}^2$ -shape soliton envelope. Two central and most widely observed ones are (i) the formation of soliton dispersive wave (DW) due to high-order dispersion terms and (ii) the presence of avoided modal crossings (AMX). The first one - DW - typically consists of the modes, which satisfy phase-matching conditions with respect to a DKS. Resulting spectrum acquires sharp but usually rather broad peak, which is in time-domain results in oscillating and decaying soliton tail, whose decay rate is much shorter than the cavity roundtrip time (here we point out, however, that in certain cases, when the phase-matching is induced by mode interactions as, for example, in the work by Yi *et al.* [46], the DW can also be spectrally narrow). While the formation of DW-induced long-range temporal ordering was predicted in simulations [223], so far no experiments were aimed to investigate this phenomenon or provide clear experimental results demonstrating such effect. On the other hand, the second reason for the spectral perturbations of the soliton spectra is the presence of avoided modal crossing. AMX results in rather localized spectral variations, leading to the strong enhancements of few comb lines, and long oscillating time-domain tails of the soliton pulses. Recently, it was shown that the presence of AMX in microresonators can lead to the formation of temporally ordered DKSs, which have become especially evident in high-number-soliton states [197]. Such temporarily-ordered soliton ensembles filling almost whole cavity and maintaining strict spacing were called *soliton crystals* by the analogy with atomic lattices of crystalline solids. In contrast to high-number multiple soliton states, which have very irregular and structured spectra, the spectra of soliton crystal have one distinctive feature - a set of strongly enhanced comb lines (we will refer to them as *supermodes*) spaced apart by multiple free spectral ranges (see Fig. 5.1(a)). The appearance of supermodes is caused by high temporal regularity and stability of the underlying soliton pulse train resulting from 1D soliton lattices formed in the cavity. The ordering of soliton pulses can be broken by the presence of shifted or missing DKS pulses, which are called *defects*, as in the regular bulk crystals (see Fig. 5.1(b)). While the spacing and the strength of the supermodes is mostly defined by the (inverse) spacing between the adjacent pulses

and their number in the ordered soliton lattice, the pattern of remaining comb lines is linked to the presence of defects in the soliton crystal lattice structure.

## 5.2 Perfect soliton crystals

Experimentally, the formation of soliton crystals was first demonstrated in silica microresonators [197]. The study also linked the presence of AMX to the DKS crystallization process (establishing of the long-range temporal order) and investigated the taxonomy of defects in soliton crystals. Recently two other works have demonstrated the soliton crystal formation in high-doped glass microresonators and attempted to study their stability chart and impact of Raman effects [224, 92]. Despite these works have highlighted some aspects of soliton crystal behavior, there are still a lot of open fundamental questions concerning their dynamics, operation stability at various system parameters and accessibility of the defect-free states. It is also unknown whether soliton crystals reproduce the typical behavior of multiple and single soliton states - if they feature similar switching mechanisms or have enough robustness to form nonstationary states such as soliton crystal breathers.

In the following sections we investigate different aspects of the soliton crystal dynamics and focus on the simplest and most ideal representatives of this class of soliton states termed *perfect soliton crystals* (PSC), which is schematically illustrated in Fig.5.2.

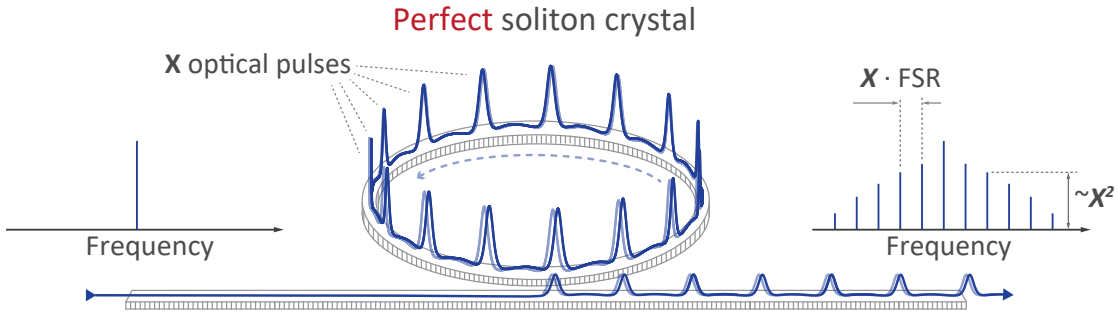


Figure 5.2 – Sketch of the perfect soliton crystal consisting of  $X$  pulses ( $X = 15$ ) formed in the CW-driven nonlinear optical microcavity. Strong CW pump in the bus waveguide is not shown for clarity.

A PSC is a set of dissipative Kerr solitons distributed evenly on the resonator circumference, whose number ( $X$ ) equals to the maximum number of solitons that such resonator can accommodate under given pumping conditions. Time-domain intracavity waveform of a PSC represents complete and defect-free circular optical soliton lattice with fixed and time-independent pulse separation of  $2\pi/X$ . In frequency domain the resulting inter-

---

We purposely introduced new variable for the number of solitons in the PSC state to distinguish it from  $N$  denoting a number of pulses in an arbitrary DKS state. For ideal system  $X = N_{\max}$  (see eq. (1.64))

ference pattern of  $X$  regularly-spaced DKS pulses leaves only supermodes and suppresses all other lines (see Fig. 5.2).

In contrast to soliton crystal states with defects, the behavior of PSC is unperturbed by missing or shifted pulses, what guarantees an access to the "pure" dynamics of soliton crystals. Apart from simplicity, PSC states bear several important features relevant for both fundamental research and applications. First, due to the high regularity of the intracavity pulses, the PSC states can be used as high-purity, ultra-high-repetition rate soliton combs, reaching a mode spacing of several THz. This is challenging to directly achieve in small microresonators (with the radii  $< 20 \mu\text{m}$ ) due to the increase of bending losses in microresonator waveguides and limitations on the dispersion control. The second advantage of PSC states is that the comb energy is distributed in a few lines (supermodes), separated by  $X \cdot \text{FSR}$ , which gives them an  $X^2$  enhancement in comparison to the single-soliton state, which can be excited under the same pump conditions in the given system (see Fig. 5.3(a)). Such significant enhancement can be especially useful for self-referencing of soliton microcombs, as well as locking to an optical reference located in the weak wings of single-soliton states. Third, we also believe that such states can provide a convenient microwave-to-THz link, enabling the stabilization of THz signals with standard RF equipment, because a PSC state establishes natural coherent link between the native FSR of the system and the mode spacing of the supermodes.

In experiments we use  $\text{Si}_3\text{N}_4$  microring resonators with various FSRs of 20, 100, 200 and 1000 GHz. The majority of results were obtained in 100-GHz devices with Q-factors  $\sim 10^6$  (linewidth  $\kappa/2\pi = 150 - 200 \text{ MHz}$ ), which were fabricated using the Photonic Damascene process [28]. In order to achieve single mode operation and suppress the effect of avoided mode crossings, a "filtering section" was added to the microresonator [45, 225]. Similarly, the photonic Damascene process was employed for the fabrication of the 200-GHz, and 1-THz devices used for the verification of our results. Finally, 20-GHz device was fabricated in the subtractive process [226, 84] and was used to demonstrate the platform-independence of the results.

Fig. 5.3(a) shows real PSC state with  $X = 15$ , experimentally obtained in a  $\sim 100$ -GHz microresonator (blue). The spectrum consist of only supermodes spaced by  $\sim 1.5 \text{ THz}$ , while all residual lines are not detectable with given OSA sensitivity and resolution bandwidth (RBW). The observed difference between the supermodes and measured noise floor was at least 60 dB. We also could not detect the native-FSR beatnote of  $\sim 100 \text{ GHz}$  electronically (see Fig. 5.3(c)), which confirms extreme regularity of the DKS pulse arrangement inside the cavity and absence of any defects. Since the spectrum of the PSC state is very similar to the primary comb state, we use VNA-based response measurements [114](see also section 3.3 of Chapter 3) to unambiguously identify the soliton formation. The inset of Fig. 5.3(a) demonstrates response measurement of the corresponding state (blue), which shows a clear double-resonance feature indicating the coexistence of DKS pulse with CW background, thus confirming the formation of the

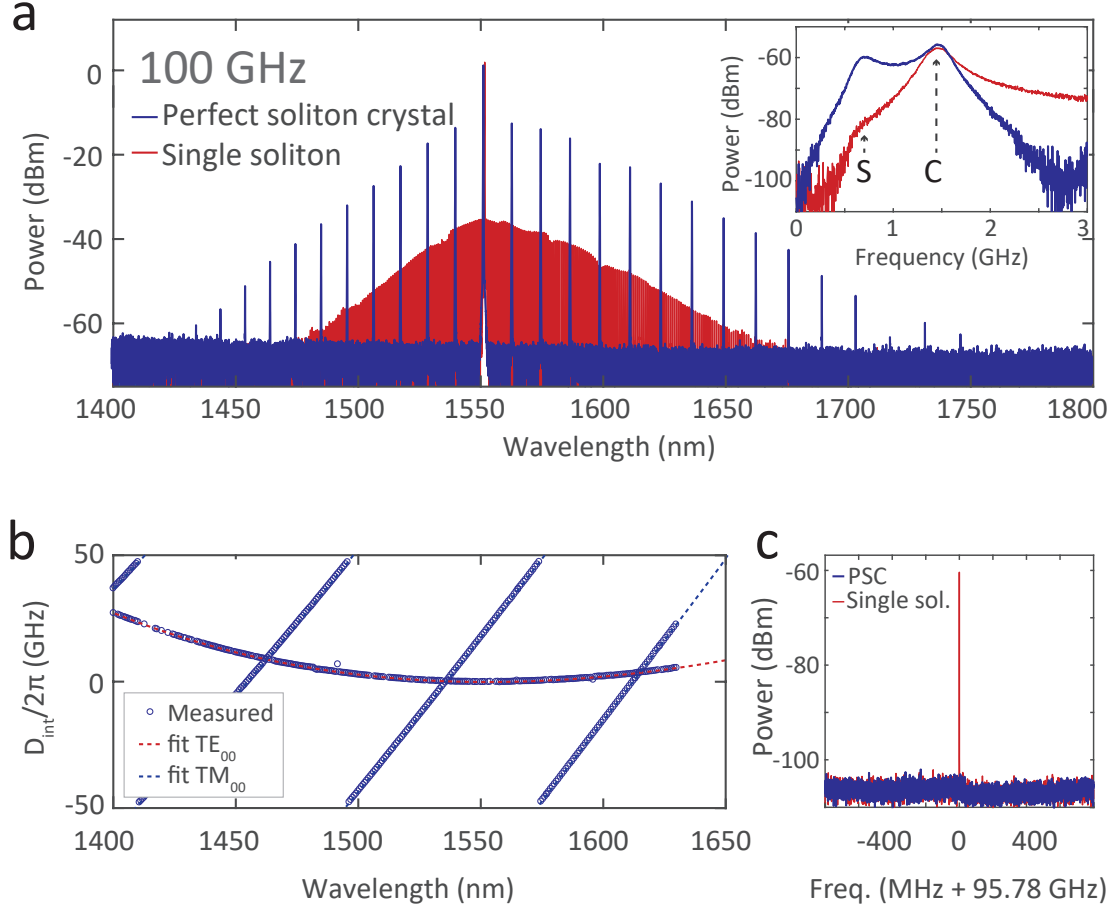


Figure 5.3 – (a) Optical spectra of the soliton crystal state (blue) and single soliton state (red) stabilized in  $\sim 100$  GHz  $\text{Si}_3\text{N}_4$  microresonator under the same conditions of pump power and effective detuning; inset shows the system response measurement using a VNA-based scheme [114] in both states.  $C$  and  $S$  letters indicate the positions of  $\mathcal{C}$ - and  $\mathcal{S}$ -resonances correspondingly. (b) Measured integrated dispersion of the  $\text{Si}_3\text{N}_4$  microresonator used in experiments (circles) and fitting curves for the fundamental TE (dashed red) and TM (dashed blue) mode families [43]. The calculated group velocity dispersion term ( $D_2/2\pi$ ) for the TE mode used for DKS formation is  $\sim 1.2$  MHz; (c) Repetition rate beatnote measurements in the single soliton state and the PSC state shown in (a). Native repetition rate of  $\sim 100$  GHz was not detected in the PSC state.

DKS state. For comparison, we also generated a single soliton state using the same device under the same pump power and effective detuning conditions (shown in red in Fig. 5.3(a)). The same value of detuning for given single soliton state can be confirmed from the position of the  $\mathcal{C}$ -resonance in VNA measurement trace, shown in the inset. Also, in accordance with the understanding that the amplitude of the  $\mathcal{S}$ -resonance scales with the number of intracavity pulses [114] (see also section 3.3 of Chapter 3), we can observe a significant difference of this feature in the VNA response between PSC state and the single soliton state. The power difference between PSC supermodes and

corresponding comb lines of the single soliton state is about 24 dB, which matches very well the expected difference of  $X^2 = 225 \sim 23.5$  dB. We also note that overall spectrum profile of the PSC state reproduces the single soliton shape and particularly maintains the Raman-induced soliton self frequency shift. This can be easily explained noting that all DKS pulses of the PSC state have the same pulse energy, pulse profile and experience the same effect of intrapulse Raman scattering.

## 5.3 Generation of perfect soliton crystals

### 5.3.1 Experimental generation of PSC

We next focus on the generation of soliton crystals. It has been experimentally demonstrated that soliton crystals can appear as a result of microresonator mode interactions [197], which through the AMX induce a modulation on the intracavity CW background, leading to the ordering of the DKS pulses [217]. It should be pointed out, however, that to the best of our knowledge all current microresonators inevitably contain AMX-s, which even in a quasi-single-mode case can appear from the interaction between fundamental modes [225, 227]. The latter means that, in principle, every microresonator system should have an ability to generate a crystal state, because a necessary requirement for the DKS crystallization is satisfied. Since the soliton crystals were rarely reported and so far not carefully investigated, it is reasonable to assume that there exists another important ingredient, enabling the formation of soliton crystals in certain cases or precluding it in the majority of others. In the following we show that such a second ingredient is the pump power of the DKS generation procedure, which predetermines the formation of soliton crystal states, and in particular PSC.

First, in experiments we observed that the generation of soliton crystal states is typically achieved at relatively low pump powers, while the same standard procedures of soliton excitation (forward tuning [9]) at high pump powers can only lead to the formation of multiple soliton states with structured spectrum and irregular arrangement of soliton pulses. This observation was made in microresonators having various designs and FSRs with only a difference in the actual threshold value ( $P_{sc}$ ) distinguishing "low" and "high" pump powers.

To clearly demonstrate the existence of such a threshold, we use four different fixed pump powers ( $P_1 \dots P_4$ : 0.15W, 0.20W, 0.25W, 0.80W) and carried out 100 pump frequency sweeps over the cavity resonance in one of our 100-GHz devices. At each pump power the success rate of the generation of PSC states was counted through the statistics of the recorded soliton steps: after defining the height of the soliton step corresponding to a PSC state, we counted the number of soliton steps with this height out of all tuning attempts. Figure 5.4(a, b) shows the histogram of such success rates for measured pump powers revealing the existence of a clear threshold for deterministic PSC formation at

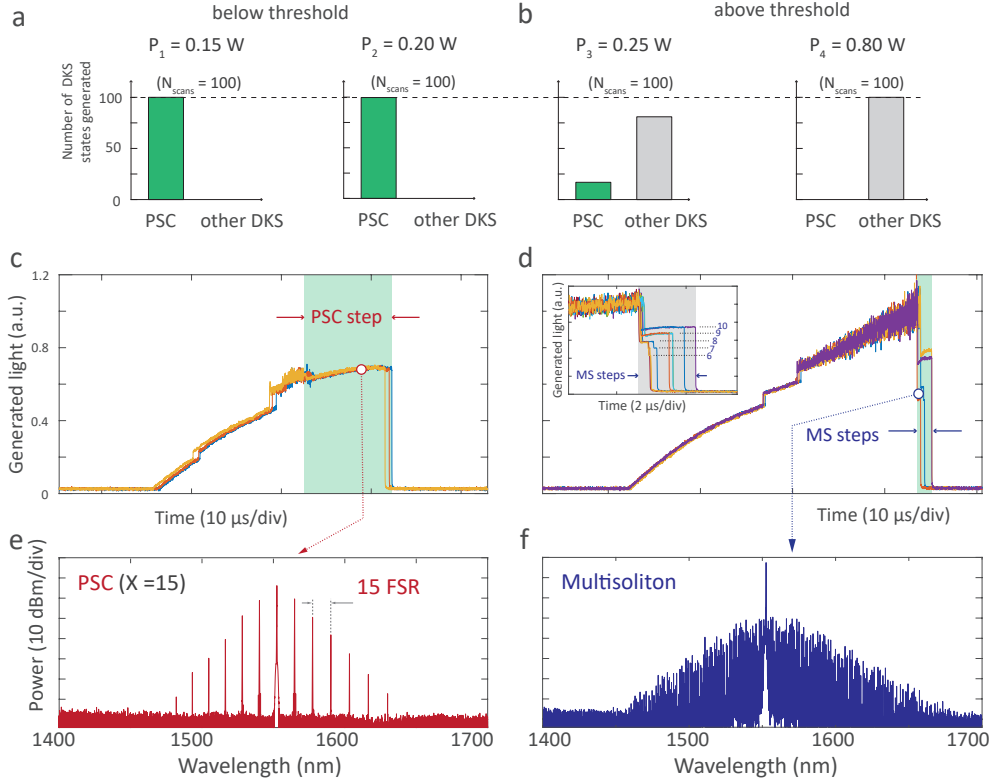


Figure 5.4 – (a) Experimental pump sweeps over the cavity resonance at two pump powers  $P_1 = 0.15\text{W}$  and  $P_2 = 0.20\text{W}$  below the threshold power  $P_{sc}$ ; statistical overview of the generated states out of 100 scans for each power - at both powers the system *always* demonstrate the step of the same height, corresponding to a PSC state with  $X = 15$ ; (b) Experimental pump sweeps over the cavity resonance at two pump powers  $P_3 = 0.25\text{W}$  and  $P_4 = 0.80\text{W}$  above the threshold power  $P_{sc}$ ; statistical overview of the generated states out of 100 scans for each power - no deterministic PSC step formation is observed, steps are formed stochastically; (c) five arbitrarily chosen scan traces at  $P_2$  showing PSC step reproducibility; (d) five arbitrarily chosen scan traces at  $P_4$  showing stochastic distribution of the generated steps; (e,f) Experimentally generated PSC (e) and multiple-soliton state (f), obtained at the powers  $P_2$  and  $P_4$  correspondingly.

around  $0.25\text{W}$ . Strikingly, for both experimental power values below the threshold -  $P_1 = 0.15\text{W}$  and  $P_2 = 0.20\text{W}$ , the system has long soliton step, which is reproduced in every scan with 100 % success rate (see Fig.5.4(c)). On this step the system *always* stabilizes in the same PSC shown in Fig.5.4(e), i.e. making the process deterministic. Due to the matching of the intracavity power levels in the MI state and the PSC state, the final state almost independent of the tuning speed, because the thermal effect does not shift the system operating point out of the soliton existence range. The system can be even tuned manually in the PSC state similarly to the soliton crystal states with defects observed earlier [197].

In contrast, reproducing an experiment at higher pump power  $P_3 = 0.25\text{W}$ , which

is already above the threshold, we can observe that soliton steps are starting to be stochastically distributed, thus reducing the success rate of the PSC generation. At a high pump power well above the threshold ( $P_4 = 0.8\text{W}$ ) the system is purely stochastic in terms of the number of generated soliton pulses (see Fig.5.4(d)), which is always well below the maximum soliton number in the PSC state ( $X = 15$ ).

#### 5.3.2 Simulations of the PSC generation

To reproduce the observed behavior in simulations and understand the underlying physics, we use Lugiato-Lefever equation (LLE) (1.55) with the parameters corresponding to our experimental  $\text{Si}_3\text{N}_4$  device:  $\text{FSR} = 95.4\text{ GHz}$ ,  $D_2/2\pi = 1.3\text{ MHz}$ ,  $\kappa/2\pi = 200\text{ MHz}$ ,  $\eta = 1/2$ ,  $\omega_0/2\pi = 193.46\text{ THz}$ . The simulations were performed with 512 modes.

In order to enable the formation of soliton crystals the LLE was perturbed in order to imitate simple avoided modal crossing (AMX). For this purpose we introduced an additional detuning change for a mode with a relative mode index  $\xi$ , such that the detuning value for such a comb line is  $\delta\omega_\xi = \omega_p - \omega_\xi = \omega_p - (\omega_0 + D_1\xi + \Delta_{AMX})$ , where  $\Delta$  accounts for the mode shifting due to the impact of the spectrally localized AMX. The parameters of the perturbation introduced for the soliton crystals are:  $\xi = 15$ ,  $\Delta_{AMX}/2\pi = 130\text{ MHz}$ . The position of the modal crossing  $\xi = 15$  was chosen to enable the formation of a perfect soliton crystal consisting of 15 DKS pulses. The "strength" of the modal crossing  $\Delta_{AMX}/2\pi$  was set to satisfy two conditions: (i) it should be large enough to enable the crystallization of the intracavity field in a PSC state with given parameters of the microresonator system; (ii) The perturbation it introduces to the system is small and does not affect the formation of multiple-soliton states (e.g. by shortening the DKS steps [98] or initiating significant inter-mode breathing [193]).

Using the perturbed LLE we implement multiple forward tuning scans at various pump powers imitating soliton generation attempts. As in experiments, we also observed the existence of a threshold pump power ( $\sim 0.25\text{W}$ , very close to the experimental value), which separates two different generation scenarios. In the first one, below the threshold, almost every simulation ends in the same PSC state, as shown in Fig.5.5(a). The process does not depend on the initial conditions and reveals determinism and extreme robustness of the generation procedure available for the PSC states below the threshold power  $P_{sc}$ . In contrast, the simulation result becomes stochastic for pump powers above the threshold. Depending on the initial conditions and scan parameters the system forms soliton crystals with defect(s) or – only in rare cases – the PSC. At high enough powers no soliton crystal formation is observed. Resulting intracavity waveform represents a typical multiple-soliton state, consisting of several sparsely-spaced DKS pulses, as shown in Fig.5.5(b). Even though the pulses can still maintain long-range temporal order (being bound to the modulated background), characteristic signatures of soliton crystal states (e.g. enhanced lines with extreme conversion efficiency) are degraded.

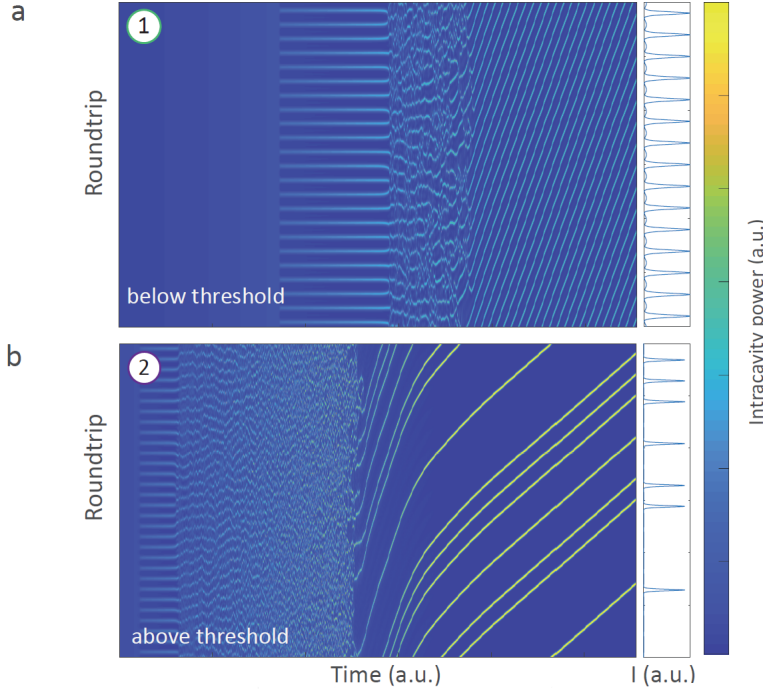


Figure 5.5 – (a,b) Simulations of the intracavity waveform evolution during two tuning attempts for the generation of DKS states below (a) and above (b) the threshold power: 1 — pump power  $P_{\text{in}} < P_{\text{sc}}$ , below the threshold, the detuning is stopped in the stable soliton regime - PSC state is generated; 2 —  $P_{\text{in}} > P_{\text{sc}}$ , above the threshold, the detuning is stopped in the stable soliton regime - multiple-soliton state is generated.

### 5.3.3 PSC stability chart

We found that in order to explain the behavior of PSC, and in particular - the presence of the threshold power, observed in experiments and simulations, one needs to employ the stability chart of our LLE system [42]. The stability chart can be directly simulated using the perturbed LLE described above. We remind that the LLE can be reduced to the dimensionless form with only two control parameters: normalized detuning  $\zeta_0$  and normalized pump amplitude  $f$  (see Chapter 1). For this reason obtained stability diagram and the following discussion can be directly generalized to any Kerr nonlinear microresonator system using dimensionless parameters  $(f, \zeta_0)$ . We also note that attempts to simulate the stability chart for soliton crystals have been made recently [228, 224], but the investigation of its complex structure and the presence of chaotic regimes was incomplete.

We initialize the system with a perfect soliton crystal solution at various values of pump-cavity detuning  $(\omega_p - \omega_0)$  and pump power  $(P_{\text{in}})$ , and propagated it for about 5000 roundtrips to let the system stabilize. Obtained stable states were classified in several regions: stable PSC state, breathing PSC state, spatiotemporal chaos, transient

### 5.3. Generation of perfect soliton crystals

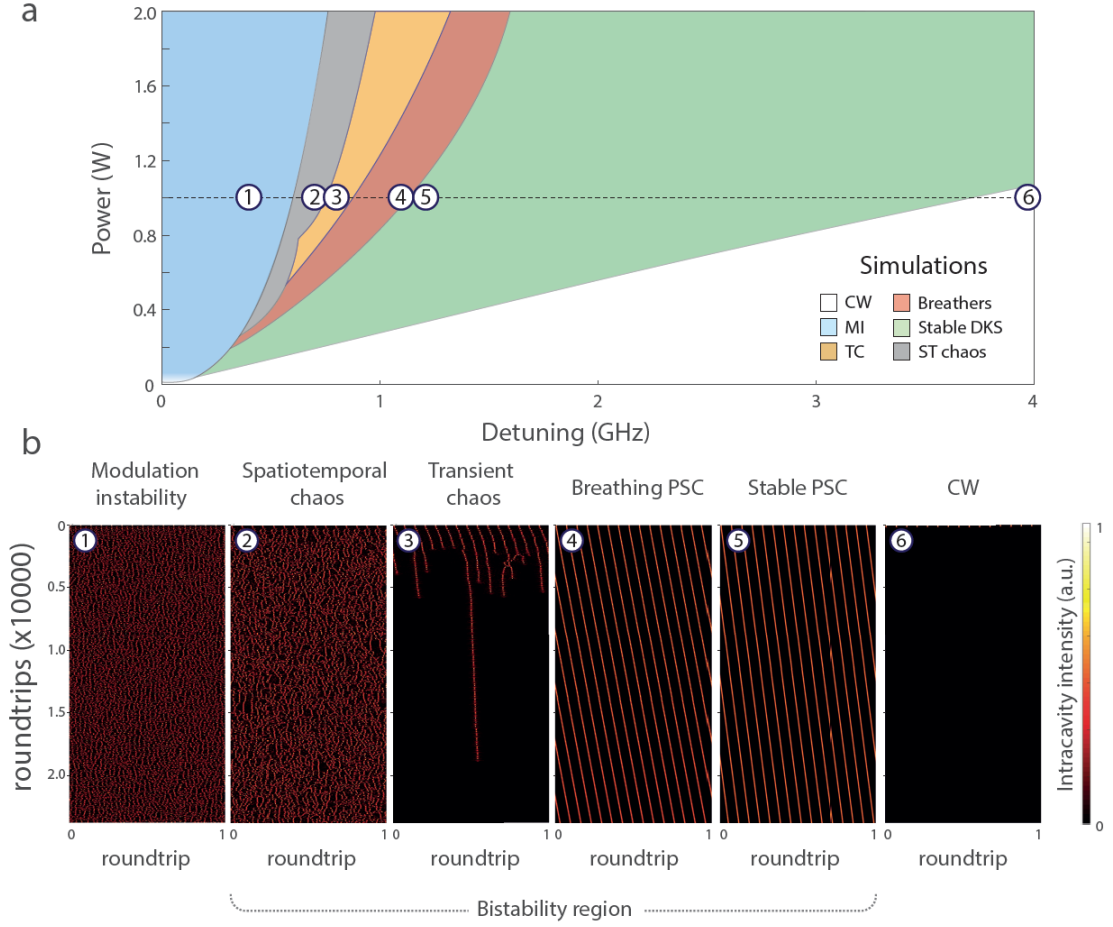


Figure 5.6 – (a) Simulated stability chart of the Lugiato-Lefever equation augmented with one AMX crossing located at  $\xi = 15$ ; Colored areas indicate different stability regions of PSC states: green - stable PSC, red - breathing PSC, blue - modulation instability, grey - spatiotemporal chaos (STC), yellow - transient chaos (TC), white - CW solutions. Numbered circles indicate six simulations made in different stability regimes. Evolution of the intracavity waveforms in these simulations is plotted in (b). (b) Simulations of the intracavity intensity evolution at fixed pump-cavity detuning and pump power in six different stability regions marked in (a). All simulations are initialized with a PSC solution and propagated for  $\sim 25000$  roundtrips (from top to bottom of each graph).

chaos, modulation instability (MI) and homogeneous (CW) solutions, which were marked with corresponding colors on the stability chart (see Fig. 5.6(a)). In order to demonstrate the behavior of the system in region, we explicitly plot the evolution of the intracavity intensity during  $\sim 25000$  roundtrips, which was seeded with a perfect soliton crystal at six different fixed detunings and the same pump power  $P_{\text{in}} = 1\text{W}$  (see Fig. 5.6(b)).

We briefly discuss all dynamical regions and the system behavior in each of them, and particularly stop at two chaotic regimes at the end (note that the regions are discussed not in the order they are numbered in Fig. 5.6):

**Stable PSC states** - in this regime the system remains in the initial PSC state maintaining all DKS pulses and their arrangement. We note that the state propagates stationary (individual pulses do not change their shape), but acquires linear drift with respect to the rotating reference frame. The drift is caused by the change in the group velocity of DKS pulses, induced by the spectral recoil from AMX.

**Breathing PSC states** - in this regime the system maintains the number of pulses from initial PSC state, but starts breathing. Similarly to the single-soliton breathers (Chapter 4) DKS pulses of the PSC state reveal synchronous periodic oscillations in their duration and amplitude. For simplicity, we do not distinguish in this region multiple-period oscillations [42, 185].

**CW states** - in this regime the system quickly (at the photon escape rate of  $\kappa$ ) decays to the homogeneous (CW) solution. No spatially localized solutions are observed here.

**Modulation instability** - in this regime the system appears in stable or chaotic MI state.

While four above-listed regions are well-known in the CW-driven Kerr nonlinear microresonators and were extensively studied in theoretical and experimental works, we would like to focus on two additional regimes, which can be identified within the bistability region. They so far did not get as much attention as others, but represent key dynamical regimes for our study - *spatiotemporal chaos* (STC) and *transient chaos* (TC) [42, 213]. First we note that both of them lie within the bistability boundaries of the system, meaning that in both regions the system has stable homogeneous solution (lower-branch solution), similar to the CW states described above.

**Spatiotemporal chaos** - in this region each of the DKS pulses forming the initial PSC state starts to seed spatiotemporal instabilities [213], which quickly merge together leading to the chaotic spatial and temporal oscillations of the whole intracavity waveform. As can be observed in plot 2 of Fig. 5.6(b), such chaotic behavior can persist (for more than 20000 roundtrips in a given simulation) with no sign of degradation or evident changes in its dynamics. The intracavity chaotic dynamics can be also represented as a set of chaotically moving transient pulses, which actively interact, collide, decay and give birth to new solitary pulses.

**Transient chaos** - before discussing this region, we recall that the transient chaos phenomenon, observed in nonlinear dynamical systems describes the system behavior, which, when the system is seeded by the random solution, demonstrates chaotic behavior for a long period of time (much longer than characteristic timescale of the system), and then abruptly switches to a different, often nonchaotic behavior [229]. The transient chaos for the PSC solutions, which is observed in our LLE system, reveals itself in the following dynamics: the initial PSC state experiences long-timescale chaotic decay to a new state. For our system the characteristic timescales are: the roundtrip time, the

photon escape rate and the breathing period, and all of them are much smaller than characteristic time of such decay. Depending on the system parameters, the final state can be a steady-state homogeneous solution, or time-varying multiple-soliton state with, however, time-independent number of pulses. An example of the intracavity intensity evolution in this region is shown in plot 3 of Fig. 5.6(b). The system is initiated with a PSC, and in this particular example for about two thousand of roundtrips maintains its spatial order, while having temporally chaotic behavior. After this, the intracavity waveform start to spontaneously lose DKS pulses. They can decay spontaneously without interaction with other pulses or due to the collisions with adjacent pulses. The process continues until the last pulse decays (around 18000 roundtrips for our simulation) and the intracavity waveform ultimately becomes only the CW solution. Depending on the seed the general pattern of the spontaneous decay from an initial PSC state to a final state may change significantly, but it always has two important distinctive features in the TC region that we demonstrated in our simulations: (i) the decay of the intracavity field mostly happens *pulse-wise*, which is in contrast to decay of the state outside of the bistability region (see e.g. plot 6 in Fig. 5.6(b)); (ii) the final state of the system has a stable attractor, which might be a CW or non-stationary multiple-soliton state.

We would like to point out some subtle differences between the stability chart we obtained for soliton crystal state (Fig. 5.6(a)) and the stability chart, obtained for single-soliton states in earlier work for similar driven Kerr-nonlinear system [42]. Apart from general similarity, one can note that the region of transient chaos that was found in the simulations by Leo *et al.* starts at around  $f = 5$ , while in our simulations its bottom extends down to  $f \sim 4$  if we recalculate our simulations to dimensionless units. The difference here is in the following, for  $f > 5$ , the system in both cases (single soliton state and PSC state) reveals transient chaotic behavior and always decays to a homogeneous solution (CW solution). While for  $4 < f < 5$  the evolution of the system initiated with a single soliton state and PSC state will differ. In the first case the intracavity waveform maintains its spatially inhomogeneous structure (DKS pulse) with periodic or possibly chaotic oscillations. In the second case, a PSC state is not maintained and relaxes to a multiple-soliton state with lower number of DKS. In the latter case the system also undergoes transient chaotic processes, where the final state is not a homogeneous solution but lower-number-soliton state. Since our map is plotted with respect to a PSC state it is natural to classify this scenario as *transient chaos*.

#### 5.3.4 Chaotic regions and the PSC generation process

Having established the different dynamical regimes of our system, we can now consider the typical generation process of forward tuning, which we used in our simulations and experiments. Since the forward tuning operates at the fixed pump power, and the only variable parameter is detuning, the tuning process can be represented in the stability chart as moving of the operation point of the system along the horizontal line, as shown

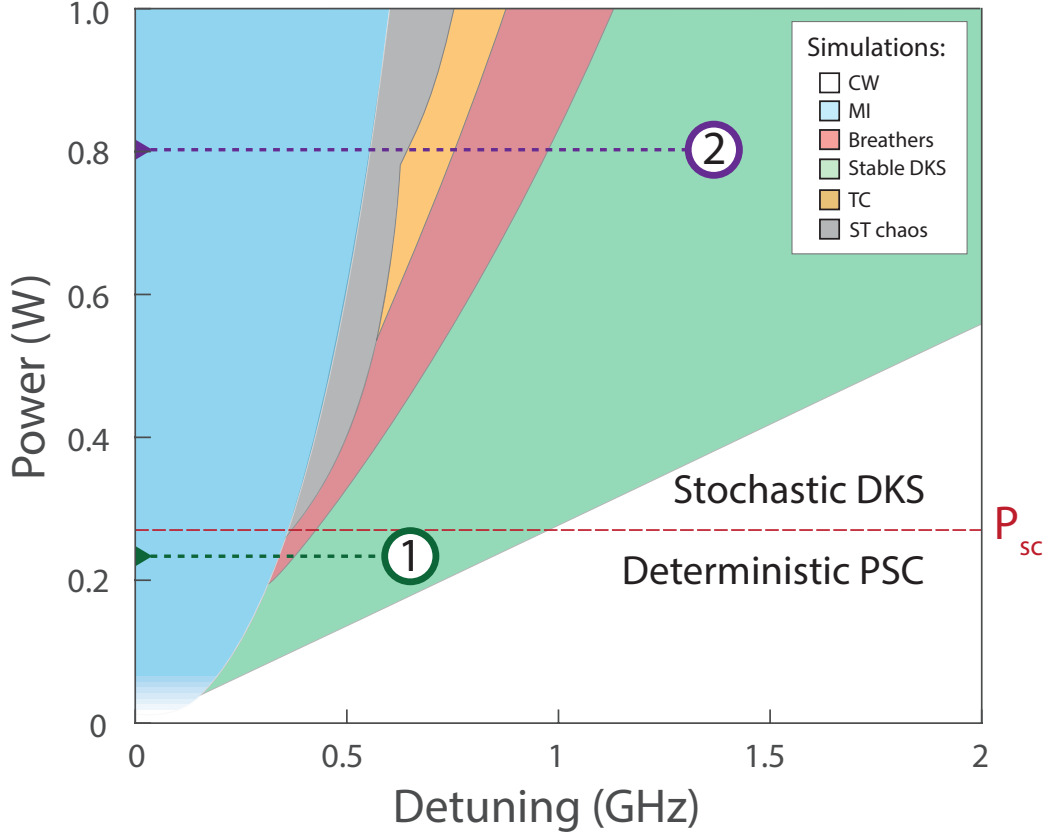


Figure 5.7 – (a) Simulated stability chart of the Lugiato-Lefever equation augmented with one AMX crossing located at  $\xi = 15$  (same as in Fig. 5.6); Colored areas indicate different stability regions of PSC states: green - stable PSC, red - breathing PSC, blue - modulation instability, grey - spatiotemporal chaos (STC), yellow - transient chaos (TC), white - CW solutions. Numbered dashed lines indicate two tuning procedures generating DKS states at fixed pump power which avoid (1), or go through the STC and TC regions (2). They correspond to the simulations shown earlier in Fig. 5.6. Red dashed line marks generation threshold for PSC states.

in Fig. 5.8.

By comparing experimental results shown in Fig. 5.4, simulations of forward scans and the stability diagram, we found that two chaotic regions - STC and TC play a major role in the formation of soliton crystal states. Excursion of the operation point of the system through any of these regions reduces the probability of generating PSC or soliton crystals with a low number of defects. First, in the region of STC, which has its lower boundary at  $P \sim 0.25\text{W}$  ( $f \sim 3$ ), the intracavity waveform experiences fluctuations in the instant number of pulses due to its complex chaotic behavior. Such fluctuations do not guarantee that the number of seed pulses, at the moment when the DKS state is stabilized, will match the number of potential "sites" introduced by the background modulation. This stochasticity results in fundamental indeterminism in the final DKS

### 5.3. Generation of perfect soliton crystals

---

state, which can be either a PSC or soliton crystal with defects.

The second region – TC, demonstrates even more dramatic impact. It is located above  $f \sim 4$  for PSC states, and immediately follows the region of STC for a forward tuning procedure. Due to the transient chaos, the number of intracavity pulses, which can become seeds for the DKS pulses when the system enters the soliton existence range, decreases as long as system stays in the TC region. This results from the gradual decay of the intracavity waveform towards flat or low-soliton-number state.

The effects of both regions explain our experimental observations and presence of threshold power. As can be seen from the simulated stability chart demonstrated in Fig. 5.8, depending on the pump power, the system operation point can pass by single chaotic regime (STC), both of them (TC and STC) or none. First, since the generation procedure of the DKS state for any power below  $f \sim 3$  ( $P_{sc} \sim 0.25\text{W}$ ) avoids both the STC and TC, and the MI region directly connects to the stable (or breather) soliton regime - the system in such process deterministically lands in a PSC state. It is enabled by MI, which provides enough number of seed intracavity pulses to fill all potential sites of the PSC state, when the system enters soliton existence range. On the other hand, when generating a soliton state in forward tuning with the pump power above the threshold  $f > 3$ , the final number of pulses becomes stochastic, and in accordance with experiments the probability of getting PSC decreases. This explains why the probability to generate a PSC state in experiment rapidly decreases above the threshold power, and the distribution of steps becomes partially stochastic (the same tuning procedure leads to the generation of the PSC states only in certain cases). In this regime, the system however is still able to generate soliton crystals with defects, because the presence of the AMX guarantees the temporal ordering of the pulses even if the number of pulses less than the potential number of sites. At high pump powers  $f > 4$ , when the system experiences the cumulative effect of both STC and TC regions, the formation of the PSC as well as soliton crystals with low number of defects is prohibited due to the impact of TC, which "clears" the cavity and limits the maximum soliton number of the generated DKS states. Although the formation of regularly spaced soliton molecules (bound states of several adjacent solitons [48]) and single solitons is still possible, typical features of soliton crystal states are degraded. The system lands in multiple-soliton states.

These results and understanding establish a critical role of the pump power in the generation process of soliton crystals, and in particular PSC states. First, it directly provides a simple approach for deterministic access to a PSC state in any microresonator system: one needs to use low pump powers, which can help to avoid STC and TC regions in the given system ( $f < 3$ ). To verify this approach we were able to deterministically generate PSC states in microresonators with vastly different FSRs (20-1000 GHz) and fabricated with different fabrication processes (see Fig. 5.7). The resulting PSC states have  $X$  ranging from 3 (1000-GHz FSR) up to 87 (20-GHz FSR). The latter one in particular corresponds to the perfect soliton crystal state consisting of 87 DKS pulses,

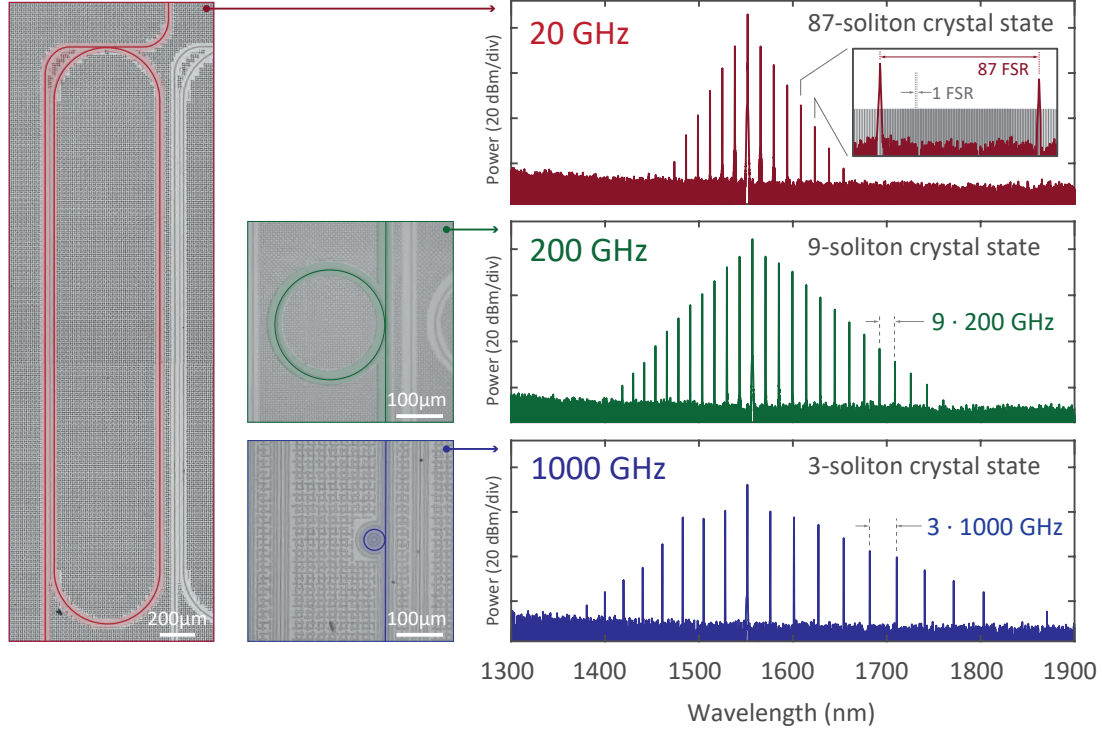


Figure 5.8 – Left: Optical microscope images of  $\text{Si}_3\text{N}_4$  microresonators with different free spectral ranges of 20 GHz, 200 GHz and 1000 GHz used for the generation of PSC states; Right: perfect soliton crystal states generated in each device (right).

which results in the interferometric power enhancement of each of its supermodes by almost 40 dB ( $87^2 = 7569$  times). Second, understanding of the power-dependency of the soliton generation process and its link to the stability chart can help to explain other observations in microcomb systems, as well as different routes observed for the generation of the DKS states.

## 5.4 PSC switching

### 5.4.1 Translation of PSC states

After deriving the conditions for the faultless and deterministic generation of PSC states we focus on their dynamical properties. We start by introducing a method to operate with soliton states in the two-dimensional parameter space of the system (pump power, effective detuning) in order to access different dynamical regimes of soliton crystals. While pump power measurement of the given DKS state is straightforward, a measurement of the effective detuning can be challenging. We use VNA soliton probing scheme described in Chapter 3. An effective detuning of the given soliton state can be identified from the position of the  $\mathcal{C}$ -peak in the VNA response of the system to a weak phase modulation

[114]. Being able thus to determine and monitor the operational point of the generated DKS, we can precisely locate it in the stability chart. Moreover, by introducing changes in the pump power or the frequency of the pump laser - we can *translate* DKS state in its parameter space. Such power- and detuning-translations were explored in various works [191, 107, 230], but due to the absence of the soliton probing scheme and impact of the thermal effects, prohibiting the measurements of the effective detuning, the mapping to the stability chart was hardly possible.

In the work we use the proposed method of well-controlled soliton state translations to explore different dynamical regimes of soliton crystals. For this we first experimentally verify that PSC states are robust with respect to power- and detuning-translations, and are maintained by the system until pump power and effective detuning stay within the soliton existence area. Figure 5.10 demonstrates, that PSC states are indeed able to sustain significant translations in power and detuning. We show two translations (one - in pump power, and one in effective detuning) of the same PSC state generated in the 100-GHz Si<sub>3</sub>N<sub>4</sub> microresonator. From the optical spectra we can see that the structure of the PSC state is maintained in both translations. Despite some slight changes in the powers of individual comb lines due to the increased pump power or change in the effective detuning (which is natural for DKS states, when the detuning or pump power are changed [231]), the system has maintained the number of pulses and exceptional level of their temporal ordering. We also note here that thanks to the soliton probing scheme, which provides direct measurements and control over the effective detuning, we can efficiently *isolate* the power translations from the detuning translations, which are coupled due to thermal effects.

The robustness of the PSC state with respect to such translations gives us a powerful opportunity to explore different dynamical regimes of soliton crystals by implementing arbitrary complex routes of PSC state transfer in power, detuning, or both.

### 5.4.2 PSC switching in experiments

We use PSC state translations to investigate the switching process of soliton crystal states. Indeed, the switching of soliton crystal states has never been reported, though as we have shown earlier in Chapter 3 DKS states can experience switching events, which reduce the number of intracavity solitons one-by-one [114].

Since the generation process of the PSC states strongly depends on the pump power it is reasonable to assume that other aspects of their dynamics including switching are also power-dependent. Due to the impact of chaotic regions, which remove potential soliton seeds from the cavity above the threshold power  $P_{sc}$ , PSC states at higher pump powers are inaccessible with simple forward tuning. In order to bypass this limitation the following procedure is suggested. We first deterministically generate the PSC state *below*

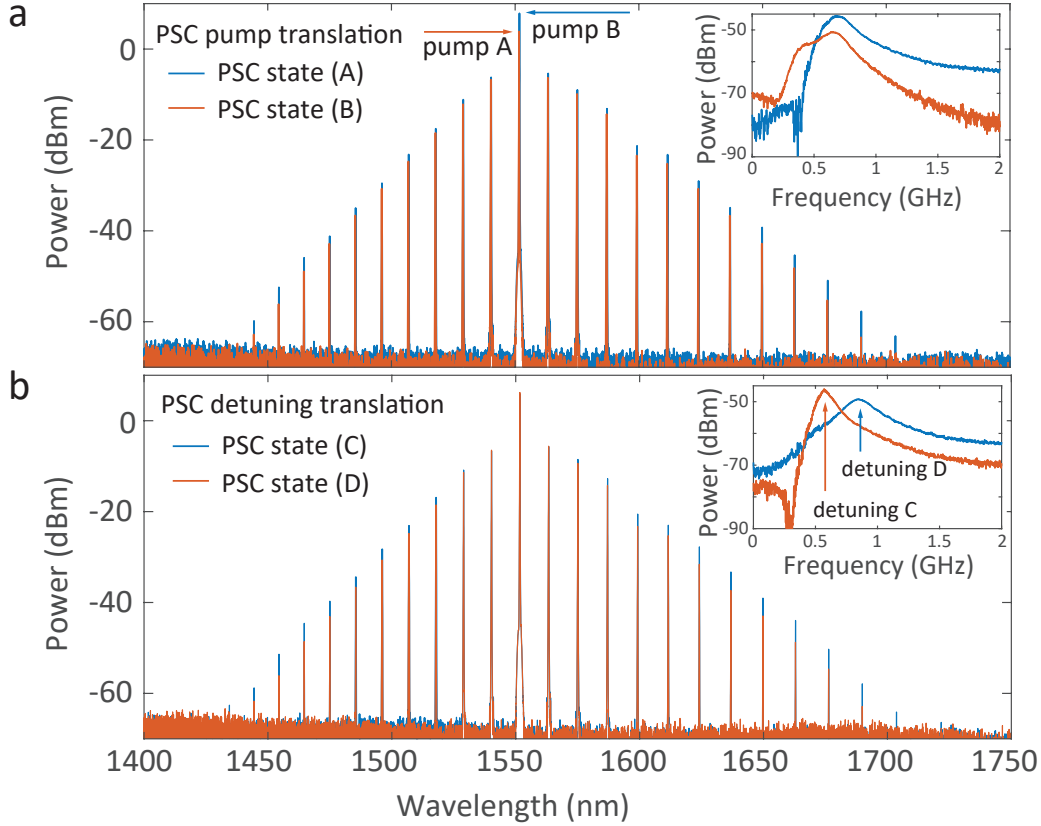


Figure 5.9 – (a) Power translation of the PSC states from the pump power A (blue) to pump power B (red), separated by  $\sim 4$  dB. Inset shows the VNA probing of the effective detuning in both states [114] to demonstrate that the detuning was maintained. (b) Detuning translation of the PSC state from the detuning value C (red) to the detuning value D (blue), separated by  $\sim 0.3$  GHz. Inset demonstrates the VNA measurement of the effective detuning in both states.

the threshold power ensuring that it is stable in the soliton existence range, and then employ power- and detuning-translations of the operating point towards higher pump powers. Such approach of two-stage routing enables access to the PSC states operating at any pump power, which is not possible with simple one-stage forward tuning.

Following this excitation scheme for the investigation of power-dependency of the switching process we constructed complex translation routes consisting of three consecutive stages (see the route demonstrated with blue dashed line in Fig. 5.10(a)): (1) Deterministic PSC generation with forward tuning at the power below  $P_{sc}$ , (2) PSC state translation to a new power  $P'$ , (3) backward tuning of the PSC state to induce soliton switching. Implementing such routes for various progressively increasing  $P'$  values in our 100-GHz  $\text{Si}_3\text{N}_4$  microresonator, we observed that the switching of PSC states suddenly becomes available above pump power  $P_{sw} \sim 0.6$  W ( $f_{sw} \sim 4$ ). Below  $P_{sw}$  the system does not show any switching behavior. The PSC state directly seeds (switches to) MI. An example

of such behavior is shown in the bottom graph of Fig.5.10(c). We also note that similar effect was also observed for individual DKS in fiber cavities [213]. Above the  $P_{sw}$  the system becomes switchable, and we are able to reduce the number of intracavity pulses before the DKS state will seed MI. It is worth mentioning that just above the switching threshold the system allows only for 1-2 switchings before it seeds MI, while as the pump power grows - more and more switchings become available, until the system is able to reach single soliton state and then be switched to a CW state by removing the last DKS pulse before seeding MI (above  $\sim 1$  W ( $f = 5$ )). In most cases at intermediate power, the direct MI seeding can still be observed, but happens after several switchings. The experiments are summarized in Fig.5.10(b), where the number of available switching events is plotted as a function of pump power.

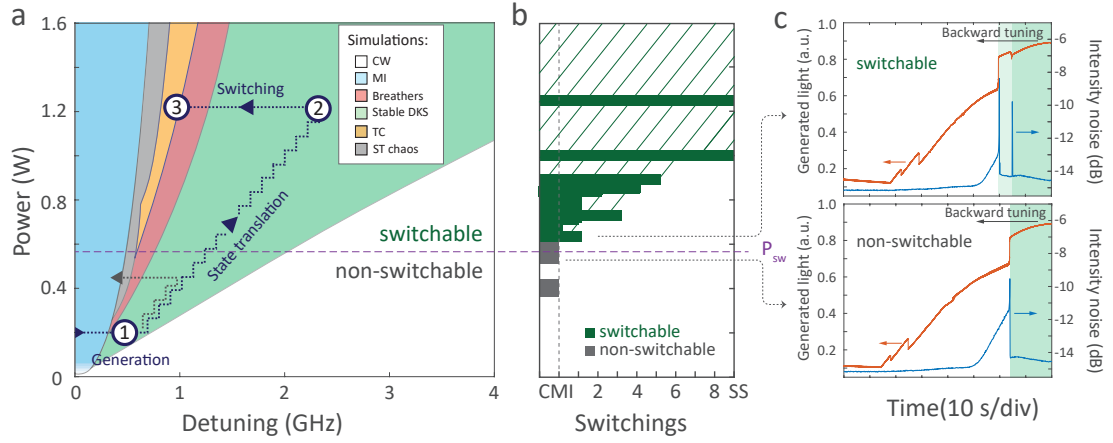


Figure 5.10 – (a) Simulated stability chart of the Lugiato-Lefever equation (same as in Fig.5.6); dark blue dashed line traces complex experimental routes for the controlled PSC state evolution: (1) generation (below TC region), (1 – 2) power and detuning translation to higher pump power  $P'$ , (2 – 3) backward tuning (into TC region) to induce switching. Grey dashed line indicates the route, when the backward tuning is implemented at too low power and system does not enter the TC region, such that no switching is induced. (b) Experimental results showing the number of switchings available to PSC state at different pump powers. The states are unswitchable (grey attempts) below a threshold power of  $P_{sw} = 0.6$  W, and are switchable above (green attempts). Horizontal axis shows the number of available switchings, CMI -chaotic modulation instability, SS - switching to single soliton state. We note that the experimentally measured transition between switchable and non-switchable states (marked with purple dashed line) matches well the bottom of the TC region obtained in simulations shown in (a). (c) Evolution of the generated light power (red) and total intensity noise (blue) measured during the backward tuning procedure from a PSC state for two pump powers: below  $P_{sw}$ (a) and just above it (b). Soliton states are shaded green, modulation instability region is unshaded. Transition to MI can also be traced by the significantly increased total intensity noise. The switching in (b) can be also identified by a characteristic spike attributed to the onset of breathing just before the switching.

In order to verify this behavior in simulations, we used the same LLE as in the previous section, and implemented backward tuning procedures of PSC states at various pump powers. Similarly to the experiments, we observed that the PSC state demonstrates switching behavior above the pump power of 0.55W, which is very close to the experimentally obtained  $P_{sw}$ . Comparing this threshold to the stability diagram, we found that, strikingly, it matches very well the lower boundary of the TC region for the PSC states (see dashed purple line Fig.5.10(a, b)). Below the TC region, all simulated PSC states are non-switchable. They directly seed MI in the backward tuning, as shown in Fig.5.11(a). In contrast, when translation route of the state passes the region of TC, one, several or all DKS pulses can decay (see Fig.5.11(b)). In particular, when the power is just above switching threshold  $P_{sw}$ , the DKS state can be switched only once - from a perfect soliton crystal state to a soliton crystal state with a defect (see bottom plot of Fig.5.11(c)). Further attempts of backward tuning at the same pump power will just transfer the system into a MI state without access to other DKS states with lower soliton numbers. On the other hand, at higher pump powers more switchings become available, and the system can reach multiple-soliton states with smaller  $N$ . Eventually, above  $f \sim 5$  the system can be switched up to a single soliton state ( $N = 1$ ) and even further - to the homogeneous solution before it enters MI state.

This behavior is in line with our early observations of the PSC state dynamics in the transient chaos regions demonstrated above, where the system spontaneously loses pulses until reaching new stable state, which can be a multiple-soliton state (for  $4 < f < 5$ ) or a CW state (for  $f > 5$ ). Interestingly, the second threshold ( $f \sim 5$ ) also matches very well with early study of the stability chart by Leo *et al* [42], which was implemented for the single soliton state.

The experiments above let us not only demonstrate that PSC states can reproduce typical dynamics of the DKS states and are switchable using backward tuning, but also explain the switching by the presence of the transient chaos region in the LLE system.

### 5.4.3 Link to DKS switching

Since the presence of transient chaos regime in the LLE system is independent of the number of pulses, and our switching experiments shown in Fig.5.11 demonstrate not only the switching of the PSC states but also include multiple-soliton switching, we can directly establish a fundamental link between the switching ability of the DKS states and the transient chaos regime of driven nonlinear microresonators. This link demonstrates that the region of TC has a significant impact not only on the process of the soliton generation, but constitutes a fundamental feature of the driven-dissipative nonlinear cavity enabling switching of the DKS states.

Such understanding of the role of transient chaos in the switching process completes the

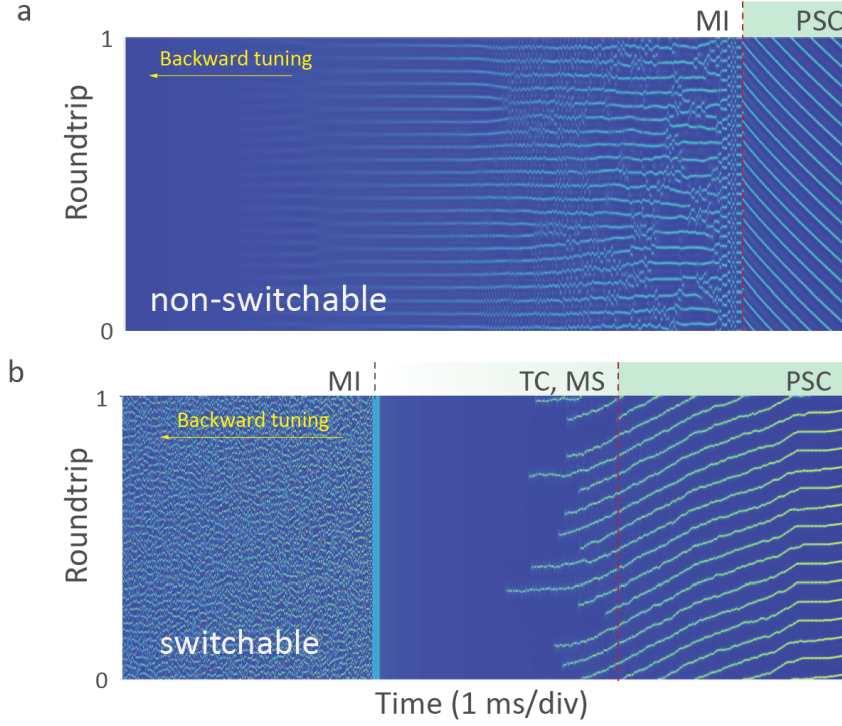


Figure 5.11 – (a, b) Simulations of the intracavity waveform evolution during backward tuning of the PSC at non-switchable pump power (a) and at switchable pump power (b). In the first case the system directly seeds MI, while in the second case the system first decays to a flat solution (CW) via multiple-soliton states (MS).

picture of this phenomenon in DKS states, presented in Chapter 3: when stable DKS state (it can be PSC, multiple-soliton state or even single soliton state) is translated in the TC region using backward tuning, the system starts to spontaneously lose pulses. When the first pulse or a couple of pulses is lost the thermal effects of cavity cooling shift the system back to the soliton existence range.

While this general picture is valid for any DKS state, certain difference can be observed for the DKS states with different number of the DKS pulses. One of them, which is often observed experimentally, is that the switching power threshold is different for high-number soliton states and single soliton states. Such behavior is particularly evident in experiments shown in Fig. 5.10(b), where the number of available switchings increases with the pump power: while reaching the soliton crystal state with defects is possible via switching at the pump powers of about 0.6 W, the switching of the single soliton states is only possible above 1 W.

We link this behavior to the inverse scaling of the lowest power boundary of the TC region with the number of intracavity pulses ( $N$ ). Indeed, the TC region for the single soliton states starts for ( $f > 5$ ) [42], while in our study for the PSC states the TC starts

already above ( $f > 4$ ). This can be explained as follows: soliton pulses forming a DKS state can develop strong chaotic oscillations, when the system is tuned in the strong breathing regime. When DKS state consist of high number of pulses or is even found in the PSC state ( $N = X$ ), the tightly-packed solitons can get easily kicked off their sites or strongly interact with the adjacent neighbors through their tails. While the system is formally still remains in the stable solitonic regimes, such interactions between tightly packed DKS pulses can lead to their collisions and decays, which technically represent and should be classified as transient chaos. Thus, certain regions of the stability chart can be regions of strong or even chaotic-like breathing for low-number soliton states with sparse positions of the DKS, while represent a transient chaos for high-number of tightly packed DKS pulses and PSC states.

This understanding can explain power-dependency of the switching process and in particular different numbers  $N$ , at which the system starts to seed MI in the experiment shown in Fig. 5.10(b). When we fix the pump power ( $P' \propto f'$ ) for the switching experiment starting with the PSC state, the bottom of the TC region was in its lowest position at around ( $f \sim 4$ ). During the switching process for each new state, it was on average growing towards  $f \sim 5$  (limit value found for a single soliton state). However, if the pump power  $f'$  is lower than 5 in dimensionless units, the bottom of the TC region after one of the switching events will become higher than  $f'$  making the system unswitchable. Thus, after the backward tuning it will enter the spatiotemporal chaos regime and seed MI.

On the other hand, if dimensionless pump power amplitude  $f$  is larger than 5, the system can be switched towards a single soliton states and further down to CW state before reaching MI. Such behavior is shown in Fig. 5.12, where our device was switched from a PSC state with 15 DKS pulses to a single soliton state, and then seeded MI.

Understanding the impact of chaotic regions on the dynamics of the DKS states and in particular PSC states provides a broad opportunities for the study of the DKS states and their applications. Taking into account the two important thresholds for the generation of PSC states ( $f_{sc} \sim 3$ ) and their switching ( $f_{sw} \sim 4$ ), one can in principle construct deterministic routes to access any soliton state available in the system.

We strongly believe that such a clear understanding of the effect of TC on these and other processes will help to uncover and explain many other phenomena of the DKS states in optical microcavities including connection to recent theories and explanation of previous observations [114, 107, 197, 224, 232, 233].

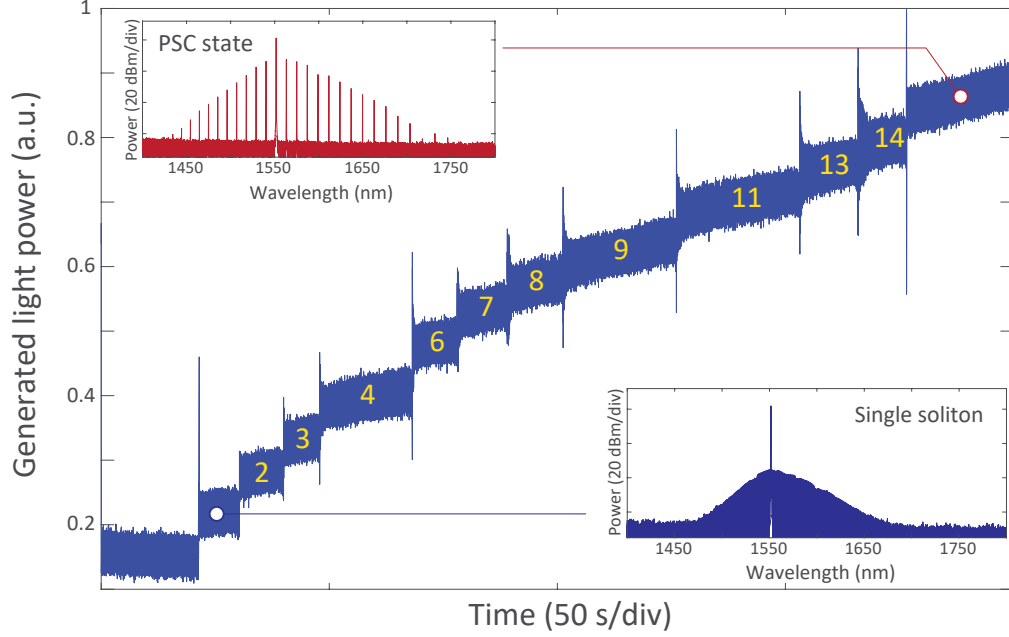


Figure 5.12 – (a) Experimental trace of generated light during the continuous switching of a PSC state to a single-soliton trace. Insets show the optical spectra of the corresponding states. Longer steps observed for  $N = 4, 9$  and  $13$  appear after switching events where two DKS pulses were switched at once.

## 5.5 Dynamics of soliton crystal states

Due to the presence of multiple temporarily ordered pulses forming the PSC states, their dynamics is more complex than that of the single soliton states, as it can include the relative motion of pulses, their switching or complex breathing patterns. In this section we focus on several examples of peculiar dynamical phenomena, which can be found in PSC states and studied using our methods developed above. We highlight three of them, which were observed using different routes of the PSC state translations (shown in Fig. 5.13(a) and Fig. 5.15(a)): reversible melting and recrystallization of the PSC state, switching between PSC states and the formation of PSC breathers.

**Soliton crystal melting and recrystallization.** First, we demonstrate that a PSC state can be consistently restored after its excursion to the MI region. This corresponds to a complete destruction of the regular soliton arrangement - “soliton crystal melting”, and its reassembling, when the system is brought back to the region of stable DKS - “soliton recrystallization” (see A–B–A route, marked with green in Fig. 5.13(a)). In experiment, an initial PSC state at the pump power below switching and generation thresholds (A) was tuned backward until it seeds MI (A – B), and then - forward (B – A) to the initial position. We trace the system evolution during this procedure by measuring the optical spectrum (see Fig. 5.13(b)). For the major part of the stable DKS region, the

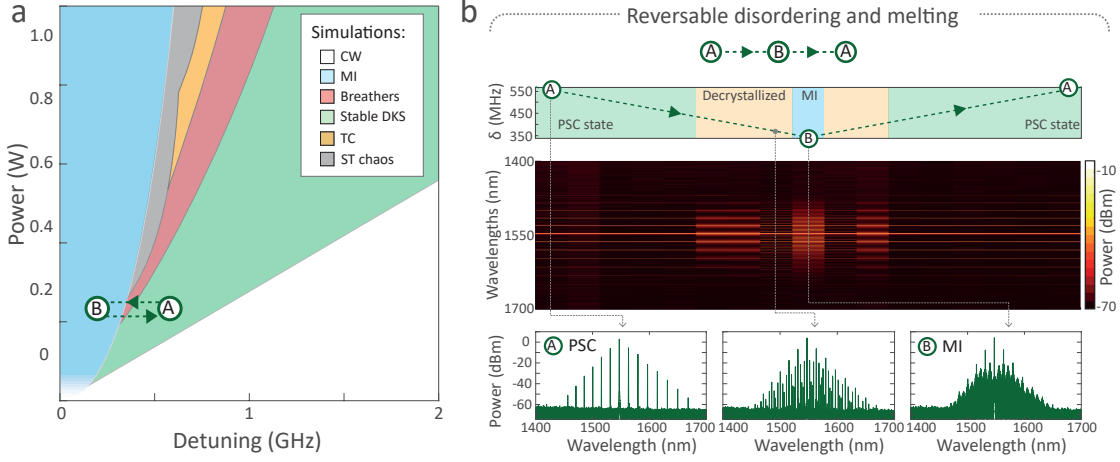


Figure 5.13 – (a) Simulated stability chart of the Lugiato-Lefever equation (similar to Fig. 5.6(a)). Experimental evolution route for the reversible soliton crystal melting and recrystallization of the PSC state is shown in green dashed lines. (b) Experimental observation of PSC melting and recrystallization. The route is shown as A – B – A in (a), and passes below STC and TC regions. The detuning was reduced linearly until the system has reached modulation instability (MI), and then increased to the starting value, as shown at the top plot. Middle map shows the evolution of the optical spectrum of a PSC state during excursion to the MI regime (crystal melting) and then back to the PSC (recrystallization after melting). The bottom plot shows three spectra at different stages, from left to right: initial PSC state, disordered soliton crystal state, and modulation instability at the corresponding stages of the tuning route.

system maintains a typical PSC spectrum consisting of only supermodes. Approaching the MI region, the state starts to develop additional lines apart from the supermodes indicating the appearance of variations in the relative positions of DKS pulses, while maintaining the overall long-range ordering. It should be noted that the system does not experience switching in this process, but demonstrates true disorder maintaining initial number of the solitons. The effect is similar to the introduction of disorder in the atomic lattice of crystalline solids. Once the system reaches MI - the spectrum suddenly changes to the typical spectrum of a noisy comb and the system acquires strong intensity noise. In this state stable DKS pulses cannot exist in the system, and the intracavity waveform is chaotic, meaning that there is no order in the time domain. Reverting the tuning direction and bringing the system back to the initial state (B – A), we observe that the system can be restored back to the initial PSC state, where the DKS pulses are again crystallized in the form of an equidistant lattice. Such restoration is 100% reproducible until the tuning procedure avoids the bistable chaotic regimes.

In order to verify such melting and recrystallization behavior of the PSC state, we reproduced the experiment in simulations (Fig. 5.14). We chose the pump power of 0.20 W (below the region of spatiotemporal chaos) and launched the initial PSC state (see left part of Fig. 5.14), then the detuning was changed linearly from 440 MHz to 240

MHz (as shown in top plot of the figure) and back in order to bring the system in the MI state and then back to the regime of stable DKS. Recording the temporal evolution of the intracavity power, we can see that the initially seeded PSC state sustains the detuning change, while the system stays within stable DKS region. Sudden change in the behavior happens when the system enters the MI region – the PSC state loses the long-range temporal ordering, and the system behavior changes to chaotic [213], in which the transient optical pulses experience multiple interactions, decays and stochastic short-timescale drifts. Once the system is brought back to the stable DKS regime, the transient pulses suddenly reorganize themselves back into the PSC state similar to the initial one.

We note that the conversion of certain SC states to MI and back has been also recently accessed in a non-deterministic fashion, with non-deterministic restoration of the initial soliton crystal [224], and was linked to the chaotic behavior in the MI state.

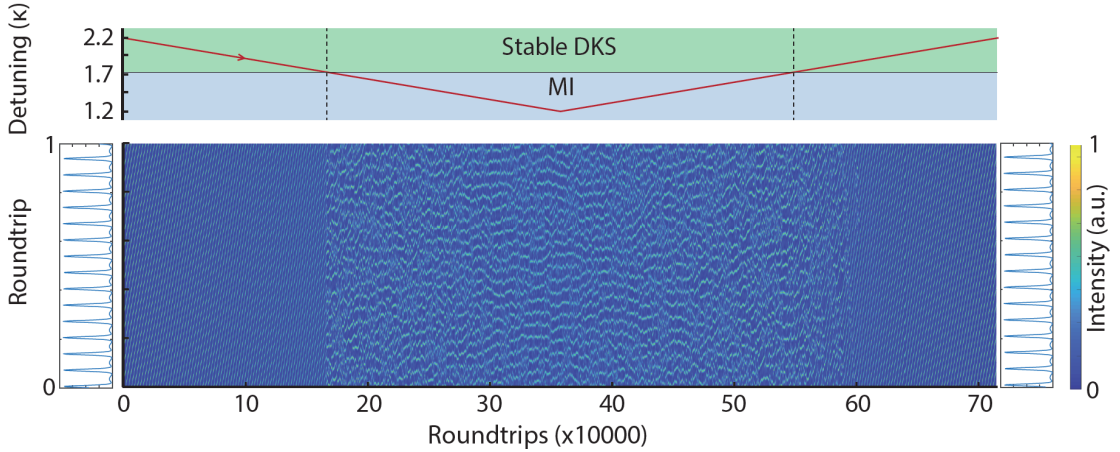


Figure 5.14 – (a) Simulations of the temporal evolution of the intracavity power in a 100-GHz  $\text{Si}_3\text{N}_4$  microresonator from its initial state (left) to its final state (right). The detuning (shown in the top figure) is linearly changed to move the system to the region of MI and back.

**Switching between PSCs.** Second, we demonstrate that under certain pumping conditions, the system can be switched from one PSC state to another PSC state with a distinct number of intracavity pulses (see A - E - F route in Fig. 5.15(a)). In our experiments it was enabled by a proper choice of the pump power (above  $P_{sw}$ ) at which the system was switched, and led to the switching from a PSC with  $X = 15$  to the one with  $X = 13$  (see Fig. 5.15(c)). We attribute this dynamic to the change in the modulation of the CW background, which could be caused by the cavity cooling after switching. Since the positions and strength of the modal crossings are sensitive to the temperature of the system [57, 56], the removal of the DKS pulses can change it and induce a new binding potential with a different number of sites. We can foresee that by properly choosing the route of the soliton crystal switching with additional temperature

control over the AMX position, one can implement the switching between several PSC states with reducing number  $X$ , down to  $X = 2$ .

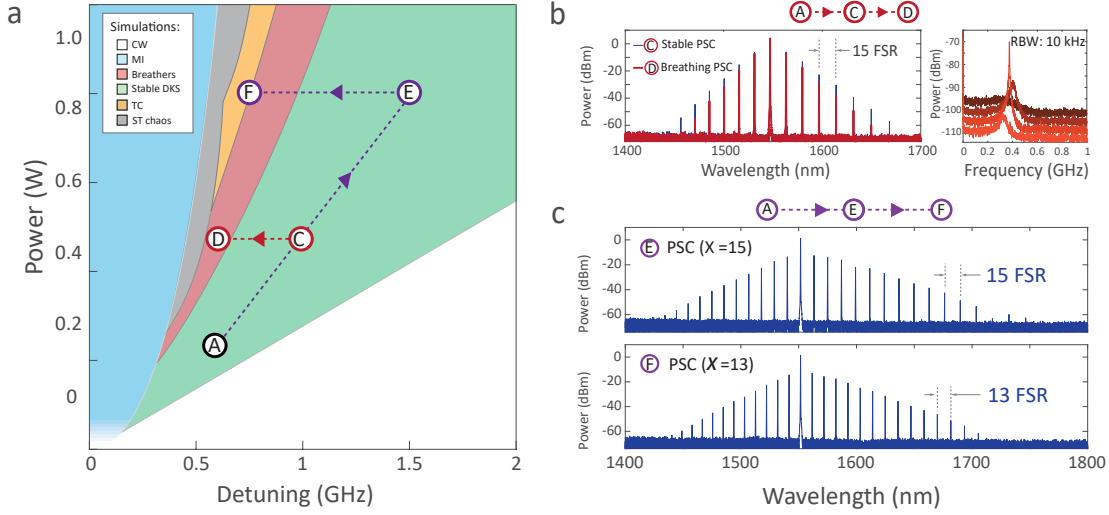


Figure 5.15 – (a) Simulated stability chart of the Lugiato-Lefever equation (similar to Fig.5.6(a)). Two experimental translation routes of the initial PSC state (A) are marked with red and violet colors. (b) Left: Optical spectra of the stable (blue) and breathing (red) PSC states. Both states maintain strict regularity of the DKS pulses. Right: Evolution of the total intensity noise spectrum as the PSC is tuned into the breathing region. The appearance and reduction of the sharp tone, corresponding to the breathing frequency can be observed. The spectra with larger detuning have darker color, the traces are shifted vertically by 5 dB each for better visualization of the evolution. (c) Switching between perfect soliton crystal states. The route is shown as A – E – F in (a). Optical spectra of the initial perfect soliton crystal state with  $X = 15$  and final perfect soliton crystal state with  $X = 13$ , obtained "on the fly" by power translation and switching from the initial.

**PSC breathing.** Third, we experimentally demonstrate the formation of the perfect soliton crystal breathers, which correspond to simultaneous oscillations in the amplitude and duration of all DKS pulses forming the PSC state. For this we brought the PSC state to the breathing region (see the route A - C - D, marked red in Fig.5.15(a)), where the characteristic indicators of the breathing DKS states have been observed, including the triangle-shaped optical spectrum, and the appearance of the narrow breathing tone, whose frequency was close to the estimated effective detuning and was decreasing as the detuning decreased (see Fig.5.15(b)) [185]. We note that despite breathing state the temporal pulse regularity is still maintained.

## 5.6 Conclusion

We have demonstrated platform-independent on-demand generation of *perfect soliton crystals*, which essentially represent defect-free soliton lattices. In comparison to the other soliton crystal states (with defects), they show maximized conversion efficiency into the supermodes spaced by  $X \cdot \text{FSR}$ , whose power moreover scales as  $X^2$ . First, both in experiments and LLE-based simulations, we discovered that the generation of PSC states is highly sensitive to the pump power, which results from the complex structure of the system stability diagram including the regions of STC (perturbing the PSC state and inducing soliton interactions) and TC (stochastically clearing the intracavity DKS pulses). Second, we have demonstrated that the region of TC has significant impact not only on the process of the soliton generation, but constitutes a fundamental feature of the driven-dissipative nonlinear cavity enabling switching of the DKS states. Finally, we demonstrated the rich dynamics of the PSC states, including their ability to sustain translation to the MI state and form the same PSC state afterwards, switching between soliton crystals and formation of the PSC breathing states.

We also would like to emphasize that the above-listed results showing the impact of chaotic regions on the formation and switching processes of solitons states as well as the translation methods we developed to study the complex dynamics of the system can be extended for any DKS states, including less temporally organized multiple-soliton states or single DKS.



# 6 Photonic-based dissipative Kerr solitons covering the biological imaging window

This chapter reports on the first experimental observation of dissipative Kerr solitons at 1  $\mu\text{m}$  wavelength in photonic-chip integrated microresonators. The results are adapted from M. Karpov *et al.*, "Photonic chip-based soliton frequency combs covering the biological imaging window", *Nature communications*, 9(1), p.1146, (2018).

## 6.1 Introduction

Since the first observation of dissipative Kerr solitons in microresonators all major studies of their properties and dynamics were primarily focused on devices operating around 1550 nm. There are several reasons for the choice of the driving wavelength in this spectral window. First, it is broad availability of tunable low-noise lasers, and efficient Erbium-doped amplifiers operating in the C- and L- optical communication bands (1530-1565 nm and 1565-1625 nm correspondingly), whose advances are driven by active development of the optical communication technologies. Second reason is an availability of passive fiber optical components and detection means, which are also essential for every experiment on DKS states. Third reason is favorable dispersion properties for the major platforms used for the first experiments of the DKS states [9, 84, 91].

However, with the active development soliton microcombs area and onset of the era of DKS applications it has become clear that the variety of promising applications available require DKS platforms to operate at other wavelengths besides optical communication bands. Two natural possible extensions of the operating ranges - towards longer wavelength, mid-IR (MIR), and towards shorter wavelengths, down to visible and UV.

The long-wavelength extension of the DKS states towards Mid-IR is primarily driven by spectroscopy applications including molecular fingerprinting, detection of hazardous or toxic chemicals and biological sensing [234]. The first attempt to extend DKS towards longer wavelengths employed silicon microresonators and was demonstrated in the work of Yu *et al.* [88], reaching combs spanning 2.4-4.3  $\mu\text{m}$ . Recently the dual-comb mid-IR

## Chapter 6. Photonic-based dissipative Kerr solitons covering the biological imaging window

---

spectroscopy was also shown using the same silicon platform [142]. We note, however, that these demonstrations relied on the low-noise comb states, with no clear evidence of soliton pulse formation. Apart from this we also point out the work by Gong *et al.* [89], where single DKS states were obtained in z-cut lithium niobate microresonators at 2  $\mu\text{m}$ .

The short-wavelength extension of the DKS operating wavelength has also a solid motivation behind. A large class of new applications of biomedical nature can be accessed with DKS-based comb sources if they can operate in the short-wavelength part of the near-infrared (NIR) domain ranging from 0.7 to 1.4  $\mu\text{m}$  wavelength. This spectral region is used for biological and medical imaging due to the highest penetration depth in biological tissues limited by the water and blood absorption outside of this spectral window [235]. Optical spectroscopy, Raman spectro-imaging and optical coherence tomography (OCT) techniques operating in this wavelength range serve as a non-invasive tool for the structural and chemical analysis of the various biological samples, including retinal and choroidal structures or tumor formations [236, 237, 238]. These biomedical imaging techniques could benefit from employing optical frequency combs as sources due to their coherence and high power per comb line [239], as well as from using dual-comb approaches allowing to interrogate the broad spectral bands with a single photodetector [138]. A specific example of dual-comb-based spectroscopy in the NIR is coherent anti-Stokes Raman spectroscopy (CARS) [140], which can utilise high repetition rates of the DKS combs for vastly increased acquisition rate, enabling real-time CARS imaging. Furthermore, the luminescence-free anti-Stokes response can benefit from the larger Raman cross section and the reduced focal spot size at a shorter wavelength, facilitating phase-matching. Such dual-DKS-comb CARS might be able to provide ultrafast multispectral *in-vivo* imaging for chemical, biological and medical purposes. Equally important, a range of other applications requiring a stabilised operation can be also accessed and improved by near-infrared DKS-based combs. The NIR domain hosts optical frequency standards in alkali vapours (e.g.  $^{87}\text{Rb}$ ,  $^{133}\text{Cs}$ ), necessary to realise chip-scale optical atomic clocks with enhanced precision [240], or employed in DKS-comb-based calibration for astronomical spectrometers [241].

Despite this large number of promising applications of near-infrared DKS-based combs, these sources have not been demonstrated until recently [242, 86]. Although attempts to generate Kerr combs in the NIR and visible domain have been made before [243, 244, 245, 246, 247], they resulted in relatively narrow and incoherent combs, and soliton formation has not been achieved.

The generation of NIR or visible soliton combs is compounded by the increased normal group velocity dispersion (GVD) of the materials due to electronic bandgap in the UV, increased scattering losses and sensitivity to the resonator waveguide dimensions which require high precision of dispersion engineering and fabrication processes. Moreover,

---

We note that the first well-defined DKS state operating at the wavelength shorter than in conventional band (around 1550 nm) was shown at 1300 nm by Pfeiffer *et al.*[87]

as shown recently, competition between Raman and Kerr effects in the NIR or visible domains can inhibit soliton formation [175].

In the following sections we describe the first experimental realization of DKS states in biological imaging window using photonic-chip integrated microresonators.

## 6.2 Microresonator design and characterization

We employ the  $\text{Si}_3\text{N}_4$  microresonator platform, which is a well-developed and extensively used basis for on-chip nonlinear and quantum photonics due to a number of advantages such as CMOS-compatibility, high effective nonlinearity, negligible two-photon absorption, and wide transparency window spanning from visible to mid-infrared [11, 23, 22]. Recent advances in the fabrication processes have enabled the fabrication of low-loss  $\text{Si}_3\text{N}_4$  waveguides with void-free coupling gaps, which guarantee high- $Q$  resonators with well-controllable properties [30, 28, 248, 87, 225]. An important advantage of this is the ability to engineer the dispersion properties of the microresonators by compensating the material dispersion with the waveguide dispersion contribution [84, 249, 87]. For DKS generation it is generally required to achieve anomalous group velocity dispersion:  $D_2 > 0$  (see Chapter 1), which can be especially challenging at short wavelengths.

In this work we used  $\text{Si}_3\text{N}_4$  microrings with FSR of  $\sim 1$  THz (radius  $\sim 23$   $\mu\text{m}$ , see Fig. 6.1(b)), which were fabricated using the photonic Damascene process [28]. The resonator waveguide width was varied from 1.3 to 1.5  $\mu\text{m}$ , and the height was targeted at 0.74  $\mu\text{m}$  (with process-related variations on the order of 20 nm). The choice of waveguide dimensions was based on the FEM simulations of the dispersion profile (see Fig. 6.1(c)), which were implemented in order to ensure anomalous GVD of the fundamental TM mode around the pumping wavelength of 1060 nm. Despite better chip coupling efficiency the fundamental TE mode has normal GVD at this wavelength in all fabricated geometries.

The bus waveguide was designed to have a pulley-style coupling section with altering width from 0.3  $\mu\text{m}$  at the in-coupling part (see Fig. 6.1(b) - C) to 0.65  $\mu\text{m}$  at the out-coupling part (see Fig. 6.1(b) - A,B). The coupling section design aims to guarantee broadband and high ideality coupling, reaching  $\sim 0.85$  at 1  $\mu\text{m}$  according to our simulations [39], which can be further optimized to reduce parasitic losses. The waveguides have inverse tapered mode converters (reducing the waveguide width down to  $\sim 150$  nm) at the input and output ends, providing  $< 3$  dB coupling loss per facet at 1  $\mu\text{m}$ .

A typical transmission trace of the fabricated devices is shown in Fig. 6.1(d). Due to comparably large width of the microring waveguide the resonator is significantly overmoded - multiple resonances from higher order modes can be observed apart from the fundamental ones. Two fundamental modes -  $\text{TE}_{00}$ ,  $\text{TM}_{00}$  - can be easily identified due

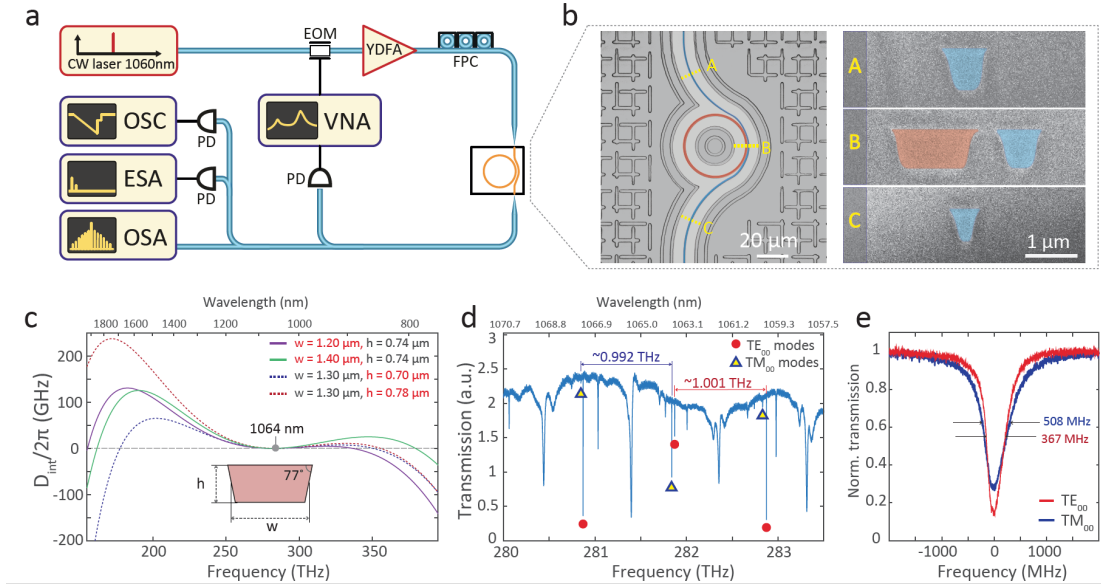


Figure 6.1 – (a) Set-up schematic used for dissipative Kerr soliton generation and characterization: A tunable external-cavity diode laser with a centre wavelength of 1050 nm is used as a seed, YDFA – ytterbium-doped fiber amplifier, FPC – fiber polarization controller, VNA – vector network analyser, EOM – electro-optical phase modulator, PD – photodiode, OSC – oscilloscope, ESA – electrical spectrum analyser, OSA – optical spectrum analyser. (b) Left: Optical microscope image of the 1-THz microring resonator (highlighted in red) with a pulley-style bus waveguide (blue). Right: Scanning electron microscope images of the resonator and bus waveguide cross sections obtained via focused ion beam at different positions (A-C) marked on the left image. (c) Simulated integrated dispersion profiles ( $D_{\text{int}}/2\pi$ ) for TM<sub>00</sub> mode of resonator waveguides having different heights of 0.70, 0.74 and 0.78  $\mu\text{m}$ , widths of 1.2, 1.3 and 1.4  $\mu\text{m}$ , and fixed sidewall angle of 77°. (d) Transmission trace of the 1-THz microresonator shown in Fig.1 (b). The two fundamental mode families (TE<sub>00</sub> and TM<sub>00</sub>) can be distinguished based on their free spectral ranges (0.992 THz for TM<sub>00</sub> and 1.001 THz for TE<sub>00</sub>), and are marked with red and blue shapes correspondingly. Other resonances correspond to higher order modes with comparably lower  $Q$ -factors. (e) Linewidth measurements of the fundamental mode families. The frequency axis was calibrated using a fiber-loop cavity. Typical loaded linewidth of the modes is  $\sim 400$  MHz for TE<sub>00</sub> and  $\sim 500$  MHz for TM<sub>00</sub>.

to their FSRs (0.992 THz for TM<sub>00</sub> and 1.001 THz for TE<sub>00</sub>) provided by the non-unity aspect-ratio. Different coupling of the TE and TM fundamental modes over the measured range in Fig. 6.1(d) is attributed to the polarization plane rotation in the optical fiber before coupling to the on-chip bus waveguide [250]. Once the polarization is properly adjusted at a certain wavelength for the resonance of a particular mode family, one can measure its  $Q$ -factor. Both fundamental modes have comparable loaded linewidths of 370 - 550 MHz, corresponding to the  $Q$ -factors of  $0.55 - 0.75 \times 10^6$  (see Fig. 6.1(e)).

### 6.3 DKS states at 1 $\mu\text{m}$

The experimental set-up for the DKS generation is shown in Fig. 6.1(a). The light from a tunable 1060-nm CW diode laser (Toptica CTL 1050) is amplified with an ytterbium-doped fiber amplifier and coupled to the chip through a lensed fiber. The output signal was collected with another lensed fiber, and its spectral and noise characteristics were analyzed. We also employ a soliton probing technique described in Chapter 3, which uses a phase-modulated pump and a vector network analyser to retrieve a system response allowing us to unambiguously identify DKS formation and track the detuning of the pump from a cavity resonance [114].

In order to access the soliton state, which by the analogy with DKS operating at 1550 nm are supported in the effectively red-detuned regime ( $\omega_p - \omega_0 = 2\pi\delta > 0$ , where  $\omega_p$  and  $\omega_0$  are the angular frequencies of the pump laser and pumped resonance), we use the pump forward tuning technique [9]. Such simple approach is sufficient for our samples, rather than complex techniques such as power kicking [84] or fast frequency modulation [106]. This can be explained with relatively small pump powers used for the soliton generation. They allowed to avoid the region of transient chaos [42] causing the elimination of intracavity pulses during the transition to a stable soliton state. In this case thermal effects associated with the change of intracavity power do not significantly affect the pump-cavity detuning, and the system stays within the soliton existence range after DKS are formed [228].

We use an on-chip pump power of  $\sim 1$  W to tune into resonances of the fundamental TM mode family, which according to our simulations should provide anomalous GVD at around 1060 nm. Low tuning speeds on the order of a few GHz/second (i.e. using the laser cavity piezo) were chosen and enabled simultaneous monitoring of the cavity state by measuring the system response signal as well as an optical spectrum of the output light in order to track the excitation of DKS states.

When tuning the pump over the cavity resonance, the cavity reveals modulation instability and noisy Kerr comb formation while the pump laser is on the blue side (see Fig. 6.2(a, top)). Apart from the characteristic spectral shape of the noisy Kerr comb, strong intensity noise is also observed (Fig. 6.2(b)) reproducing the typical behavior of the driven microresonator system at 1550 nm. Upon further pump tuning we observe the transition to soliton regime. It is accompanied by a sudden change of the optical spectrum to the secant hyperbolic-like shape, and an appearance of the double-peak structure in the system response representing the coexistence of the soliton ( $\mathcal{S}$ -resonance) and the CW-background ( $\mathcal{C}$ -resonance) components inside the cavity (see Chapter 3 for more details). To explore the soliton existence range of the generated DKS state, the response measurements were also carried out while tuning the pump laser towards longer wavelength corresponding to the increase of the effective detuning (Fig. 6.2(d)). The shift of the  $\mathcal{C}$ -resonance position (which indicates effective detuning) to higher frequencies is

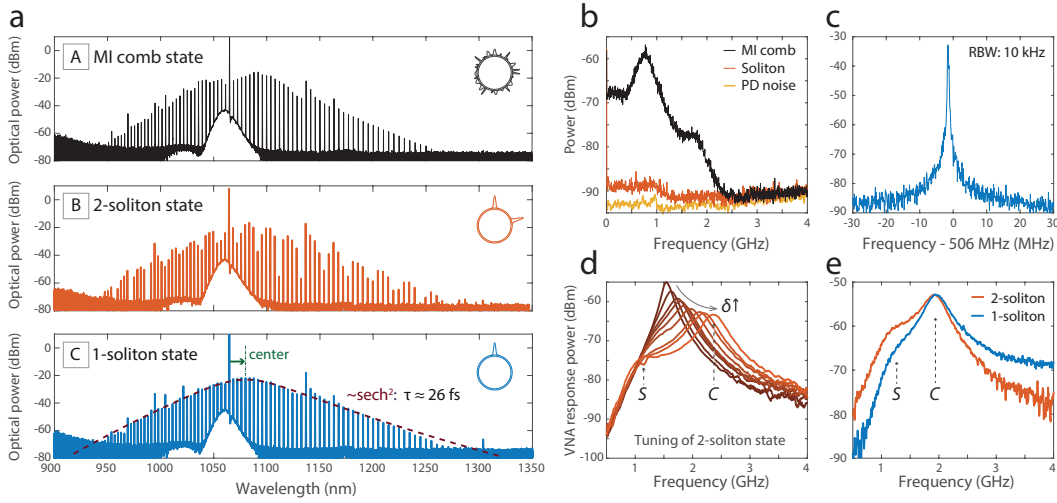


Figure 6.2 – (a) Optical spectra of the modulation-instability comb state (A) and two soliton states (B, C) obtained in a 1-THz  $\text{Si}_3\text{N}_4$  microresonator (pump is located at around 1065 nm). The transition from two-soliton state (B) to single soliton state (C) was obtained by a backward tuning technique of the pump laser. Insets show the estimated positions of the DKS in corresponding states. The single soliton state was fitted with a  $\text{sech}^2$  envelope (dashed dark blue), with estimated duration of 26 fs. The green arrow shows the Raman-induced red spectral shift of the soliton spectrum with respect to the pump line. (b) Intensity noise of MI comb state (black), soliton states (red) shown in (a) and the noise floor of the photodiode (PD) used for measurements (yellow). (c) Heterodyne beatnote of the soliton comb line around 1050 nm with a second CW laser. (d) System response evolution in the two-soliton state shown in (a), when increasing the pump-cavity detuning ( $\delta$ ). The positions of characteristic  $\mathcal{C}$ - and  $\mathcal{S}$ -resonance are indicated with  $C$  and  $S$  letters correspondingly. (e) System response evolution when the DKS state is switched from two-soliton to single soliton state. The amplitude of the  $\mathcal{S}$ -resonance has decreased, because the number of intracavity solitons reduced.

clearly seen and essentially reproduces the dynamics of similar response signals measured for DKS at 1550 nm [114]. Finally, the transition to the soliton regime has also been verified by the drastic reduction of the intensity noise of the output light (see Fig. 6.2(b)), and a narrow heterodyne beatnote of the selected comb line at around 1050 nm with another low-linewidth CW diode laser (Fig. 6.2(c)).

We also demonstrate that the obtained soliton states can experience switching by applying the backward tuning technique, which relies on the thermal nonlinearity of microresonators, and due to the presence of transient chaos region (see Chapter 5) allows the number of DKS circulating inside the cavity to be changed in a robust and controllable manner [114]. Figure 6.2(a) shows the switching from a two-soliton to a single-soliton state. The switching has been confirmed with the response measurements as shown in figure 6.2(e). A decrease in the amplitude of the soliton-number-related  $\mathcal{S}$ -resonance of the response indicates the reduction of the intracavity number of pulses, while the

cavity-related  $\mathcal{C}$ -resonance is almost unchanged.

By fitting the spectrum of the final single soliton state with a  $\text{sech}^2$  envelope we can estimate the soliton duration (Fourier-transform-limited) from its 3-dB bandwidth - it corresponds to 26 fs. We also note the presence of significant soliton red spectral shift ( $\sim 4.1$  THz in the present case) with respect to the pump line, which is mainly attributed to the Raman effect and observed for all DKS states generated above [158, 231].

## 6.4 Octave-spanning soliton states driven at 1 $\mu\text{m}$

Reaching the octave-spanning operation of DKS is an important step in the development of Kerr frequency combs, as it enables the common  $f - 2f$  scheme for offset frequency detection and self-referencing required by multiple applications in optical frequency metrology and low-noise microwave synthesis [251]. Octave-spanning DKS states have been only recently demonstrated experimentally [249, 87]. In the present section we demonstrate that DKS-based combs operating at 1  $\mu\text{m}$  can be engineered to have octave-spanning bandwidths despite operating close to the normal GVD region in the  $\text{Si}_3\text{N}_4$  platform.

### 6.4.1 Dispersion engineering of silicon nitride microresonators at 1 $\mu\text{m}$

The access to the broadband and octave-spanning optical combs is possible via the formation of soliton dispersive waves, enabling the extension of the soliton comb spectrum in the normal GVD region [84]. In order to control the spectral positions of dispersive waves, one needs to be able to engineer the dispersion of the microresonator waveguide, which in the simplest case is achieved by the variation of the dimensions of the waveguide cross-section.

In order to experimentally demonstrate the ability to engineer the dispersion of silicon nitride microresonators at around 1- $\mu\text{m}$  wavelength, one needs to show a consistent trend in the measured dispersion matching to the simulations prediction, when the geometry of the devices is changed. However, due to large free spectral range of our devices ( $\sim 1$  THz) and small dispersion terms (e.g.  $D_2/2\pi \sim 20 - 30$  MHz), one has to measure resonance frequencies within a broad range of several hundreds of nanometers in order to estimate the dispersion with an acceptable level of precision [43, 44].

Instead of doing this challenging measurements, one can also measure the spectral locations of the phase-matching-induced enhancements of comb lines in the noisy comb states, which correspond to  $D_{\text{int}}/2\pi = 0$  and provide a rough estimation for the position of soliton dispersive wave for a given geometry [164, 84, 252]. The positions of such phase-matched regions strongly depend on dispersion parameters and are easily tracked in experiment using optical spectrum analyzer, allowing for convenient comparison to

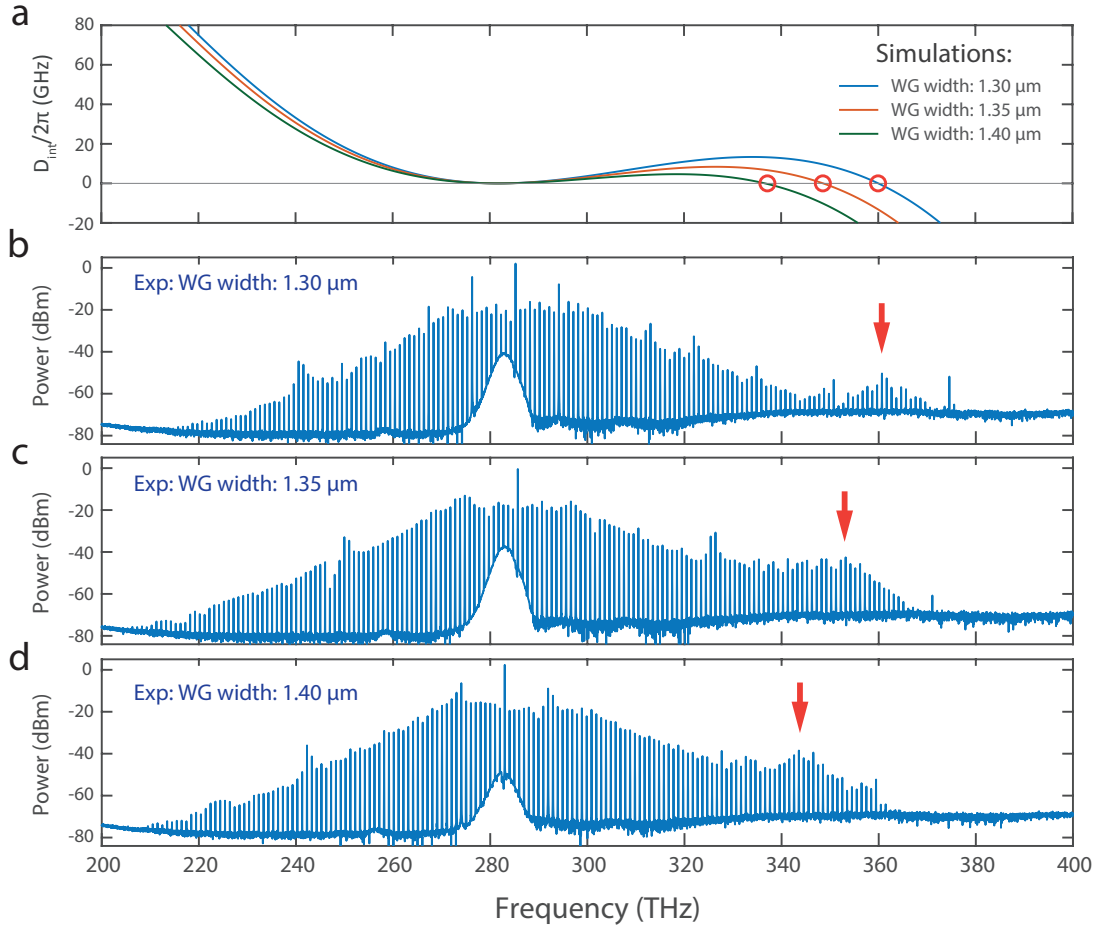


Figure 6.3 – (a) FEM-based simulations of integrated dispersion ( $D_{\text{int}}/2\pi$ ) in 1-THz silicon nitride microring resonator with waveguide height of 0.74  $\mu\text{m}$ , various waveguide widths of 1.30, 1.35, 1.40  $\mu\text{m}$ , and sidewall angle of 77°. Red circles mark spectral position of the phase-matching points ( $D_{\text{int}}/2\pi = 0$ ); (b)-(d) Experimental optical spectra of the fabricated 1-THz  $\text{Si}_3\text{N}_4$  microresonators with the height of 0.74  $\mu\text{m}$  and waveguide widths of 1.30, 1.35 and 1.40  $\mu\text{m}$  (by design). The positions of the short-wavelength phase-matching regions are indicated with red arrows.

simulations. It is important, however, to highlight here that the generation of solitons is not needed for these measurements, and may even give improper results, because the exact spectral position of the dispersive in a soliton state is slightly shifted from the phase-matched region where  $D_{\text{int}}/2\pi = 0$  [252].

We measure optical spectra of noisy Kerr comb states (i.e. operating in regime of chaotic modulation instability) in fabricated devices with a different geometry (height of 0.74  $\mu\text{m}$  and widths of 1.30, 1.35, 1.40  $\mu\text{m}$ ) and traced the positions of the short-wavelength phase-matching region (see Figure 6.3(b-d)). The positions are marked with red arrows, and demonstrate an increasing trend from 343 THz to 360 THz as the waveguide widths decreases.

## 6.4. Octave-spanning soliton states driven at 1 $\mu\text{m}$

We have also simulated the dispersion profile for the same set of the resonator waveguide geometries with height of 0.74  $\mu\text{m}$ , widths of 1.30, 1.35 and 1.40  $\mu\text{m}$  and sidewall angle of  $77^\circ$ . The positions of phase-matching points (marked with circles in Fig.1(a)) show similar trend as in fabricated samples, and coincide well with the experimentally obtained phase-matching regions.

### 6.4.2 Experimental generation of octave-spanning DKS states

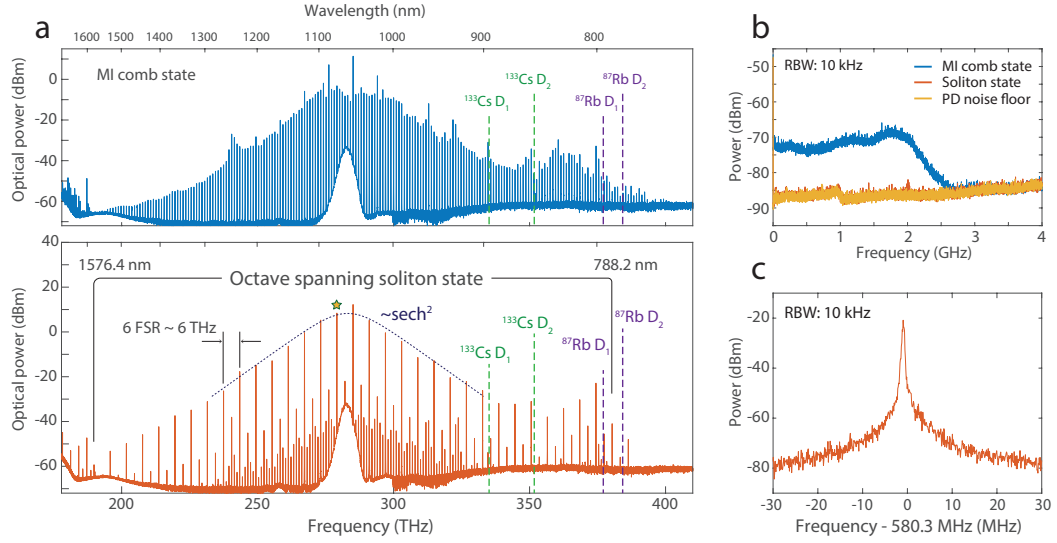


Figure 6.4 – (a) Spectrum of a noisy Kerr comb state, obtained with  $\sim 800$  mW on-chip power (pump is located at around 1051.5 nm), from the microresonator with optimized dispersion for octave-spanning operation. Green and purple dashed vertical lines indicate the spectral locations of Cs and Rb optical atomic transitions. (b) Spectrum of the octave-spanning soliton state obtained in the same microresonator. The spectrum is fitted with  $\text{sech}^2$  envelope (dashed dark blue), from which a soliton duration of  $\sim 18$  fs is inferred. The set of enhanced lines below 190 THz corresponds to the second diffraction order of the optical spectrum analyser diffraction grating and are thus artefacts. (c) Intensity noise of the octave-spanning MI comb state (blue) and soliton state (red) shown in (a). Yellow trace shows the noise floor of the photodetector used for the measurements. (d) Heterodyne beatnote of the soliton comb line (marked with a star in panel (b)) with a second CW laser.

For the generation of the octave-spanning DKS states we used the same set of microresonators with FSR of 1 THz as described in section 6.2. Based on the results of the previous subsection, we choose the devices having a waveguide geometry of  $1.30 \times 0.74 \mu\text{m}$ , which was designed to have low anomalous GVD and satisfy phase-matching conditions at around 800 nm for dispersive wave formation[84]. This spectral region is particularly interesting due to the presence of optical frequency standards based on the two-photon Rb transitions [253] which can be used for comb referencing. We applied the aforementioned low-speed tuning technique with an estimated on-chip power of  $\sim 800$  mW to achieve the

formation of the noisy comb (see Fig. 6.4(a)) followed by the soliton state (Fig. 6.4(b)).

The resulting spectrum of the soliton state spans over more than an octave from 776 to 1630 nm ( $> 200$  THz). As expected from the simulations, it is significantly extended towards shorter wavelengths due to the emission of the dispersive wave via soliton-induced Cherenkov radiation at 800 nm. The 3-dB bandwidth of the spectrum fitted with a  $\text{sech}^2$  envelope is estimated as 18 THz, which corresponds to a pulse duration of  $\sim 18$  fs. A peculiar shape of the DKS state is attributed to the formation of a soliton crystal state, which here is estimated to be formed by ordered co-propagating DKS ensemble of 6 soliton pulses [197, 228]. As discussed in Chapter 5 such soliton crystals are typically formed in the presence of strong local spectrum deviations caused by inter-mode interactions among transverse mode families (avoided mode crossings), and in contrast to single-soliton states are featuring high conversion efficiency (owing to the high number of intracavity pulses), which in the present case approached 50%. Similarly to the DKS states demonstrated in the previous section 6.3, the presented state is also characterized by a low-noise performance with a strongly suppressed intensity noise in comparison to the noisy modulation-instability (MI) comb (see Fig. 6.4(c)), and a narrow heterodyne beatnote of the generated comb line with another CW laser (Fig. 6.4(d)).

### 6.5 DKS states in hybridized modes

The behavior of Kerr combs and, in particular, DKS states are in a large extent defined by the dispersion properties of the cavity. One of the key requirements for DKS formation is the anomalous GVD of the microresonator, which can be achieved by overcompensating the normal material dispersion with the waveguide dispersion contribution (see Chapter 1). At short wavelengths, however, increased normal material GVD can represent a significant issue (e.g. for  $\text{Si}_3\text{N}_4$  in the visible domain) as it can hardly be compensated for the fundamental guided modes thus hindering bright DKS formation. Apart from the global dispersion landscape comprised of the material- and waveguide-related components, the dispersion properties also include spectrally localised dispersion modifications - avoided mode crossings. AMX are typically result from the formation of guided hybridized modes, which can appear due to the interaction of different transverse mode families [254]. Although being spectrally localised, such AMX-s can lead to complex and diverse effects on the dynamics of DKS states, such as dispersive wave formation, soliton recoil, temporal soliton ordering, appearance of quiet operation points and inter-mode soliton breathing [9, 193, 46, 197, 228].

All of these effects were normally investigated in the regime, when the position of modal crossing is quite far from the pumped microresonator mode, however the hybridized modes forming the AMX can be also *directly* used for the soliton generation. This can happen when one of the two hybridizing modes acquire significant spectrally localized boost in the anomalous GVD (while another one acquires significant normal GVD).

## 6.5. DKS states in hybridized modes

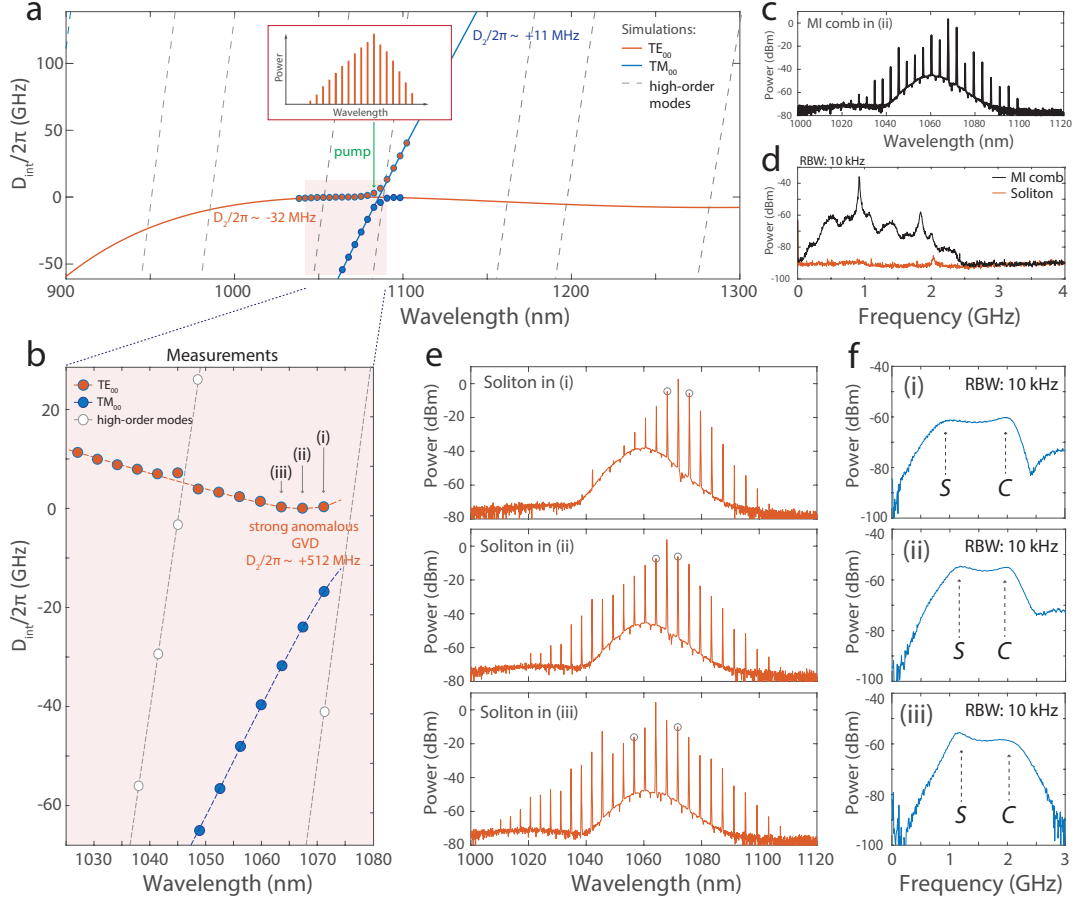


Figure 6.5 – (a) Scheme of the avoided mode crossing formation. Solid and dashed lines show the simulated integrated dispersion for the fundamental and high-order modes of 1-THz Si<sub>3</sub>N<sub>4</sub> microresonator with dimensions of  $1.45 \times 0.74 \mu\text{m}$ . Red and blue circles schematically indicate the dispersion profile of the hybridised modes forming AMX. (b) Measurements [43] of the mode structure of a 1-THz Si<sub>3</sub>N<sub>4</sub> microresonator with the dimensions of  $1.45 \times 0.74 \mu\text{m}$  simulated in (a). Mode families are distinguished based on their FSRs. General dispersion trends cannot be faithfully identified due to the bandwidth limitations of our measurement setup, however a strong local anomalous group velocity dispersion for three consecutive resonances (i), (ii), (iii) of the TE<sub>00</sub> mode family above 1064 nm can be observed. Dashed lines fit the integrated dispersion of different modes within the measurements range. (c) Optical spectrum of a noisy comb state, obtained in resonance (ii) from (b). (d) Intensity noise measurements of the noisy modulation-instability comb (MI comb, black) and the dissipative Kerr soliton (soliton, red) states, obtained by pumping the resonance (i) from (b). (e) Optical spectra of the DKS states obtained by pumping resonances (i), (ii), (iii) from (b). Grey circles indicate the positions of primary comb lines. (f) Response measurements of DKS states represented in (e). The positions of characteristic  $\mathcal{C}$ - and  $\mathcal{S}$ -resonance are indicated with  $C$  and  $S$  letters, correspondingly.

The principle is schematically explained in Figure 6.5(a), where the simulated integrated dispersion is plotted (solid lines) for several modes of the 1-THz resonator ( $0.74 \times 1.45 \mu\text{m}$ , sidewall angle  $77^\circ$ ). We consider the TE fundamental mode family, which according to our simulations has normal GVD ( $D_2/2\pi = -32$  MHz), and note that it has multiple modal crossings with other mode families. The frequency degeneracy of different mode families that appears at such modal crossings can lead to mode interaction mediated by scattering processes in the microresonator and induce the formation of AMX. The dispersion profile of one of these AMX is schematically shown in figure 6.5(a) (circles) to highlight its strong deviation from the simulation results obtained in the absence of scattering. Figure 6.5(b) shows the measured [43, 44] mode structure of one of the fabricated samples with the same geometry ( $0.74 \times 1.45 \mu\text{m}$ ), where the formation of the described AMX is experimentally observed to be close to the simulated spectral position of 1080 nm (see Fig. 6.5(b)). Mode-interaction-induced strong resonance shifts cause a dramatic change on the local GVD of the TE mode family turning it from normal with  $D_2/2\pi = -32$  MHz (simulated) to highly anomalous, with  $D_2/2\pi$  reaching  $+510$  MHz (measured). We therefore evidence an AMX-induced change in the local group velocity dispersion.

We also make a side remark here to highlight that the mode interactions that happens in our microresonator and lead to dispersion alterations differ from the mode interactions often observed in integrated waveguides due to the phase-matching between different transverse mode families (matching of effective refractive indices) [255]. In our case, the mode interaction process, which induces dispersion deviation used for DKS is caused by Rayleigh scattering from surface and volume inhomogeneities as well as the bus-resonator coupler. In order to demonstrate this fact we simulated effective refractive indices for fundamental and two high-order modes in our waveguide (see figure 6.6). One can see that the fundamental mode families ( $\text{TE}_{00}$ ,  $\text{TM}_{00}$ ) do not cross over the full simulated frequency range, and thus main process enabling the mode interaction here (if the modes are frequency-degenerate) is scattering. We note that this mode hybridization process is different from the phase-matching-based mode hybridization used in the work by Lee *et al.* [86], which is inherent to the geometry.

Driving the modes with strong anomalous GVD of  $\sim 510$  MHz as we observed in our device (when  $\sqrt{\kappa/D_2} < 1$ ) should result in the formation of a natively mode-spaced comb [66, 59], whose primary lines appear 1 FSR away from the pump due to the closely-located MI gain peaks. Previous works have reported that such combs can appear directly in a mode-locked regime [55] which, however, is in contrast with our observations.

In experiments we again used the same pump tuning technique as in previous sections, applied to hybridized modes forming AMX. Using the system response and intensity noise measurements we observe the standard soft-excitation-route of a Kerr comb formation, which includes the appearance of primary comb lines, development of the chaotic modulation instability (MI, Fig. 6.5(c)) and the transition to a soliton regime (Fig. 6.5(e)),

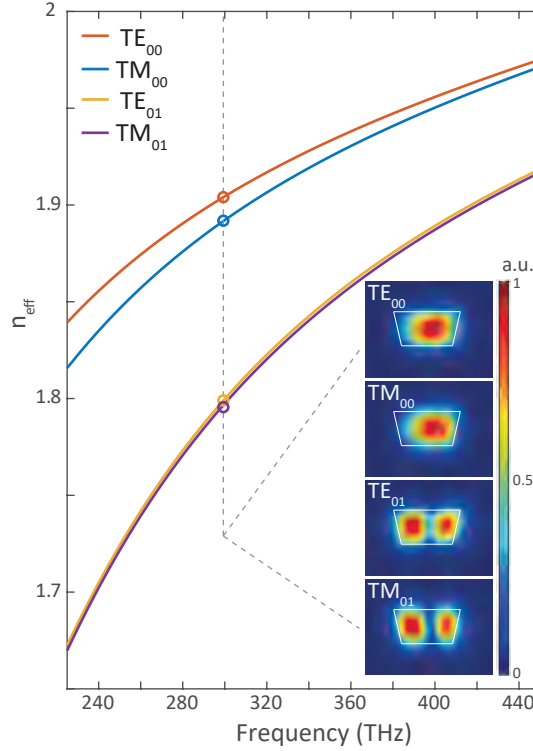


Figure 6.6 – (a) Effective refractive indices of different transverse mode families in silica-cladded silicon nitride waveguide with waveguide width of  $1.45\ \mu\text{m}$ , height of  $0.74\ \mu\text{m}$  and sidewall angle of  $77^\circ$ . Insets show the normalized field distribution of four modes:  $\text{TE}_{00}$ ,  $\text{TM}_{00}$ ,  $\text{TE}_{01}$  and  $\text{TM}_{01}$  obtained for the optical frequencies marked with the dashed line.

which was verified by the appearance of a characteristic dual-peak system response and low intensity noise (Fig. 6.5(e,f)). Similar behavior was observed over three consecutive resonances (cases I, II, III in Fig. 6.5(e)), where the corresponding soliton states were generated. An interesting observation can be made regarding the spectral bandwidth of the obtained soliton states. As a result of the localised character of the anomalous GVD of hybridized modes, the actual value of the dispersion terms (and particularly  $\frac{D_2}{2\pi}$  term) varies from one resonance to another, leading to the different effective detunings for generated comb lines and altering the resulting spectral width. We also note here, that due to the contribution of higher-order dispersion terms around AMX, the obtained DKS spectra cannot be faithfully fitted with a  $\text{sech}^2$  envelope.

We finally closely investigated one of the dissipative Kerr soliton (DKS) states, obtained in hybridized modes. We have generated the state pumping the resonance at 1067 nm (resonance (ii) in the Fig. 6.5(b)). In order to unambiguously demonstrate the formation of DKS, we implemented slow backward pump tuning with a speed  $< 0.5\ \text{GHz/s}$ . At the same time we monitored the state using soliton probing technique [114], as well as the measured optical spectrum of the state and its intensity noise. Figure 6.7(a) shows the evolution of the system response from the initial state (on the right) to the final state (on

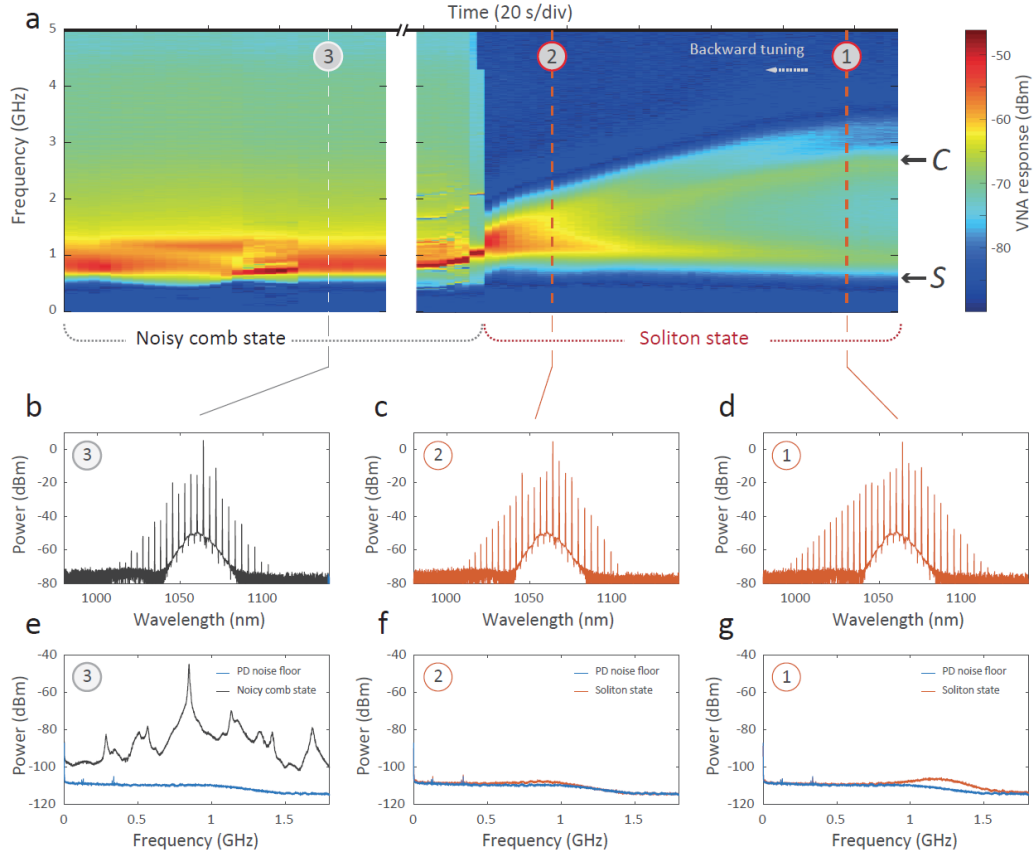


Figure 6.7 – (a) Evolution of the response measurements of the state obtained by pumping the hybridized mode at 1067 nm (resonance (ii) in Fig. 6.5(b)). The state evolves from the right to the left, following the backward tuning sweep of the pump laser (from longer to the shorter wavelengths). Initial positions of  $\mathcal{C}$ - and  $\mathcal{S}$ -resonances are indicated with  $\mathcal{C}$  and  $\mathcal{S}$ . (b) - (d) Optical spectra obtained at different stages (1-3) of the backward tuning shown in (a). (e) - (h) Intensity noise of the total comb power obtained at different stages (1-3) of the backward tuning shown in (a).

the left). Response measurement of the initial state reveals an existence of two response peaks, which we attribute to the cavity ( $\mathcal{C}$ -) and soliton ( $\mathcal{S}$ -) contributions. While tuning the state backward [114], we can see how the response evolves: the two peaks are getting closer to each other indicating the reduction of the pump detuning. The spectrum of the state maintains a smooth envelope with moderate line-to-line variation except a small modal crossing at around 1050 nm. The low intensity noise also stays almost unchanged reaching the photodiode noise floor. After  $\mathcal{C}$ - and  $\mathcal{S}$ -resonances are merged, the system suddenly returns to the noisy comb state, which is indicated by broadband intensity noise (Fig.2(e)) and a structured optical spectrum (Fig.2(b)). These measurements are qualitatively similar to the evolution of response measurements of the bright soliton states in  $\text{Si}_3\text{N}_4$  and  $\text{MgF}_2$  platforms at 1550 nm, when the system switches from the DKS to a comb state [114] (see also Chapter 3).

The demonstrated soliton states generated in hybridised modes by exploiting their strong anomalous GVD can represent an alternative way to deterministically generate soliton-based optical combs in arbitrary wavelength regions. This approach can be especially useful for presented here  $\text{Si}_3\text{N}_4$  platform to generate soliton states operating at 780 nm or even further into the visible domain, where the normal GVD cannot be efficiently compensated by standard means, but can be locally altered using e.g. predesigned or thermally-controlled AMX-s [56].

## 6.6 Conclusion

We have demonstrated the first photonic-chip-integrated soliton-based optical frequency comb sources driven with 1  $\mu\text{m}$  pump source. The spectra of achieved DKS states are able to span over an octave, and cover the common optical frequency standards in alkali vapors, as well as the significant part of the near-infrared window for biological tissues. Moreover, we have shown that DKS states can be generated in hybridized modes of the microresonators around avoided mode crossings by directly exploiting their localized anomalous GVD, what represents an alternative approach for the generation of DKS combs in the regions with strong normal GVD (e.g. at shorter wavelength in SiN, and in other materials). From the broader perspective, our work gives a strong evidence of the technological readiness of  $\text{Si}_3\text{N}_4$  platform for the soliton-based operation in the near-infrared regime around 1  $\mu\text{m}$  (including comparably good quality factors and the means of dispersion engineering), which makes it a highly promising candidate for multiple biological and other applications in this wavelength domain, including OCT and dual-comb CARS.

Finally, we also would like to draw the readers attention to few other recent works, where the formation of the DKS states was demonstrated at 780 nm [86, 256, 17].



# 7 Applications of dissipative Kerr solitons

This chapter covers two main applications of dissipative Kerr solitons - for massively parallel optical coherent communication, and ultrafast distance measurements. The results demonstrate the potential of Kerr soliton combs, both as multi-wavelength optical sources and local oscillators for massively parallel WDM transmission as well as efficient LiDAR engines using the dual-comb synthetic-wavelength interferometry approach. The results are adapted from P. Marin-Palomo\*, J.N. Kemal\*, **M. Karpov\*** *et al.*, "Microresonator-based solitons for massively parallel coherent optical communications", *Nature*, 546 (7657), p. 274, (2017) and P. Trocha\*, **M. Karpov\*** *et al.*, "Ultrafast optical ranging using microresonator soliton frequency combs", *Science*, 359 (6378), pp. 887-891, (2018).

## 7.1 Dissipative Kerr solitons for massively parallel coherent communication

Today's pace of the development of new technologies, increasing number of internet users, and their usage of multiple video and audio streaming services as well as the game industry have led to an enormous amount of data which is being continuously generated, stored and transmitted all over the world. This nearly exponential growth in data traffic has obtained an additional boost with the recent advent of cloud storage and cloud computing technologies, as well as the onset of the internet-of-things (IoT) era, which is expected to provide the next generation with an additional 90 zettabytes of data from IoT devices by 2025 (current sum of the all the world's data to be around 33 zettabytes for 2018 [257]). All of the above set an increasing demand for high-speed high capacity systems and channels for data transmission.

Since the early 1980-s optical fiber communication has become a standard for long-distance (long-haul) data transmission due to the high frequencies of optical carriers ( $\sim 100$  THz) and consequently - higher available bandwidth, as well as low losses of

---

\*These authors contributed equally to the work

optical fibers. This has allowed data transmission over tens and even hundreds of kilometers. The new era in fiber optics communication has begun with the advent of wavelength-division multiplexing (WDM), which has enabled a significant increase in line rates of communication systems. The concept of WDM consist in multiplexing the number of optical data carriers transmitted through the same fiber using different wavelengths for encoding independent data streams. WDM optical links have become increasingly important and now represent a standard for long-haul and metropolitan networks, where the majority of today's traffic is being circulated.

Recently, it has been suggested that frequency combs could revolutionize high-speed optical communications, offering tens or even hundreds of well-defined narrow-band optical carriers for massively parallel WDM [258, 259, 260]. Unlike carriers derived from a bank of individual laser modules, the tones of a comb are intrinsically equidistant in frequency, thereby eliminating the need for individual wavelength control and for inter-channel guard bands [258, 260]. In addition, when derived from the same comb source, stochastic frequency variations of optical carriers are strongly correlated, permitting efficient compensation of impairments caused by nonlinearities of the transmission fiber [261]. For application in optical communications, frequency comb sources must be compact. In recent years, various chip-scale comb sources have been demonstrated [262, 263] that enable transmission of WDM data streams with line rates of up to 12 Tbit/s. However, transmission at higher line rates requires more carriers and lower noise levels, and still relies on spectral broadening of narrow-band seed combs using dedicated optical fibers [258, 259, 260] or nanophotonic waveguides [264]. In addition, generating uniform combs with a broadband spectral envelope often requires delicate dispersion management schemes, usually in combination with intermediate amplifiers [259]. Such schemes are difficult to miniaturize and are not readily amenable to chip-scale integration. Moreover, with a few exceptions at comparatively low data rates [265], all advanced comb-based transmission experiments exploit the scalability advantages only at the transmitter, not at the receiver, where individual continuous-wave lasers are still used as optical local oscillators for coherent detection.

Kerr combs, generated in integrated photonic microresonators are able to provide broadband optical combs that can overcome the scalability limitations of massively parallel optical transmission at both the transmitter and the receiver. Microresonator-based Kerr comb sources [7, 266] have advantages such as a small footprint (the physical area covered by the comb source), a large number of narrow-linewidth optical carriers, and line spacings of tens of gigahertz, which can be designed to fit established WDM frequency grids. However, although these advantages have been recognized, previous transmission experiments [69] were limited to aggregate line rates of 1.44 Tbit/s owing to strong irregularities of the optical spectrum associated with the specific Kerr comb states. These limitations can be overcome by using DKS combs, which we demonstrate in the present chapter.

## 7.2 Microresonator device and experimental setup

The experiment relies on integrated  $\text{Si}_3\text{N}_4$  microresonators for the generation of DKS frequency combs (Fig. 7.1). We use devices similar to the ones described in the Chapter 2. The microresonators are fabricated using the photonic Damascene process [28], the microresonator waveguides have a height of 800 nm and a width of about 1500 nm allowing for anomalous GVD. The resonators have an FSR of  $\sim 100$  GHz and intrinsic quality ( $Q$ ) factors exceeding  $10^6$ .

A setup for the DKS comb generation is shown in Fig. 7.1(a). It includes an ECD laser as a seed (TLB-6700 New Focus and/or TSL-220 Santec), amplified with an EDFA. A high-power bandpass filter is used to suppress amplified spontaneous emission (ASE) before coupling to the chip via lensed fibers. The outcoupled light is fed through a notch filter located at the pump wavelength to suppress the strong pump before employing the comb for transmission experiments. In order to access DKS states a standard forward tuning procedure was used [9], which consists of tuning the pump frequency through the resonance from a blue-detuned wavelength to a predefined red-detuned wavelength and results in the generation of a multiple-soliton state. Since for our experiments, the formation of the single soliton states was essential, because it provides a smooth envelope with no significant power variation over the operational bandwidth (C and L telecommunication bands), we also used the backward tuning approach (see Chapter 3) in order to deterministically switch the initial multiple soliton state to a single-soliton (see Fig. 7.1(b)). The resulting power spectrum of the single DKS state is shown in Fig. 7.1(c) and exhibits a 3-dB spectral bandwidth of approximately 6 THz. The soliton comb states are remarkably stable for many hours in a laboratory environment, which is key to the transmission experiments presented in the following sections.

## 7.3 Optical coherent communication experiments with DKS

We focus on three experiments, which exploit the extraordinarily smooth, broadband spectral envelope and the inherently low phase noise of DKS combs for massively parallel coherent communications.

In the first experiment, we transmit data on 94 carriers that span the entire telecommunication C and L bands with a line spacing of about 100 GHz. Using 16-state quadrature amplitude modulation (16QAM) to encode data on each of the lines, we achieve an aggregate line rate of 30.1 Tbit/s. In the second experiment, we double the number of carriers by interleaving two DKS combs generated in two separate  $\text{Si}_3\text{N}_4$  microresonators. This gives a total of 179 carriers and an aggregate line rate of 55.0 Tbit/s. We use these carriers for a data transmission experiment over a distance of 75 km - the highest data with a chip-scale frequency comb source in comparison to previous demonstrations. In the third experiment, we demonstrate coherent detection using a DKS comb as a

multi-wavelength local oscillator. We use two DKS combs with 93 carriers to transmit and receive an aggregated line rate of 37.2 Tbit/s. In this experiment, the local-oscillator comb is coarsely synchronized to the transmitter comb, and digital signal processing is used to account for remaining frequency differences.

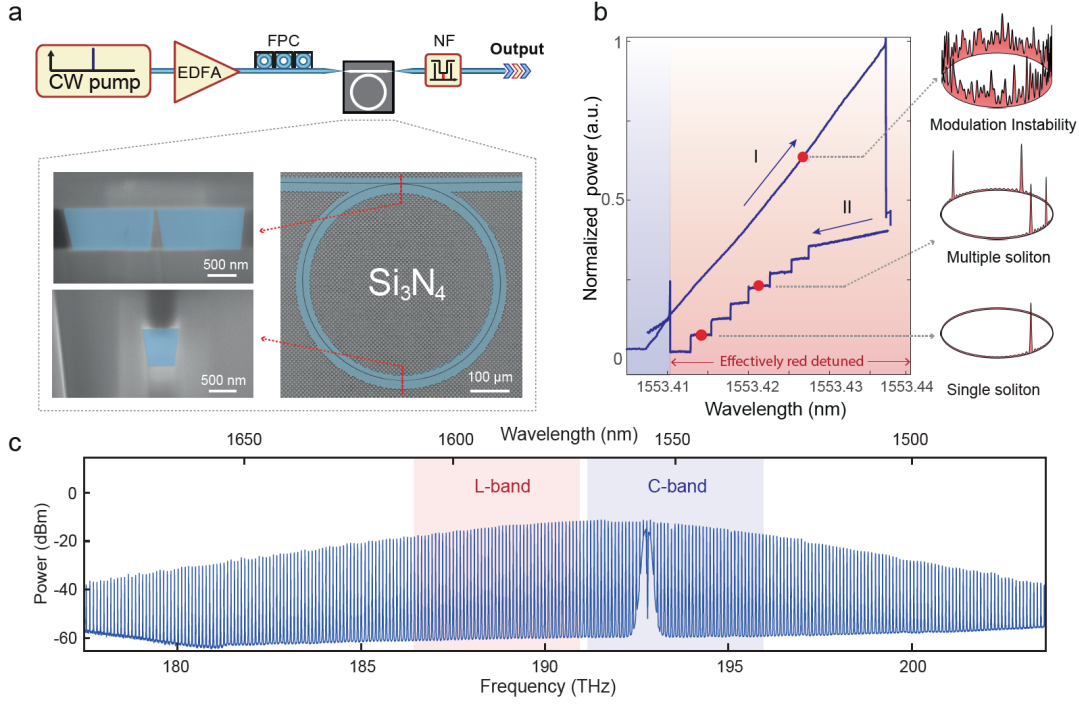


Figure 7.1 – (a) Setup for the soliton comb generation used in experiments: 100-GHz Si<sub>3</sub>N<sub>4</sub> microresonator is pumped by a tunable CW laser (CW pump) amplified by an erbium-doped fiber amplifier (EDFA). Lensed fibers are used to couple light to the chip. A fiber polarization controller (FPC) is used to match the input light polarization to one of the microresonator mode families. After the microresonator, a notch filter (NF) suppresses the remaining pump light. The insets show false-color scanning electron microscopy images of a Si<sub>3</sub>N<sub>4</sub> microresonator. Right inset: Top view. Left insets: cross-sections of the resonator waveguide ( $0.8 \times 1.65 \mu\text{m}^2$ ) at the coupling point (top) and at the tapered section (bottom,  $0.8 \times 0.6 \mu\text{m}^2$ ). The tapered section is used for suppressing higher order modes families [225] while preserving high  $Q$ -factors ( $Q \sim 10^6$ ). (b) The evolution of the generated comb power versus pump laser wavelength in the single-soliton generation process consisting of two steps: (I) forward tuning for the generation of multiple-soliton state (II) backward tuning to access the single soliton state. The insets on the right schematically show the corresponding intracavity waveforms in different states (MI, multiple and single soliton state). (c) Measured spectrum of a single-soliton frequency comb after suppression of residual pump light. The frequency comb features a smooth spectral envelope with a 3-dB bandwidth of 6 THz comprising hundreds of optical carriers extending beyond the telecommunication C and L bands (blue and red, respectively).

#### 7.3.1 Optical transmission using single DKS

The general concept of massively parallel data transmission using a frequency comb as a multi-wavelength light source is depicted in Fig. 7.2(a) and demonstrated in the first transmission experiment. To generate a single-soliton comb we use the setup similar to the one described in Fig. 7.1(a) and marked in the current figure as FCG (frequency comb generator). The comb is amplified in the first amplification stage to a level of approximately 5 dBm/carrier, and then is sent to a demultiplexer (DEMUX). In our experiment, the demultiplexer is implemented by two programmable filters (Finisar WaveShaper) along with C- and L-band filters, which act as deinterleavers to separate the comb first into the C- and L-bands, and then each of the resulting parts into two sets of even and odd carriers. In this stage, the waveshapers are also used to equalize the powers in respective bands compensating the  $\text{sech}^2$ -profile. Each of the programmable filters separates its own part of the DKS comb (C or L) in even and odd lines, and each of them is again amplified in the second amplification stage, which comprises 4 EDFAs (2 for odd and even carriers of the C band, and 2 for the L-band). After this the odd and even carriers from the C and L bands are recombined using a C/L multiplexer, and are fed to two IQ modulators (IQ-mod on the Fig. 7.1(a)). To emulate massively parallel WDM transmission in our laboratory, we rely on a simplified scheme that uses two independent data streams on neighboring channels, which explains the DKS comb separation in the even and odd sets. We use pseudorandom bit sequences (PRBS) with lengths of  $2^{11} - 1$  using quadrature phase-shift keying (QPSK) or 16QAM at a symbol rate of 40 gigabauds (GBd) along with band-limited Nyquist pulses. Nyquist pulse shaping leads to approximately 40 GHz wide rectangular power spectra for each of the carriers (Fig. 7.2(b)). We note that in our emulation experiment the same data stream is encoded on *all* carriers of even or odd sets. After data encoding, the independent data streams are combined using an optical multiplexer (MUX), which in our experiments was represented by a regular fiber coupler followed by an emulation of the polarization-division multiplexing using the split-and-combine method, whereby the data stream of one polarization is delayed by approximately 240 bits with respect to the other to generate uncorrelated data [267]. Finally, the resulting DKS comb with encoded data was amplified in the third amplification stage using the C+L-band amplifier and sent through the 75 km of optical fiber.

At the receiver side, each channel is individually characterized using a continuous-wave laser as the local oscillator along with an optical modulation analyzer, which extracts signal quality parameters such as the error-vector magnitude (EVM) and the bit error ratio (BER). The BERs of the first transmission experiment are depicted in Fig. 7.2(e) using red triangles, with different BER thresholds indicated as horizontal dashed lines. For a given forward error correction (FEC) scheme, these thresholds define the maximum BER of the raw data channel that can still be corrected to a BER of less than  $10^{-15}$ , which is considered error-free [268]. Among the 101 carriers derived from the comb in the C and L bands, 94 channels were used for data transmission, resulting in a total line

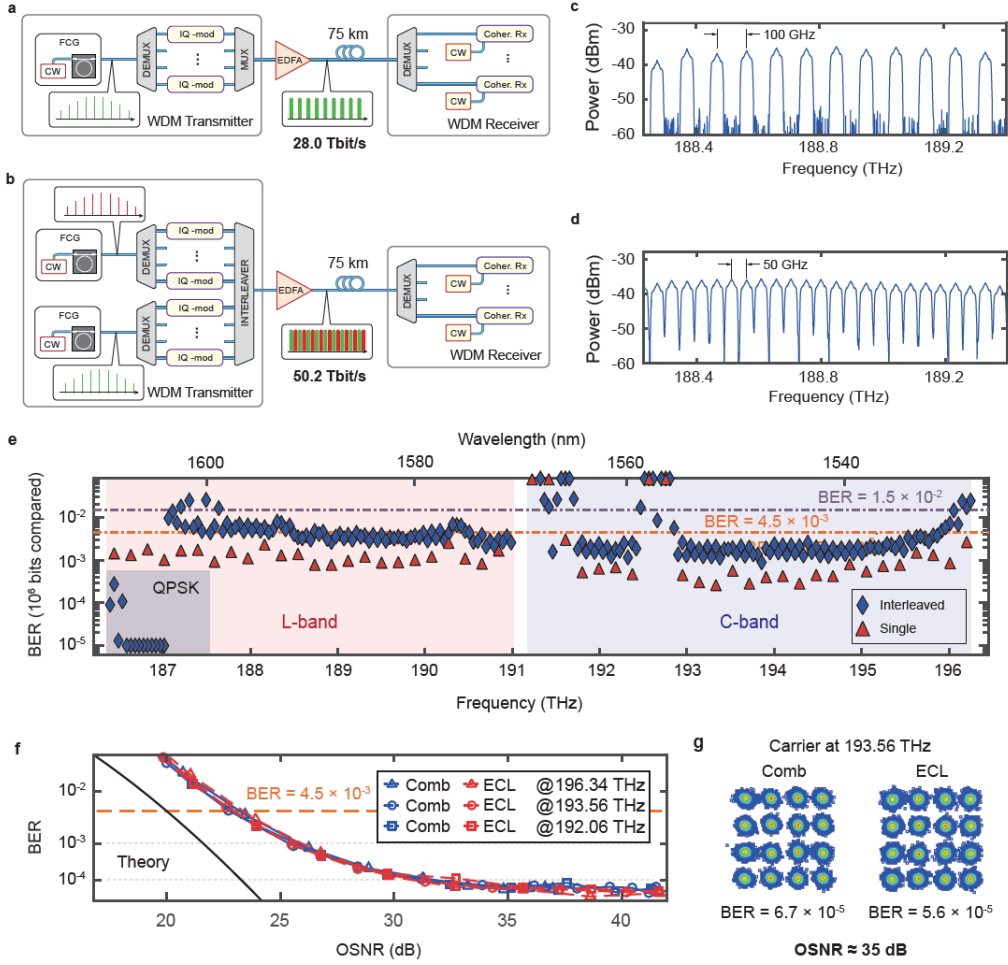


Figure 7.2 – (a) Principle of data transmission using a single DKS comb generator (FCG) as optical source at the transmitter. DEMUX, demultiplexer; IQ-mod, in-phase/quadrature (IQ) modulators; MUX, multiplexer; EDFA, erbium-doped fiber amplifier; Coh. Rx, digital coherent receivers; CW, individual CW lasers as local oscillators or seeds for FCG. (b) Principle of data transmission using interleaved DKS combs. (c) Section of the optical spectrum of the WDM data stream for single DKS. (d) Section of the optical spectrum of the WDM data stream for interleaved DKS. (e) Measured bit error ratios (BER) of the transmitted channels for the single-comb and the interleaved-comb experiment, along with the BER thresholds [268] for error-free propagation when applying forward error correction schemes with 7 % overhead ( $4.5 \times 10^{-3}$ , dashed orange line) and 20 % overhead ( $1.5 \times 10^{-2}$ , dashed blue line). For the interleaved-comb experiment, the outer 14 lines at the low-frequency edge of the L-band were modulated with quadrature phase-shift keying (QPSK) signals rather than 16QAM due to the low OSNR of these carriers. (f) Measured BER vs. OSNR of three different channels derived from a DKS frequency comb (blue) and a high-quality ECDL (red), all with 16QAM signalling at 40 GBd. A total of 106 bits were compared. (g) Constellation diagrams obtained for an ECDL and DKS comb tone at 193.56 THz.

### 7.3. Optical coherent communication experiments with DKS

---

rate of 30.1 Tbit/s. In our experiment, the transmission capacity is restricted by the fact that the line spacing of about 100 GHz substantially exceeds the signal bandwidth of about 40 GHz, leading to unused frequency bands between neighbouring channels (Fig. 7.2(b)) and hence to a rather low spectral efficiency of 2.8 bit/s/Hz.

These restrictions can be overcome by using interleaved frequency combs, see Fig. 7.2(c). The scheme relies on a pair of DKS combs with practically identical line spacing (95.80 GHz and 95.82 GHz), but shifted with respect to each other by half the line spacing using thermal tuning. The overall experimental scheme is not changed apart from doubling the equipment of the FCG part of the setup and the additional fiber coupler which merges interleaved DKS combs from two setups and then sends them to the same transmission experiment setup. At the receiver, this scheme still relies on individual CW lasers as LO for coherent detection. The interleaved comb features a line spacing of  $\sim 50$  GHz, which allows for dense packing of 40 GBd data channels in the spectrum, see Fig. 7.2(d). The BER results of the second transmission experiment with interleaved DKS combs are depicted in Fig. 7.2(e) using blue diamonds. We find a total of 204 tones in the C and L band, out of which 179 carriers could be used for data transmission. The remaining channels were not usable due to remaining ASE noise from the pump light from FCGs (region around 192.7 THz), and limited performance of the C/L multiplexer at the low-frequency end of the C-band (region around 191.4 THz). The transmission performance is slightly worse than in the single comb experiment since twice the number of carriers had to be amplified by the same EDFA, which were operated at their saturation output power such that the power per data channel reduced accordingly. Nevertheless, data was successfully transmitted over 75 km of standard single mode fiber at a symbol rate of 40 GBd using a combination of 16QAM and QPSK. The total line rate amounts to 55.0 Tbit/s, and the net data rate is 50.2 Tbit/s. This is the highest data rate achieved with a chip-scale frequency comb source, and compares very well to the highest capacity of 102.3 Tbit/s ever transmitted through a single-mode fiber core [269] using more than 200 discrete DFB lasers as optical sources at the transmitter. In addition, we achieve an unprecedented spectral efficiency of 5.2 bit/s/Hz, owing to the densely packed spectrum, Fig. 7.2(d). In the experiments, limited saturation output power of the employed EDFA is the main constraint of signal quality and BER. The presented data rates are hence not limited by the DKS comb source, but by the components of the current transmission setup, leaving room for further improvement. We also note that field-deployed WDM systems rely on statistically independent data channels rather than on transmitting identical data streams on the even and odd channels. As a consequence, real-world signals will suffer much less from coherent addition of nonlinear interference noise than the signals used in our experiments [270]. With respect to nonlinear impairments, our experiments therefore represent a worst-case scenario.

To exemplify the potential of DKS combs for data transmission, we compare the transmission performance of a single-comb line to that of a reference carrier derived from a high-quality benchtop-type external-cavity diode laser (ECDL) with an optical linewidth

of approximately 10 kHz, an optical output power of 15 dBm and an optical carrier-to-noise ratio in excess of 60 dB. As a metric for the comparison, we use the optical signal-to-noise ratio penalty at a BER of  $4.5 \times 10^{-3}$ , which corresponds to the threshold for FEC with 7% overhead [268]. The results for 40-GBd 16QAM transmission are shown in Fig. 7.2(f) for three different comb lines and for ECDL reference transmission experiments at the corresponding comb line frequencies. The optical signal-to-noise ratios are defined for a reference bandwidth of 0.1 nm. As shown, no additional penalty is observed for the frequency comb when compared with the high-quality ECDL: for both sources we observe an optical signal-to-noise ratio penalty of 2.6 dB with respect to the theoretically required value (black line in Fig. 7.2(f)) for a BER of  $4.5 \times 10^{-3}$ . The comb lines do not show any additional penalty in comparison with the ECDL tones. Similar results were obtained at other symbol rates such as 28 GBd, 32 GBd, or 42.8 GBd. DKS-based light sources can therefore markedly improve the scalability of WDM systems without impairing the signal quality under realistic transmission conditions. The error floor in Fig. 7.2(f) is attributed to transmitter nonlinearities and electronic receiver noise in our setup. In Fig. 7.2(g) we show the measured constellation diagrams for the ECDL and the comb line at 193.56 THz, both taken at the same optical signal-to-noise ratio of 35 dB.

### 7.3.2 Optical coherent communication using two DKS

To demonstrate the potential of DKS frequency combs as multi-wavelength LO at the receiver, we perform a third experiment shown schematically in Fig. 7.3(a). At the transmitter, a first DKS comb generator with an FSR of 95.80 GHz serves as an optical source. At the receiver, a second DKS comb source having approximately the same FSR of 95.70 GHz is used to generate the corresponding LO tones, each featuring an optical linewidth below 100 kHz. As in the previous experiments, WDM transmission is emulated by encoding independent data streams on adjacent channels. Note that the C/L multiplexer of the deinterleaver stage has been replaced by a directional coupler to avoid the power attenuation of the carriers at the low-frequency edge of the C-band (which was observed around 191.4 THz). The WS are also used to compensate the power differences of the carriers and the spectral variations of the EDFA gain profile, thereby producing an overall flat spectrum at the input of the IQ modulators. The modulators are again driven by 16QAM drive signals generated by a high-speed arbitrary waveform generator using PRBS of length  $2^{11} - 1$ . We use a symbol rate of 50 GBd. The larger analog bandwidth of the used arbitrary waveform generator (32 GHz) allowed us to use higher symbol rates as compared to the experiments in the previous section. Polarization-division multiplexing (PDM) is again emulated by split-and-combine method: by temporally delaying one of the polarizations using a delay line and combining on orthogonal polarizations in a polarization beam combiner. The WDM data stream is amplified and transmitted over 75 km of standard single-mode fiber as in early experiments.

### 7.3. Optical coherent communication experiments with DKS

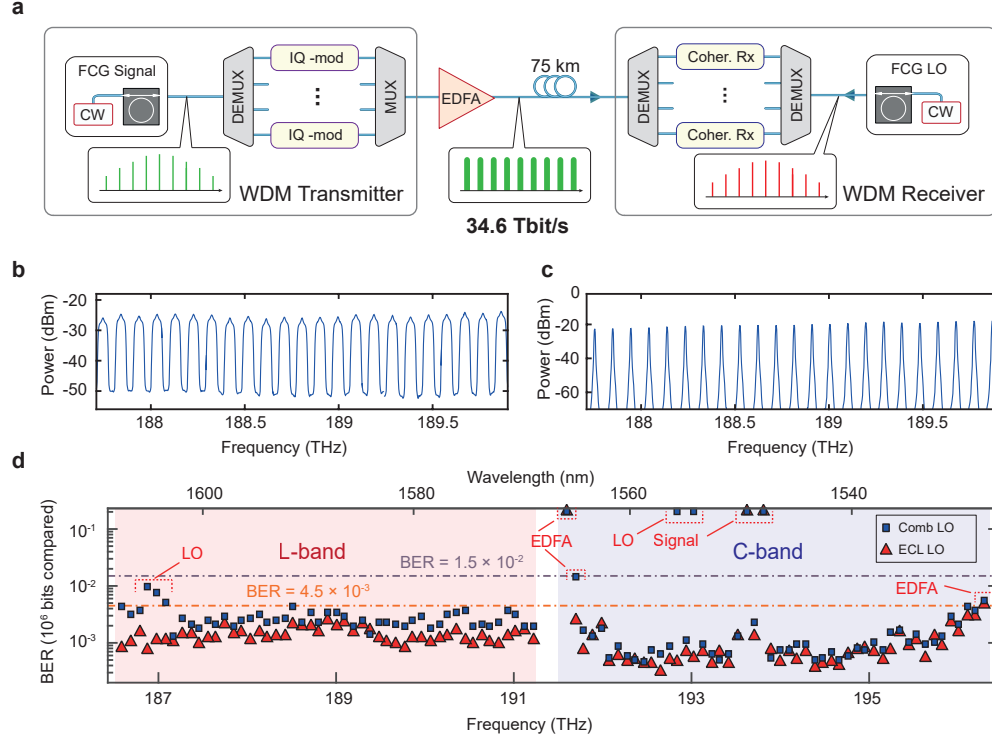


Figure 7.3 – (a) Massively parallel WDM data transmission scheme using DKS frequency combs as both multi-wavelength source at the transmitter and multi-wavelength local oscillator (LO) at the receiver. FCG Signal/LO, frequency comb generator at the transmitter/receiver; DEMUX, demultiplexer; IQ-mod, in-phase/quadrature modulators; MUX, multiplexer; EDFA, erbium-doped fiber amplifier (EDFA); Coh. Rx, digital coherent receivers; In contrast to Fig. 7.2(a), a single optical source provides all of the LO tones that are required for coherent detection. An extra demultiplexer is used to route each LO tone to the respective coherent receiver. (b) Section of the spectrum of the transmitted channels. (c) Corresponding section of the spectrum of the LO frequency comb. Note that the comparatively large width of the depicted spectral lines is caused by the resolution bandwidth of the spectrometer (0.1 nm) and does not reflect the sub-100-kHz optical linewidth of the local-oscillator tones. (d) Measured BERs for each data channel. Blue squares show the results obtained when using a DKS comb as the multi-wavelength local oscillator and red triangles correspond to a reference measurement using a high-quality ECDL. Dashed lines mark the BER thresholds the same as in Fig. 7.2(e). Black circles show the channels with BERs above the threshold for 7% FEC and specify the reasons for low signal quality: a low optical carrier-to-noise ratio of the carriers from the LO comb (‘LO’) and the signal comb (‘Signal’), and bandwidth limitations of the C-band EDFA (‘EDFA’).

Figures 7.3(b, c) show a section of the transmitted data spectrum along with the corresponding section of the LO comb. When using the carriers from the LO DKS comb for coherent intradyne detection, such difference in line spacing translates into a non-zero intermediate frequency (IF). The IF can be brought down to values below 100 MHz near

the center of the frequency combs at around 191.5 THz but it reaches relatively high frequencies of approximately 4 GHz when coherently demodulating the signals at the low frequency edge of the L band and at the high frequency edge of the C band. The high IF, however, does not prohibit data transmission as it can be removed using digital signal processing after detection of the transmitted signal with our coherent receiver. However, for high IF, the received signal is slightly affected by the limited electrical bandwidth ( $BW = 33$  GHz) of the analog-to-digital convertor (ADC) of our coherent receiver. This leads to a reduction of the electrical power, and thus of the electrical signal-to-noise ratio, of our baseband signal. The high IF, nevertheless, can be avoided by carefully matching the line spacing of the two Kerr soliton frequency comb sources during fabrication.

At the receiver, each transmitted channel is selected individually by an optically tunable BPF, followed by an EDFA and a second BPF to suppress ASE noise. The selected channel is then sent to a dual-polarization coherent receiver which consists of an optical modulation analyzer together with two real-time oscilloscopes (Keysight DSO-X 93204A, 80 GSa/s), and in contrast to the data transmission experiment described in previous section, uses a spectral line from the Kerr soliton comb at the receiver side as a local oscillator (LO). As a reference, the same experiment was repeated using a high-quality ECDL with a 10 kHz linewidth as an LO for channel-by-channel demodulation. Overall, an aggregate data rate of 34.6 Tbit/s is obtained. The resulting BER values of all 99 channels for both methods are shown in Fig. 7.3(d). Some of the channels showed signal impairments due to limitations of the available equipment. However, we cannot observe any considerable penalty that could be systematically attributed to using the DKS comb as an LO.

While frequency combs offer fundamental technical advantages compared to discrete lasers, they can also serve to reduce the power consumption of the transmission system. In this context, the power conversion efficiency of the DKS comb generator is an important metric, defined as the ratio between the power of the pump and that of the generated comb lines. The power conversion efficiency of our current comb sources is limited to rather small values between 0.1 % and 0.6 % due to the fundamental principle that bright soliton generation only occurs with the pump laser being far detuned from the optical resonance. Still, the overall power consumption can already now compete with massively parallel arrays of commercially available integrated tunable laser assemblies (ITLA).

### 7.4 Dissipative Kerr solitons for ultrafast optical ranging

We next focus on the second demonstrated application of dissipative Kerr solitons – ultrafast distance measurements. Laser-based light detection and ranging (LiDAR) is widely used in science and industry, offering unique advantages such as high precision, long range, and fast acquisition [271, 272]. Over the last decades, LiDAR systems have found their way into a wide variety of applications, comprising, e.g., industrial process

---

#### 7.4. Dissipative Kerr solitons for ultrafast optical ranging

---

monitoring [273], autonomous driving [274], satellite formation flying [275], or drone navigation [276].

When it comes to fast and accurate ranging over extended distances, optical frequency combs [277] have been demonstrated to exhibit unique advantages, exploiting time-of-flight (TOF) schemes [278], where the distance is calculated from the time which takes the optical pulse to fly to the target and back to the receiver after reflection; interferometric approaches [279], where the distance is inferred from interferometric measurements of the phase shift of the reflected light; or combinations thereof [280].

In early experiments by Minoshima *et al.* [278], mode-locked fiber lasers were used for TOF ranging, thereby primarily exploiting the stability of the repetition rate. Regarding interferometric schemes, optical frequency combs were exploited to stabilize the frequency interval between continuous-wave (CW) lasers used in synthetic-wavelength interferometry [279, 281]. Dual-comb schemes, which rely on multi-heterodyne detection by coherent superposition of a pair of slightly detuned frequency combs, allow one to combine TOF measurements with optical interferometry, thereby simultaneously exploiting the radio frequency coherence of the pulse train and the optical coherence of the individual comb tones [280]. More recently, comb-based schemes have been demonstrated as a viable path to high-speed sampling with acquisition times down to 500 ns [139].

However, besides accuracy and acquisition speed, footprint has become an important metric for LiDAR systems, driven by emerging high-volume applications such as autonomous drone or vehicle navigation, which crucially rely on compact and lightweight solutions, and by recent advances in photonic integration showing that large-scale nanophotonic phased arrays [279, 282, 283, 284] open a promising path towards ultra-compact systems for rapid high-resolution beam steering. To harness the full potential of these approaches, the optical phased arrays need to be complemented by chip-scale LiDAR engines that combine high precision with ultrafast acquisition and that are amenable to efficient mass production. Existing dual-comb LiDAR concepts cannot fulfill these requirements since they either rely on cavity-stabilized mode-locked fiber lasers [280] or on spectral broadening of initially narrowband seed combs [139], which typically requires delicate fiber-based dispersion management schemes, usually in combination with intermediate amplifiers. These approaches are not suited for chip-scale photonic integration.

In the following sections we demonstrate that integrated DKS comb sources provide a route to chip-scale LiDAR systems that combine sub-wavelength accuracy and unprecedented acquisition speed with the ability to exploit advanced photonic integration concepts for cost-efficient mass manufacturing.

## 7.5 Synthetic-wavelength interferometry

We start by describing the principle we used for ultrafast distance measurements. It combines synthetic-wavelength interferometry with massively parallel comb-based multi-heterodyne detection and is illustrated in Fig. 7.4.

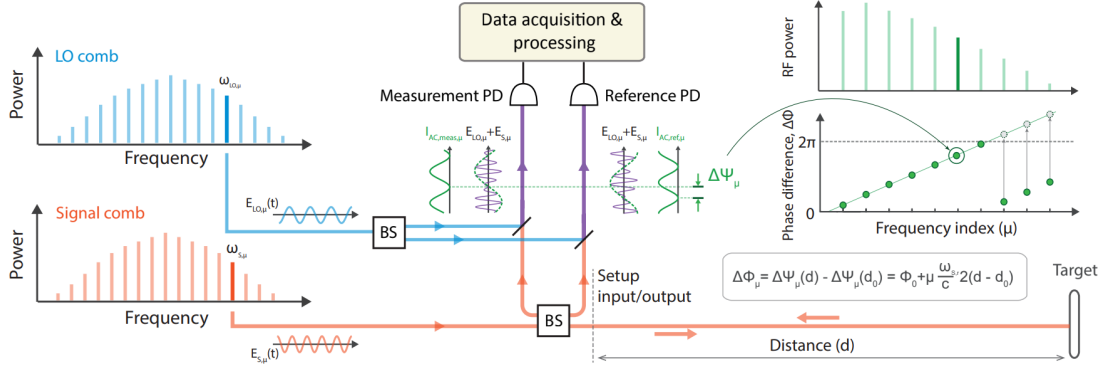


Figure 7.4 – Principal scheme of dual-comb synthetic-wavelength interferometry: The signal comb (orange) and the LO comb (blue) consist of discrete tones at frequencies  $\omega_{S,\mu}$  and  $\omega_{LO,\mu}$ . The superposition of these comb lines on the measurement and reference PD leads to a multitude of beat notes in the RF spectrum of the photocurrent (green) at frequencies  $\Delta\omega_\mu = |\omega_{LO,\mu} - \omega_{S,\mu}|$ , which can be separated by a Fourier transformation. The phases of these beat notes reveal the phase shifts  $\Psi_{\text{meas},\mu}$  and  $\Psi_{\text{ref},\mu}$  that the optical waves have accumulated. The distance is finally obtained by estimating the slope of the phase differences  $\Delta\Phi_\mu$  according to eq. (7.2) as a function of mode index  $\mu$ .

We give a brief outline of the technique using a simplified approach, which however does not hinder the physical principle of the implemented distance measurements. We consider two optical combs - signal comb (S) and local oscillator comb (LO), consisting of discrete monochromatic optical tones  $\omega_{S,\mu} = \omega_{S,0} + \mu \cdot \omega_{S,r}$  and  $\omega_{LO,\mu} = \omega_{LO,0} + \mu \cdot \omega_{LO,r}$ , where  $\omega_{S,\mu}$  and  $\omega_{LO,\mu}$  are the repetition rates. Without loss of generality we assume that the indexing of both combs is done through the integer  $\mu = 0, \pm 1, \pm 2, \dots$  such that comb lines with the same  $\mu$  from S and LO combs have minimum frequency spacing. This will guarantee that comb lines with the same  $\mu$  give a detectable RF tone smaller than the repetition rates of the combs.

The first part of the signal comb lines  $\omega_{S,\mu}$  accumulate phase shifts  $\Psi_{\text{meas},\mu}$  when propagating back and forth over the measurement distance  $d$  to the target. The other part of the signal comb is directly guided to the reference detector (Reference PD), thereby accumulating phase shifts of  $\Psi_{\text{ref},\mu}$ ,

$$\begin{aligned}\Psi_{\text{meas},\mu} &= -\frac{\omega_{S,\mu}}{c} (L_{\text{meas}} + 2d), \\ \Psi_{\text{ref},\mu} &= -\frac{\omega_{S,\mu}}{c} L_{\text{ref}}.\end{aligned}\tag{7.1}$$

## 7.5. Synthetic-wavelength interferometry

In this relation,  $L_{\text{meas}}$  and  $L_{\text{ref}}$  refer to the optical path lengths that the two parts of the signal comb propagate on the chips from the common comb generator to the respective photodetector, and  $d$  is the single-pass free-space distance towards the target. The two parts of the signal comb are superimposed with portions of the LO comb on the respective photodetector, thus leading to a multitude of sinusoidal signals in the corresponding baseband photocurrents. In essence, the phases of these sinusoidals reveal the differences  $\Delta\Psi_\mu(d) = \Psi_{\text{ref},\mu} - \Psi_{\text{meas},\mu}$  of the phases  $\Psi_{\text{meas},\mu}$  and  $\Psi_{\text{ref},\mu}$  that the respective signal comb tones have accumulated along the measurement and the reference path. To eliminate the internal optical path lengths  $L_{\text{meas}}$  and  $L_{\text{ref}}$ , a calibration measurement at a known distance  $d_0$  is performed. The target distance  $(d - d_0)$  can then be extracted by estimating the slope of the phase differences  $\Delta\Phi_\mu = \Delta\Psi_\mu(d) - \Delta\Psi_\mu(d_0)$  as a function of frequency index  $\mu$ ,

$$\begin{aligned}\Delta\Phi_\mu &= \Delta\Phi_0 + \mu \frac{\omega_{\text{S},r}}{c} \times 2(d - d_0), \\ \Delta\Phi_0 &= \frac{\omega_{\text{S},0}}{c} \times 2(d - d_0).\end{aligned}\tag{7.2}$$

In this relation,  $\Delta\Phi_0$  denotes a phase offset that is independent of  $\mu$ . The slope of  $\Delta\Phi_\mu$  with respect to  $\mu$  is extracted from the measured phases by means of a linear fit. Note that this technique allows one to directly check the validity of a certain distance measurement by using the fit error as a quality criterion – unreliable raw data leads to large fit errors, based on which erroneous points can be discarded.

The unique advantages of DKS combs for high-speed high-precision sampling can be understood by analyzing the fundamental limitations of measurement accuracy and acquisition speed. Note that, for high-speed sampling, it is important to keep the number  $N$  of baseband beat notes as small as possible: For  $N$  beat notes that are equally distributed over a given acquisition bandwidth  $f_{\text{ADC}}$  of the ADC, the frequency spacing  $\Delta f_r = \Delta\omega_r/2\pi$  of the beat notes is at most  $f_{\text{ADC}}/N$ . To spectrally resolve these beat notes by a Fourier transformation, a minimum observation time of  $T_{\text{min}} = 1/\Delta f_r \geq N/f_{\text{ADC}}$  is required. This leads to a maximum distance acquisition rate of  $T_{\text{min}}^{-1} = \Delta f_r \leq f_{\text{ADC}}/N$ .

On the other hand, the number  $N$  of optical tones used for distance measurement will also influence the accuracy with which we can estimate the slope of the phase differences  $\Delta\Phi_\mu$  vs.  $\mu$  from the noisy measurement data. Using basic relations of linear regression analysis, the standard deviation of the measured distance can be estimated from the overall optical bandwidth  $\Omega_{\text{S}} = N\omega_{\text{S},r}$  of the comb, the standard deviation  $\sigma_\phi$  of the individual phase measurements, and the number  $N$  of optical tones:

$$\sigma_d = \sqrt{\frac{3}{N}} \frac{c}{\Omega_{\text{S}}} \sigma_\phi.\tag{7.3}$$

For a fixed number  $N$  of optical lines, the only option that remains for improving the measurement accuracy is to increase the overall optical bandwidth  $\Omega_{\text{S}} = N\omega_{\text{S},r}$  of the

comb, which requires a comb source that provides a large free spectral range. DKS combs stand out due to a unique combination of large overall optical bandwidth and large FSR. They hence feature comparatively few optical lines and are thus perfectly suited for simultaneously achieving high sampling and high measurement accuracy. This is demonstrated in the following section by using a simplified model system that combines a pair of DKS comb sources with fiber-optic components and a high-speed oscilloscope for data acquisition and offline processing.

### 7.6 Experiment - reproducibility and benchmarking

We demonstrate the viability of the described dual-comb synthetic-wavelength interferometry scheme for realization of a chip-scale LiDAR engine, which critically relies on integrated DKS comb generators as core components. Note that all other integrated components of the LiDAR engine can utilize the standard device portfolio of photonic integration and have been established in prior work [285, 286, 287].

The experimental setup for our proof-of-concept demonstration is depicted in Fig. 7.5(a). For DKS comb generation, we use a pair of CW-pumped  $\text{Si}_3\text{N}_4$ -microring resonators on separate chips similar to the ones described in Section 7.2. For multi-heterodyne detection, the two resonators have slightly different free spectral ranges of  $\omega_{\text{S},r}/2\pi = 95.646$  GHz and  $\omega_{\text{LO},r}/2\pi = 95.549$  GHz respectively. To demonstrate that our concept does not require phase locking of the DKS combs, we used a pair of independent *free-running* pump lasers, even though a single pump laser could have been used as well [288, 289]. The pump light is amplified with EDFA and then coupled to the microresonator chips. The generation of DKS states is implemented via the same two-step pump tuning scheme as described in section 7.2. Thus, a single soliton-based frequency comb with spectrally smooth  $\text{sech}^2$ -shape envelope is deterministically achieved. After the chip, a fiber Bragg grating (not shown in the figure) is used to suppress remaining pump light. The resulting combs are amplified in C+L band EDFA to improve phase extraction of the individual beat notes. The spectra of the amplified combs with filtered out pumps are shown in Fig. 7.5(c) for the signal (red) and the LO (blue) comb. Both combs cover a range of approximately 11 THz, limited by the gain bandwidth of the respective EDFA. This gives about 115 of usable comb lines for each combs, which is sufficient for our experiments. Both spectra feature a slight dip near 191 THz, which is caused by internal multiplexing and demultiplexing filters of the EDFA. The increase of the noise background around 192.50 THz (193.46 THz) in the signal (LO) comb is caused by residual amplified spontaneous emission (ASE) originating from the pump EDFA.

For distance measurement, the signal comb (red) is split by a fiber-based 50:50 coupler, and one part is routed to the target and back to a balanced measurement PD (meas. PD), while the other part is directly sent to the balanced reference detector (ref. PD), see Fig. 7.5(a). Measurement and reference PD feature bandwidths of 43 GHz. Note that in

## 7.6. Experiment - reproducibility and benchmarking

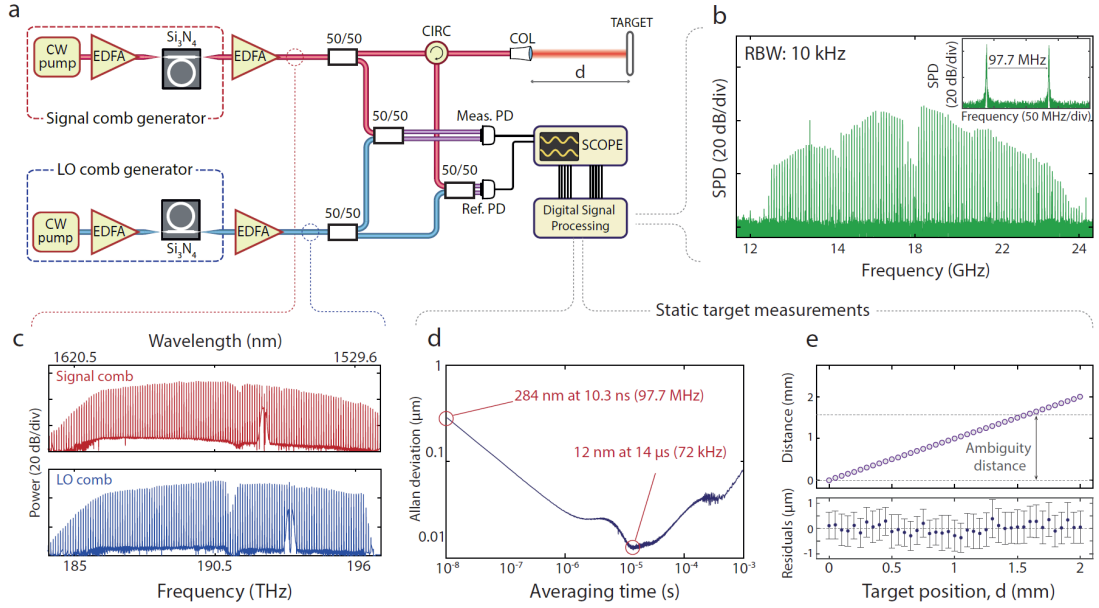


Figure 7.5 – (a) Experimental setup. DKS combs are generated by a pair of  $\text{Si}_3\text{N}_4$  microresonators, driven by two CW lasers and erbium-doped fiber amplifiers (EDFA). The combs are detuned in line spacing by  $|\omega_{\text{LO},r} - \omega_{\text{S},r}|/2\pi \approx 98$  MHz as well as in center frequency by  $\Delta\omega_0/2\pi = |\omega_{\text{LO},0} - \omega_{\text{S},0}|/2\pi \approx 18$  GHz. CIRC, optical circulator; COL, collimator; SCOPE, real-time sampling oscilloscope. As a target, we use a silver mirror that can be positioned with an accuracy of better than 50 nm using a feedback-stabilized stage. (b) Numerically calculated Fourier transform of a recorded time-domain signal. The baseband spectrum consists of discrete spectra centered around 18 GHz with spacings of  $\approx 98$  MHz. (c) Optical spectra of the signal and the LO comb after amplification. (d) Allan deviation of measured distances as a function of averaging time. The highest acquisition speed is limited by the spacing of the baseband beat notes in the photocurrent and amounts to approximately 98 MHz (acquisition time of 10.3 ns). At this speed, an Allan deviation of 284 nm is achieved, that decreases to a record-low value of 12 nm at an averaging time of 14  $\mu\text{s}$ . The increase towards longer averaging times is attributed to drifts in the fiber-optic setup. (e) Top: Scan of measured position vs. set position in steps of 50  $\mu\text{m}$  over the full ambiguity distance (marked by dashed lines). The points outside the ambiguity interval are manually unwrapped. Bottom: Residual deviations ("residuals") between measured and set positions. The residuals are of the same order of magnitude as the 50 nm positioning accuracy of the positioning stage. Error bars indicate the standard deviation obtained for each position of the mirror. Importantly, the residuals do not show any cyclic error.

contrast to Fig. 7.4, we use a circulator (CIRC) in conjunction with a directional coupler for splitting forward and backward-propagating light in the measurement path. Similarly, the LO comb is split in two portions, which are routed to the measurement PD and the reference PD for multiheterodyne detection. The resulting baseband beat signals are recorded by a 32 GHz real-time sampling oscilloscope. Data processing and evaluation is performed offline. Figure 7.5(b) shows a numerically calculated Fourier transform of a

recorded time-domain signal that reveals a multitude of discrete beat notes between the signal and LO comb lines. The spacing of the beat notes is given by the difference of the line spacing of the LO and the signal comb and amounts to  $\Delta f_r = \Delta \omega_r / 2\pi = 97.7$  MHz, thereby dictating a minimum possible acquisition time of  $T_{\min} = 1/\Delta f_r = 10.3$  ns and a maximum possible distance acquisition rate of 97.7 MHz.

For a thorough stability and precision analysis of our dual-comb scheme, we evaluate the Allan deviation [290] over a 10.3 ms long measurement that is composed of a series of  $10^6$  individual data points taken from a static mirror at an acquisition time of 10.3 ns per point. The results are plotted in Fig. 7.5(d). At an averaging time of 10.3 ns, an Allan deviation of 284 nm is obtained, that decreases to 12 nm for an averaging time of 14  $\mu$ s. The initial linear decrease of the Allan deviation implies dominating high-frequency noise, which is attributed to an amplified spontaneous emission (ASE) background originating from the deployed EDFA. This ASE noise impacts the phase estimation of the individual beat notes and therefore the extracted distance. For longer averaging times, the Allan deviation increases, which we attribute to thermal drift of the fibers and to mechanical vibrations.

Besides the Allan deviation of a distance measurement to a static target, we estimated the accuracy of our technique for measuring variable distances to a target that is moved over a full ambiguity distance, see Fig. 7.5(d). In this experiment, the target mirror is stepped in increments of 50  $\mu$ m using a high-precision translation stage with an accuracy of better than 50 nm. To eliminate the impact of fiber drift, the distance measurement is continuously switched between the movable target mirror and a static calibration mirror in quick succession, taking between 6 500 and 9 500 measurements on each mirror. To minimize the impact of high-frequency noise, an averaging time of 100  $\mu$ s is chosen. In the upper part of Fig. 7.5(e), the measured distance is plotted as a function of the distance set by the translation state. Measured distances exceeding the ambiguity interval of 1.51 mm are unwrapped manually. The bottom part of Fig. 7.5(e) shows the deviations of the measured from the set positions along with the respective standard deviations indicated as error bars. Importantly, no cyclic error is observed throughout the ambiguity interval. We determine the accuracy of our measurement to 188 nm, defined as the standard deviation of the residuals. These residuals are of the same order of magnitude as the 50 nm positioning accuracy of the positioning stage specified by the manufacturer [291]. In this measurement, the refractive index of air is considered according to Ciddors formula for ambient lab conditions [292].

To validate the reproducibility of our system and to benchmark the results with respect to existing techniques, we measure the profile of a quickly rotating disk having grooves on its surface, see Fig. 7.6(a). In this experiment, the measurement beam is focused to the surface near the edge of the disk, which rotates at a frequency of about 600 Hz, resulting in an edge velocity of 160 m/s. The distance acquisition rate amounts to 97.1 MHz, limited by the spectral spacing of  $\Delta \omega_r / 2\pi$  of the beat notes in the baseband photocurrent,

## 7.6. Experiment - reproducibility and benchmarking

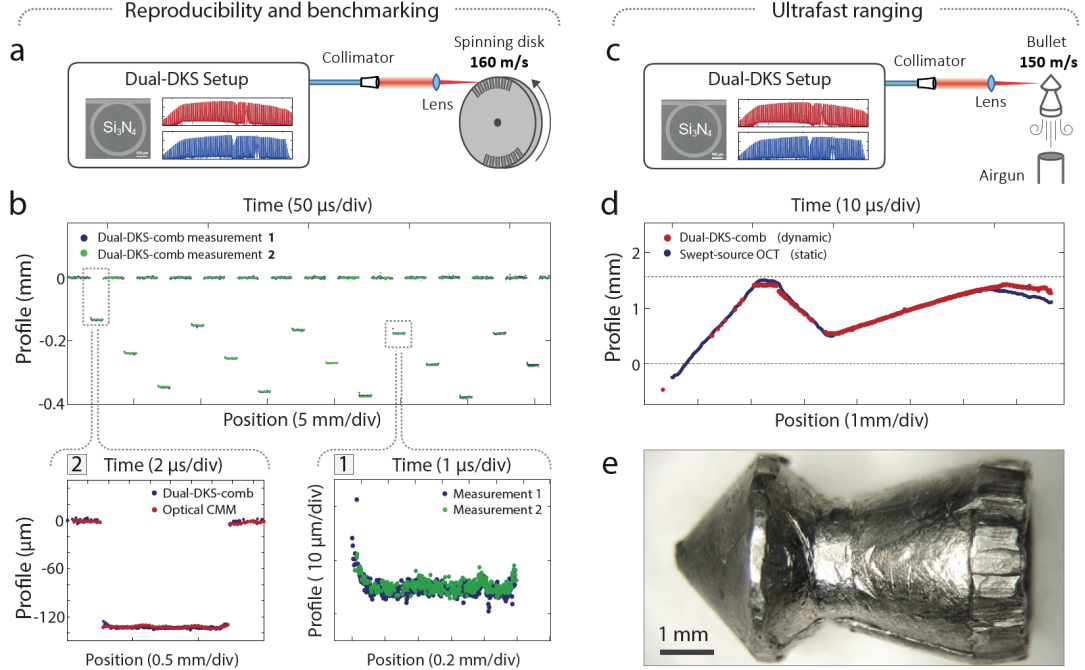


Figure 7.6 – (a) Setup for reproducibility and benchmarking experiments. The measurement beam is focused on the surface of a spinning disk (600 Hz) having grooves of different depths on its surface. (b) Measured surface profile of the disk as a function of position (bottom) and time (top) for two independent measurements at the same position. Inset 1: Reproducibility demonstration by detailed comparison of the two independent measurements plotted in (b). The results exhibit good agreement regarding both macroscopic features such as the groove depth and width as well as microscopic features such as surface texture and a decrease of depth towards the edge of the groove. Inset 2: Benchmarking of the high-speed dual-DKS-comb measurement to the results obtained from an industrial optical coordinate-measuring machine (CMM). (c) Setup for ultrafast ranging experiment. The measurement beam is focused into free space. An air-gun bullet is then fired through the focal spot of the beam and the profile is recorded. The bullet travels at a speed of  $\sim 150$  m/s (Mach 0.47). (d) Measured profile of the projectile obtained from in-flight dual-DKS-comb measurement (red), along with a swept-source OCT profile scan that was recorded on the static projectile after recovery from the backstop. For better comparison, the two profiles were rotated and an actual speed of the bullet of 149 m/s was estimated for best agreement of the two profiles. Both curves show good agreement, demonstrating the ability of the dual-DKS-comb technique to obtain reliable results even for ultrafast sampling on rapidly moving targets with naturally scattering surfaces. (e) Image of the projectile after being fired. Deformations during the shot have lead to a strong corrugation of the bullet towards its back.

but not by the acquisition speed of our oscilloscopes. The resulting profiles are shown in Fig. 7.6(b) for two measurements, which were taken independently from one another. Measurement points close to the edges of the grooves may suffer from strong scattering and low power levels, which lead to unreliable distance information. Using the fit error of

the linear phase characteristic according to eq. (7.2) as a quality criterion, our technique allows bad measurement points to be identified and automatically discarded from the data. The raw data of both measurements was further subject to vibrations of the disk arising from the driving engine. These vibrations have been removed by fitting a polynomial to the top surface of the disk and by using it for correction of the overall measurement data. In a first experiment, we analyze the reproducibility of the technique by a detailed comparison of the results obtained from the two measurements, see Fig. 7.6(b), Inset 1. The measured profiles exhibit good agreement regarding both macroscopic features such as the groove depth and width as well as microscopic features such as surface texture and a decrease of depth towards the edge of the groove. Deviations are attributed to the fact that the two measurements have been taken independently and might hence not have sampled the exact same line across the groove. In addition, we benchmark our technique by comparing the obtained profile of a single groove with a profile obtained from an industrial optical coordinate-measuring machine (CMM, Werth VideoCheck HA), Fig. 7.6(b), Inset 2. Both profiles are in good agreement, with some minor deviations that we attribute to slightly different measurement positions within the analyzed groove.

### 7.7 Experiment - profiling of a flying bullet

In a final experiment, we demonstrate ultrafast ranging by measuring the profile of a flying air-gun bullet that is *shot* through the focus of the measurement beam, see Fig. 7.6(c). The projectile moves at a speed of 150 m/s, i.e. Mach 0.47, which, together with the acquisition rate of 97.7 MHz, results in a lateral distance of 1.5  $\mu\text{m}$  between neighbouring sampling points on the surface of the bullet. The measured profile is depicted in red in Fig. 7.6(d) along with a reference measurement of the profile obtained from the static bullet using a swept-source OCT system (dark blue). Both curves clearly coincide and reproduce the shape of the fired projectile that can be seen in Fig. 7.6(e). Missing data points in the dual-DKS-comb measurement at the tip of the projectile are caused by low power levels of the back-coupled signal, which is inevitable for such steep surfaces in combination with the limited numerical aperture of the lens used for focusing the beam. These measurement points have been discarded from the data based on a large fit error of the linear phase characteristic according to eq. (7.2). An image of the projectile after recovery from the backstop exhibits a strong corrugation of the bullet towards its back, Fig. 7.6(e). This leads to deviations of the measured profiles in Fig. 7.6(d) towards the right-hand side, since the strongly corrugated surface of the projectile in this area has very likely been sampled at two different positions. These experiments clearly demonstrate the viability of the dual-DKS-comb approach and its extraordinary performance advantages for ultrafast high-precision sampling. Thanks to the high sampling rate, the technique would allow to track continuous movements of objects at any practical speed, with an ambiguity limit 144 000 m/s. The ambiguity distance of the dual-DKS-comb approach can be greatly increased by combination with

a comparatively simple low-accuracy time-of-flight system.

### 7.8 Vision of the chip-scale DKS-based LiDAR system

Our experiments demonstrate the viability of chip-scale DKS comb generators to act as optical sources for high-performance ranging systems and are a key step toward fully integrated chip-scale LiDAR engines, as illustrated as an artist's view in Fig. 7.7. In this vision, the LiDAR system is realized as a photonic multichip assembly, in which all photonic integrated circuits are connected by photonic wire bonds (Fig. 7.7, Inset 2) [293]. The comb generators are pumped by integrated CW lasers, and a dedicated optical chip is used to transmit and receive the optical signals [262]. The receiver is

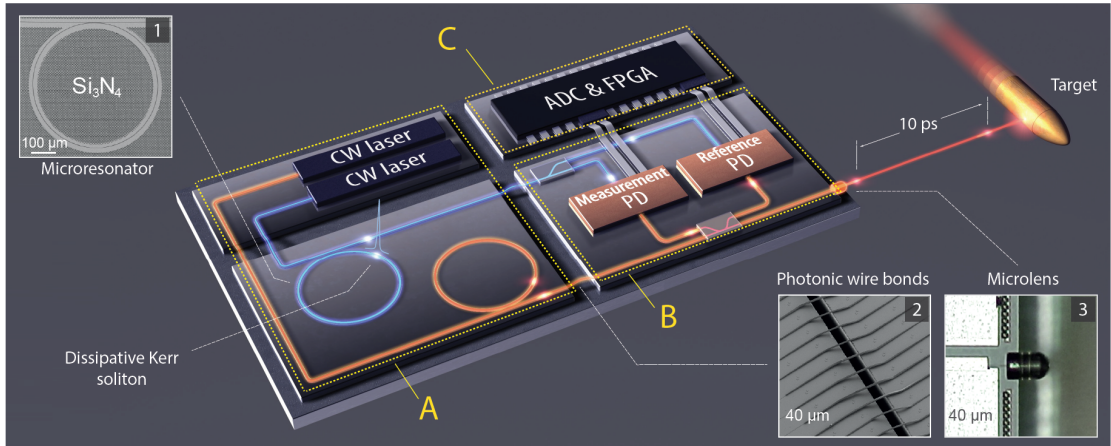


Figure 7.7 – (a) Artist's view of a dual-comb chip-scale LiDAR engine. The system consists of a dual frequency comb source (A), a photonic integrated circuit (PIC) for transmission and detection of the LiDAR signal (B), as well as data acquisition and signal processing electronics (C). For comb generation, light of two continuous-wave (CW) pump lasers is coupled to the silicon nitride ( $\text{Si}_3\text{N}_4$ ) microresonators of the dual-comb source (inset (1)), where dissipative Kerr solitons (DKS) with broadband smooth spectra are generated via four-wave mixing processes [84]. All photonic integrated circuits are connected by photonic wire bonds (inset (2)) [293]. One of the two DKS combs is used for measuring the distance to the target ("signal comb", orange), whereas the other comb acts as a local oscillator ("LO comb", blue) for multi-heterodyne detection on balanced photodetectors (PD). On the LiDAR PIC, the signal comb is split in two parts. One part is collimated by a chip-attached micro-lens (inset (3)), sent to the measurement target, and the scattered light is coupled back into the on-chip waveguide and superimposed with a first portion of the LO comb in the measurement photodetector (Measurement PD). The other part of the signal comb is directly guided to the reference photodetector (Reference PD) along with the other portion of the LO comb. Distance information is extracted from the electrical beat notes in the photocurrents by a combination of analog-to-digital converters (ADC) and a field-programmable gate array (FPGA).

equipped with a chip- attached microlens that collimates the emitted light toward the target (Fig. 7.7, Inset 3) [294]. The electrical signals generated by the photodetectors are sampled by analog-to-digital converters (ADC) and further evaluated by digital signal processing in powerful field-programmable gate arrays (FPGA) or application-specific integrated circuits. Free-running pump lasers greatly simplify the implementation in comparison with configurations where two comb generators are simultaneously pumped by a single light source. Although most of the technological building blocks for realizing this vision have already been demonstrated, one of the remaining key challenges is to reduce the power levels required for DKS generation to typical output power levels of state-of-the-art diode lasers. This requires  $\text{Si}_3\text{N}_4$  microresonators with higher quality factors that can be achieved by optimizing the waveguide geometry and the fabrication processes. We expect that such optimization will allow increasing the  $Q$ -factor by about one order of magnitude, thus reducing the pump power requirements by two orders of magnitude [102, 32, 295]. Alternatively, other integration platforms, such as  $\text{SiO}_2$  or  $\text{AlGaAs}$ , can be used, permitting comb generation with only a few milliwatts of pump power [15, 296]. These power levels are realistically achievable with integrated pump laser diodes. Based on these findings, we believe that DKS-based dual-comb LiDAR could have a transformative impact on all major application fields that require compact LiDAR systems and high- precision ranging, in particular when combined with large-scale nanophotonic phased arrays [283, 284]. Acquisition rates of hundreds of megahertz could enable ultrafast three-dimensional imaging with megapixel resolution and update rates of hundreds of frames per second.

### 7.9 Conclusion

In summary, we have demonstrated the potential of chip-scale DKS frequency combs for two applications - massively parallel WDM at data rates of tens of terabit/s and high-precision optical ranging.

In the first application, two DKS combs acting as multi-wavelength source at the transmitter and as LO at the receiver are used, and we show in both cases that there is no systematic penalty compared to using a high quality ECDL. While our experiments achieve the highest data rate with chip-scale frequency comb sources in comparison to all previous demonstrations, there is still room for increasing the transmission capacity by optimizing the transmission system or by using the adjacent S- and U-bands for telecommunications in the near infrared. For long transmission distances, comb-based transmission schemes might allow for compensation of nonlinear impairments and hence lead to an improved signal quality compared to conventional WDM schemes [261]. The results prove the tremendous potential of DKS comb generators for high-speed data transmission, both in petabit/s intra-datacenter networks [297] and in inter-datacenter connections.

In the second application, we have shown that DKS combs offer a unique combination of large optical bandwidth and large free spectral range, thereby enabling the fastest ranging experiment to date. We achieve distance acquisition rates of 97.7 MHz while maintaining sub- $\mu\text{m}$  precision on a macroscopic scale, thereby outperforming the fastest previous demonstrations by more than an order of magnitude. We investigate the reproducibility of our system, benchmark it with respect to an industrial coordinate measuring machine, and finally demonstrate its performance by sampling the naturally scattering surface of air-gun bullets on the fly. Our results may impact both scientific and industrial applications that require fast and precise contact-less distance measurements. The scheme is fully amenable to photonic integration, thereby offering a promising route towards cost-efficient mass-production of compact LiDAR engines with ultra-high sampling rates.

Finally, we would like to draw the readers attention to another work, where dual-soliton-combs generated in counter-propagating modes of a single silica microdisc was used to demonstrate fast TOF-based distance measurements [145].



## 8 Standalone microcomb source

This chapter reports on the process of building the standalone transportable version of the setup for the DKS generation.

### 8.1 Introduction

Rapid development of the DKS-based optical comb sources, which has started with the seminal paper by Herr *et al.* [9] and sparked an in-depth exploration of their physics, has quickly led to the employment of such soliton-based microcombs in a variety of applications, some of which were presented previously in Chapter 7. Although the advantages of soliton microcombs are quite evident: chip-scale footprint and low complexity of the microresonators, wafer-scale mass-fabrication, access to large repetition rates in the microwave and terahertz domains, as well as convenient ability to engineer the operation window and spectral envelope of the resulting optical frequency combs, they still remain an in-lab technology, and their potential for real world applications has hardly been realized and demonstrated.

One of the key limiting factors of soliton microcombs is that their operation does not solely rely on the properties of the microresonators used for the generation of DKS. While the microresonator parameters, such as  $Q$ -factor, dispersion profile, bus-waveguide coupling and others indeed play a major role in defining the resulting spectrum, access to soliton states and their dynamics, the microresonator itself is a passive device, which unavoidably needs a driving laser for continuous operation. The requirements on the driving laser can be quite challenging, as it should be able to provide enough tuning capabilities to launch soliton states, work without mode hopping, and, depending on the application, have a high level of coherence. Furthermore, launching DKS states can be rather challenging and require complex tuning mechanisms, as well as additional components and stabilization electronics such as single (dual)-sideband modulator or a Pound-Drever-Hall (PDH) scheme. This is especially the case in a microresonator having a complex dispersion

profile and strong thermal effects, and when the DKS comb bandwidth becomes as wide as an octave. Depending on the  $Q$ -factors and chip input-output coupling efficiency the power of the pump laser should be also high enough to ensure access to the single-soliton states (see Chapters 2 and 5) and provide a high power-per-line. Finally, the microcomb operation also often needs the usage of stabilization techniques, requiring additional components in order to maintain the DKS state or lock it to atomic resonances.

All of the above establish strict requirements on the supply equipment and infrastructure needed to launch a soliton state and maintain its operation. As an example, a typical laboratory setup used for the generation of the DKS-combs in  $\text{Si}_3\text{N}_4$  microresonators is shown in Fig. 8.1. It comprises a number of bulky devices including a low-noise tunable ECDL, high-power EDFA, oscilloscope, vector network analyzer, optical spectrum analyzers, coupling stage and several optical breadboards with passive optics and photodiodes. As a result, all microcomb applications so far were mostly limited to the laboratory environment with constant monitoring of the system operation, short operation time scales, and the usage of unique, costly and large-scale equipment which invalidated the size, weight and power (SWaP) advantages of the soliton microcomb technology. Another drawback of the present microcombs is that they require a good understanding of DKS physics, significant hands-on experience with the given system as well as with the process of soliton excitation in order to excite the DKS state and maintain it in the operation regime.

Therefore, for further maturing soliton microcombs and making them readily available for industrial and academic users there is a clear need for the compact *standalone* microcomb system, which would include a minimum set of components required for the soliton generation in a microresonator device, and which would clearly demonstrate SWaP advantage of the technology while satisfying the needs of various applications in terms of performance, stability and ease of usage.

Few steps towards such systems have already been made recently with chip-scale laser sources [298, 299, 126]. However, the system operation either was not stable or required additional equipment and a lot of fine-tuning and adjustments for the microcomb operation. Apart from these attempts, to the best of the author's knowledge, no fully standalone microcomb system has been developed so far. On the one hand, such a system can be quite simple and highly application- and microresonator-oriented, because most of the applications do not require large tunability of the optical combs and system variability. This allows the usage of cost-effective OEM components and a significant reduction in the system footprint with respect to the laboratory-based version, shown in Fig. 8.1. On the other hand, in order to maintain the SWaP advantages of the microcombs, the development of such a system still requires a solution of challenging engineering tasks and intelligent software, which would be able to initiate, stabilize and control the system with minimum intervention from the user.

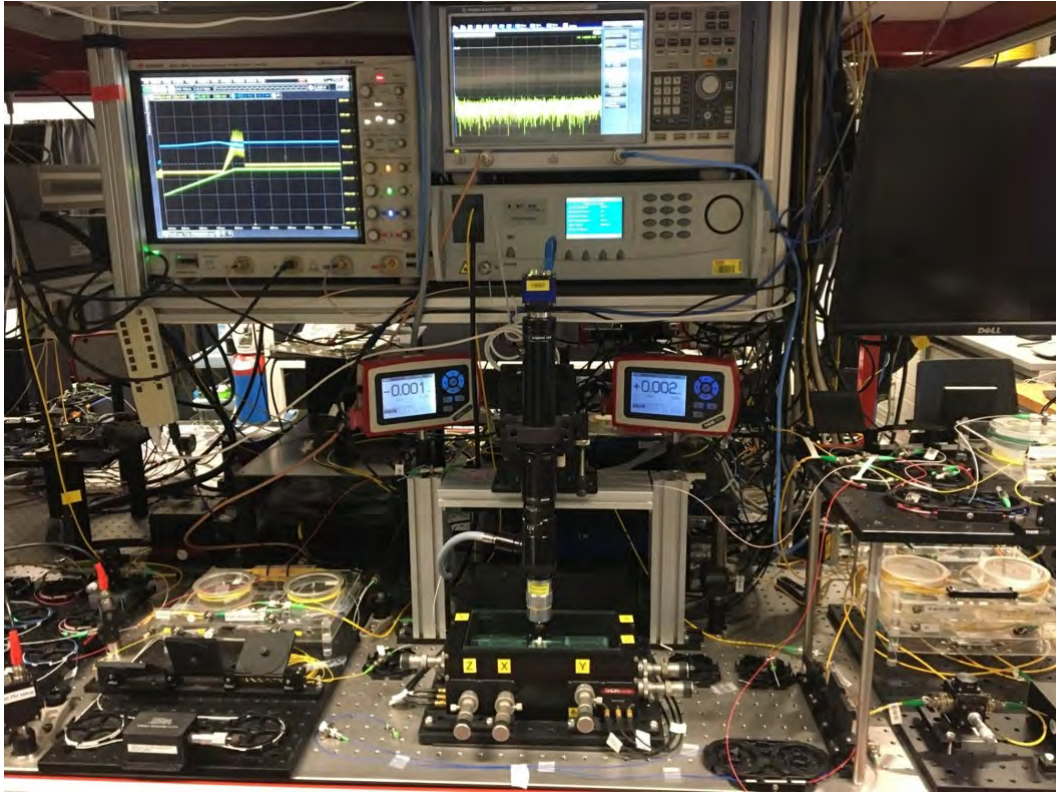


Figure 8.1 – Laboratory setup for the generation of soliton microcombs in  $\text{Si}_3\text{N}_4$  microresonators.

In the following sections we cover two iterations of building such a standalone, fully operational microcomb system. In the first iteration a breadboard-based prototype was built, tested and employed in collaboration with Microsoft Research (UK) in a new microcomb application for data centers - ultrafast optical circuit switching. The aim of the first iteration was to validate the developed system scheme as well as to test the system transportation and operation in a close-to-the field environment. The second iteration, currently in progress, focuses on a rack-mountable unit of the microcomb system, which can be used for the real field deployment, testing of the custom solutions for components and further system optimization. Apart from advancing microcomb technology and opening doors for a variety of real applications, our work is aimed at creating a solid basis for its further industrial development.

## 8.2 Breadboard-based prototype

Since the breadboard-based prototype (further – prototype) has become the first iteration of the standalone microcomb developments process, it was constructed from commercial off-the-shelf components and standard available optical breadboards. This would allow

us to test various available subsystems and choose optimal cost-performance solutions, simplify mounting and space organization as well as maintain system flexibility at the early development stages.

The engineering of such a prototype system consists of multiple aspects, which include the development of the system layout, search and testing of the hardware parts, development of control software, and the microresonator testing and fiber packaging of the chips. Each of these sides of the project are full of challenging tasks, and it should be emphasized that the development of the prototype system was overall a team effort. Many people at LPQM were involved and significantly contributed to the system at its various stages, including Alexandre Goy, Michael Geiselmann, Arslan Raja, Xin Fu and Jordan Wachs.

### 8.2.1 Hardware

The work on the hardware part of the system was primarily aimed at designing a compact system architecture with a minimum set of components, which would enable robust and repeatable launching of DKS states in the chip-integrated devices and guarantee stable operation of the soliton state afterwards. On the other hand, in the first iteration we also wanted to maintain the prototype variability (to be able to replace different components with minimum effort), which would facilitate the process of system integration during the development stage. In addition, this also allowed us to test and compare the performance of different components (e.g. passive fiber optical components, or seed lasers and EDFAs from different vendors), when the system integration is completed. Finally, the prototype board was supposed to be used with different microresonator devices, which, depending on their FSR and other parameters, may require different components.

The hardware part of the prototype consists of two optical breadboards stacked vertically. The two-layered approach is chosen for compactness of the system and convenient access

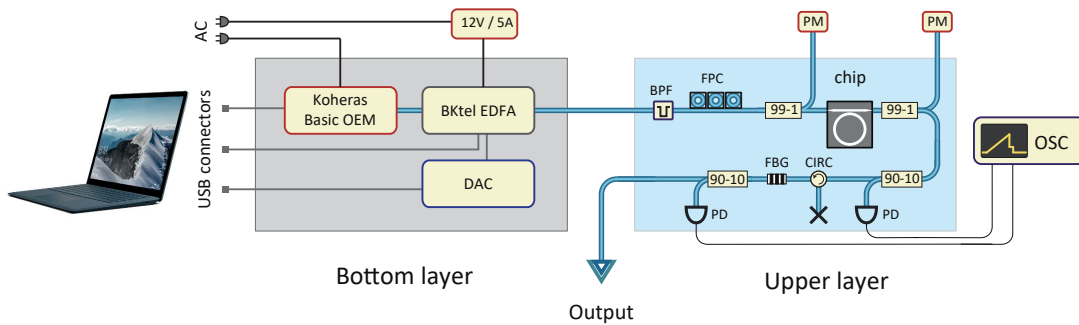


Figure 8.2 – Layouts of the breadboard-based microcomb prototype. The system is organized in two layers and consists of: DAC - Data acquisition board, BPF - bandpass filter, FPC - fiber polarization controller, PM - powermeter, PD - photodiode, FBG - fiber Bragg grating, OSC - oscilloscope.

## 8.2. Breadboard-based prototype

to the equipment requiring the most adjustments during the system testing and operation. The layouts of both boards are schematically shown in Fig. 8.2.

The bottom layer of the breadboard prototype - "backend" - contains all electro-optical components and data acquisition card, which do not require mechanical adjustments and can be fully controlled through the software. The backend is organized on the  $30 \times 45$  cm optical breadboard and includes the seed laser (Koheras Basik C15 - OEM fiber laser, operating at 1550 nm), compact Erbium-doped fiber amplifier (BkTel, OEM EDFA with maximum output power  $> 2$  W) and multifunction I/O device (NI USB 6003, 100 kS/s), used as the data acquisition and driving function generator for the pump laser. The fiber laser was chosen for the prototype due to its compactness, thermal stability and low linewidth, as well as convenient slow (thermal) and fast (piezo) ways of wavelength tuning. They can be successfully used to realize three main procedures required during the excitation of the DKS states - searching for the operational resonance, launching of the initial soliton state and switching to the single soliton state. Despite a rather high output power of the pump laser ( $> 10$  mW), the prototype still relies on the EDFA to amplify the CW seed to the level of 1-2 W, which is aimed at compensating the losses in the passive optical components before the chip and the limited fiber-to-chip couplings efficiency. Apart from these three key components, the system also contains a corresponding power- and interface adapter for the laser, which is intended for convenient communication with the device. We note that the prototype system does not contain any mounted power supplies for active components on the board, which was mainly defined by the speed and convenience of the development process and was changed in the second iteration of the system designed. In the described prototype, an off-board standalone power supply was used for the EDFA and a vendor-supplied power adapter for the laser. The data acquisition board was powered through the USB cable.

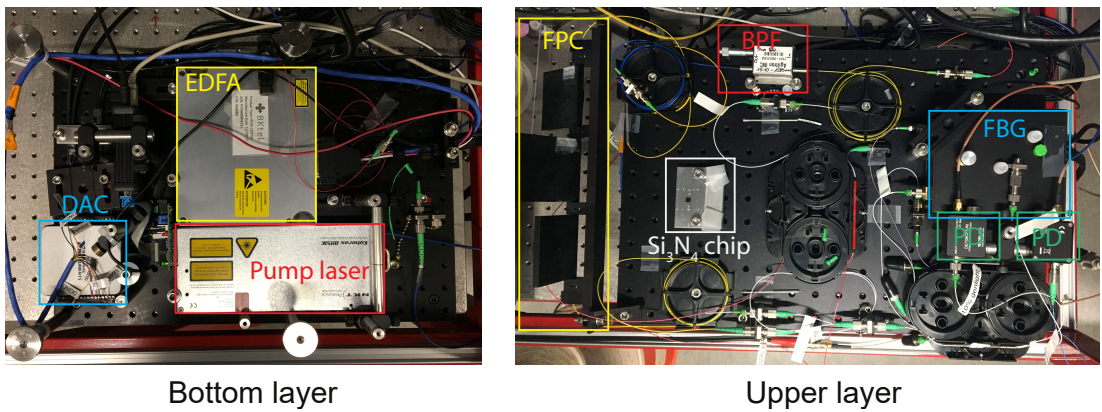


Figure 8.3 – Photos of the prototype system's backend and frontend layers. Components are marked in accordance with Fig. 8.2.

The upper layer of the board - "frontend" - was designed to contain passive fiber optical components, packaged  $\text{Si}_3\text{N}_4$  chip and photodiodes for characterization purposes and

monitoring of the soliton excitation process. Similarly to the backend board it is also organized on the  $30 \times 45$  cm optical breadboard, and consists of individual off-the-shelf components including a bandpass filter (BPF) for ASE noise suppression of the EDFA, fiber polarization controller (FPC), two 99-1 splitters for transmission monitoring purposes, fiber-packaged  $\text{Si}_3\text{N}_4$  microresonator, two 90-10 fiber splitters for characterization and soliton launching, and a circulator and fiber Bragg grating (FBG), for filtering the unused pump light after the chip and preventing its reflection back into the chip. Finally, two photodiodes (Thorlabs DET08CFC/M) are also mounted on the frontend to detect the transmitted and generated lights.

At an early testing stage of the prototype system it relied on the external oscilloscope (OSC) for detecting the transmitted and generated light powers, as shown in Fig. 8.2. However, at later stages the data acquisition was restricted to only generated light, which was implemented through the DAC. We also note that no splicing was performed for the fiber optical components of the setup to reserve the possibility of using different components during the testing phase.

In the current layout of the setup, the light from the CW seed laser is first amplified by the EDFA on the bottom layer. It is then transferred to the frontend layer, where the BPF is used to filter EDFA-induced ASE noise. The polarization is adjusted with the FPC to match the corresponding fundamental waveguide mode (TE or TM). The chip transmission is measured using two off-board powermeters, which allow tracking the transmission fluctuations or long-term drifts. They are used to monitor possible fiber-chip coupling degradation or for preliminary polarization adjustment to match the required modes. The latter is allowed by the transmission selectivity of the corresponding transverse mode families due to the non-unity aspect ratio of the designed on-chip waveguides. After the chip, 10% of the output signal is directly used for the measurements of the transmitted light using the first PD. The rest is directed to the circulator and FBG to filter the strong pump from the comb spectrum and dump it in the beam trap. After the FBG another 10% of the light is used to characterize the generated light, and the rest is available to the user for particular application of the prototype. The final comb power is about 60% of the comb power exiting the chip due to several control taps and fiber connectors.

Figure 8.3 shows the actual view of both prototype layers, where different components are marked. The overall size of the setup after stacking both layers together with cables and fiber organization was  $23 \times 55 \times 35$  cm excluding off-board components.

### 8.2.2 Control software

The control of the prototype system was realized in MATLAB. It includes control of the seed laser, EDFA and data acquisition card (DAC), which were implemented through the corresponding serial or USB interfaces.

## 8.2. Breadboard-based prototype

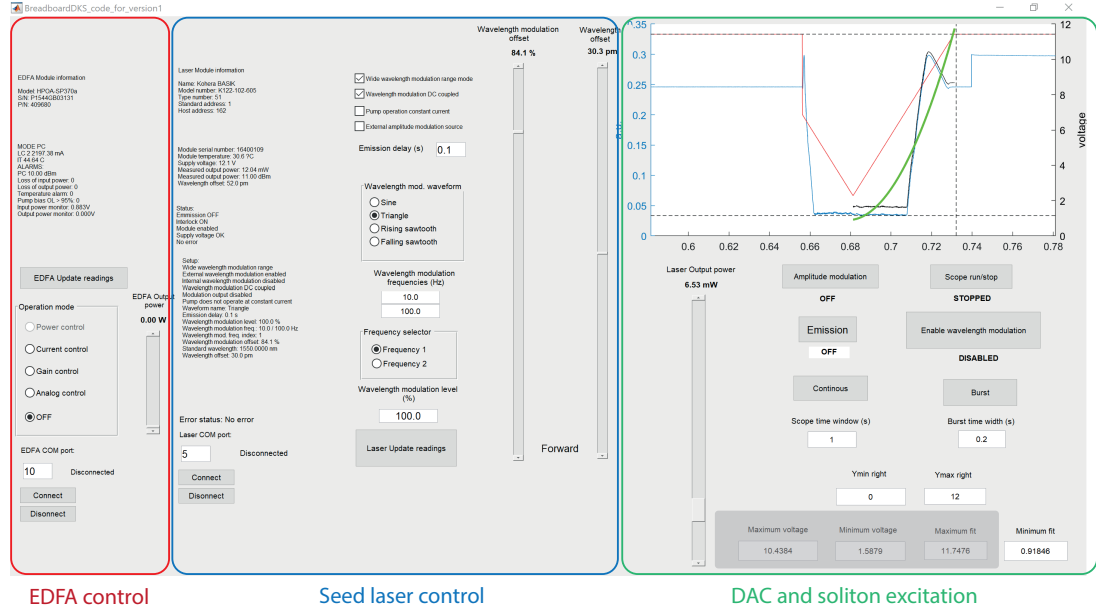


Figure 8.4 – MATLAB-based GUI of the control software developed for the breadboard prototype of the standalone soliton microcomb system. Colored frames indicate control elements of three main active subsystems - seed laser, EDFA and DAC.

The control software is designed to provide access to the key functionality of the corresponding active elements of the prototype enabling the soliton generation. For the pump laser it corresponds to the turning on and off emission, reading internal parameters of the laser, slow temperature tuning of the central wavelength as well as access to the controller of the internal piezo element for fast wavelength tuning. For the EDFA the required control is limited to control of the emission, output power level and reading the internal parameters of the device. The DAC has more versatile functionality. It reads the signal of external photodiode(s) used for the detection of the generated light (transmitted signal and generated light) and provides a driving voltage to the seed laser control input for fast frequency sweeps. Two control sequences of the seed laser tuning were implemented in accordance with the typically required tuning signals used for the soliton launching in laboratory setup. First is the continuous laser scanning (triangular continuous sweep) used for locating the resonance, polarization adjustment and soliton step search. Second - is the single V-shape driving signal (burst) which corresponds to the standard forward tuning technique [9] and allows for DKS state seeding if the initial conditions (burst amplitude and tuning speed) are properly adjusted.

For convenience all controls are organized in a single-window graphical user interface (GUI). The controls are grouped together based on the devices they are used for and augmented with a plot displaying the recorded data traces, which is updated online as the DAC collects new data. The GUI snapshot is shown in Fig. 8.4, where different control components are marked.

### 8.2.3 Microresonator chip packaging

As for the laboratory setup the core element of the prototype is a fiber-packaged  $\text{Si}_3\text{N}_4$  chip with an integrated microring resonator and bus waveguide. The chips are designed for edge-coupling, where the input and output of the integrated optical waveguide are located at the edge facet of the chip. The usual approach of the pump coupling established in LPQM uses the lensed fibers with a short working distance of about 10–20  $\mu\text{m}$  and spot diameter of 3–4  $\mu\text{m}$ . Together with inverse tapering of the integrated waveguide [29], which serves to expand the mode size close to the edge of the chip, one could achieve quite a high coupling efficiency of  $< 1.5$  dB/facet. However, that solution is quite bulky, as it requires precise positioners for lensed fiber alignment. There are also other disadvantages with such contactless fiber coupling. First, there is the significant power-dependency of the coupling due to the thermal expansion of the chip and its holder operating under high pump powers. Second, there is the mechanical oscillations of the fiber tips which can pick up surrounding acoustic noises.

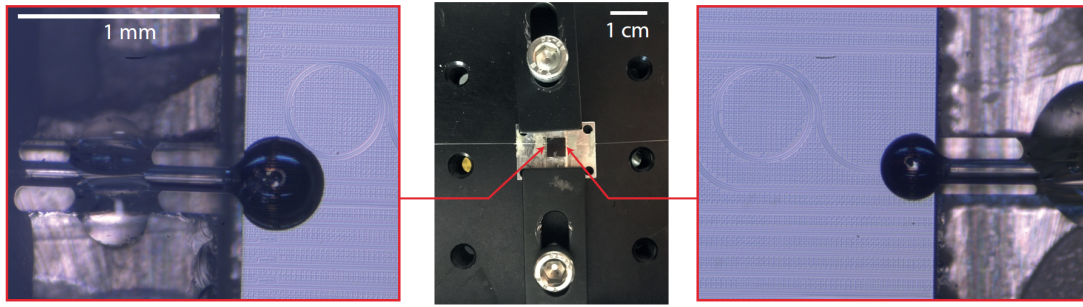


Figure 8.5 – Photographs of the fiber-packaged  $\text{Si}_3\text{N}_4$  chip (middle), and fiber-chip connection points after curing of the glue (left and right). One can observe that the size of the glue drops can be kept well below 1 mm, which potentially can allow packaging of a single chip with multiple fibers. Courtesy to Arslan S. Raja for images of the fiber-chip coupling

In order to avoid these described issues, the lensed fiber approach was changed to fiber butt-coupling, when the fiber tip is brought in direct contact with the chip and fixed with UV glue after optimizing the power transmission. Since the core size of a standard single mode fiber (SMF28) is significantly larger than the mode size at the chip facet, an additional short piece of ultrahigh-numerical-aperture fiber (UHNA) having a smaller fiber core diameter was spliced with the SMF28 to facilitate mode matching at the fiber-chip interface. This allows the fiber to be fixed rigidly against the chip while maintaining a high level of transmission. Besides fiber butt coupling, we also used a bulk aluminum substrate to mount the chip, which enables easy handling of the packaged chip, adds robustness to the package during its mounting in the prototype system and enables fiber gluing to the substrate close to the fiber-chip interfaces in order to reinforce the weakest part of the full assembly. Also, the metal post is designed for mounting of a temperature-sensitive element close to the chip for the thermal stabilization.

Figure 8.5 shows the full packaged chip assembly (center), and two glued fiber-chip interfaces at both sides of the chip (left, right). Due to the small size of the glue drop needed to fix the fiber-chip interface, which takes about 10% of the full chip facet length (5 mm for the current design), mounting of several fibers is possible on both sides of the chip.

After curing of the glue, which can take up to 24 hours, the measured transmission is stable on the order of 10 - 15% for different chips (see Fig. 8.6). Since the beginning of 2018 several chips were packaged and stored in an unprotected environment under room temperature. Regular testings have confirmed the absence of evidence for degradation of the fiber-to-chip coupling efficiency, despite mechanical impacts, transportation between laboratories and occasional short-term operation under high powers of about 2 W.

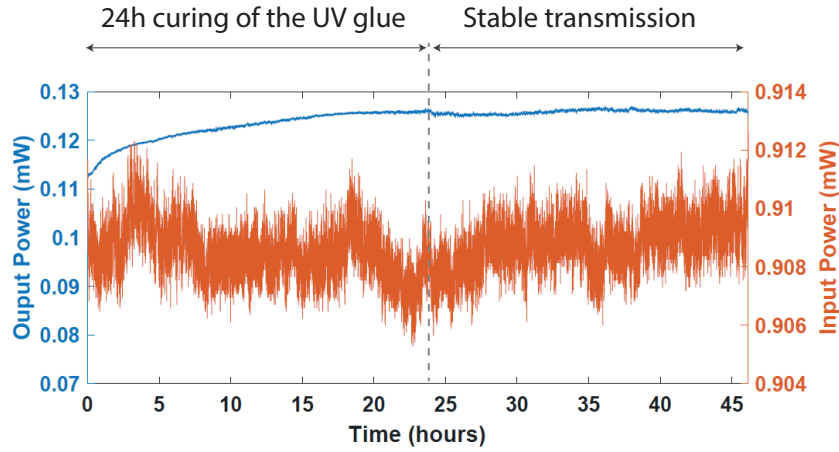


Figure 8.6 – 46-hours long transmission measurements of the fiber-packaged microresonator chip under the load of about 1 W of optical power starting from the fiber gluing moment. The transmission is increased up to more than 12% during first  $\sim 24$  hours, which is the typical passive curing time of cationic UV adhesives. Afterwards the transmission stabilizes.

### 8.2.4 Prototype system testing

For the in-house prototype testing we used several fiber-packaged 100-GHz  $\text{Si}_3\text{N}_4$  chips. The primary goal was to validate the possibility of launching a single soliton state with the developed prototype architecture and software as well as to test the system stability and performance.

To launch the DKS state, the frequency of the seed laser is thermally tuned to the closest resonance of the TE or TM fundamental modes. First, a multiple-soliton state is excited using the burst function for tuning the seed laser. Second, it is followed by a backward tuning [114] for the switching to a single soliton state.

We applied this procedure to three packaged devices - DKS002, DKS004 and DKS005, which were fabricated in different runs and fiber-packaged to the microresonators with different resonator-waveguide gaps. Single soliton states were achieved in all devices (see Fig. 8.7) with input powers of 1-2 W. The resulting comb spectra have maximum power-per-line reaching -17 dBm, estimated OSNR of  $> 45$  dB (0.1 nm bandwidth) and were covering several telecommunication bands, including the C- and L-bands with power-per-line  $> -40$  dBm. We also tested comb postamplification implemented with a C-band compact OEM EDFA (Neptecos) having low input powers. The results are also shown in Fig. 8.7. Due to the impact of the ASE, we observed a significant reduction in the OSNR (to below 35 dB), but the maximum power-per comb line in the C-band was brought to almost milliwatt-level per line.

Furthermore, the stability of the system was verified on the 1 hour scale with the free running system and with no thermal stabilization of the chip.

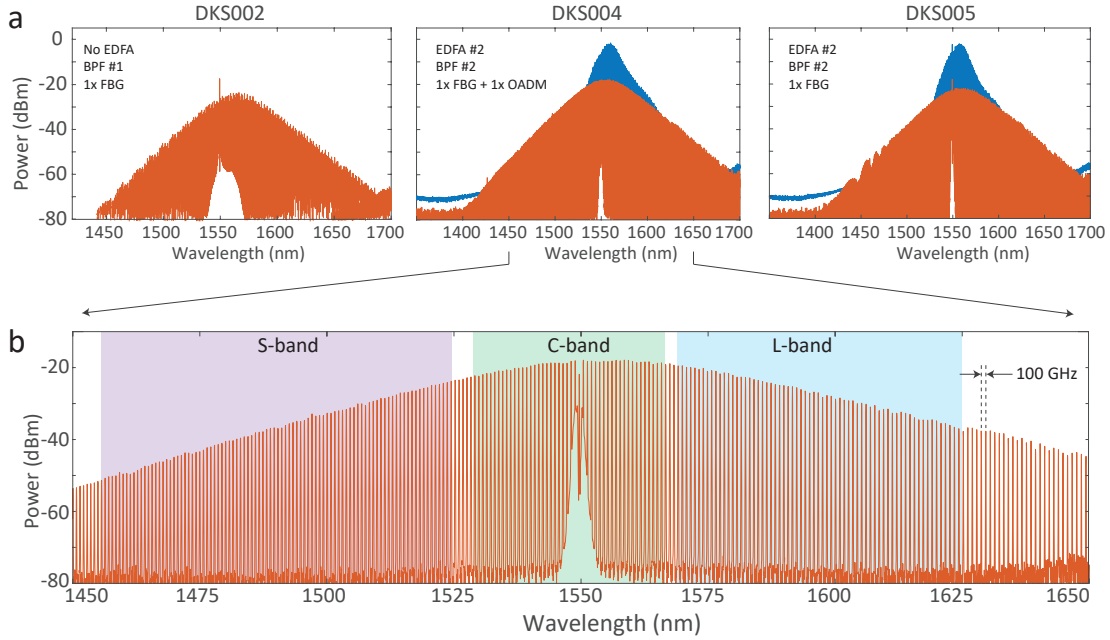


Figure 8.7 – (a) optical spectra of three fiber-packaged  $\text{Si}_3\text{N}_4$  microresonators - DKS002, DKS004 and DKS005 (red), and their amplified spectra (blue). DKS002 was one of the first packaged devices, and was not tested with additional postamplification. Also, devices are tested with different filters (BPF - bandpass filter, FBG - fiber Bragg grating and OADM - optical add-drop multiplexer) to suppress ASE noise from the seed laser EDFA, and suppress the pump after the packaged microresonator. (b) Zoom in of the single soliton spectrum, generated in DKS004 using the breadboard prototype. Colored regions mark three optical telecommunication bands (C-, L- and S-band) covered by the soliton spectrum.

### 8.3 Prototype application in optical circuit switching experiment

The prototype of the standalone microcomb generator developed in the first iteration was employed for a new application of soliton microcombs in data centers - **optical circuit switching** for data center networks (DCNs).

DCN play a key role in a data center by connecting together its resources and forming a backbone of large-scale enterprise applications. Multiple services from leading technological companies such as Google, Facebook or Microsoft rely on massive data centers with hundreds of thousands of servers whose interconnects are critical for service performance. The ability to rapidly switch the network topology and link capacities between server racks is central to adapt to dynamically changing traffic patterns. Current architecture of the traditional DCNs involves a multi-stage system of electrical or hybrid (electrical/optical) switches [300]. These switches are space consuming, lack flexibility, have a limited number of ports and poor intra-server connectivity. Due to multiple conversions of the signal between the optical and electrical domain during the routing of data packets, such an approach can be rather inefficient.

One possible solution to overcome this problem is to implement **optical circuit switching (OCS)** [301, 302]. Different solutions ranging from 3D-MEMs [303] and electro-absorption modulators (EAMs) [304, 305] to arrayed waveguide grating routers (AWGRs) [306] for optical switching in DCNs have been proposed. Today, optical circuit switching is already commercially employed in data centers for top-of-rack (ToR) communication, based on 3D MEMS, which offer a cost effective solution, as the technology is transparent to data speed, protocol independent and offers high bandwidth (up to 100 Gbit/s and beyond). However currently employed 3D MEMS switches have several challenges. First and foremost 3D MEMS switching times are slow, e.g. currently available commercial system CALIENT S320-OCS has a switching time of 50 ms, which is significantly larger than the nanosecond-low latency limit required to handle burst mode data center applications. The full potential of optical circuit switching can only be unfolded with *nanosecond* switching times. A promising data-center architecture that can overcome this, is based on a passive edge (e.g. using a passive multiplexer based on arrayed waveguide gratings (AWG)), and a fast tunable laser. As it is physically impossible to achieve ns switching times with a laser across all telecommunication bands, one can use the same concepts as in WDM: An array of diode lasers emits radiation, and is followed by a bank of electro-absorption modulators (EAMs) [304, 305]. The output of the EAMS is next coupled to an arrayed waveguide grating routers (AWGRs) [306] and transmitted to the passive edge, which routes to the selected ToR. Although these approaches are highly promising, the use of individual laser modules hampers the scalability of channel counts, increasing size, weight and power consumption.

---

<https://www.calient.net/products/s-series-photonic-switch/>

Chip-scale soliton microcombs as the compact multiwavelength sources represent here an ideal solution to replace laser arrays, because they can provide hundreds of equidistantly spaced carriers covering several telecommunication bands, which are also suitable for both coarse WDM (CWDM, channels are 20 nm apart) and dense WDM (DWDM, channels are 25/50/100 GHz apart) transmissions. Among other advantages of the microcombs is their low power consumption in comparison to the laser diodes, CMOS compatibility as well as no need for the guard bands or individual channel control due to the strict spacing of the comb lines.

### 8.3.1 First experimental results

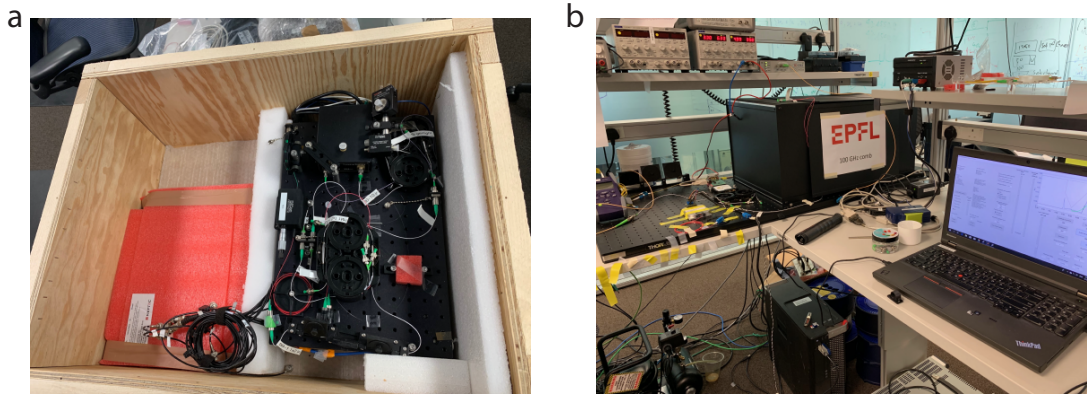


Figure 8.8 – Photographs of the prototype breadboard during shipment (a) and after installation at System and Networking group Microsoft Research (Cambridge, UK)

The optical switching experiment was implemented in collaboration with Microsoft Research Lab (Cambridge, UK) which used our prototype system as the multiwavelength source. The prototype was shipped to Microsoft Research and installed in the laboratory environment with an additional enclosure for laser safety (see Fig. 8.8).

The single-soliton comb state was used in two early-stage experiments for optical switching. Both experiments were implemented with discrete components, when the switching setup consist only of bulk discrete devices such as the arrayed waveguide grating (AWG) and the semiconductor optical amplifiers (SOA) used for ultrafast switching and others. The first experiment was aimed at estimating the switching performance provided by the soliton comb generated in the prototype board. The scheme of the first experiment is shown in Fig. 8.9(a). Here, the soliton comb was first amplified using a C-band EDFA (Neptecos), tested in section 8.2.4, in order to precompensate the insertion losses in following passive components (see spectrum in Fig. 8.9(b)). After amplification, the comb lines are demultiplexed using athermal AWG (DEMUX) and then after adjustment of input polarization are sent to an SOA (SOA-1).

For the testing of the switching, the SOA was continuously turned off and on using

### 8.3. Prototype application in optical circuit switching experiment

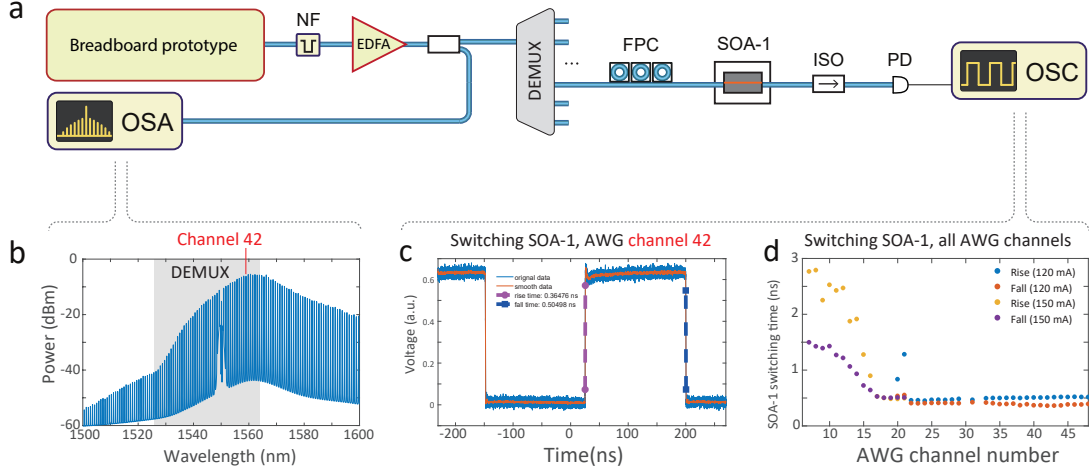


Figure 8.9 – (a) Setup scheme for the single-channel switching experiment with the soliton microcomb breadboard prototype as a source. NF - notch filter, EDFA erbium-doped fiber amplifier, DEMUX - demultiplexer (here an AWG was used as demultiplexer), FPC - fiber polarization controller, SOA-1 - semiconductor optical amplifier, ISO - fiber isolator, PD - photodiode, OSC - oscilloscope, OSA - optical spectrum analyzer. (b) Optical spectrum of the amplified single-soliton state generated in the prototype breadboard in the packaged device DKS005 (100 GHz). Shaded part of the spectrum indicates the spectral coverage of the used AWG. (c) Switching signal of a single channel (channel 42, marked in b with red color), both estimated rise and fall times are on the order of half a nanosecond. (d) Switching rise and fall times for multiple channels available with AWG

an external clock, and the transmission signal was recorded on a 160 GS/s real-time oscilloscope. The resulting switching signal for one of the AWG channels (CH42) is shown in Fig. 8.9(c), and demonstrates that both rise and fall times (10% - 90% of the signal) are below 0.5 ns. Similar measurements were implemented for almost all available channels of the AWG (see Fig. 8.9), except the ones with significantly reduced OSNR around the pump due to leakage of the unfiltered ASE noise. Channels with a higher power-per-comb line, where 120 mA of SOA current was used for switching the channel on and off demonstrate similar performance to CH42 with mean sub-ns switching time. However as we move to the side of the comb spectrum, where the optical power is decreased, and where we have to utilize higher SOA current (150 mA), the mean switching time increases.

In the second experiment multichannel switching was tested. In this experiment, four AWG channels were used at once with respective SOAs (SOA-1... SOA-4). The signal after SOAs was combined in a single fiber and recorded with the fast real-time oscilloscope as in the previous experiment. By consequently turning on different SOAs (a single SOA at a time), the switching between 4 channels was demonstrated in two scenarios - when the channels were either separated by multiple comb lines (see Fig. 8.10(b)) or when they are close to each other (Fig. 8.10(c)).

Further experiments are now in progress, they will include testing of the switching with actual data transmission using NRZ or PAM4 data modulation techniques using similar discrete components. In future, the switching device is supposed to be integrated with an AWG in a single chip-scale system and tested with the next iterations of the standalone microcomb system.

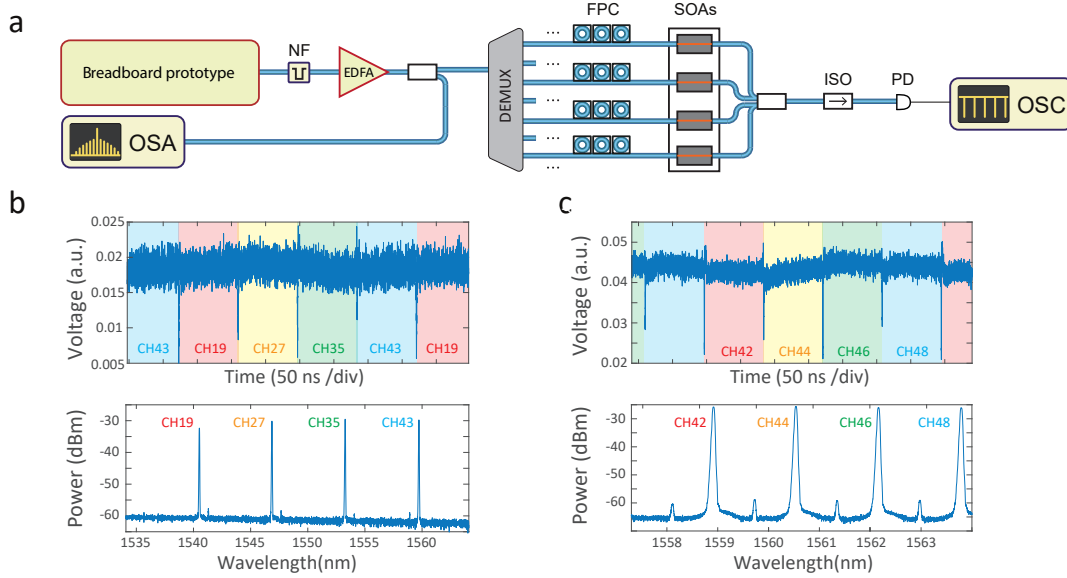


Figure 8.10 – Setup scheme for the multi-channel switching experiment with the soliton microcomb breadboard prototype as a source. Setup elements are marked with the same abbreviations as in Fig. 8.9(a); (b) Multi-channel switching of the channels separated by several nanometers. Top: transmission signal of four AWG channels, which consecutively turned on and off. At each time slot of  $\sim 90$  ns only one of the SOAs is on, and the other are off. Bottom: optical spectrum of 4 used channels, separated by  $\sim 6.4$  nm. (c) The same as (b), but the switching channels are located close to each other.

### 8.4 Rack-mountable microcomb source

After the construction and successful laboratory-based testing (at EPFL and Microsoft Research Lab) of the prototype breadboard described in the previous section, we focused on the second iteration of the standalone microcomb system. In this iteration we aimed at building a more compact version of the prototype board, which would fit in a rack-mountable 19" chassis, and paid particular attention to overall system integration, optimization of interior design and customization of certain components.

The final goal of this iteration is to build a complete fully functional system enclosed in a single chassis with minimum external connections and off-board components, where furthermore the amount of necessary user interventions to the hardware would be reduced to a minimum during the system operation.

## 8.4.1 Hardware

In the second iteration of the standalone soliton microcomb system development several advancements were made with respect to the system architecture and the components used.

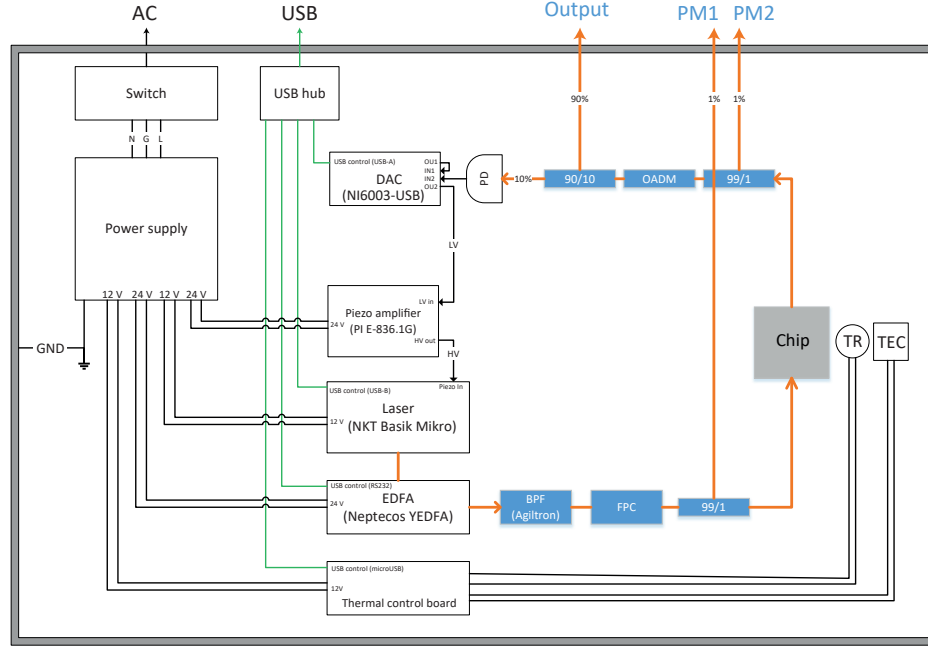


Figure 8.11 – Wiring diagram of the rack-mountable soliton microcomb system. Electro-optical components are shown with white boxes, passive fiber optical components are shown with blue boxes, orange lines indicate optical fibers, electrical connections are shown in green (digital) and black (analog). AC - AC power plug, PM1 and PM2 - powermeters, OADM - optical add-drop multiplexer, BPF - bandpass filter, TR - thermistor, TEC - thermoelectric cooler (Peltier element).

An electro-optical scheme of the standalone microcomb source is shown in Fig. 8.11. It has been changed to increase the compactness, simplicity and level of the system integration in comparison to the first breadboard prototype.

First, we introduced the system enclosure. We use a 19" rack chassis of 3RU height (1RU - 1 rack unit, equals 4.445 cm) with an integrated optical breadboard, which is supposed to facilitate the mounting of the system components inside. Second, we used a more compact version of the seed laser (NKT Koheras Mikro - OEM fiber laser, operating at 1550 nm) and a more compact EDFA (Neptecos, < 2 W) with an additional PCB test/breakout board. Due to the absence of an internal piezo voltage amplifier in the present version of the seed laser, a separate piezo voltage amplifier (PI E-836) was installed in the chassis. For the laser control and data acquisition, we used the same model of the multifunction I/O device (NI USB 6003), which has good enough performance for our purpose. Third,

chip temperature stabilization subsystem, composing of thermoelectric cooler (TEC), thermistor and TEC current driver with PID control, was added to the system. It allows for the stabilization of the chip temperature against environmental temperature fluctuations or compensation of optical-power- induced chip heating with a precision better than 0.01 K. The temperature control of the chip also enables the temperature tuning of the microcavity, which can be used for fine tuning of the FSR or tuning of the absolute resonance positions (e.g. to match the ITU frequency grid). Fourth, an internal switching power supply with multiple outputs of 12 and 24 V was installed in the system to provide power to all active components, distributed from a single standard 220 V power plug. Finally, a compact USB hub is used to route controls of all the components inside the system through the single USB cord connected to an external PC.

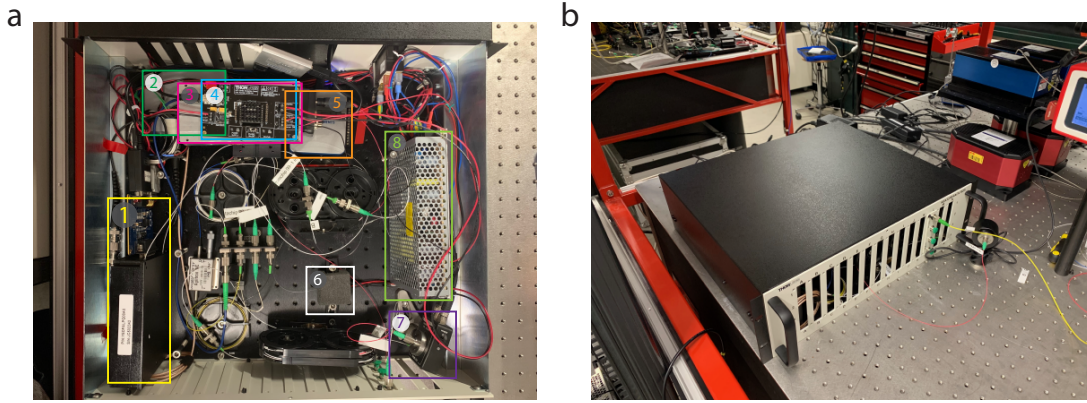


Figure 8.12 – Photographs of the rack-mountable soliton microcomb system. (a) Inside view. Numbered frames indicate system components: 1 - EDFA with additional PCB board, 2 - Piezo voltage amplifier, 3 - NKT Basik Mikro fiber laser, 4 - Thorlabs thermal control board (TEC driver and PID control), 5 - multifunction I/O device NI USB6003, 6 - packaged chip with TEC and thermistor (not visible, because is covered with foam-rubber protection cap), 7 - Thorlabs amplified Photodiode for the generated light measurements. 8 - Power supply unit. (b) Exterior view of the 19"-rack mountable system chassis with output fiber (yellow).

The passive fiber optical part of the system also experienced a few changes in comparison to the prototype. First, after the prototype testing we restrict data acquisition to the generated light, which provides enough information for launching the soliton state and system control. This allowed us to reduce the number of fiber 90:10 splitters and photodiodes to 1 after the packaged chip. We also replaced the bulk tunable FBG with a wavelength-fixed optical add-drop multiplexer (OADM) specified for a given channel of the ITU grid (CH34 for our case of 1550-nm centered seed laser). While reducing the flexibility of the setup it helps to save space in the chassis. The actual layout of the components inside the chassis is shown in Fig. 8.12, where the photographs of top- and front-view of the system are shown. The resulting system has a size of  $450 \times 450 \times 132$  mm, weighs about 15 kg and has  $< 100$  W of power consumption.

### 8.4.2 Software

The control software for the rack-mountable unit was developed based on the software developed in the first iteration. Taking into account experience obtained during the prototype system testing and operation, we have reduced the laser functionality available to potential users and introduced other changes in the GUI concerning the layout of the control elements and representation of the collected transmission traces and tuning voltages. Figure 8.10 shows a GUI snapshot of the main window of the rack mountable unit.

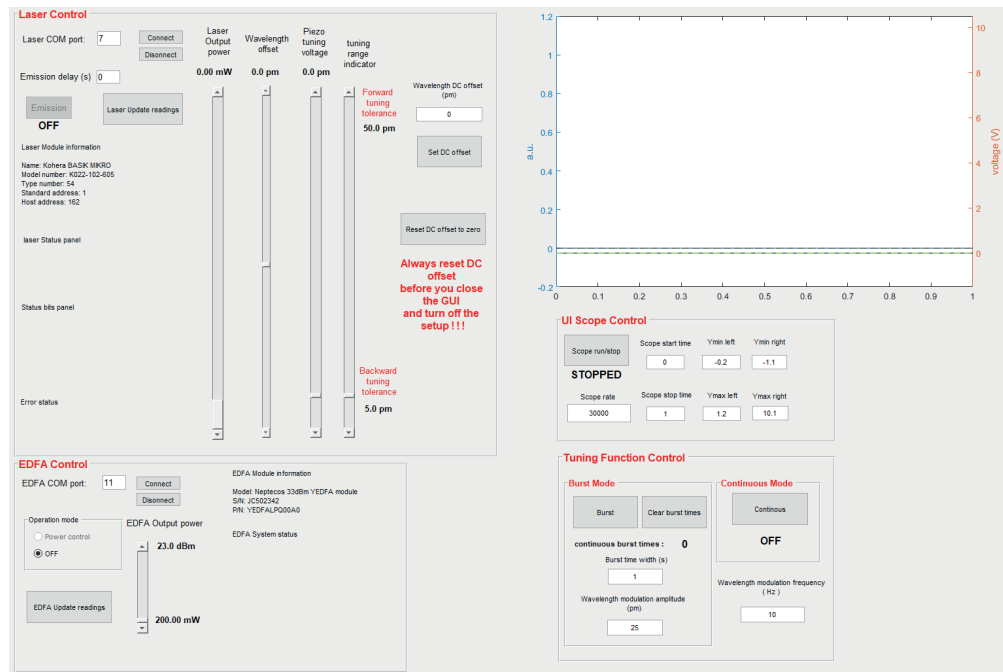


Figure 8.13 – GUI snapshot of the control software developed for the rack-mountable soliton microcomb unit. Control elements of different subsystems (seed laser, EDFA, data acquisition and tuning voltage control) are grouped together.

A new control software is currently being developed using Python 3 in order to avoid the license-demanding MATLAB, and lower the system requirements for the laptop (or PC) used with the setup.

### 8.4.3 Testing

The standalone microcomb system developed in the second iteration has been tested in the laboratory environment with an early fiber-packaged 100-GHz device (DKS002). The soliton generation was demonstrated together with the ability to switch to a single soliton state (see Fig. 8.14) in an enclosed system with only remote access to the system functions. The single-soliton state was shown to maintain long-term operation on an hour-timescale.

Additionally as in the section 8.2.4 we tested an additional compact external EDFA (Boxoptronics, -45 dBm input power)) for the soliton comb postamplification, shown in Fig. 8.14.

After the in-house testing, the system has been successfully shipped and installed at University of Münster in the Laboratory of Responsive Nanosystems (Prof. Wolfram Pernice), where it is planned to be used in experiments on all-optical convolution neural networks with phase-change materials [307, 308].

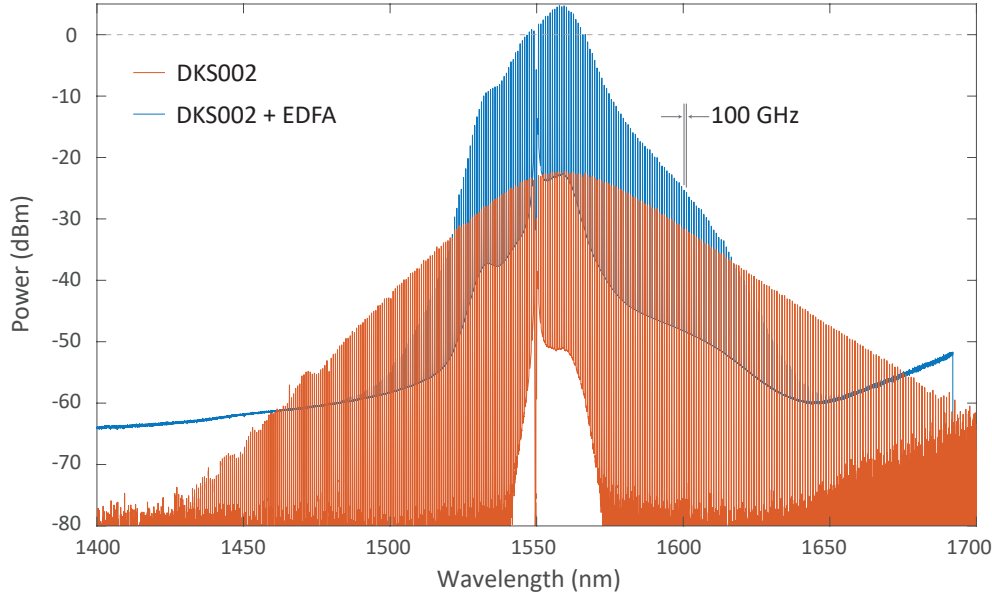


Figure 8.14 – Single soliton state (red) and its amplified spectrum (blue), generated in the DKS002 fiber-packaged device using the rack-mountable soliton microcomb system. An external compact EDFA was used for the amplification. The pump is suppressed with an additional OADM before amplification.

## 8.5 Conclusion

We have implemented two stages of the development process aimed to build a compact standalone soliton microcomb system. In the first stage a fully operational prototype of the system was engineered, tested and is now being used for the optical switching experiments in data center networks. In the second stage we developed and tested an enclosed rack-mountable unit with an optimized system architecture.

Following efforts will be aimed at reducing the size of the system by customizing electronics and mechanical components. We also plan to develop an efficient and compact chip-packaging solution with integrated thermal stabilization, introduce system stabilization and fully automate the excitation of the DKS states.

## 9 Conclusion and Outlook

This Thesis covers a study of the dynamics and applications of Dissipative Kerr solitons in optical microresonators. Chapters 2 - 5 explore several dynamical phenomena arising from nonlinear, thermal and dispersion effects, as well as from intrinsic dynamical complexity of a driven nonlinear microresonator system. The chapters report the appearance of Raman-induced soliton self-frequency shift and its interplay with dispersive wave formation, the phenomenon of soliton switching, which can be induced deterministically using the developed backward tuning procedure together with the VNA-based soliton probing scheme, the formation of soliton breathers and perfect soliton crystals states as well as the exploration of their non-trivial dynamics and stability regimes. Relying on the developed understanding of the system behavior, Chapter 6 demonstrates the formation of dissipative Kerr soliton states covering the biological imaging window. In Chapter 7, single DKS states enabled by the backward tuning procedure in 100 GHz  $\text{Si}_3\text{N}_4$  microresonators are used for two key applications of soliton microcombs – massively parallel coherent optical coherent communication achieving more than 50 Tbit/s data rates, and ultrafast distance measurements with sub-micron precision. Lastly, the first steps towards a standalone soliton microcomb system are reported in Chapter 8, which have already resulted in the employment of the developed prototypes in two new applications – optical circuit switching and all-optical convolution networks.

During the course of this Thesis the field of microresonator-based optical combs has significantly matured. Apart from the rich physics, which has been actively explored in the field over the past years, especially with respect to DKS formation, a multitude of new microresonator platforms and soliton generation techniques have emerged. Soliton microcombs have been employed for a growing number of frequency comb applications to show that they can outperform other modern solutions. Despite such active development, there are still a lot of challenges and perspectives, which can be addressed. We highlight a few among them, which are particularly relevant and interesting in the context of this Thesis:

**Soliton control and manipulation:** while some basic aspects of DKS control and monitoring, including deterministic switching of soliton states and seeding of the perfect soliton crystals, have been demonstrated in this Thesis, the access to direct manipulation of individual DKS pulses (which has been developed for fiber cavities), as well as seeding of predefined soliton formations are still not experimentally achieved. Together with soliton imaging schemes [309, 185, 100], such DKS control would open broad possibilities for the in-depth study of DKS interactions, such as the formation of bound states or complex soliton ensembles. The last ones could be particularly interesting for on-chip all-optical buffers [41], access to the DKS states with controllable FSR (by launching and stabilizing of soliton sets with equidistant temporal separations) or even pump-probe optical spectroscopy techniques.

**Complex microresonator systems:** the majority of the works on Kerr combs and DKS states so far have been mostly focused on systems consisting of a single microresonator. This driven dissipative Kerr-nonlinear system augmented with thermal and other effects (e.g. complex dispersion, second-order nonlinearity, Raman effects or generation of free carriers) already provide a rather complex basis leading to peculiar Kerr-comb dynamics and a rich panel of mode-locked states. However, such single-cavity operation can impose certain limitations on the system performance in terms of the dispersion control, efficiency of the soliton states and others. Instead, by exploring multi-resonator assemblies one may achieve the complex dispersion profiles [310, 311] enabling the formation of DKS states in the visible, boost the conversion efficiency [312], or explore the formation of novel mode-locked states existing over multiple resonators. Furthermore, with the active interest in periodically-driven linear microresonator networks in the rapidly emerging field of topological photonics [313], such multi-cavity systems may be of interest from the perspective of topologically-protected edge state formation in strongly driven nonlinear networks.

**Microcomb miniaturization and photonic integration:** despite recent advances in the understanding of soliton dynamics and a variety of demonstrated applications using DKS states, Kerr comb sources still have to rely on bulky active components, such as laser diodes and amplifiers. Thus, while having the number of advantages over other modern optical comb solutions, soliton microcombs cannot fully realize their potential and remain a laboratory technology. Alongside with the results of this Thesis, a few other steps towards the industrialization of the technology [178, 298, 314, 126] have been already made. However, major engineering challenges still need to be solved in order for this technology to compete with other existing solutions for industrial and research applications. An important direction here is the full photonic system integration, where nonlinear microresonators can be integrated with active optical components and electronics on a single multi-chip assembly to create a versatile DKS comb engine.

# Bibliography

- [1] S. Spillane, T. Kippenberg, and K. Vahala, *Nature* **415**, 621 (2002).
- [2] K. E. Webb, M. Erkintalo, S. Coen, and S. G. Murdoch, *Optics Letters* **41**, 4613 (2016).
- [3] T. J. Kippenberg, S. M. Spillane, and K. J. Vahala, *Phys. Rev. Lett.* **93**, 083904 (2004).
- [4] H. Lee, T. Chen, J. Li, K. Y. Yang, S. Jeon, O. Painter, and K. J. Vahala, *Nature Photonics* **6**, 369 (2012).
- [5] D. Chen, A. Kovach, X. Shen, S. Poust, and A. M. Armani, *Acs Photonics* **4**, 2376 (2017).
- [6] I. S. Grudinin, A. B. Matsko, A. A. Savchenkov, D. Strekalov, V. S. Ilchenko, and L. Maleki, *Optics Communications* **265**, 33 (2006).
- [7] P. Del’Haye, a. Schliesser, O. Arcizet, T. Wilken, R. Holzwarth, and T. J. Kippenberg, *Nature* **450**, 1214 (2007), 0708.0611 .
- [8] P. Del’Haye, S. A. Diddams, and S. B. Papp, *Applied Physics Letters* **102**, 221119 (2013).
- [9] T. Herr, V. Brasch, J. D. Jost, C. Wang, M. Kondratiev, M. L. Gorodetsky, and T. J. Kippenberg, *Nature Photonics* **8**, 145 (2014).
- [10] L. Razzari, D. Duchesne, M. Ferrera, R. Morandotti, S. Chu, B. Little, and D. Moss, *Nature Photonics* **4**, 41 (2010).
- [11] J. Levy, A. Gondarenko, M. Foster, A. Turner-Foster, A. Gaeta, and M. Lipson, *Nat. Photon.* **4**, 37 (2010).
- [12] A. Griffith, R. Lau, J. Cardenas, Y. Okawachi, A. Mohanty, R. Fain, Y. H. D. Lee, M. Yu, C. Phare, C. B. Poitras, A. Gaeta, and M. Lipson, *Nat. Commun.* **6** (2015).

## Bibliography

---

- [13] B. Hausmann, I. Bulu, V. Venkataraman, P. Deotare, and M. Lončar, *Nature Photonics* **8**, 369 (2014).
- [14] H. Jung, C. Xiong, K. Y. Fong, X. Zhang, and H. X. Tang, *Optics letters* **38**, 2810 (2013).
- [15] M. Pu, L. Ottaviano, E. Semenova, and K. Yvind, *Optica* **3**, 823 (2016).
- [16] C. Wang, M. Zhang, M. Yu, R. Zhu, H. Hu, and M. Loncar, *Nature communications* **10**, 978 (2019).
- [17] Y. He, Q.-F. Yang, J. Ling, R. Luo, H. Liang, M. Li, B. Shen, H. Wang, K. Vahala, and Q. Lin, *Optica* **6**, 1138 (2019).
- [18] D. J. Wilson, K. Schneider, S. Hoenl, M. Anderson, T. J. Kippenberg, and P. Seidler, *arXiv preprint arXiv:1808.03554* (2018).
- [19] D. Braje, L. Hollberg, and S. Diddams, *Physical review letters* **102**, 193902 (2009).
- [20] E. Obrzud, S. Lecomte, and T. Herr, *Nature Photonics* **11**, 600 (2017).
- [21] D. Rowland and J. Love, *IEE Proceedings J (Optoelectronics)* **140**, 177 (1993).
- [22] D. Moss, R. Morandotti, L. Gaeta, and M. Lipson, *Nat. Photon.* **7**, 597 (2013).
- [23] Q. Li, M. Davanço, and K. Srinivasan, *Nature Photonics* (2016).
- [24] C. Reimer, M. Kues, P. Roztock, B. Wetz, F. Grazioso, B. E. Little, S. T. Chu, T. Johnston, Y. Bromberg, L. Caspani, *et al.*, *Science* **351**, 1176 (2016).
- [25] G. Moille, X. Lu, A. Rao, Q. Li, D. A. Westly, L. Ranzani, S. B. Papp, M. Soltani, and K. Srinivasan, *arXiv preprint arXiv:1906.06554* (2019).
- [26] V. Brasch, Q.-F. Chen, S. Schiller, and T. J. Kippenberg, *Optics express* **22**, 30786 (2014).
- [27] J. Liu, A. S. Raja, M. H. Pfeiffer, C. Herkommer, H. Guo, M. Zervas, M. Geiselmann, and T. J. Kippenberg, *Optics letters* **43**, 3200 (2018).
- [28] M. H. P. Pfeiffer, A. Kordts, V. Brasch, M. Zervas, M. Geiselmann, J. D. Jost, and T. J. Kippenberg, *Optica* **3**, 20 (2016).
- [29] V. R. Almeida, R. R. Panepucci, and M. Lipson, *Optics letters* **28**, 1302 (2003).
- [30] A. Gondarenko, J. S. Levy, and M. Lipson, *Optics express* **17**, 11366 (2009).
- [31] M. H. P. Pfeiffer, *Photonic Damascene process for integrated high Q microresonator based nonlinear photonic devices*, Ph.D. thesis (2018).

- [32] Z. Ye, K. Twayana, P. A. Andrekson, and V. Torres-Company, arXiv preprint arXiv:1909.10251 (2019).
- [33] M. H. Pfeiffer, J. Liu, A. S. Raja, T. Morais, B. Ghadiani, and T. J. Kippenberg, *Optica* **5**, 884 (2018).
- [34] W. Bogaerts, P. De Heyn, T. Van Vaerenbergh, K. De Vos, S. Kumar Selvaraja, T. Claes, P. Dumon, P. Bienstman, D. Van Thourhout, and R. Baets, *Laser & Photonics Reviews* **6**, 47 (2012).
- [35] J. Heebner, R. Grover, T. Ibrahim, and T. A. Ibrahim, *Optical microresonators: theory, fabrication, and applications*, Vol. 138 (Springer Science & Business Media, 2008).
- [36] J. E. Romain, *Res. Natl Bur. Stand. B* **66**, 97 (1962).
- [37] H. A. Haus, *Waves and fields in optoelectronics* (Prentice-Hall, 1984).
- [38] S. Spillane, T. Kippenberg, O. Painter, and K. Vahala, *Physical Review Letters* **91**, 043902 (2003).
- [39] M. H. Pfeiffer, J. Liu, M. Geiselmann, and T. J. Kippenberg, *Physical Review Applied* **7**, 024026 (2017).
- [40] G. Agrawal, *Nonlinear Fiber Optics*, Academic Press (Academic Press, 2013).
- [41] F. Leo, S. Coen, P. Kockaert, S.-P. Gorza, P. Emplit, and M. Haelterman, *Nat. Photon.* **4**, 471 (2010).
- [42] F. Leo, L. Gelens, P. Emplit, M. Haelterman, and S. Coen, *Optics express* **21**, 9180 (2013).
- [43] P. Del’Haye, O. Arcizet, M. L. Gorodetsky, R. Holzwarth, and T. J. Kippenberg, *Nature Photonics* **3**, 529 (2009).
- [44] J. Liu, V. Brasch, M. H. P. Pfeiffer, A. Kordts, A. N. Kamel, H. Guo, M. Geiselmann, and T. J. Kippenberg, *Opt. Lett.* **41**, 3134 (2016).
- [45] T. Herr, V. Brasch, J. D. Jost, I. Mirgorodskiy, G. Lihachev, M. L. Gorodetsky, and T. J. Kippenberg, *Phys. Rev. Lett.* **113**, 123901 (2014).
- [46] X. Yi, Q.-F. Yang, X. Zhang, K. Y. Yang, X. Li, and K. Vahala, *Nature Communications* **8**, 14869 (2017).
- [47] H. Gibbs, S. McCall, and T. Venkatesan, *Physical Review Letters* **36**, 1135 (1976).
- [48] C. Godey, I. Balakireva, A. Coillet, and Y. Chembo, *Phys. Rev. A* **89**, 063814 (2014).

## Bibliography

---

- [49] K. J. Vahala, *nature* **424**, 839 (2003).
- [50] T. Carmon, L. Yang, and K. Vahala, *Opt. Express* **12**, 4742 (2004).
- [51] V. B. Braginsky, M. L. Gorodetsky, and V. S. Ilchenko, *Physics Letters A* **137**, 393 (1989).
- [52] L. He, Y.-F. Xiao, J. Zhu, S. K. Ozdemir, and L. Yang, *Optics express* **17**, 9571 (2009).
- [53] A. B. Matsko, A. A. Savchenkov, D. Strekalov, V. S. Ilchenko, and L. Maleki, *Phys. Rev. A* **71**, 033804 (2005).
- [54] Y. K. Chembo and N. Yu, *Phys. Rev. A* **82**, 033801 (2010).
- [55] Y. Liu, Y. Xuan, X. Xue, P.-H. Wang, S. Chen, A. J. Metcalf, J. Wang, D. E. Leaird, M. Qi, and A. M. Weiner, *Optica* **1**, 137 (2014).
- [56] X. Xue, Y. Xuan, P.-H. Wang, Y. Liu, D. E. Leaird, M. Qi, and A. M. Weiner, *Laser & Photonics Reviews* **9**, L23 (2015).
- [57] X. Xue, Y. Xuan, Y. Liu, P.-H. Wang, S. Chen, J. Wang, D. E. Leaird, M. Qi, and A. M. Weiner, *Nature Photonics* **9**, 594 (2015).
- [58] T. Hansson, D. Modotto, and S. Wabnitz, *Physical Review A* **88**, 023819 (2013).
- [59] T. Herr, K. Hartinger, J. Riemensberger, C. Wang, E. Gavartin, R. Holzwarth, M. L. Gorodetsky, and T. J. Kippenberg, *Nat. Photon.* **6**, 480 (2012).
- [60] N. L. B. Sayson, K. E. Webb, S. Coen, M. Erkintalo, and S. G. Murdoch, *Optics letters* **42**, 5190 (2017).
- [61] Y. Okawachi, K. Saha, J. Levy, H. Wen, M. Lipson, and A. Gaeta, *Opt. Lett.* **36**, 3398 (2011).
- [62] A. M. Turing, *Bulletin of mathematical biology* **52**, 153 (1990).
- [63] A. Savchenkov, A. Matsko, V. Ilchenko, I. Solomatine, D. Seidel, and L. Maleki, *Phys. Rev. Lett.* **101**, 093902 (2008).
- [64] J. Li, H. Lee, T. Chen, and K. J. Vahala, *Physical review letters* **109**, 233901 (2012).
- [65] S. B. Papp and S. A. Diddams, *Physical Review A* **84**, 053833 (2011).
- [66] F. Ferdous, H. Miao, D. E. Leaird, K. Srinivasan, J. Wang, L. Chen, L. T. Varghese, and A. M. Weiner, *Nat. Photon.* **5**, 770 (2011).
- [67] P.-H. Wang, F. Ferdous, H. Miao, J. Wang, D. E. Leaird, K. Srinivasan, L. Chen, V. Aksyuk, and A. M. Weiner, *Optics express* **20**, 29284 (2012).

- 
- [68] J. Pfeifle, A. Coillet, R. Henri t, K. Saleh, P. Schindler, C. Weimann, W. Freude, I. V. Balakireva, L. Larger, C. Koos, and Y. K. Chembo, *Phys. Rev. Lett.* **114**, 093902 (2015).
- [69] J. Pfeifle, V. Brasch, M. Lauermann, Y. Yu, D. Wegner, T. Herr, K. Hartinger, P. Schindler, J. Li, D. Hillerkuss, R. Schmogrow, C. Weimann, R. Holzwarth, W. Freude, J. Leuthold, T. J. Kippenberg, and C. Koos, *Nat. Photon.* **8**, 375 (2014).
- [70] J. S. Levy, K. Saha, Y. Okawachi, M. A. Foster, A. L. Gaeta, and M. Lipson, *IEEE Photonics Technology Letters* **24**, 1375 (2012).
- [71] P. Grelu, *Nonlinear optical cavity dynamics: from microresonators to fiber lasers* (John Wiley & Sons, 2015).
- [72] L. A. Lugiato and R. Lefever, *Phys. Rev. Lett.* **58**, 2209 (1987).
- [73] M. Haelterman, S. Trillo, and S. Wabnitz, *Opt. Commun.* **91**, 401 (1992).
- [74] K. Ikeda, *Optics communications* **30**, 257 (1979).
- [75] A. Pasquazi, M. Peccianti, L. Razzari, D. J. Moss, S. Coen, M. Erkintalo, Y. K. Chembo, T. Hansson, S. Wabnitz, P. DelHaye, *et al.*, *Physics Reports* **729**, 1 (2018).
- [76] S. Coen, H. Randle, T. Sylvestre, and M. Erkintalo, *Opt. Lett.* **38**, 37 (2013).
- [77] A. Matsko, A. Savchenkov, W. Liang, V. Ilchenko, D. Seidel, and L. Maleki, in *Proceedings of the 7th Symposium Frequency Standards and Metrology* (2009) pp. 539–558.
- [78] A. Matsko, A. Savchenkov, W. Liang, V. Ilchenko, D. Seidel, and L. Maleki, *Opt. Lett.* **36**, 2845 (2011).
- [79] T. Hansson and S. Wabnitz, *JOSA B* **32**, 1259 (2015).
- [80] S. Coen and M. Haelterman, *Physical review letters* **79**, 4139 (1997).
- [81] M. Anderson, Y. Wang, F. Leo, S. Coen, M. Erkintalo, and S. G. Murdoch, *Physical Review X* **7**, 031031 (2017).
- [82] N. J. Zabusky and M. D. Kruskal, *Physical review letters* **15**, 240 (1965).
- [83] N. N. Akhmediev and A. Ankiewicz, “Solitons Around Us: Integrable, Hamiltonian and Dissipative Systems,” in *Optical Solitons: Theoretical and Experimental Challenges*, edited by K. Porsezian and V. C. Kuriakose (Springer Berlin Heidelberg, Berlin, Heidelberg, 2003) pp. 105–126.

## Bibliography

---

- [84] V. Brasch, M. Geiselmann, T. Herr, G. Lihachev, M. H. P. Pfeiffer, M. L. Gorodetsky, and T. J. Kippenberg, *Science* **351**, 357 (2016).
- [85] M. Karpov, M. H. Pfeiffer, and T. J. Kippenberg, arXiv:1706.06445 (2017).
- [86] S. H. Lee, D. Y. Oh, Q.-F. Yang, B. Shen, H. Wang, K. Y. Yang, Y. H. Lai, X. Yi, and K. Vahala, *Nature Communications* **8**, 1295 (2017).
- [87] M. H. P. Pfeiffer, C. Herkommer, J. Liu, H. Guo, M. Karpov, E. Lucas, M. Zervas, and T. J. Kippenberg, *Optica* **4**, 684 (2017).
- [88] M. Yu, Y. Okawachi, A. G. Griffith, M. Lipson, and A. L. Gaeta, *Optica* **3**, 854 (2016).
- [89] Z. Gong, X. Liu, Y. Xu, M. Xu, J. B. Surya, J. Lu, A. Bruch, C. Zou, and H. X. Tang, *Optics letters* **44**, 3182 (2019).
- [90] W. Liang, D. Eliyahu, V. Ilchenko, A. Savchenkov, A. Matsko, D. Seidel, and L. Maleki, *Nature communications* **6** (2015).
- [91] X. Yi, Q.-F. Yang, K. Y. Yang, M.-G. Suh, and K. Vahala, *Optica* **2**, 1078 (2015).
- [92] Z. Lu, W. Wang, W. Zhang, M. Liu, L. Wang, S. T. Chu, B. E. Little, J. Zhao, P. Xie, X. Wang, *et al.*, *Optical Materials Express* **8**, 2662 (2018).
- [93] Z. Gong, A. Bruch, M. Shen, X. Guo, H. Jung, L. Fan, X. Liu, L. Zhang, J. Wang, J. Li, *et al.*, *Optics letters* **43**, 4366 (2018).
- [94] M. Yu, Y. Okawachi, R. Cheng, C. Wang, M. Zhang, A. L. Gaeta, and M. Lončar, arXiv preprint arXiv:1909.00249 (2019).
- [95] S. Wabnitz, *Opt. Lett.* **18**, 601 (1993).
- [96] K. Nozaki and N. Bekki, *Journal of the Physical Society of Japan* **54**, 2363 (1985).
- [97] I. V. Barashenkov and Y. S. Smirnov, *Phys. Rev. E* **54**, 5707 (1996).
- [98] H. Zhou, S. W. Huang, Y. Dong, M. Liao, K. Qiu, and C. W. Wong, *IEEE Photonics Journal* **7**, 1 (2015).
- [99] E. G. A. Lucas, *Physics of Dissipative Kerr Solitons in Optical Microresonators and Application to Low-noise Frequency Synthesis*, Ph.D. thesis (2019).
- [100] A. Dutt, C. Joshi, X. Ji, J. Cardenas, Y. Okawachi, K. Luke, A. L. Gaeta, and M. Lipson, *Science advances* **4**, e1701858 (2018).
- [101] N. Pavlov, S. Koptyaev, G. Lihachev, A. Voloshin, A. Gorodnitskiy, M. Ryabko, S. Polonsky, and M. Gorodetsky, *Nature Photonics* **12**, 694 (2018).

- 
- [102] J. Liu, A. S. Raja, M. Karpov, B. Ghadiani, M. H. Pfeiffer, B. Du, N. J. Engelsen, H. Guo, M. Zervas, and T. J. Kippenberg, *Optica* **5**, 1347 (2018).
  - [103] J. Liu, E. Lucas, J. He, A. S. Raja, R. N. Wang, M. Karpov, H. Guo, R. Bouchand, and T. J. Kippenberg, arXiv preprint arXiv:1901.10372 (2019).
  - [104] V. Brasch, M. Geiselmann, M. H. Pfeiffer, and T. J. Kippenberg, *Optics Express* **24**, 29312 (2016).
  - [105] J. Wang, D. Chen, H. Cai, F. Wei, and R. Qu, *Optics Express* **23**, 7038 (2015).
  - [106] J. R. Stone, T. Briles, T. Drake, D. Spencer, X. Yi, K. Y. Yang, K. Vahala, S. Diddams, and S. Papp, in *Conference on Lasers and Electro-Optics* (Optical Society of America, 2017) p. STu4J.4.
  - [107] C. Joshi, J. K. Jang, K. Luke, X. Ji, S. A. Miller, A. Klenner, Y. Okawachi, M. Lipson, and A. L. Gaeta, *Optics Letters* **41**, 2565 (2016).
  - [108] T. J. Kippenberg, A. L. Gaeta, M. Lipson, and M. L. Gorodetsky, *Science* **361**, eaan8083 (2018).
  - [109] M.-G. Suh, X. Yi, Y.-H. Lai, S. Leifer, I. S. Grudinin, G. Vasisht, E. C. Martin, M. P. Fitzgerald, G. Doppmann, J. Wang, *et al.*, *Nature Photonics* **13**, 25 (2019).
  - [110] P. J. Marchand, J.-J. Ho, M. H. Pfeiffer, J. Liu, C. Hauger, T. Lasser, and T. J. Kippenberg, arXiv preprint arXiv:1902.06985 (2019).
  - [111] M. Yu, Y. Okawachi, A. G. Griffith, M. Lipson, and A. L. Gaeta, *Optics letters* **42**, 4442 (2017).
  - [112] C. Bao, M.-G. Suh, and K. Vahala, *Optica* **6**, 1110 (2019).
  - [113] J. Pfeifle, V. Brasch, M. Lauermann, Y. Yu, D. Wegner, T. Herr, K. Hartinger, P. Schindler, J. Li, D. Hillerkuss, R. Schmogrow, C. Weimann, R. Holzwarth, W. Freude, J. Leuthold, T. J. Kippenberg, and C. Koos, *Nature photonics* **8**, 375 (2014).
  - [114] H. Guo, M. Karpov, E. Lucas, A. Kordts, M. Pfeiffer, V. Brasch, G. Lihachev, V. Lobanov, M. Gorodetsky, and T. Kippenberg, *Nature Physics* **13**, 94 (2017).
  - [115] P. Marin-Palomo, J. N. Kemal, M. Karpov, A. Kordts, J. Pfeifle, M. H. P. Pfeiffer, P. Trocha, S. Wolf, V. Brasch, M. H. Anderson, R. Rosenberger, K. Vijayan, W. Freude, T. J. Kippenberg, and C. Koos, *Nature* **546**, 274 (2016).
  - [116] P. Liao, C. Bao, A. Kordts, M. Karpov, M. H. Pfeiffer, L. Zhang, Y. Cao, A. Al-maiman, A. Mohajerin-Ariaei, M. Tur, *et al.*, *Optics letters* **42**, 3177 (2017).

## Bibliography

---

- [117] A. Fülöp, M. Mazur, A. Lorences-Riesgo, Ó. B. Helgason, P.-H. Wang, Y. Xuan, D. E. Leaird, M. Qi, P. A. Andrekson, A. M. Weiner, *et al.*, *Nature communications* **9**, 1598 (2018).
- [118] P. Liao, C. Bao, A. Kordts, M. Karpov, M. H. Pfeiffer, L. Zhang, Y. Cao, A. Al-maiman, A. Mohajerin-Ariaei, F. Alishahi, *et al.*, *Optics letters* **43**, 2495 (2018).
- [119] M. Mazur, M.-G. Suh, A. Fülöp, J. Schröder, V. Torres-Company, M. Karlsson, K. J. Vahala, and P. A. Andrekson, *arXiv preprint arXiv:1812.11046* (2018).
- [120] Ó. B. Helgason, A. Fülöp, J. Schröder, P. A. Andrekson, A. M. Weiner, *et al.*, *JOSA B* **36**, 2013 (2019).
- [121] N. Kuse, T. Tetsumoto, G. Navickaite, M. Geiselmann, and M. E. Fermann, *arXiv preprint arXiv:1908.07044* (2019).
- [122] L. Stern, J. R. Stone, S. Kang, D. C. Cole, M.-G. Suh, C. Fredrick, Z. Newman, K. Vahala, J. Kitching, S. A. Diddams, *et al.*, *arXiv preprint arXiv:1812.09789* (2018).
- [123] A. Shchekin, S. Koptyaev, M. Ryabko, A. Medvedev, A. Lantsov, H.-S. Lee, and Y.-G. Roh, *Applied optics* **57**, 632 (2018).
- [124] T. E. Drake, T. C. Briles, J. R. Stone, D. T. Spencer, D. R. Carlson, D. D. Hickstein, Q. Li, D. Westly, K. Srinivasan, S. A. Diddams, *et al.*, *Physical Review X* **9**, 031023 (2019).
- [125] Z. Newman, V. Maurice, T. Drake, J. Stone, T. Briles, D. Spencer, C. Fredrick, Q. Li, D. Westly, B. Ilic, *et al.*, *arXiv preprint arXiv:1811.00616* (2018).
- [126] D. T. Spencer, T. Drake, T. C. Briles, J. Stone, L. C. Sinclair, C. Fredrick, Q. Li, D. Westly, B. R. Ilic, A. Bluestone, *et al.*, *Nature* **557**, 81 (2018).
- [127] E. Lucas, P. Brochard, R. Bouchand, S. Schilt, T. Südmeyer, and T. J. Kippenberg, *arXiv preprint arXiv:1903.01213* (2019).
- [128] J. D. Jost, T. Herr, C. Lecaplain, V. Brasch, M. H. P. Pfeiffer, and T. J. Kippenberg, *Optica* **2**, 706 (2015).
- [129] P. Del’Haye, A. Coillet, T. Fortier, K. Beha, D. C. Cole, K. Y. Yang, H. Lee, K. J. Vahala, S. B. Papp, and S. A. Diddams, *Nature Photonics* (2016), 10.1038/nphoton.2016.105.
- [130] V. Brasch, E. Lucas, J. D. Jost, M. Geiselmann, and T. J. Kippenberg, *Light: Science & Applications* **6**, e16202 (2017).
- [131] J. Wu, X. Xu, T. G. Nguyen, S. T. Chu, B. E. Little, R. Morandotti, A. Mitchell, and D. J. Moss, *IEEE Journal of Selected Topics in Quantum Electronics* **24**, 1 (2018).

- 
- [132] X. Xu, J. Wu, T. G. Nguyen, T. Moein, S. T. Chu, B. E. Little, R. Morandotti, A. Mitchell, and D. J. Moss, *Photonics Research* **6**, B30 (2018).
  - [133] X. Xue, Y. Xuan, H.-J. Kim, J. Wang, D. E. Leaird, M. Qi, and A. M. Weiner, *Journal of Lightwave Technology* **32**, 3557 (2014).
  - [134] X. Xu, M. Tan, J. Wu, T. G. Nguyen, S. T. Chu, B. E. Little, R. Morandotti, A. Mitchell, and D. J. Moss, *APL Photonics* **4**, 026102 (2019).
  - [135] X. Xu, J. Wu, M. Shoeiby, T. G. Nguyen, S. T. Chu, B. E. Little, R. Morandotti, A. Mitchell, and D. J. Moss, *Apl Photonics* **2**, 096104 (2017).
  - [136] X. Ji, X. Yao, A. Klenner, Y. Gan, A. L. Gaeta, C. P. Hendon, and M. Lipson, *Optics express* **27**, 19896 (2019).
  - [137] E. Obrzud, M. Rainer, A. Harutyunyan, M. H. Anderson, J. Liu, M. Geiselmann, B. Chazelas, S. Kundermann, S. Lecomte, M. Cecconi, *et al.*, *Nature Photonics* **13**, 31 (2019).
  - [138] I. Coddington, N. Newbury, and W. Swann, *Optica* **3**, 414 (2016).
  - [139] V. Ataie, P. P. Kuo, A. Wiberg, Z. Tong, C. Huynh, N. Alic, and S. Radic, *Optical Fiber Communication Conference/National Fiber Optic Engineers Conference 2013*, OTh3D.2 (2013).
  - [140] T. Ideguchi, S. Holzner, B. Bernhardt, G. Guelachvili, N. Picqué, and T. W. Hänsch, *Nature* **502**, 355 (2013).
  - [141] M.-G. Suh, Q.-F. Yang, K. Y. Yang, X. Yi, and K. Vahala, *Science* **6516**, 600 (2016).
  - [142] M. Yu, Y. Okawachi, A. G. Griffith, N. Picqué, M. Lipson, and A. L. Gaeta, *Nature communications* **9**, 1869 (2018).
  - [143] M. Yu, Y. Okawachi, A. G. Griffith, M. Lipson, and A. L. Gaeta, in *CLEO: QELS\_Fundamental Science* (Optical Society of America, 2019) pp. JW2A–82.
  - [144] Q.-F. Yang, B. Shen, H. Wang, M. Tran, Z. Zhang, K. Y. Yang, L. Wu, C. Bao, J. Bowers, A. Yariv, *et al.*, *Science* **363**, 965 (2019).
  - [145] M.-G. Suh and K. J. Vahala, *Science* **359**, 884 (2018).
  - [146] P. Trocha, M. Karpov, D. Ganin, M. H. Pfeiffer, A. Kordts, S. Wolf, J. Krockenberger, P. Marin-Palomo, C. Weimann, S. Randel, *et al.*, *Science* **359**, 887 (2018).
  - [147] M. F. Saleh, A. Armaroli, A. Marini, and F. Biancalana, *Optics letters* **40**, 4058 (2015).

## Bibliography

---

- [148] P. Balla, S. Buch, and G. P. Agrawal, JOSA B **34**, 1247 (2017).
- [149] F. Luan, D. Skryabin, A. Yulin, and J. Knight, Optics express **14**, 9844 (2006).
- [150] B.-J. Hong and C.-C. Yang, JOSA B **8**, 1114 (1991).
- [151] H. Haus and M. Nakazawa, JOSA B **4**, 652 (1987).
- [152] V. Serkin, T. Belyaeva, G. Corro, and M. Granados, Quant. Electron. **33**, 456 (2003).
- [153] J. Gordon, Opt. Lett. **11**, 662 (1986).
- [154] N. Akhmediev, W. Krolikowski, and A. Lowery, Opt. Commun. **131**, 260 (1996).
- [155] J. Santhanam and G. Agrawal, Opt. Commun. **222**, 413 (2003).
- [156] A. Yulin and D. Skryabin, Opt. Lett. **31**, 3092 (2006).
- [157] A. Gorbach and D. Skryabin, Opt. Express **16**, 4858 (2008).
- [158] C. Milián, A. V. Gorbach, M. Taki, A. V. Yulin, and D. V. Skryabin, Phys. Rev. A **92**, 033851 (2015).
- [159] L. Zhang, Q. Lin, L. Kimerling, and J. Michel, arXiv:1404.1137 (2014).
- [160] C. Bao, L. Zhang, A. Matsko, Y. Yan, Z. Zhao, G. Xie, A. Agarwal, L. Kimerling, J. Michel, L. Maleki, and A. Willner, Opt. Lett. **39**, 6126 (2014).
- [161] N. Wada, S. Solin, J. Wong, and S. Prochazka, Journal of Non-Crystalline Solids **43**, 7 (1981).
- [162] R. H. Stolen, J. P. Gordon, W. Tomlinson, and H. A. Haus, JOSA B **6**, 1159 (1989).
- [163] M. Erkintalo, Y. Xu, S. Murdoch, J. Dudley, and G. Genty, Phys. Rev. Lett. **109**, 223904 (2012).
- [164] N. Akhmediev and M. Karlsson, Phys. Rev. A **51**, 2602 (1995).
- [165] D. Skryabin, F. Luan, J. Knight, and P. Russell, Science **301**, 1705 (2003).
- [166] S. Vlasov, V. Petrishchev, and V. Talanov, Radiophys. Quantum El. **14**, 1062 (1971).
- [167] Q. Lin and G. Agrawal, Opt. Lett. **31**, 3086 (2006).
- [168] X. Liu, C. Xu, W. Knox, J. Chandalia, B. Eggleton, S. Kosinski, and R. Windeler, Opt. Lett. **26**, 358 (2001).

- 
- [169] R. Halir, Y. Okawachi, J. Levy, M. Foster, M. Lipson, and A. Gaeta, *Opt. Lett.* **37**, 1685 (2012).
- [170] H. Zhao, B. Kuyken, S. Clemmen, F. Leo, A. Subramanian, A. Dhakal, P. Helin, S. Severi, E. Brainis, G. Roelkens, and R. Baets, *Opt. Lett.* **40**, 2177 (2015).
- [171] J. P. Epping, T. Hellwig, M. Hoekman, R. Mateman, A. Leinse, R. G. Heideman, A. van Rees, P. J. van der Slot, C. J. Lee, C. Fallnich, *et al.*, *Optics express* **23**, 19596 (2015).
- [172] X. Yi, Q.-F. Yang, K. Y. Yang, and K. Vahala, *Optics letters* **41**, 3419 (2016).
- [173] Q.-F. Yang, X. Yi, K. Y. Yang, and K. Vahala, *Nature Physics* **13**, 53 (2017).
- [174] Y. Wang, M. Anderson, S. Coen, S. G. Murdoch, and M. Erkintalo, *Physical review letters* **120**, 053902 (2018).
- [175] Y. Okawachi, M. Yu, V. Venkataraman, P. M. Latawiec, A. G. Griffith, M. Lipson, M. Lončar, and A. L. Gaeta, *Opt. Lett.* **42**, 2786 (2017).
- [176] H. Jung, Z. Gong, X. Liu, X. Guo, C.-l. Zou, and H. X. Tang, *Optics express* **27**, 22246 (2019).
- [177] X. Liu, C. Sun, B. Xiong, L. Wang, J. Wang, Y. Han, Z. Hao, H. Li, Y. Luo, J. Yan, *et al.*, *ACS Photonics* **5**, 1943 (2018).
- [178] M.-G. Suh, C. Y. Wang, C. Johnson, and K. J. Vahala, *Optics letters* **44**, 1841 (2019).
- [179] M. A. Foster, J. S. Levy, O. Kuzucu, K. Saha, M. Lipson, and A. L. Gaeta, *Opt. Express* **19**, 14233 (2011).
- [180] V. S. Ilchenko, A. A. Savchenkov, A. B. Matsko, and L. Maleki, *Phys. Rev. Lett.* **92**, 043903 (2004).
- [181] I. S. Grudinin, A. B. Matsko, A. A. Savchenkov, D. Strekalov, V. S. Ilchenko, and L. Maleki, *Opt. Commun.* **265**, 33 (2006).
- [182] W. Liang, A. A. Savchenkov, A. B. Matsko, V. S. Ilchenko, D. Seidel, and L. Maleki, *Opt. Lett.* **36**, 2290 (2011).
- [183] A. E. Fomin, M. L. Gorodetsky, I. S. Grudinin, and V. S. Ilchenko, *J. Opt. Soc. Am. B* **22**, 459 (2005).
- [184] E. Lucas, H. Guo, J. D. Jost, M. Karpov, and T. J. Kippenberg, *Physical Review A* **95**, 043822 (2017).
- [185] E. Lucas, M. Karpov, H. Guo, M. Gorodetsky, and T. Kippenberg, *Nature communications* **8**, 736 (2017).

## Bibliography

---

- [186] J. K. Wahlstrand, J. T. Willits, T. R. Schibli, C. R. Menyuk, and S. T. Cundiff, *Opt. Lett.* **32**, 3426 (2007).
- [187] C. Bao, A. C. Funk, C. Yang, and S. T. Cundiff, *Opt. Lett.* **39**, 3266 (2014).
- [188] C.-C. Lee and T. R. Schibli, *Phys. Rev. Lett.* **112**, 223903 (2014).
- [189] A. B. Matsko and L. Maleki, *Phys. Rev. A* **91**, 013831 (2015).
- [190] A. Gasch, B. Wedding, and D. Jager, *Applied Physics Letters* **44**, 1105 (1984).
- [191] C. Bao, J. A. Jaramillo-Villegas, Y. Xuan, D. E. Leaird, M. Qi, and A. M. Weiner, *Phys. Rev. Lett.* **117**, 163901 (2016).
- [192] F. Alishahi, A. Fallahpour, A. Mohajerin-Ariaei, Y. Cao, A. Kordts, M. H. P. Pfeiffer, M. Karpov, A. Almainan, P. Liao, K. Zou, *et al.*, *Optics letters* **44**, 1852 (2019).
- [193] H. Guo, E. Lucas, M. H. P. Pfeiffer, M. Karpov, M. Anderson, J. Liu, M. Geiselmann, J. D. Jost, and T. J. Kippenberg, *Phys. Rev. X* **7**, 041055 (2017).
- [194] P. Parra-Rivas, D. Gomila, M. A. Matías, S. Coen, and L. Gelens, *Phys. Rev. A* **89**, 043813 (2014).
- [195] V. Lobanov, G. Lihachev, T. Kippenberg, and M. Gorodetsky, *Optics express* **23**, 7713 (2015).
- [196] A. Coillet, I. Balakireva, R. Henriet, K. Saleh, L. Larger, J. M. Dudley, C. R. Menyuk, and Y. K. Chembo, *IEEE Photonics Journal* **5**, 6100409 (2013).
- [197] D. C. Cole, E. S. Lamb, P. Del’Haye, S. A. Diddams, and S. B. Papp, *Nature Photonics* **11**, 671 (2017).
- [198] A. B. Matsko, A. A. Savchenkov, and L. Maleki, *Opt. Lett.* **37**, 4856 (2012).
- [199] M. Yu, J. K. Jang, Y. Okawachi, A. G. Griffith, K. Luke, S. A. Miller, X. Ji, M. Lipson, and A. L. Gaeta, *Nature communications* **8**, 14569 (2017).
- [200] E. A. Kuznetsov, *Sov. Phys. Dokl.* **22**, 507 (1977).
- [201] Y. C. Ma, *Studies in Applied Mathematics* **60**, 43 (1979).
- [202] N. N. Akhmediev, V. M. Eleonskii, and N. E. Kulagin, *Theoretical and Mathematical Physics* **72**, 809 (1987).
- [203] J. M. Dudley, G. Genty, F. Dias, B. Kibler, and N. Akhmediev, *Optics express* **17**, 21497 (2009).
- [204] G. Van Simaey, P. Emplit, and M. Haelterman, *Physical review letters* **87**, 033902 (2001).

- 
- [205] E. Fermi, J. Pasta, and S. Ulam, Los Alamos Report LA-1940 **978** (1955).
  - [206] B. Kibler, J. Fatome, C. Finot, G. Millot, G. Genty, B. Wetzel, N. Akhmediev, F. Dias, and J. M. Dudley, Scientific reports **2**, 463 (2012).
  - [207] A. Chabchoub, B. Kibler, J. M. Dudley, and N. Akhmediev, Philosophical Transactions of the Royal Society A: Mathematical, Physical and Engineering Sciences **372**, 20140005 (2014).
  - [208] A. Chabchoub, N. Hoffmann, M. Onorato, and N. Akhmediev, Physical Review X **2**, 011015 (2012).
  - [209] J. M. Dudley, F. Dias, M. Erkintalo, and G. Genty, Nature Photon. **8**, 755 (2014).
  - [210] N. Akhmediev, B. Kibler, F. Baronio, M. Belić, W.-P. Zhong, Y. Zhang, W. Chang, J. M. Soto-Crespo, P. Vouzas, P. Grelu, *et al.*, Journal of Optics **18**, 063001 (2016).
  - [211] M. Yu, J. K. Jang, Y. Okawachi, A. G. Griffith, K. Luke, S. A. Miller, X. Ji, M. Lipson, and A. L. Gaeta, Nature Communications **8** (2017).
  - [212] A. Coillet, J. Dudley, G. Genty, L. Larger, and Y. K. Chembo, Physical Review A **89**, 013835 (2014).
  - [213] M. Anderson, F. Leo, S. Coen, M. Erkintalo, and S. G. Murdoch, Optica **3**, 1071 (2016).
  - [214] T. Herr, M. L. Gorodetsky, and T. J. Kippenberg, “Nonlinear optical cavity dynamics: From microresonators to fiber lasers,” (Wiley, 2016) Chap. Dissipative Kerr Solitons in Optical Microresonators, p. 456.
  - [215] J. A. Jaramillo-Villegas, X. Xue, P.-H. Wang, D. E. Leaird, and A. M. Weiner, Opt. Express **23**, 9618 (2015).
  - [216] D. Turaev, A. G. Vladimirov, and S. Zelik, Physical Review Letters **108**, 1 (2012).
  - [217] Y. Wang, F. Leo, J. Fatome, M. Erkintalo, S. G. Murdoch, and S. Coen, Optica **4**, 855 (2017).
  - [218] B. A. Malomed, in *Large Scale Structures in Nonlinear Physics* (Springer, 1991) pp. 288–294.
  - [219] B. A. Malomed, Physical Review A **45**, R8321 (1992).
  - [220] B. A. Malomed, Physical Review E **47**, 2874 (1993).
  - [221] K. Luo, Y. Xu, M. Erkintalo, and S. G. Murdoch, Optics letters **40**, 427 (2015).
  - [222] S. Kelly, Electronics Letters **28**, 806 (1992).

## Bibliography

---

- [223] H. Taheri, A. B. Matsko, and L. Maleki, *The European Physical Journal D* **71**, 153 (2017).
- [224] W. Wang, Z. Lu, W. Zhang, S. T. Chu, B. E. Little, L. Wang, X. Xie, M. Liu, Q. Yang, L. Wang, *et al.*, *Optics letters* **43**, 2002 (2018).
- [225] A. Kordts, M. H. P. Pfeiffer, H. Guo, V. Brasch, and T. J. Kippenberg, *Optics Letters* **41**, 452 (2016).
- [226] K. Luke, A. Dutt, C. B. Poitras, and M. Lipson, *Optics Express* **21**, 22829 (2013).
- [227] I. S. Grudinin, V. Huet, N. Yu, A. B. Matsko, M. L. Gorodetsky, and L. Maleki, *Optica* **4**, 434 (2017).
- [228] M. Karpov, H. Guo, M. Pfeiffer, E. Lucas, M. Geiselmann, M. Anderson, and T. J. Kippenberg, in *Conference on Lasers and Electro-Optics* (Optical Society of America, 2017) p. FTu1D.2.
- [229] Y.-C. Lai and T. Tél, *Transient chaos: complex dynamics on finite time scales*, Vol. 173 (Springer Science & Business Media, 2011).
- [230] X. Yi, Q.-F. Yang, K. Y. Yang, and K. Vahala, *Opt. Lett.* **41**, 2037 (2016).
- [231] M. Karpov, H. Guo, A. Kordts, V. Brasch, M. H. P. Pfeiffer, M. Zervas, M. Geiselmann, and T. J. Kippenberg, *Phys. Rev. Lett.* **116**, 103902 (2016).
- [232] Z. Lu, W. Wang, W. Zhang, S. T. Chu, B. E. Little, M. Liu, L. Wang, C.-L. Zou, C.-H. Dong, B. Zhao, *et al.*, *AIP Advances* **9**, 025314 (2019).
- [233] C. Sun, T. Askham, and J. N. Kutz, *JOSA B* **35**, 1341 (2018).
- [234] Schliesser, Albert and Picque, Nathalie and Hansch, Theodor W., *Nat. Photon.* **6**, 440 (2012).
- [235] A. M. Smith, M. C. Mancini, and S. Nie, *Nature nanotechnology* **4**, 710 (2009).
- [236] W. Drexler, U. Morgner, R. K. Ghanta, F. X. Kärtner, J. S. Schuman, and J. G. Fujimoto, *Nature medicine* **7**, 502 (2001).
- [237] G. Reich, *Advanced drug delivery reviews* **57**, 1109 (2005).
- [238] R. Richards-Kortum and E. Sevick-Muraca, *Annual review of physical chemistry* **47**, 555 (1996).
- [239] M. Siddiqui, B. J. Vakoc, A. Nam, and N. Lippok, in *Conference on Lasers and Electro-Optics* (Optical Society of America, 2017) p. AW4A.2.
- [240] S. B. Papp, K. Beha, P. Del’Haye, F. Quinlan, H. Lee, K. J. Vahala, and S. A. Diddams, *Optica* **1**, 10 (2014).

- 
- [241] F. Quinlan, G. Ycas, S. Osterman, and S. A. Diddams, Review of Scientific Instruments **81**, 063105 (2010).
  - [242] M. Karpov, M. Pfeiffer, and T. J. Kippenberg, in *Conference on Lasers and Electro-Optics* (Optical Society of America, 2017) p. JTh5B.6.
  - [243] K. Saha, Y. Okawachi, J. S. Levy, R. K. Lau, K. Luke, M. A. Foster, M. Lipson, and A. L. Gaeta, Optics express **20**, 26935 (2012).
  - [244] X. Guo, C.-L. Zou, H. Jung, Z. Gong, A. Bruch, L. Jiang, and H. X. Tang, arXiv:1704.04264 (2017).
  - [245] L. Wang, L. Chang, N. Volet, M. H. Pfeiffer, M. Zervas, H. Guo, T. J. Kippenberg, and J. E. Bowers, Laser & Photonics Reviews **10**, 631 (2016).
  - [246] A. Savchenkov, A. Matsko, W. Liang, V. Ilchenko, D. Seidel, and L. Maleki, Nat. Photon. **5**, 293 (2011).
  - [247] Y. Yang, X. Jiang, S. Kasumie, G. Zhao, L. Xu, J. M. Ward, L. Yang, and S. N. Chormaic, Optics Letters **41**, 5266 (2016).
  - [248] C. Herkommer, A. Billat, D. Grassani, H. Guo, M. H. Pfeiffer, C.-S. Bres, and T. J. Kippenberg, arXiv:1704.02478 (2017).
  - [249] Q. Li, T. C. Briles, D. A. Westly, T. E. Drake, J. R. Stone, B. R. Ilic, S. A. Diddams, S. B. Papp, and K. Srinivasan, Optica **4**, 193 (2017).
  - [250] E. M. Frins and W. Dultz, Journal of lightwave technology **15**, 144 (1997).
  - [251] N. R. Newbury, Nat. Photon. **5**, 186 (2011).
  - [252] A. V. Cherenkov, V. E. Lobanov, and M. L. Gorodetsky, Phys. Rev. A **95**, 033810 (2017).
  - [253] D. J. Jones, S. A. Diddams, J. K. Ranka, A. Stentz, R. S. Windeler, J. L. Hall, and S. T. Cundiff, Science **288**, 635 (2000).
  - [254] A. A. Savchenkov, A. B. Matsko, W. Liang, V. S. Ilchenko, D. Seidel, and L. Maleki, Opt. Express **20**, 27290 (2012).
  - [255] D. Dai and M. Zhang, Optics express **23**, 32452 (2015).
  - [256] Y. Zhao, X. Ji, B. Y. Kim, P. Donvalkar, J. Jang, C. Joshi, M. Yu, R. R. Domenegueti, F. A. Barbosa, P. Nussenzveig, *et al.*, in *CLEO: Science and Innovations* (Optical Society of America, 2019) pp. STh3J–1.
  - [257] D. Reinsel, J. Gantz, and J. Rydning, Framingham: International Data Corporation (2018).

## Bibliography

---

- [258] B. Puttnam, R. Luís, W. Klaus, J. Sakaguchi, J.-M. D. Mendinueta, Y. Awaji, N. Wada, Y. Tamura, T. Hayashi, M. Hirano, *et al.*, in *2015 European Conference on Optical Communication (ECOC)* (IEEE, 2015) pp. 1–3.
- [259] V. Ataie, E. Temprana, L. Liu, E. Myslivets, B. P.-P. Kuo, N. Alic, and S. Radic, *Journal of Lightwave Technology* **33**, 694 (2015).
- [260] D. Hillerkuss, R. Schmogrow, M. Meyer, S. Wolf, M. Jordan, P. Kleinow, N. Lindenmann, P. C. Schindler, A. Melikyan, X. Yang, *et al.*, *Journal of Optical Communications and Networking* **4**, 715 (2012).
- [261] E. Temprana, E. Myslivets, B.-P. Kuo, L. Liu, V. Ataie, N. Alic, and S. Radic, *Science* **348**, 1445 (2015).
- [262] C. Weimann, P. Schindler, R. Palmer, S. Wolf, D. Bekele, D. Korn, J. Pfeifle, S. Koeber, R. Schmogrow, L. Alloatti, *et al.*, *Optics express* **22**, 3629 (2014).
- [263] J. Kemal, P. Marin-Palomo, K. Merghem, G. Aubin, C. Calo, R. Brenot, F. Lelarge, A. Ramdane, S. Randel, W. Freude, *et al.*, in *Optical Fiber Communication Conference* (Optical Society of America, 2017) pp. Th5C–3.
- [264] H. Hu, F. Da Ros, M. Pu, F. Ye, K. Ingerslev, E. P. da Silva, M. Nooruzzaman, Y. Amma, Y. Sasaki, T. Mizuno, *et al.*, *Nature Photonics* **12**, 469 (2018).
- [265] J. N. Kemal, J. Pfeifle, P. Marin-Palomo, M. D. G. Pascual, S. Wolf, F. Smyth, W. Freude, and C. Koos, *Optics express* **24**, 25432 (2016).
- [266] T. J. Kippenberg, R. Holzwarth, and S. A. Diddams, *Science* **332**, 555 (2011).
- [267] D. Hillerkuss, R. Schmogrow, T. Schellinger, M. Jordan, M. Winter, G. Huber, T. Vallaitis, R. Bonk, P. Kleinow, F. Frey, *et al.*, *Nature photonics* **5**, 364 (2011).
- [268] F. Chang, K. Onohara, and T. Mizuochi, *IEEE Communications Magazine* **48**, S48 (2010).
- [269] A. Sano, T. Kobayashi, S. Yamanaka, A. Matsuura, H. Kawakami, Y. Miyamoto, K. Ishihara, and H. Masuda, in *National Fiber Optic Engineers Conference* (Optical Society of America, 2012) pp. PDP5C–3.
- [270] R. Dar, S. Chandrasekhar, A. H. Gnauck, B. Li, J. Cho, E. C. Burrows, and P. J. Winzer, in *ECOC 2016; 42nd European Conference on Optical Communication* (VDE, 2016) pp. 1–3.
- [271] M.-C. Amann, T. Bosch, M. Lescure, R. Myllyla, and M. Rioux, *Optical Engineering* **40**, 10 (2001).
- [272] G. Berkovic and E. Shafir, *Advances in Optics and Photonics* **4**, 441 (2012).

- 
- [273] Y.-C. Park and S.-W. Kim, *International Journal of Machine Tools and Manufacture* **34**, 1019 (1994).
- [274] J. Levinson, J. Askeland, J. Becker, J. Dolson, D. Held, S. Kammel, J. Z. Kolter, D. Langer, O. Pink, V. Pratt, *et al.*, in *Intelligent Vehicles Symposium (IV)*, 2011 *IEEE* (IEEE, 2011) pp. 163–168.
- [275] K. Sassen, Z. Wang, and D. Liu, *Journal of Geophysical Research: Atmospheres* **113** (2008).
- [276] R. Li, J. Liu, L. Zhang, and Y. Hang, in *Inertial Sensors and Systems Symposium (ISS)*, 2014 *DGON* (IEEE, 2014) pp. 1–15.
- [277] T. Udem, R. Holzwarth, and T. W. Hänsch, *Nature* **416**, 233 (2002).
- [278] K. Minoshima and H. Matsumoto, *Applied Optics* **39**, 5512 (2000).
- [279] N. Schuhler, Y. Salvadé, S. Lévêque, R. Dändliker, and R. Holzwarth, *Optics Letters* **31**, 3101 (2006).
- [280] I. Coddington, W. C. Swann, L. Nenadovic, and N. R. Newbury, *Nature Photonics* **3**, 351 (2009).
- [281] Y.-S. Jang, G. Wang, S. Hyun, H. J. Kang, B. J. Chun, Y.-J. Kim, and S.-W. Kim, *Scientific Reports* **6**, srep31770 (2016).
- [282] J. K. Doylend, M. Heck, J. T. Bovington, J. D. Peters, L. Coldren, and J. Bowers, *Optics Express* **19**, 21595 (2011).
- [283] J. Sun, E. Timurdogan, A. Yaacobi, E. S. Hosseini, and M. R. Watts, *Nature* **493**, 195 (2013).
- [284] J. C. Hulme, J. K. Doylend, M. J. R. Heck, J. D. Peters, M. L. Davenport, J. T. Bovington, L. A. Coldren, and J. E. Bowers, *Optics Express* **23**, 5861 (2015).
- [285] G. Roelkens, L. Liu, D. Liang, R. Jones, A. Fang, B. Koch, and J. Bowers, *Laser & Photonics Reviews* **4**, 751 (2010).
- [286] M. R. Billah, M. Blaicher, J. N. Kemal, T. Hoose, H. Zwickel, P.-I. Dietrich, U. Troppe, M. Möhrle, F. Merget, A. Hofmann, *et al.*, in *Optical Fiber Communication Conference* (Optical Society of America, 2017) pp. Th5D–6.
- [287] C. Weimann, M. Lauermann, T. Fehrenbach, R. Palmer, F. Hoeller, W. Freude, and C. G. Koos, in *Conference on Lasers and Electro-Optics* (Optical Society of America, 2014) pp. STh4O–3.
- [288] C. S. Joshi, Y. Okawachi, M. Yu, A. Klenner, J. Xingchen, K. Luke, M. Lipson, and A. L. Gaeta, *Conference on Lasers and Electro-Optics*, FTh4D.2 (2017), arXiv:1610.01121 .

## Bibliography

---

- [289] M. Yu, Y. Okawachi, A. G. Griffith, N. Picqué, M. Lipson, and A. L. Gaeta, *Nature communications* **9**, 1869 (2018).
- [290] D. W. Allan, *Proceedings of the IEEE* **54**, 221 (1966).
- [291] *MP84E User Manual M-511.HD Ultra-High-Resolution Positioner*, Physics Instruments.
- [292] P. E. Ciddor, *Applied Optics* **35**, 1566 (1996).
- [293] N. Lindenmann, G. Balthasar, D. Hillerkuss, R. Schmogrow, M. Jordan, J. Leuthold, W. Freude, and C. Koos, *Optics Express* **20**, 17667 (2012).
- [294] P.-I. Dietrich, M. Blaicher, I. Reuter, M. Billah, T. Hoose, A. Hofmann, C. Caer, R. Dangel, B. Offrein, U. Troppenz, *et al.*, *Nature Photonics* **12**, 241 (2018).
- [295] Z. Ye, A. Fülöp, Ó. B. Helgason, P. A. Andrekson, *et al.*, *Optics Letters* **44**, 3326 (2019).
- [296] L. Chang, W. Xie, H. Shu, Q. Yang, B. Shen, A. Boes, J. D. Peters, W. Jin, S. Liu, G. Moille, *et al.*, arXiv preprint arXiv:1909.09778 (2019).
- [297] C. Kachris and I. Tomkos, *IEEE Communications Surveys & Tutorials* **14**, 1021 (2012).
- [298] A. S. Raja, A. S. Voloshin, H. Guo, S. E. Agafonova, J. Liu, A. S. Gorodnitskiy, M. Karpov, N. G. Pavlov, E. Lucas, R. R. Galiev, *et al.*, *Nature communications* **10**, 680 (2019).
- [299] B. Stern, X. Ji, Y. Okawachi, A. L. Gaeta, and M. Lipson, *Nature* **562**, 401 (2018).
- [300] M. Al-Fares, A. Loukissas, and A. Vahdat, **38**, 63 (2008).
- [301] R. Takahashi, T. Nakahara, K. Takahata, H. Takenouchi, T. Yasui, N. Kondo, and H. Suzuki, *J. Opt. Netw.* **3**, 914 (2004).
- [302] N. Calabretta and W. Miao, *Optical Switching in Next Generation Data Centers*, edited by F. Testa and L. Pavesi (Springer International Publishing, Cham, 2018) pp. 45–69.
- [303] S. Han, T. J. Seok, N. Quack, B.-W. Yoo, and M. C. Wu, *Optica* **2**, 370 (2015).
- [304] T. Segawa, M. Nada, M. Nakamura, Y. Suzaki, and R. Takahashi, *39th European Conference and Exhibition on Optical Communication (ECOC 2013)*, , 1 (2013).
- [305] Y. Muranaka, T. Segawa, Y. Ogiso, T. Fujii, and R. Takahashi, *IEEE Photonics Journal* **8**, 1 (2016).
- [306] Y. D. Jin, Q. Jiang, and M. Kavehrad, *IEEE Photonics Technology Letters* **7**, 1210 (1995).

- [307] C. Ríos, M. Stegmaier, P. Hosseini, D. Wang, T. Scherer, C. D. Wright, H. Bhaskaran, and W. H. Pernice, *Nature Photonics* **9**, 725 (2015).
- [308] M. Stegmaier, C. Rios, H. Bhaskaran, and W. H. Pernice, *ACS Photonics* **3**, 828 (2016).
- [309] X. Yi, Q.-F. Yang, K. Y. Yang, and K. Vahala, *Nature communications* **9**, 3565 (2018).
- [310] S. Kim, K. Han, C. Wang, J. A. Jaramillo-Villegas, X. Xue, C. Bao, Y. Xuan, D. E. Leaird, A. M. Weiner, and M. Qi, *Nature communications* **8**, 372 (2017).
- [311] A. Lukashchuk, F. Gremion, M. Karpov, J. Liu, and T. J. Kippenberg, in *CLEO: QELS\_Fundamental Science* (Optical Society of America, 2019) pp. FF2D–1.
- [312] X. Xue, X. Zheng, and B. Zhou, *Nature Photonics* , 1 (2019).
- [313] T. Ozawa, H. M. Price, A. Amo, N. Goldman, M. Hafezi, L. Lu, M. C. Rechtsman, D. Schuster, J. Simon, O. Zilberberg, *et al.*, *Reviews of Modern Physics* **91**, 015006 (2019).
- [314] B. Stern, X. Ji, Y. Okawachi, A. L. Gaeta, and M. Lipson, *Nature* **562**, 401 (2018).



# Maxim Karpov






**E-mail:** maxim.karpov@epfl.ch  
**Phone:** +41 78 715 5421

**Date of birth:** January 23, 1991  
**Citizenship:** Russian  
**Current address:** EPFL SB IPHYS LPQM1,  
CH-1015 Lausanne,  
Switzerland

## Education

---

Mar 2015 – present	<b>PhD in Physics</b> École Polytechnique Fédérale de Lausanne (EPFL), Laboratory of Photonics and Quantum Measurements	Lausanne, Switzerland
		
Sep 2012 – Jun 2014	<b>MSc in Applied Physics and Mathematics</b> Moscow Institute of Physics and Technology, Department of Physical and Quantum Electronics. <i><b>Thesis:</b></i> “Metal-insulator transition in epitaxial LaMnO <sub>3</sub> films” GPA - 3.94 (4.00)	Moscow, Russia
		
Sep 2008- Jul 2012	<b>BSc in Applied Physics and Mathematics</b> Moscow Institute of Physics and Technology, Department of Physical and Quantum Electronics. <i><b>Thesis:</b></i> “The effect of crystal symmetry on metal-insulator transition in LaMnO <sub>3</sub> thin films” GPA - 3.96 (4.00)	Moscow, Russia
		

## Work experience

---

Sep 2014 – Mar 2015	<b>Trainee</b> , École Polytechnique Fédérale de Lausanne (EPFL), Laboratory of Photonics and Quantum Measurements (Prof. Tobias Kippenberg)	Lausanne, Switzerland
Apr 2011 – Sep 2014	<b>Engineer</b> , Institute of Radio Engineering and Electronics RAS, Thin Film Oxide Electronics Laboratory (Prof. Gennady Ovsyannikov)	Moscow, Russia
Jul 2013 – Sep 2013	<b>Visiting Student Researcher</b> , CalTech, Solid State Ionics and Electroceramics Research Group (Prof. Sossina Haile).	Pasadena (CA), USA
Jan 2013 – Feb 2013	<b>Visiting scientist</b> , Chalmers University of Technology Department of Microtechnology and Nanoscience, Quantum Device Physics Laboratory	Gothenburg, Sweden
Jun 2012 – Sep 2012	<b>Trainee researcher</b> , Fermi National Accelerator Laboratory Technical Division, Magnet system department	Batavia (IL), USA 209

## Achievements

---

- Multiple winner at second and third stage of the All-Russian Olympiads in Physics and Mathematics (2006-2008)
- Multiple Winner of the MIPT Scholarship for Academic Achievements (2009-2011), <http://foundation.phystech.edu>
- PARTI Internship Fermi National Accelerator Laboratory (2012)
- 3-rd prize at Competition of young scientists at IREE RAS (2012)
- 1-st degree diploma at competition of research works of students and graduate students at 55-th Conference MIPT (2012)
- Multiple Winner of the federal grant program of Vladimir Potanin (2012, 2013), <http://www.fondpotanin.ru/>
- Winner of the State Academic Scholarship (MIPT, 2013)
- MC-ITN FACT PhD fellowship (2015 – 2017)
- ESA PhD fellowship (2017 – 2019)

## Additional qualifications

---

Languages	Russian (mother tongue) English (fluent) French (basic knowledge)
Cleanroom trainings	SEM, AFM, PLD, XRD, FIB, photolithography, etching, magnetron sputtering
Simulations & other software	COMSOL, Lumerical, SolidWorks
Programming	Matlab, Python, C